Comenius University Bratislava
Faculty of Mathematics, Physics and Informatics

Measurement of $K^+ \to \pi^+\mu^+\mu^-$ Decay Form Factor and Evaluation of Muon Veto and Charged Hodoscope Efficiencies at NA62 Experiment at CERN

PhD Thesis

Mgr. Ľuboš Bičian

Study field: 1124 Nuclear And Subnuclear Physics
Study program: Nuclear And Subnuclear Physics

Supervisor: **doc. RNDr. Vladimír Černý, CSc.**

Department of Theoretical Physics

Consultant: **Mgr. Michal Koval', PhD.**

European Organization for Nuclear Research

BRATISLAVA, 2019

67077460

Univerzita Komenského v Bratislave
Fakulta matematiky, fyziky a informatiky

ZADANIE ZÁVEREČNEJ PRÁCE

Meno a priezvisko študenta: Mgr. Ľuboš Bičian
Študijný program: jadrová a subjadrová fyzika (Jednoodborové štúdium, doktorandské III. st., denná forma)
Študijný odbor: jadrová a subjadrová fyzika
Typ záverečnej práce: dizertačná
Jazyk záverečnej práce: anglický
Sekundárny jazyk: slovenský

Názov: Measurement of K+ --> pi+ mu+ mu- Decay Form Factor and Evaluation of Muon Veto and Charged Hodoscope Efficiencies at NA62 Experiment at CERN
Meranie form-faktoru rozpadu K+ --> pi+ mu+ mu- a určenie efektivít miónového veta a hodoskopu na NA62 experimente v CERNe

Anotácia: NA62 je kaónový experiment, nachádzajúci sa v laboratóriu CERN, zameraný na štúdium rozpadov kaónov, hlavne veľmi zriedkavého rozpadu K+ --> pi+ nu nu. Cieľom autorovej dizertačnej práce bolo štúdium vlastností zriedkavého rozpadu kaónu K+ --> pi+ mu+ mu-. Autor taktiež vyvinul nástroje na meranie efektivít dvoch NA62 sub-detektorov: MUV3 a CHOD.

Cieľ: Prieskum možností merania parametrov zriedkavého rozpadu nabitého kaónu na pión a miónový pár (K+ --> pi+ mu+ mu-) na experimente NA62. Prieskum vyžaduje vývoj selekcie signálneho rozpadu a uskutočnenie prvotného merania za účelom overenia možnosti získania signifikantnej štatistiky a odhadu hlavných systematických chýb.

Školiteľ: doc. RNDr. Vladimír Černý, CSc.
Konzultant: Mgr. Michal Koval', PhD.
Katedra: FMFI.KTF - Katedra teoretickej fyziky
Vedúci katedry: doc. RNDr. Tomáš Blažek, PhD.

Dátum zadania: 21.02.2014

Dátum schválenia: 14.04.2014

prof. RNDr. Jozef Masarik, DrSc.
garant študijného programu

....
študent školiteľ

67077460

Comenius University in Bratislava
Faculty of Mathematics, Physics and Informatics

THESIS ASSIGNMENT

Name and Surname: Mgr. Ľuboš Bičian
Study programme: Nuclear and Subnuclear Physics (Single degree study, Ph.D. III. deg., full time form)
Field of Study: Nuclear And Subnuclear Physics
Type of Thesis: Dissertation thesis
Language of Thesis: English
Secondary language: Slovak

Title: Measurement of K+ --> pi+ mu+ mu- Decay Form Factor and Evaluation of Muon Veto and Charged Hodoscope Efficiencies at NA62 Experiment at CERN

Annotation: The NA62 is a dedicated kaon experiment located at CERN and focusing on rare decays of positive kaons, mainly the ultra-rare K+ --> pi+ nu nu decay. The goal of the author's dissertation thesis was the measurement of the properties of a rare kaon decay K+ --> pi+ mu+ mu-. In addition to the main measurement, the author developed tools for evaluation of the efficiency of two NA62 sub-detector systems: MUV3 and CHOD.

Aim: Preliminary measurement of parameters of a rare kaon decay K+ --> pi+ mu + mu- at NA62 experiment. The main goals are development of signal event selection and preliminary determination of the decay parameters with the aim to investigate the possibility of acquiring competitive signal sample and to estimate the main contributions to systematic errors.

Tutor: doc. RNDr. Vladimír Černý, CSc.
Consultant: Mgr. Michal Koval', PhD.
Department: FMFI.KTF - Department of Theoretical Physics
Head of department: doc. RNDr. Tomáš Blažek, PhD.

Assigned: 21.02.2014

Approved: 14.04.2014 prof. RNDr. Jozef Masarik, DrSc.
Guarantor of Study Programme

....
Student Tutor

Acknowledgements

I would like to use this place to thank the people without whom this thesis would not have seen the light of day.

I am grateful to Michal Kovaľ and Evgueni Goudzovski for their valuable advice and guidance throughout my studies. I specifically thank Evgueni Goudzovski for suggesting the main topic of this dissertation and for countless discussions on how to improve the analysis. I then thank Michal Kovaľ for his immense help with the finalisation of the selection and discussions about the fitting procedure and systematics.

A separate thanks goes to Christopher Parkinson and Andrew Sturgess, who worked on the same analysis using different dataset, and with whom I collaborated on the development of event selections.

I would also like to thank my supervisor Vladimír Černý for introducing me to the NA62 experiment and for discussions about the analysis, during which many important questions I did not remember to ask myself emerged. I am also grateful to Vladimír Černý, Tomáš Blažek and especially Michal Kovaľ for proofreading the thesis.

I thank the whole NA62 Collaboration for allowing me to use the collected data for this thesis and for all the suggestions I received during the meetings. I thank Comenius University for giving me the place to work and allowing me to teach, which I found to be a challenging, rewarding and entertaining job.

I am immensely grateful to my family and friends for their support and for providing a place to escape from all the work in the last five years. Finally, to Zuzana, for her extraordinary patience and unwavering support I received.

Abstract

NA62 is a cutting-edge kaon experiment located at CERN, focusing primarily on rare decays of positively charged kaons in flight.

The main focus of the presented thesis is the measurement of form factor parameters and the branching fraction of a rare kaon decay $K^+ \to \pi^+\mu^+\mu^-$ ($K_{\pi\mu\mu}$) at the NA62 experiment, using a sub-sample of data collected in 2017. Therefore, a motivation for the measurement, a summary of the theoretical description within the scope of the Chiral Perturbation Theory and a review of the previous measurements of the $K_{\pi\mu\mu}$ decay parameters are given.

The central part of the work contains detailed description of the main $K_{\pi\mu\mu}$ analysis done by the author, together with the derivation and validation of the fitting procedure used to obtain the $K_{\pi\mu\mu}$ form factor parameters. Based on the sample of 3074 observed $K_{\pi\mu\mu}$ event candidates in the dataset, we obtain form factor parameter values $a = -0.564 \pm 0.042$ and $b = -0.797 \pm 0.164$, which gives a model-dependent branching fraction $\mathcal{B}(K_{\pi\mu\mu}) = (9.32 \pm 0.29) \times 10^{-8}$, consistent with the previous measurements.

Low background contamination of the selected signal sample makes the contribution from statistical errors smaller by $\approx$ 10–20% with respect to the currently most precise $K_{\pi\mu\mu}$ measurement performed by the NA48/2 experiment, which collected similar number of $K_{\pi\mu\mu}$ event candidates but with $\approx 3\%$ background contamination.

However, the total systematic uncertainty is of a similar size as the statistical one, which makes the precision of the presented result worse by $\approx$ 10–20% compared to the NA48/2 result. Improvement of systematic uncertainties is crucial for achieving the world-leading measurement in the future, particularly when the full available NA62 dataset, expected to contain at least 5-times more $K_{\pi\mu\mu}$ event candidates than the NA48/2 dataset, is analysed.

In addition to the main $K_{\pi\mu\mu}$ analysis, efficiency evaluation studies for sub-detectors MUV3 and CHOD carried out by the author are summarised in the thesis. The measured efficiencies were monitored during the NA62 data taking in 2016–2018 using the developed tools. Their values were stable over the period and above 99%. The results of MUV3 efficiency measurements are also used in the main $K_{\pi\mu\mu}$ analysis.

The main goal of the NA62 experiment is the measurement of the branching fraction of an ultra-rare $K^+ \to \pi^+\nu\bar{\nu}$ ($K_{\pi\nu\nu}$) decay, sometimes referred to as the "golden decay" due to the fact that it is theoretically very clean and sensitive to contributions of New Physics. These properties make the $K_{\pi\nu\nu}$ decay an excellent probe of the physics beyond the Standard Model. The measurement of the $K_{\pi\nu\nu}$ decay branching fraction is discussed in the thesis and the first result of the analysis performed on the 2016 data sample is summarised.

Keywords: NA62 experiment, rare kaon decays, charged kaon form factor

Abstrakt

Experiment NA62 je špičkovým kaónovým experimentom nachádzajúcim sa v CERN-e, zameraným na štúdium zriedkavých rozpadov nabitých kaónov za letu.

Hlavným cieľom práce je meranie parametrov form-faktoru a pravdepodobnosti zriedkavého kaónového rozpadu $K^+ \to \pi^+\mu^+\mu^-$ ($K_{\pi\mu\mu}$) na NA62 experimente, použitím časti dát z roku 2017. Z tohoto dôvodu práca opisuje motiváciu merania, zhŕňa teoretický opis v rámci chirálnej poruchovej teórie a vymenúva predchádzajúce merania parametrov rozpadu $K_{\pi\mu\mu}$.

Centrálnou časťou práce je detailný opis $K_{\pi\mu\mu}$ analýzy vykonanej autorom, ako aj odvodenie a validovanie fitovacej procedúry použitej na získanie parametrov form faktoru rozpadu $K_{\pi\mu\mu}$. Na základe vzorky 3074 kandidátov na rozpad $K_{\pi\mu\mu}$, pozorovaných v analyzovanej vzorke dát z roku 2017, sme zmerali hodnoty parametrov form-faktoru $a = -0.564 \pm 0.042$ a $b = -0.797 \pm 0.164$, čo dáva hodnotu modelovo závislej pravdepodobnosti rozpadu $\mathcal{B}(K_{\pi\mu\mu}) = (9.32 \pm 0.29) \times 10^{-8}$. Dosiahnuté výsledky sú v zhode s predchádzajúcimi meraniami.

Vďaka nízkej kontaminácii vybranej vzorky pozaďovými rozpadmi sú výsledné štatistické chyby o $\approx$ 10–20% menšie v porovnaní s doteraz najpresnejším meraním $K_{\pi\mu\mu}$ rozpadu vykonaného experimentom NA48/2 na približne rovnako veľkej vzorke $K_{\pi\mu\mu}$ rozpadov, avšak s $\approx$ 3% pozaďových eventov.

Odhad systematických neistôt v našej analýze je však na úrovni štatistických chýb, čo robí výslednú presnosť nášho výsledku o $\approx$ 10–20% horšiu ako v prípade NA48/2. Zníženie systematických chýb je kľúčovým predpokladom na dosiahnutie svetovo významného výsledku, najmä po analyzovaní celého dostupného NA62 datasetu. Očakávaný počet signánlych eventov je aspoň 5-krát väčší ako počet $K_{\pi\mu\mu}$ rozpadov zaznamenaných na NA48/2.

Okrem analýzy $K_{\pi\mu\mu}$ rozpadu autor uskutočnil merania efektivít sub-detektorov MUV3 a CHOD, výsledky ktorých sú taktiež opísané v práci. Efektivity merané vyvinutými nástrojmi boli monitorované počas zberu dát v rokoch 2016–2018. Ich hodnoty sú stabilné a vyššie ako 99%. Výsledky merania efektivity MUV3 sú tiež použité v hlavnej analýze parametrov rozpadu $K_{\pi\mu\mu}$.

Hlavným cieľom NA62 experimentu je meranie tzv. ultra-zriedkavého rozpadu $K^+ \to \pi^+\nu\bar{\nu}$ ($K_{\pi\nu\nu}$), niekedy označovaného za "zlatý rozpad" kvôli čistote jeho teoretickej predpovede a cistlivosti na novú fyziku. Tieto vlastnosti robia rozpad $K_{\pi\nu\nu}$ výborným kandidátom na hľadanie fyziky za Štandardným Modelom. Predložená dizertačná práca opisuje meranie rozpadu $K_{\pi\nu\nu}$ a uvádza výsledky $K_{\pi\nu\nu}$ analýzy vykonanej na dátach zozbieraných v roku 2016.

Kľúčové slová: NA62 experiment, Zriedkavé rozpady kaónov, Form-faktor nabitého kaónu

Contents

Introduction

The Standard Model of particle physics (SM) [1, 2, 3, 4] currently represents our best description of elementary particles and their interactions. The last-to-be observed SM particle was the Higgs boson, discovered in 2012 [5, 6] by the ATLAS [7] and CMS [8] Collaborations at the Large Hadron Collider (LHC) [9] at CERN[1].

The recent confirmation of the existence of the SM Higgs boson [10] is only a single instance of many in which the SM proved to be a successful description of physics at the smallest experimentally accessible scales. Some of the most notable triumphs of the SM were the observation of weak neutral currents in the Gargamelle neutrino experiment [11] or precise measurements of the anomalous magnetic moment of the electron [12]. One can argue however, that despite the overwhelming success of the SM supported by countless experimental tests performed to date, there are still reasons to believe that it is not the final theory of microworld.

On the experimental side, the SM does not contain any candidate particle for the dark matter [13]; it was originally formulated only for massless neutrinos that have been ruled out by discovery of neutrino oscillations [14, 15, 16]; nor does it explain the observed surplus of matter over antimatter in the Universe [17].

On the theory side, the observed fermion masses ranging across many orders of magnitude are only parametrised without any dynamical explanation [18]. Additionally, the SM does not explain charge quantisation, the number of fermionic families and much more.

Although not included in the minimal SM, neutrino oscillations are firmly established phenomenon that requires Lepton Flavour Violation (LFV) in the neutral lepton sector. Despite many efforts of finding charged LFV (cLFV), which would be an indication of New Physics (NP), no cLFV processes have been observed.

Another type of processes that could be affected by NP contributions are those involving Flavour Changing Neutral Currents (FCNC). Consistent with the GIM mechanism [19], there are no FCNC terms in the SM lagrangian. Nevertheless, FCNC processes can be induced at a loop level, where they remain suppressed by the GIM mechanism.

The efforts for the discovery of NP beyond the SM, that should provide explanation for the phenomena not described in the SM framework, are pursued following two separate approaches.

The first one is based on progressively increasing achievable energies in particle accelerators with the aim of discovering new heavy particles. Previously unseen unstable particles could, for example, be observed as resonances in invariant mass spectra of

---

[1] `https://home.cern`

their decay products. Investigations of other quantities such as missing energy or angular distributions could also point towards NP contributions. The ATLAS and CMS experiments are two currently best known examples of such experiments and the Higgs boson discovery followed this approach.

Another method of NP searches relies on improving SM predictions on measurable quantities. Any significant deviations of measurements from the predicted values could indicate the presence of a NP. Contrary to the energy frontier approach described above, hints of NP in the precision frontier would originate from corrections to higher order terms in perturbation expansions caused by the presence of beyond SM particles. One of the best known contemporary representatives of the experiment probing the precision frontier is the LHCb experiment [20] at CERN aiming to discover NP in processes involving b quarks [18]. Recently observed tensions between SM predictions and LHCb measurements in the B-sector [21, 22, 23, 24, 25] could be an indication of NP. Among these, the results suggesting Lepton Flavour Universality Violation (LFUV) [23, 24] are the most interesting ones from the perspective of the presented work. We discuss the above LHCb observations in more detail in subsection 1.3.1.

The NA62 experiment[2] at CERN is another example of an experiment focusing on the precision frontier. The main goal of the experiment are studies of rare decays of charged kaons, mainly the measurement of the branching fraction of an ultra-rare FCNC decay $K^+ \to \pi^+\nu\bar{\nu}$ ($K_{\pi\nu\nu}$). Thanks to the robust design of the NA62 experiment [26], studies of other rare FCNC kaon decays, tests of LFU or searches for forbidden (cLFV) processes are possible in addition to the main physics programme. The NA62 experiment recently finished its first 4-year-long data taking period with the continuation of the experiment after the LHC Long Shutdown 2 (LS2) awaiting approval.

This thesis is divided into four chapters and summarises author's work done during his PhD studies as a member of the NA62 Collaboration.

In the first chapter, a brief history of kaon physics and theoretical motivation for the $K_{\pi\nu\nu}$ branching fraction measurement by the NA62 experiment is given. Furthermore, a summary of the current theoretical description of the $K^\pm \to \pi^\pm l^+ l^-$ ($K_{\pi ll}$) decays is also shown. Measurement of form factor parameters of the muonic decay channel $K^+ \to \pi^+\mu^+\mu^-$ ($K_{\pi\mu\mu}$) is the main goal of this dissertation. The $K_{\pi\mu\mu}$ form factor measurement could be used to test the LFU by comparing the $K_{\pi\mu\mu}$ results to those obtained from the electron mode $K^+ \to \pi^+e^+e^-$ ($K_{\pi ee}$).

The second chapter is the central part of the thesis and contains full description of the NA62 detector setup and the author's $K_{\pi\mu\mu}$ analysis. The fitting procedure derived in order to obtain the form factor parameters is described in Appendix B together with the method used for the validation of the procedure.

---

[2] `https://na62.web.cern.ch/na62/`, [26]

In the third chapter, MUV3 and CHOD sub-detector efficiency measurement tools, developed by the author in the first two years of his PhD studies, are described. Resulting outputs from these tools are shown and a description of the treatment of the measured efficiencies in the main $K_{\pi\mu\mu}$ analysis is given.

In the last chapter, a summary of the $K_{\pi\nu\nu}$ analysis performed on the 2016 dataset is presented and prospects for the future are summarised.

1 Kaon Decay Physics: Motivation and Theory

This chapter is split into three sections. The first section contains a short introduction to the kaon physics and emphasises the important role it played in the development of the current state of particle physics. In the second section, a theoretical motivation for the study of $K \to \pi\nu\bar{\nu}$ decays is laid out. Also, a brief overview of the theory describing the charged kaon decay mode $K^+ \to \pi^+\nu\bar{\nu}$ is given together with the previous measurements of its branching fraction. The last section contains a summary of the theoretical description of charged kaon decays $K^\pm \to \pi^\pm l^+ l^-$, explains the motivation for their measurements as an experimental test of the LFU and mentions previous experimental results regarding these decays.

1.1 Historical Overview

Several years after the discovery of previously unobserved *charged* and *neutral* particles in cosmic rays by Rochester and Butler in 1947 [27], particle physicists were intrigued by a phenomenon that now bears the name $\tau - \theta$ puzzle: a charged particle was decaying into two final states of different parity P. Since, at that time, parity was assumed to be one of the fundamental symmetries of Nature, it was theorised that the mysterious particle was in fact two particles τ^+ ($P = -1$) and θ^+ ($P = 1$), each decaying into one of the parity eigenstates

$$\begin{aligned} &\theta^+ \to \pi^+ + \pi^0, \\ &\tau^+ \to \pi^+ + \pi^+ + \pi^- \ . \end{aligned} \tag{1.1}$$

It was however unclear why Nature would "allow" the existence of two, in almost every way identical particles, differing only in their parity. A possible solution to this puzzle came from theoretical physicists Lee and Yang. After reviewing the available literature, they concluded that the contemporary experimental evidence did neither prove, nor disprove the parity conservation in weak interactions. In 1956, Lee and Yang proposed that maybe parity was indeed not conserved [28]. Subsequent confirmation of parity violation in weak interactions performed by an experiment led by Wu later that year [29] resulted in Nobel Prize for Lee and Yang[1]. The τ^+ and θ^+ were in fact one particle,

---

[1] Let us mention that the charge conjugation C is also violated in weak interactions. This is easily seen by the non-existence of left-handed anti-neutrinos and right-handed neutrinos, into which the left-handed neutrinos and right-handed anti-neutrinos are transformed by charge conjugation, respectively.

now called the positive kaon K^+. The antiparticle to K^+ is the negatively charged kaon K^-.

Additionally, the cross sections for creation processes of kaons and several other hadrons coupled with their relatively large masses indicated much shorter lifetimes than those actually observed [30, 31]. The difference in the creation and decay rates of kaons and some baryons (e.g. Λ baryon) was attributed to a new quantum number called *strangeness*. The strangeness was conserved in strong and electromagnetic interactions but violated in weak interactions.

It was not even a decade after the discovery of parity violation that particle physics faced another broken symmetry. This time, it was the violation of the combined symmetry of charge conjugation C and parity inversion P, the CP symmetry. The CP violation was observed in 1964 by Christenson, Cronin, Fitch and Turlay [32] in the decays of one of the two weak eigenstates[2] of neutral kaons, K_L^0 (K-long), into two pions. This decay would be forbidden if the CP symmetry were conserved, since the in- and out-states would be different CP eigenstates.

One possible explanation of experimental observation of the $K_L^0 \to 2\pi$ decay was that the K_L^0 and the other weak eigenstate, K_S^0 (K-short), are in fact *not* CP eigenstates but are rather equal to linear combinations of CP eigenstates $|K_+\rangle$ and $|K_-\rangle$

$$\begin{aligned}|K_S^0\rangle &= \frac{1}{\sqrt{1+\epsilon^2}}\left(|K_+\rangle + \epsilon|K_-\rangle\right),\\ |K_L^0\rangle &= \frac{1}{\sqrt{1+\epsilon^2}}\left(|K_-\rangle + \epsilon|K_+\rangle\right),\end{aligned} \tag{1.2}$$

where ϵ is a small real parameter. This interpretation is currently known as the *indirect* CP violation.

Another possible explanation required non-zero amplitude for the process $K_- \to 2\pi$, i.e. *direct* CP violation. However, experimental results at the time were consistent with the explanation by the indirect CP violation and no other manifestations of CP violation were observed.

In the following decades the Standard Model [1, 2, 3, 4] of particle physics was built and the explanation of non-zero strangeness was found in the presence of strange quarks. In 1973, Kobayashi and Maskawa introduced a unitary 3×3 mixing matrix V_{CKM} called the CKM matrix [33] as a three-family extension of the 2×2 Cabibbo matrix proposed in 1963 by Nicola Cabbibo [34].

---

[2] The neutral kaons are created in their strong (mass) eigenstates $K^0(d\bar{s})$ and $\overline{K^0}(\bar{d}s)$, but decay as the weak eigenstates K_L^0 and K_S^0. The K_L^0 and K_S^0 differ massively in their lifetimes $\tau_{K_L^0} = (5.116 \pm 0.021) \times 10^{-8}$ and $\tau_{K_S^0} = (8.954 \pm 0.004) \times 10^{-11}$, but are very similar, although not identical, in masses: $m_{K_L^0} - m_{K_S^0} = (3.484 \pm 0.006) \times 10^{-12}$ MeV/c^2 [18]. The charged kaons are both created and decay as $K^\pm$.

The CKM matrix, discussed in more detail in Appendix A, mixes the strong/mass quark eigenstates d, s, b into the weak eigenstates d', s', b' and can be expressed in terms of four parameters: three real Euler angles and one complex phase, which introduces the *direct* CP violation into the SM. The direct CP violation was discovered by the NA31 experiment at CERN in studies of rare decays of neutral kaons in 1990s [35]. The discovery was later confirmed by its successor, NA48 [36] and independently by the KTeV experiment [37].

The size of the indirect and direct CP violation contributions to the amplitudes of neutral kaon decays producing pion pairs is given by two parameters ε and ε', related to the ratios of kaon decay amplitudes in the following way [38, 39]

$$\begin{aligned} \varepsilon + \varepsilon' &= \frac{A(K_L \to \pi^+\pi^-)}{A(K_S \to \pi^+\pi^-)}, \\ \varepsilon - 2\varepsilon' &= \frac{A(K_L \to \pi^0\pi^0)}{A(K_S \to \pi^0\pi^0)} \ . \end{aligned} \tag{1.3}$$

The decay amplitude ratios were measured by the NA48 and KTeV experiments, giving the current world average value of ε'/ε [40]

$$\mathrm{Re}\left(\frac{\varepsilon'}{\varepsilon}\right)_{\mathrm{Exp}} = (16.6 \pm 2.3) \times 10^{-4}, \tag{1.4}$$

while the current computations within the SM predict the value

$$\mathrm{Re}\left(\frac{\varepsilon'}{\varepsilon}\right)_{\mathrm{SM}} = (1.9 \pm 4.5) \times 10^{-4}, \tag{1.5}$$

showing $\sim 3\sigma$ discrepancy between the SM prediction and the experimental value.

The world average value for the indirect CP violation parameter is

$$|\varepsilon| = (2.228 \pm 0.011) \times 10^{-3}, \text{ [18]} \ . \tag{1.6}$$

One of the most anticipated results in kaon physics today are measurements of branching fractions of $K \to \pi\nu\bar{\nu}$ decays currently performed at the NA62 experiment at CERN [26, 41] and at the KOTO experiment in Japan [42]. Results from these experiments can be used for independent fit of the full CKM unitarity triangle described in Appendix A. More details are given in the following section 1.2.

Since the presented thesis focuses on positive kaon decays at the NA62 experiment, we list here (Table 1.1) the most relevant charged kaon decay modes together with their measured branching fractions.

Decay mode	Abbreviation	Type	Branching fraction ($\mathcal{B}$)
$K^+ \to \mu^+\nu_\mu$	$K_{\mu 2}$	leptonic	$(63.56 \pm 0.11)\%$
$K^+ \to \pi^+\pi^0$	$K_{2\pi}$	hadronic	$(20.67 \pm 0.08)\%$
$K^+ \to \pi^+\pi^+\pi^-$	$K_{3\pi}$	hadronic	$(5.583 \pm 0.024)\%$
$K^+ \to \pi^0 e^+\nu_e$	K_{e3}	semileptonic	$(5.07 \pm 0.04)\%$
$K^+ \to \pi^0\mu^+\nu_\mu$	$K_{\mu 3}$	semileptonic	$(3.352 \pm 0.033)\%$
$K^+ \to \pi^+\pi^- e^+\nu_e$	K_{e4}	semileptonic	$(4.247 \pm 0.024) \times 10^{-5}$
$K^+ \to \pi^+\pi^-\mu^+\nu_\mu$	$K_{\mu 4}$	semileptonic	$(1.4 \pm 0.9) \times 10^{-5}$
$K^+ \to \pi^+ e^+ e^-$	$K_{\pi ee}$	semileptonic	$(3.00 \pm 0.09) \times 10^{-7}$
$K^+ \to \pi^+\mu^+\mu^-$	$K_{\pi\mu\mu}$	semileptonic	$(9.4 \pm 0.6) \times 10^{-8}$
$K^+ \to e^+\nu_e e^+ e^-$	$K_{e\nu ee}$	leptonic	$(2.48 \pm 0.20) \times 10^{-8}$
$K^+ \to \mu^+\nu_\mu\mu^+\mu^-$	$K_{\mu\nu\mu\mu}$	leptonic	$< 4.1 \times 10^{-7}$ at 90% CL
$K^+ \to \pi^+\nu\bar{\nu}$	$K_{\pi\nu\nu}$	semileptonic	$(1.7 \pm 1.1) \times 10^{-10}$

Table 1.1: Positive kaon decays relevant for this thesis and their measured branching fractions, [18].

1.2 $K \to \pi\nu\bar{\nu}$ Decays

The NA62 experiment at CERN aims to measure the branching fraction of the charged variant of the FCNC $K \to \pi\nu\bar{\nu}$ decays, namely the $K^+ \to \pi^+\nu\bar{\nu}$ decay to a 10% precision. This section describes the current theoretical understanding of this process within the SM framework and possible scenarios of an emergence of beyond the SM physics. Previous experimental measurements of the $K^+ \to \pi^+\nu\bar{\nu}$ decay are discussed as well.

1.2.1 $K \to \pi\nu\bar{\nu}$ in the Standard Model

The semileptonic kaon decays $K \to \pi\nu\bar{\nu}$ are of great interest to the contemporary flavour physics due to their theoretically clean nature [43, 44, 45]. The most recent summary of the physics of these decays has been given in [46] with the theoretical predictions for the $K \to \pi\nu\bar{\nu}$ branching fractions

$$\begin{aligned} \mathcal{B}(K^+ \to \pi^+\nu\bar{\nu})_{\text{SM}} &= (8.4 \pm 1.0) \times 10^{-11}, \\ \mathcal{B}(K_L \to \pi^0\nu\bar{\nu})_{\text{SM}} &= (3.4 \pm 0.6) \times 10^{-11}, \end{aligned} \tag{1.7}$$

where the dominant part of the errors originates from the the uncertainties on the CKM matrix parameters $|V_{cb}|$, $|V_{ub}|$ and γ, as can be seen from the following relations [46]

$$\begin{aligned}
\mathcal{B}(K^+ \to \pi^+\nu\bar{\nu})_{\text{SM}} &= (8.39 \pm 0.30) \times 10^{-11} \left[\frac{|V_{cb}|}{40.7 \times 10^{-3}}\right]^{2.8} \left[\frac{\gamma}{73.2°}\right]^{0.74}, \\
\mathcal{B}(K_L \to \pi^0\nu\bar{\nu})_{\text{SM}} &= (3.36 \pm 0.05) \times 10^{-11} \left[\frac{|V_{ub}|}{3.88 \times 10^{-3}}\right]^{2} \cdot \\
&\cdot \left[\frac{|V_{cb}|}{40.7 \times 10^{-3}}\right]^{2} \left[\frac{\sin(\gamma)}{\sin(73.2°)}\right]^{2}, \qquad (1.8)
\end{aligned}$$

where the formula for $\mathcal{B}(K_L \to \pi^0\nu\bar{\nu})_{\text{SM}}$ is exact and the formula for $\mathcal{B}(K^+ \to \pi^+\nu\bar{\nu})_{\text{SM}}$ is approximate to within 1%, depending on the actual choice of $|V_{cb}|$ and γ.

The charged kaon decay $K^+ \to \pi^+\nu\bar{\nu}$ is dominated by short-distance contributions from one-loop penguin and box diagrams (shown in Fig. 1.1) and is suppressed by a power-like GIM mechanism [19].

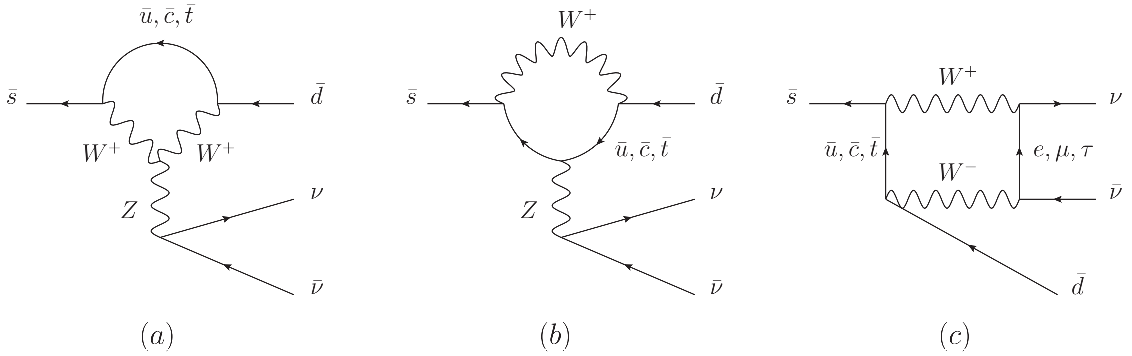

Figure 1.1: Diagrams showing dominant contributions to $K_{\pi\nu\nu}$ decay, [43].

The $K^+ \to \pi^+\nu\bar{\nu}$ branching fraction can be written as [46]

$$\begin{aligned}
\mathcal{B}(K^+ \to \pi^+\nu\bar{\nu})_{\text{SM}} &= \kappa_+(1 + \Delta_{\text{EM}}) \cdot \\
&\cdot \left[\left(\frac{\text{Im}\lambda_t}{\lambda^5} X(x_t)\right)^2 + \left(\frac{\text{Re}\lambda_c}{\lambda} P_c(X) + \frac{\text{Re}\lambda_t}{\lambda^5} X(x_t)\right)^2\right], \qquad (1.9)
\end{aligned}$$

with $x_t = m_t^2/M_W^2$ with m_t and M_W being masses of top quark and W boson respectively [18], $\lambda = |V_{us}|$, $\lambda_i = V_{is}^* V_{id}$, $\Delta_{\text{EM}} = -0.003$ accounts for electromagnetic radiative corrections, functions $X(x_t)$ and $P_c(x)$ describe top and charm loop contributions (for more details, see [46]). The relevant hadronic matrix elements are included in factor κ_+, measured from semileptonic kaon decays and equal to

$$\kappa_+ = (5.173 \pm 0.025) \times 10^{-11} \left[\frac{\lambda}{0.225}\right]^8 . \qquad (1.10)$$

1.2.2 $K \to \pi\nu\bar{\nu}$ Beyond the Standard Model

When investigating possible NP scenarios from the perspective of flavour physics, it is instructive to look at more than one single process. Correlations of carefully chosen observables may not only indicate the presence of NP, but may also hint at the type of NP scenario at play.

As already stated in the previous subsection 1.2.1, one such pair of processes are the $K \to \pi\nu\bar{\nu}$ decays. In addition to these, decays of B mesons, mainly $B \to \mu^+\mu^-$, play an important role in searches for NP as well [46].

The most recent measurement of the $B_s \to \mu^+\mu^-$ decay was performed by the LHCb Collaboration [47] and reads

$$\overline{\mathcal{B}}(B_s \to \mu^+\mu^-)_{\text{Exp}} = \left(3.0 \pm 0.6_{\text{stat}} + (^{+0.3}_{-0.2})_{\text{syst}}\right) \times 10^{-9}, \tag{1.11}$$

where $\overline{\mathcal{B}}$ represents average time-integrated branching fraction, defined in [48], while the current theoretical prediction is equal to [49]

$$\overline{\mathcal{B}}(B_s \to \mu^+\mu^-)_{\text{SM}} = (3.65 \pm 0.23) \times 10^{-9} \ . \tag{1.12}$$

Figure 1.2 shows correlations of the above mentioned branching fractions for various values of the CKM angles γ and β [46]. Dashed regions correspond to 68% CL determined by the uncertainties on all inputs except the angles γ (left) and β (right). Filled regions are defined only by the uncertainties on the remaining CKM parameters.

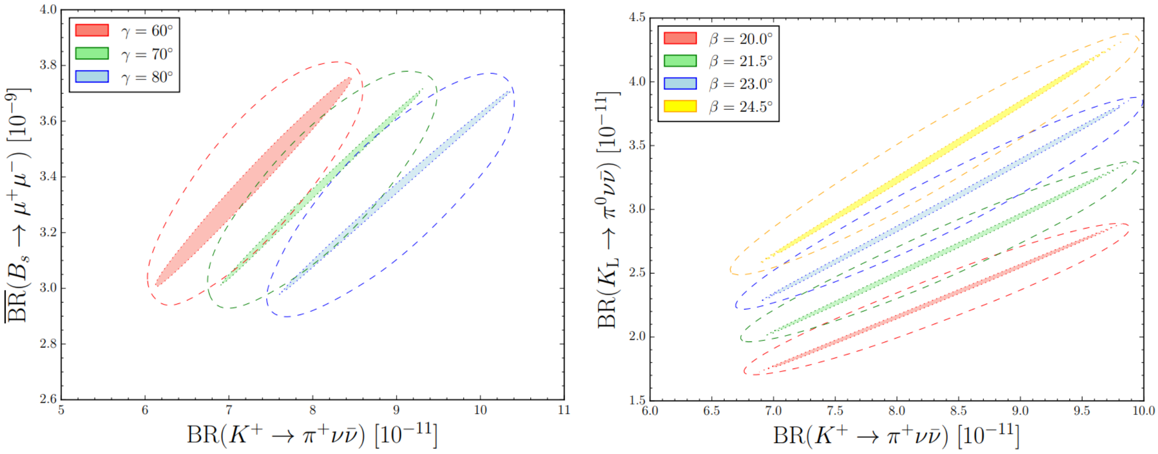

Figure 1.2: Correlations between $\overline{\mathcal{B}}(B_s \to \mu^+\mu^-)$ and $\mathcal{B}(K^+ \to \pi^+\nu\bar{\nu})$ for different values of γ (left) and correlations between $\mathcal{B}(K_L \to \pi^0\nu\bar{\nu})$ and $\mathcal{B}(K^+ \to \pi^+\nu\bar{\nu})$ for different values of β (right), [46].

In light of the upcoming measurements of $K^+ \to \pi^+\nu\bar{\nu}$ decay by NA62 and $K_L \to \pi^0\nu\bar{\nu}$ by the KOTO [42] experiment[3], a summary of selected NP scenarios was given in

---

[3] http://koto.kek.jp/pub/p14.pdf

[50, 51]. Among these scenarios are Littlest Higgs models [52, 53], Z' models [54], Minimal Supersymmetric SM [55, 56] or LFUV models [57].

Figure 1.3 (left) shows the correlations between $K_L \to \pi^0\nu\bar{\nu}$ and $K^+ \to \pi^+\nu\bar{\nu}$ decay branching fractions for three main categories of NP scenarios [51]:

- Red region represents models with general left-handed and right-handed NP couplings. In these models no correlation between $\mathcal{B}(K_L \to \pi^0\nu\bar{\nu})$ and $\mathcal{B}(K^+ \to \pi^+\nu\bar{\nu})$ is present.
- Green region corresponds to NP scenarios with a CKM-like structure of flavour interactions obeying constrained Minimal Flavour Violation.
- Blue region is defined by models with new flavour or CP-violating interactions with only left-handed or right-handed currents fully dominating.

In light of the recently observed tensions between SM and experiment observed in B-sector and discussed in subsection 1.3.1, prospects of LFU tests in correlations of $K^+ \to \pi^+\nu\bar{\nu}$ and $B \to K^{*+}\nu\bar{\nu}$ decays have been investigated in [51] and are shown in Fig. 1.3.

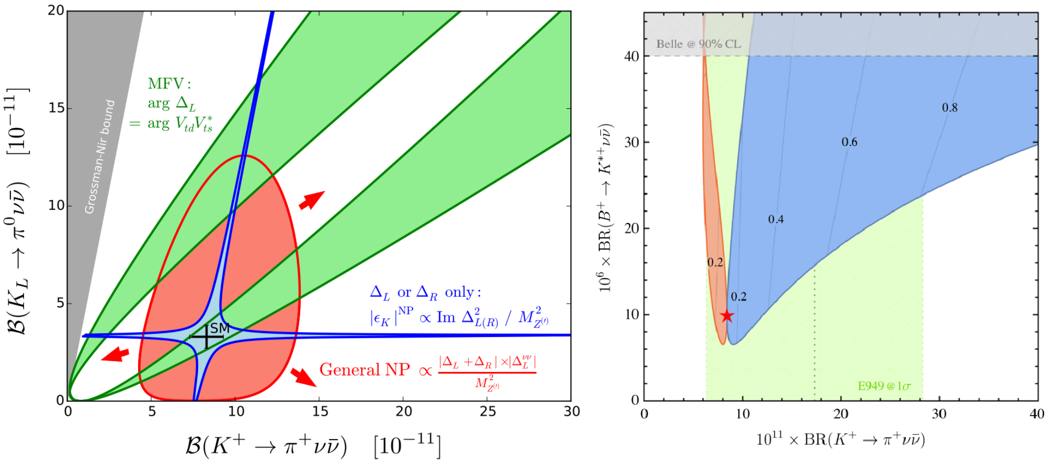

Figure 1.3: Left: correlation between $\mathcal{B}(K_L \to \pi^0\nu\bar{\nu})$ and $\mathcal{B}(K^+ \to \pi^+\nu\bar{\nu})$ in three main categories of NP scenarios (see details in the text), [51]. Right: correlation between $\mathcal{B}(K^+ \to \pi^+\nu\bar{\nu})$ and $\mathcal{B}(B \to K^{*+}\nu\bar{\nu})$ for different values of LFUV NP parameters (blue and red regions), together with the SM value (star) and experimental values (grey and green regions). More details can be found in [57].

1.2.3 Experimental Status of $K \to \pi\nu\bar{\nu}$ Measurements

The most recent result on the $K_L \to \pi^0\nu\bar{\nu}$ decay branching fraction was achieved by the KOTO experiment in 2018 [58, 42]. The experiment is situated at the J-PARC Hadron Experimental Facility[4] in Japan and uses neutral kaon beam generated from a primary 30 GeV/c protons impinging on a gold target. The neutral kaons K_L decay inside a

---

[4] https://j-parc.jp/en/date.html

3-metre-long decay volume with decay products detected by photon and charged particle vetoes and the CSI electromagnetic calorimeter. The $K_L \to \pi^0\nu\bar{\nu}$ event signature is a pair of photons from $\pi^0 \to \gamma\gamma$ decays reconstructed in CSI with “nothing else” in the detector.

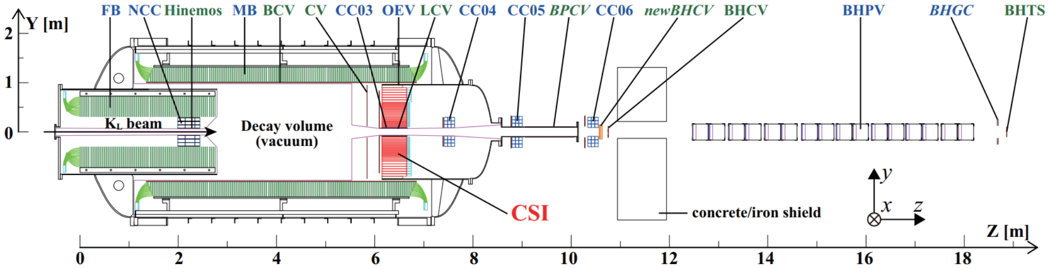

Figure 1.4: Schematic view of the KOTO experiment, [42]. K_L beam comes from the left. Sub-detectors shown in blue (green) are photon (charged particle) vetoes. CSI (shown in red) is the main electromagnetic calorimeter.

The recent analysis of 2015 data presented in [42] found no signal candidate events and the upper limit at 90% CL on $\mathcal{B}(K_L \to \pi^0\nu\bar{\nu})$ was set to be

$$\mathcal{B}(K_L \to \pi^0\nu\bar{\nu})_{\text{Exp}} < 3.0 \times 10^{-9}, \tag{1.13}$$

which is almost an order of magnitude better that the previous upper limit set by the E391a experiment at the KEK 12-GeV proton synchrotron [59]. Figure 1.5 shows the remaining data and Monte Carlo (MC) events after the full $K_L \to \pi^0\nu\bar{\nu}$ event selection together with the signal region definition. To reach the SM sensitivity in next years, various upgrades are planned both for the beam line and the KOTO detector itself.

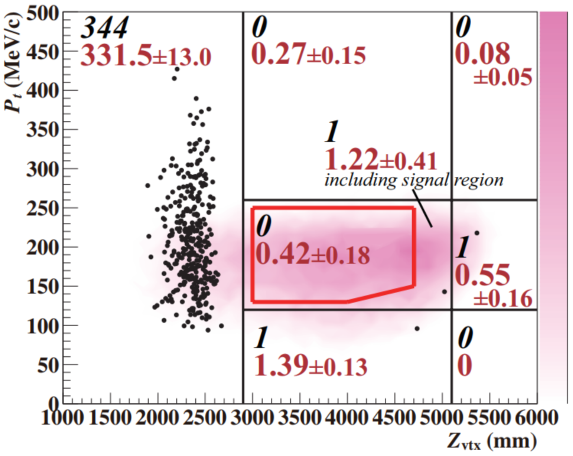

Figure 1.5: Reconstructed π^0 transverse momentum versus π^0 decay vertex Z position measured by the KOTO experiment, [42]. The signal region is surrounded by red lines. The pink contour corresponds to $K_L \to \pi^0\nu\bar{\nu}$ MC events passing the event selection.

The best measurement of the $K^+ \to \pi^+\nu\bar{\nu}$ ($K_{\pi\nu\nu}$) branching fraction to date was done by the *stopped-kaon* experiments E787 and E949 at the Brookhaven National

Laboratory[5] [60], and reads

$$\mathcal{B}(K_{\pi\nu\nu})_{\text{Exp}} = (17.3^{+11.5}_{-10.5}) \times 10^{-11} \ . \tag{1.14}$$

This result (Fig. 1.6) comes from the total number of *seven* $K_{\pi\nu\nu}$ decay candidates.

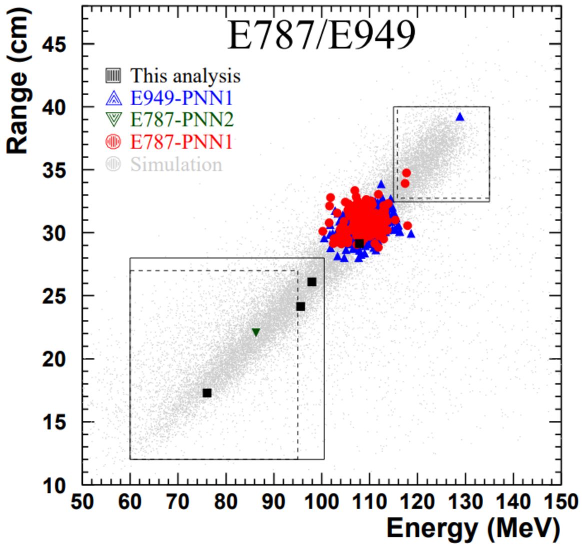

Figure 1.6: The seven $K^+ \to \pi^+\nu\bar{\nu}$ signal events selected by the E787 and E949 analyses. The solid and dashed lines define signal regions. See [60] for more details.

A completely new technique of $K_{\pi\nu\nu}$ branching fraction measurement using kaon decays in-flight is being exploited at the NA62 experiment[6] at CERN. The most recent result [41] from data collected by NA62 in 2016 reports one event observed in the predefined signal regions, which gives an upper limit on the $K_{\pi\nu\nu}$ branching fraction $\mathcal{B}(K_{\pi\nu\nu}) < 14 \times 10^{-10}$ at 95% confidence level. The corresponding $K_{\pi\nu\nu}$ analysis is summarised in chapter 4.

1.3 $K \to \pi l^+ l^-$ Decays

In this section we give the motivation for the measurement, summarise theoretical description and list previous analyses focusing on rare kaon decays $K \to \pi l^+ l^-$ with an emphasis on the charged decay modes $K^+ \to \pi^+ l^+ l^-$.

1.3.1 Connection to the Current B-sector Anomalies

The rare kaon decays $K^\pm \to \pi^\pm l^+ l^-$ (Table 1.1) are excellent processes for studies of physics involving FCNC within the SM. Moreover, precise measurements of parameters of both $K^+ \to \pi^+\mu^+\mu^-$ ($K_{\pi\mu\mu}$) and $K^+ \to \pi^+ e^+ e^-$ ($K_{\pi ee}$) modes represent a potential test of the LFU. Due to the recently observed tensions (sometimes referred to as

---

[5] https://www.bnl.gov/world/

[6] http://na62.web.cern.ch/NA62/

anomalies) in B-physics discussed in large extent in [21, 22, 23, 24, 25, 61], studies challenging LFU are becoming increasingly important when searching for NP.

Statistically significant discrepancies in B-sector today are:

- Approximately 2.5σ tension in P_5' variable (defined in [62]) prediction and LHCb measurement [21] in $B \to K^* \mu^+ \mu^-$ decays was observed. More details are given for example in [63] or [22].
- More importantly for the presented work, a discrepancy of $\sim 2.6\sigma$ between the SM prediction of

  $$(R_K)_{\mathrm{SM}} = \frac{\mathcal{B}(B^+ \to K^+ \mu^+ \mu^-)}{\mathcal{B}(B^+ \to K^+ e^+ e^-)} = 1.0003 \pm 0.0001, \ [64] \tag{1.15}$$

  and the experimental value measured by the LHCb experiment

  $$(R_K)_{\mathrm{Exp}} = 0.745 + (^{+0.090}_{-0.074})_{\mathrm{stat}} \pm 0.036_{\mathrm{syst}}, \ [23] \tag{1.16}$$

  in the $1 < m_{ll}^2 < 6 \ \mathrm{GeV}^2/c^4$ range suggests possibility of LFU violation.
- Another hint of LFUV was also observed in B decays involving third lepton family, namely in variable $R(D^*)$ with the SM prediction equal to

  $$R(D^*)_{\mathrm{SM}} = \frac{\mathcal{B}(B \to D^{*+} \tau^- \nu_\tau)}{\mathcal{B}(B \to D^{*+} \mu^- \nu_\mu)} = 0.252 \pm 0.003, \ [65] \tag{1.17}$$

  and the LHCb measurement

  $$R(D^*)_{\mathrm{Exp}} = 0.336 \pm 0.027_{\mathrm{stat}} \pm 0.030_{\mathrm{syst}}, \ [24], \tag{1.18}$$

  which constitutes $\sim 3\sigma$ discrepancy.

In light of these observed tensions, investigations of possibilities to probe LFUV and LFV at NA62 and other kaon experiments have been carried out in [66]. Charged kaon decays $K^\pm \to \pi^\pm l^+ l^-$ are mentioned as examples of LFUV tests. We will discuss this more at the end of subsection 1.3.4. Searches for LFV decays $K^+ \to \pi^+ l_1^+ l_2^-$ can be performed at NA62 as well.

1.3.2 $K^\pm \to \pi^\pm l^+ l^-$ Decay Width

An extensive work [67, 68, 69, 70, 71] has been done towards theoretical understanding of $K^\pm \to \pi^\pm l^+ l^-$ decays, mainly their dominant contributions mediated by one virtual photon exchange $K^\pm \to \pi^\pm \gamma^* \to \pi^\pm l^+ l^-$ and involving long-distance hadronic effects. As these effects are difficult to describe, the calculations were done in the scope of the Chiral Perturbation Theory (ChPT) up to the next-to-leading order (NLO) [69] as well as in the combined framework of the ChPT and the Large-N_c QCD [70]. More recent attempts of lattice QCD calculations of $K^\pm \to \pi^\pm l^+ l^-$ amplitudes [72] are still operating with unphysical meson masses.

Since the presented thesis is focused on the muonic decay mode $K^+ \to \pi^+ \mu^+ \mu^-$ ($K_{\pi\mu\mu}$), from now on we substitute muons in place of the out-going leptons in $K^\pm \to \pi^\pm l^+ l^-$. Assuming LFU, all relations hold also for the electron mode as long as proper lepton mass is used.

At low energies, the $K_{\pi\mu\mu}$ decay is described by an effective theory derived in [67, 69]. The dominant long-distance contribution to the $K_{\pi\mu\mu}$ decay, originating from the radiative transition $K^+ \to \pi^+ \gamma^*$, is given by the effective lagrangian of the ChPT [67]

$$\mathscr{L}_{\text{eff}} = -\frac{1}{4} F_{\mu\nu} F^{\mu\nu} + \mathscr{L}_{\text{strong}} + \mathscr{L}_{\text{elmag}} - \frac{G_F}{\sqrt{2}} V_{ud} V_{us}^* \left(\mathscr{L}_{\Delta S=1} + \mathscr{L}_{\Delta S=1}^{\text{elmag}} \right), \tag{1.19}$$

where $F_{\mu\nu}$ is the electromagnetic field strength tensor, $\mathscr{L}_{\text{strong}}$ is a non-linear sigma model lagrangian describing the chiral low-energy limit of QCD, $\mathscr{L}_{\text{elmag}}$ is an electromagnetic interaction lagrangian, $\mathscr{L}_{\Delta S=1}$ and $\mathscr{L}_{\Delta S=1}^{\text{elmag}}$ are strangeness-changing ($\Delta S = 1$) non-leptonic weak lagrangians.

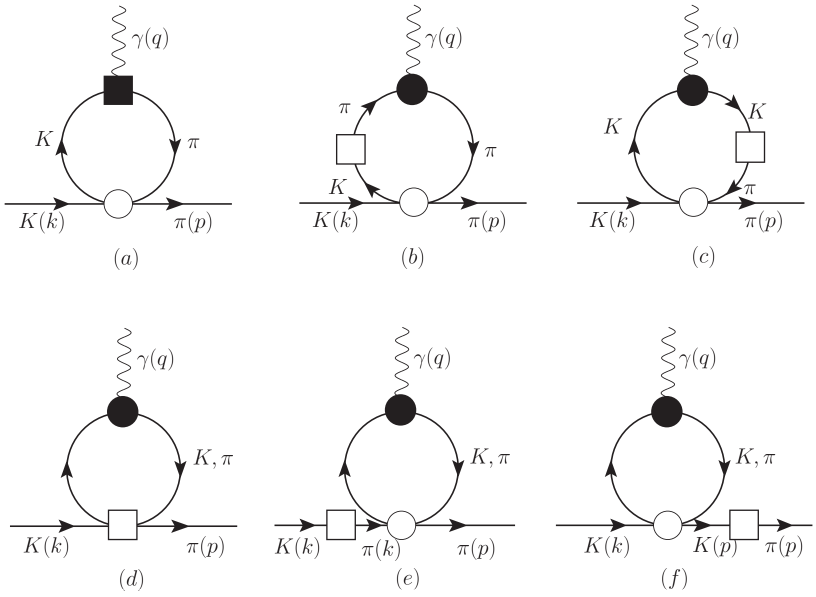

Figure 1.7: One-loop diagrams contributing to the $K^+ \to \pi^+ \gamma^*$ process, [67].

The amplitude of the transition $K^+ \to \pi^+ \gamma^*$ vanishes at tree-level [67] and the first non-zero contribution to this process comes from one-loop diagrams displayed in Fig.1.7 with the four different vertices originating from four interaction lagrangians in Eq. 1.19:

- vertices shown as filled circles come from $\mathscr{L}_{\text{elmag}}$,
- vertex shown as a filled square comes from $\mathscr{L}_{\Delta S=1}^{\text{elmag}}$,
- vertices shown as empty circles come from $\mathscr{L}_{\text{strong}}$ and
- vertices shown as empty squares come from $\mathscr{L}_{\Delta S=1}$.

Let us denote the momenta of the particles involved in the $K^+ \to \pi^+\mu^+\mu^-$ decay in the following way

$$K^+(k) \to \pi^+(p)\mu^+(q_+)\mu^-(q_-) \ . \tag{1.20}$$

The evaluation of one-loop contributions proportional to $(k+p)_\mu$ and shown in Fig. 1.7 was done in [67]. All diagrams can be expressed in terms of a function $I(q^2, m_1^2, m_2^2)$ dependent on the meson masses m_1 and m_2 and the momentum $q = q_+ + q_-$ of the virtual photon

$$I(q^2, m_1^2, m_2^2) = \frac{1}{16\pi^2}\left[\frac{\nu^{-\varepsilon}}{3\hat{\varepsilon}}\left[3(m_1^2+m_2^2) - q^2\right] + J(q^2, m_1^2, m_2^2, \nu^2)\right], \tag{1.21}$$

with

$$\begin{aligned}
\frac{1}{\hat{\varepsilon}} &= -\frac{1}{\varepsilon} + \frac{1}{2}\left(\gamma_{\mathrm{E}} - \log(4\pi) - 1\right) + \mathcal{O}(\varepsilon),\\
\gamma_{\mathrm{E}} &\simeq 0.577 \text{ (Euler's constant)},\\
\text{dimension} &= 4 - \varepsilon,\\
J(q^2, m_1^2, m_2^2, \nu^2) &= \int_0^1 \mathrm{d}\xi \left[m_1^2(1-\xi) + m_2^2\xi - q^2\xi(1-\xi)\right] \times\\
&\quad \times \log\left[m_1^2(1-\xi) + m_2^2\xi - q^2\xi(1-\xi)\right]/\nu^2,
\end{aligned} \tag{1.22}$$

where ν is an arbitrary renormalisation scale. Function $I(q^2, m_1^2, m_2^2)$ does not vanish for $q^2 = 0$ due to contributions from additional diagrams proportional to $(k+p)_\mu$ not directly dependent on q^2 but dependent on m_1^2 and m_2^2. However, gauge invariance dictates that the overall coefficient of $(k+p)_\mu$ terms is proportional to q^2. Thus the universal function $\hat{I}(q^2, m_1^2, m_2^2)$ can be obtained from $I(q^2, m_1^2, m_2^2)$ by subtracting its value at $q^2 = 0$

$$\hat{I}(q^2, m_1^2, m_2^2) = I(q^2, m_1^2, m_2^2) - I(0, m_1^2, m_2^2) \ . \tag{1.23}$$

Defining functions F_{KK}, $F_{K\pi}$ and $F_{\pi\pi}$ such that

$$\begin{aligned}
F_{KK} &= \hat{I}(q^2, M_K^2, M_K^2),\\
F_{K\pi} &= \hat{I}(q^2, M_K^2, m_\pi^2),\\
F_{\pi\pi} &= \hat{I}(q^2, m_\pi^2, m_\pi^2),
\end{aligned} \tag{1.24}$$

where M_K and m_π are nominal charged kaon and pion masses [18] respectively, one can write contributions to the $K^+ \to \pi^+\gamma^*$ amplitude from one-loop diagrams in Fig. 1.7 in the following way [67]

$$\begin{aligned}
\text{Diagram (a)} &= F_{K\pi}, \\
\text{Diagram (b)} &= \frac{M_K^2 F_{KK} - m_\pi^2 F_{K\pi}}{m_\pi^2 - M_K^2}, \\
\text{Diagram (c)} &= \frac{m_\pi^2 F_{\pi\pi} - M_K^2 F_{K\pi}}{M_K^2 - m_\pi^2}, \\
\text{Diagram (d)} &= F_{KK} + F_{\pi\pi}, \\
\text{Diagram (e)} &= \frac{M_K^2}{m_\pi^2 - M_K^2} \left(F_{KK} + 2F_{\pi\pi}\right), \\
\text{Diagram (f)} &= \frac{m_\pi^2}{M_K^2 - m_\pi^2} \left(F_{\pi\pi} + 2F_{KK}\right) \ . \qquad (1.25)
\end{aligned}$$

Summing all these one-loop contributions yields divergent result. The divergencies are cancelled out by adding tree-level contributions from an effective electroweak chiral lagrangian to fourth order in derivatives and meson masses [67].

Combining the one-loop contributions from the lowest-order effective chiral lagrangian with tree-level contributions from the 4-th order lagrangian, a final decay amplitude is obtained, shown here using conventions listed in [69]

$$A\left(K^+(k) \to \pi^+(p)\mu^+(q_+)\mu^-(q_-)\right) = -\frac{e^2}{M_K^2(4\pi)^2} W(z)(k+p)^\mu \bar{u}(q_-)\gamma_\mu v(q_+), \qquad (1.26)$$

where $k^2 = M_K^2$, $p^2 = m_\pi^2$, $q = k - p = q_+ + q_-$, $z = q^2/M_K^2$, γ^μ are gamma matrices, u and v are fermionic fields corresponding to outgoing muons, and $W(z)$ is a form factor describing dynamics of the decay. We postpone the discussion of the various parametrisations of the form factor to the following subsection.

Finally, the differential decay width in terms of the di-muon invariant mass is[7]

$$\frac{\mathrm{d}\Gamma_0}{\mathrm{d}z} = \frac{\alpha^2 M_K}{12\pi(4\pi)^4} \lambda^{3/2}(1, z, r_\pi^2) \sqrt{1 - 4\frac{r_\mu^2}{z}} \left(1 + 2\frac{r_\mu^2}{z}\right) |W(z)|^2, \qquad (1.27)$$

with $r_i = m_i/M_K$, $\lambda(a,b,c) = a^2 + b^2 + c^2 - 2(ab + ac + bc)$ and $4r_\mu^2 \le z \le (1 - r_\pi)^2$.

1.3.3 Coulomb Corrections

Corrections arising from long-distance electromagnetic interactions between pairs of $K_{\pi\mu\mu}$ decay products are of an order of a few percent [73] and therefore have to be taken into account. In order to accommodate Coulomb corrections to the $K_{\pi\mu\mu}$ differential decay width, one needs to start with a two dimensional $\mathrm{d}^2\Gamma_0/\mathrm{d}x\mathrm{d}z$ rather than $\mathrm{d}\Gamma_0/\mathrm{d}z$

---

[7] The “0” in the subscript of the differential decay width $\mathrm{d}\Gamma_0/\mathrm{d}z$ is meant to indicate that the Coulomb corrections have not been applied yet.

shown in Eq. 1.27. The reason is that the Coulomb corrections depend on the relative velocities of the decay products [73] and a single kinematic variable z is insufficient to obtain all relative velocities for a particular decay event: the $K_{\pi\mu\mu}$ decay is completely described in terms of two kinematic variables

$$\begin{aligned} x &= M(\pi^+, \mu^+)/M_K^2 = (p + q_+)^2/M_K^2, \\ z &= M(\mu^+, \mu^-)/M_K^2 = (q_+ + q_-)^2/M_K^2, \end{aligned} \tag{1.28}$$

where $M(i,j)$ is the invariant mass of particle pair i,j. The (Coulomb) uncorrected two-dimensional differential decay width is given by formula [71][8]

$$\frac{\mathrm{d}^2\Gamma_0}{\mathrm{d}x\mathrm{d}z} = \frac{\alpha^2 M_K}{8\pi(4\pi)^4}\eta(x,z)|W(z)|^2, \tag{1.29}$$

with

$$\eta(x,z) = \left(2x + z - 2 - 2r_\mu^2\right)\left(-2x - z + 2r_\pi^2 + 2r_\mu^2\right) + z(z - 2 - 2r_\pi^2)\ . \tag{1.30}$$

The uncorrected decay width shown in Eq. 1.29 is corrected for long-distance Coulomb interactions using functions $\Omega_\mathrm{C}(s_{ij})$ [73]

$$\frac{\mathrm{d}^2\Gamma}{\mathrm{d}x\mathrm{d}z} \equiv \frac{\mathrm{d}^2\Gamma_0}{\mathrm{d}x\mathrm{d}z} \times \frac{\mathrm{d}^2\Gamma_\mathrm{Coulomb}}{\mathrm{d}x\mathrm{d}z} = \frac{\mathrm{d}^2\Gamma_0}{\mathrm{d}x\mathrm{d}z} \times \Omega_\mathrm{C}(s_{\pi^+\mu^+}) \times \Omega_\mathrm{C}(s_{\pi^+\mu^-}) \times \Omega_\mathrm{C}(s_{\mu^+\mu^-}), \tag{1.31}$$

where $s_{ij} = (p_i + p_j)^2$ and $(ij) \in \{\pi^+\mu^+, \pi^+\mu^-, \mu^+\mu^-\}$. The Coulomb term for each particle pair (ij) in the final state is defined as

$$\Omega_\mathrm{C}(s_{ij}) = \frac{2\pi\alpha Q_i Q_j}{\beta_{ij}(s_{ij})} \times \left[e^{\frac{2\pi\alpha Q_i Q_j}{\beta_{ij}(s_{ij})}} - 1\right]^{-1}, \tag{1.32}$$

with

$$\beta_{ij}(s_{ij}) = \left[1 - \frac{4m_i^2 m_j^2}{(s_{ij} - m_i^2 - m_j^2)^2}\right]^{1/2}\ . \tag{1.33}$$

We rewrite the s_{ij} in terms of variables x and z in the following way

$$\begin{aligned} s_{\mu^+\mu^-} &= zM_K^2, \\ s_{\pi^+\mu^+} &= xM_K^2, \\ s_{\pi^+\mu^-} &= (1 - x - z)M_K^2 + m_\pi^2 + 2m_\mu^2\ . \end{aligned} \tag{1.34}$$

---

[8] At this place we would like to point out a factor 2 discrepancy between formulas (39) and (40) in [71]. In Fig.1.9 (left) of the presented work, one can see the plot of equation (40) in red and a plot of integrated equation (39), *multiplied by a factor of 2*, in green.

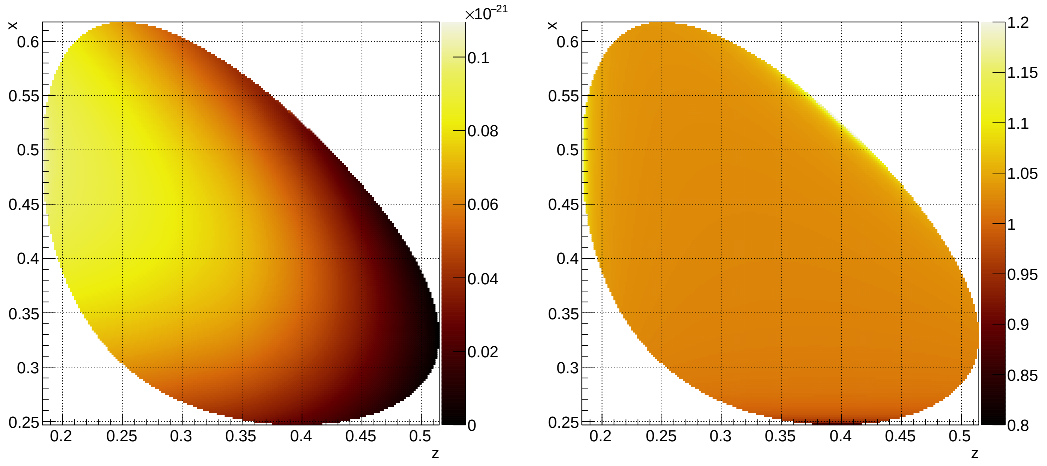

Figure 1.8: Left: $K_{\pi\mu\mu}$ decay Dalitz plot (i.e. $\mathrm{d}^2\Gamma/\mathrm{d}x\mathrm{d}z$) with Coulomb corrections applied. Right: Coulomb corrections (i.e. $\mathrm{d}^2\Gamma_{\mathrm{Coulomb}}/\mathrm{d}x\mathrm{d}z$). The correction is most significant for regions where the pairs of decay products have small relative velocities. It is enhancing for oppositely charged particles and diminishing for likely charged particles.

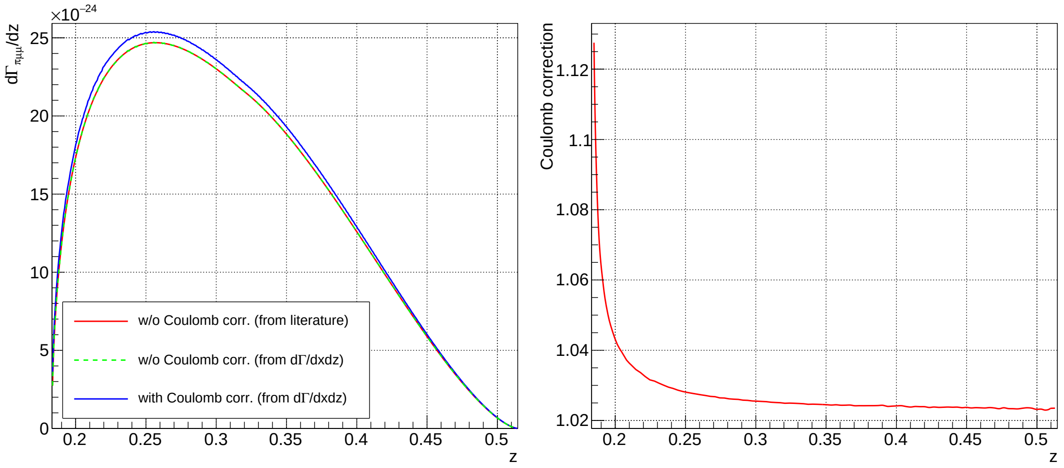

Figure 1.9: Left: $K_{\pi\mu\mu}$ differential decay width $\mathrm{d}\Gamma/\mathrm{d}z$ with and without Coulomb corrections. Green line is meant as a sanity check: it represents our numerically integrated 2D decay width $\mathrm{d}^2\Gamma/\mathrm{d}x\mathrm{d}z$ along x when no Coulomb corrections are applied. It is identical to the red line, which is a plot of formula 1.27, found for example in [69]. Right: $\mathrm{d}^2\Gamma_{\mathrm{Coulomb}}/\mathrm{d}z$ computed as a ratio of the blue and green curves in the left plot. The correction diverges in the limit of low z, which corresponds to zero relative velocity of the muon pair.

The uncorrected decay width $\mathrm{d}\Gamma_0/\mathrm{d}z$ as well as the effect of Coulomb corrections is shown in figures 1.8 and 1.9. The plots are obtained using the form factor $W(z)$ parameters set to the values measured by the NA48/2 [74] (see below). For this particular choice of the form factor parameter values, the Coulomb corrections amount to $\approx 3\%$ increase in the total $K_{\pi\mu\mu}$ branching fraction.

Let us now discuss the various parametrisations of the form factor $W(z)$. The NA48/2 paper [74], being the latest publication regarding the measurement of the $K_{\pi\mu\mu}$ decay, examines the following $W(z)$ parametrisations:

1. Linear: $W(z) = G_F M_K^2 f_0(1 + \delta z)$, where G_F is the Fermi coupling constant and f_0 and δ are free parameters,
2. NLO in the ChPT [69]: $W(z) = G_F M_K^2(a + bz) + W^{\pi\pi}(z)$ with a and b as free parameters and $W^{\pi\pi}(z)$ explicitly calculated in [69] and shown in Eq. 1.36,
3. Combined framework of the ChPT and the large-N_c QCD [70], where $W(z) \equiv W(\tilde{w}, \beta, z)$ with $\tilde{w}$ and β as free parameters,
4. ChPT parametrisation [71] involving meson form factors, where $W(z) \equiv W(M_a, M_\rho, z)$ with M_a and M_ρ as free parameters.

For the purposes of this work, we chose the parametrisation in the scope of the ChPT shown in the second point

$$W(z) = G_F M_K^2(a + bz) + W^{\pi\pi}(z), \tag{1.35}$$

with the pion loop term $W^{\pi\pi}(z)$, arising from contributions of $K^+ \to \pi^+\pi^+\pi^-$ with $\pi^+\pi^- \to \gamma^*$ rescattering, given by [69]

$$W^{\pi\pi}(z) = \frac{1}{r_\pi^2}\left[\alpha + \beta\frac{z - z_0}{r_\pi^2}\right] F(z)\chi(z), \tag{1.36}$$

where $\alpha = -20.6 \cdot 10^{-8}$, $\beta = -2.8 \cdot 10^{-8}$, $z_0 = 1/3 + r_\pi^2$, the electromagnetic form factor $F(z)$ for transition $\pi^+\pi^- \to \gamma^*$ is equal to $F(z) = 1 + z/2.5$, and the one-loop function

$$\chi(z) = \frac{4}{9} - \frac{4r_\pi^2}{3z} - \frac{1}{3}\left(1 - \frac{4r_\pi^2}{z}\right) G(z/r_\pi^2),$$

$$G(t) = \begin{cases} \sqrt{4/t - 1}\,\arcsin(\sqrt{t}/2) & t \leq 4 \\ -\frac{1}{2}\sqrt{1 - 4/t}\left[\ln\frac{1-\sqrt{1-4/t}}{1+\sqrt{1-4/t}} + i\pi\right] & t > 4 \end{cases}. \tag{1.37}$$

For a more convenient implementation of the form factor into the fitting algorithm, we decompose $W(z)$ into the real and imaginary parts $W_{\mathrm{Re}}(z)$ and $W_{\mathrm{Im}}(z)$[9].

---

[9] This decomposition is almost trivial, as can be seen from equations 1.35 - 1.37, but it helped improving the speed of the fitting algorithm significantly. More details on this subject can be found in Appendix B.

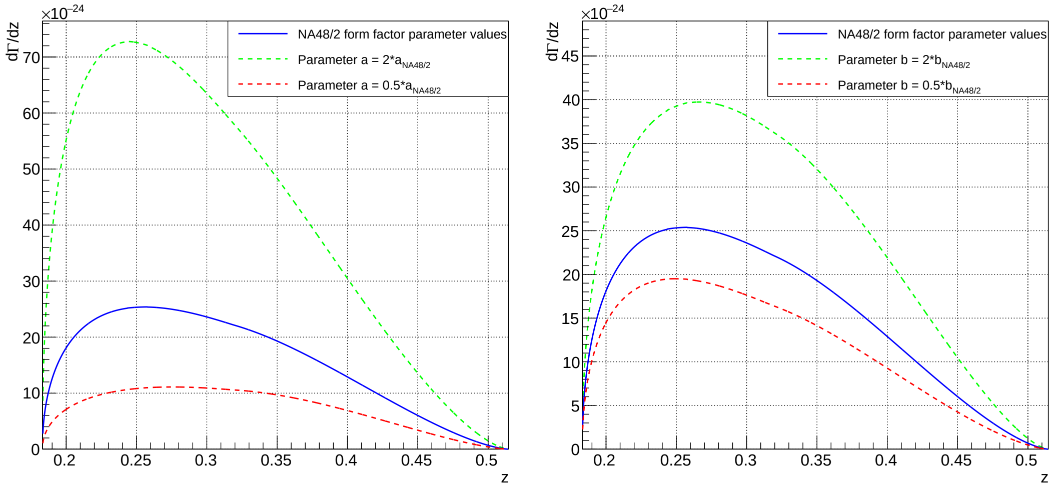

Figure 1.10: $K_{\pi\mu\mu}$ differential decay width for various values of parameter a (left) and parameter b (right).

Using $K_{\pi\mu\mu}$ decays, the NA48/2 experiment measured the form factor parameters a and b to be [74]

$$\begin{aligned} a^{\mu}_{\mathrm{NA48/2}} &= -0.575 \pm 0.038_{\mathrm{stat.}} \pm 0.006_{\mathrm{syst.}} \pm 0.002_{\mathrm{ext.}} = -0.575 \pm 0.039_{\mathrm{total}}, \\ b^{\mu}_{\mathrm{NA48/2}} &= -0.813 \pm 0.142_{\mathrm{stat.}} \pm 0.028_{\mathrm{syst.}} \pm 0.005_{\mathrm{ext.}} = -0.813 \pm 0.145_{\mathrm{total}}, \end{aligned} \tag{1.38}$$

while with the $K_{\pi ee}$ sample, the parameters were determined to be [75]

$$\begin{aligned} a^{e}_{\mathrm{NA48/2}} &= -0.578 \pm 0.012_{\mathrm{stat.}} \pm 0.008_{\mathrm{syst.}} \pm 0.007_{\mathrm{ext.}} = -0.578 \pm 0.016_{\mathrm{total}}, \\ b^{e}_{\mathrm{NA48/2}} &= -0.779 \pm 0.053_{\mathrm{stat.}} \pm 0.036_{\mathrm{syst.}} \pm 0.017_{\mathrm{ext.}} = -0.779 \pm 0.066_{\mathrm{total}}\ . \end{aligned} \tag{1.39}$$

The Monte Carlo decay generator used in the NA62 software framework[10] generates $K_{\pi\mu\mu}$ events with parameters

$$a_{\mathrm{NA62\ MC}} = -0.584 \qquad\qquad b_{\mathrm{NA62\ MC}} = -0.700, \tag{1.40}$$

which is an average of the NA48/2 and E865 results [74, 75, 76, 77].

Figure 1.10 shows the dependence of the differential decay width $\mathrm{d}\Gamma/\mathrm{d}z$ on the values of form factor parameters a and b with the central values taken from Eq. 1.38.

Theoretical predictions for the $K_{\pi\mu\mu}$ decay branching fraction are usually shown parametrised in terms of form factor parameters [68, 69, 78]. Some publications use experimental results from the electron modes $K^{\pm} \to \pi^{\pm} e^{+} e^{-}$ to give predictions on

---

[10] https://na62-sw.web.cern.ch/sites/na62-sw.web.cern.ch/files/doxygen/index.html

the full $K_{\pi\mu\mu}$ decay branching fraction. We quote two such predictions

$$\mathcal{B}_{\mathrm{SM}}(K_{\pi\mu\mu}) = (8.7 \pm 2.8) \times 10^{-8}\ [70], \quad \mathcal{B}_{\mathrm{SM}}(K_{\pi\mu\mu}) = (12 \pm 3) \times 10^{-8}\ [71]\ . \tag{1.41}$$

1.3.4 Previous Measurements

In this subsection, a list of previous $K_{\pi\mu\mu}$ decay measurements together with their results is given. The list is shown in the chronological order and is based on the PDG Listings [18].

E787 experiment at the BNL, 1997, [79] – was a stopped-kaon experiment carried out at the Brookhaven Alternating Gradient Synchrotron (AGS) using the E787 detector. The data taking took place in 1989 and 1991, during which a sample of 207 $K_{\pi\mu\mu}$ candidate events was observed, and the $K_{\pi\mu\mu}$ branching fraction was determined to be

$$\mathcal{B}_{\mathrm{E787}}(K_{\pi\mu\mu}) = (5.0 \pm 0.4_{\mathrm{stat}} \pm 0.7_{\mathrm{syst}} \pm 0.6_{\mathrm{th}}) \times 10^{-8}\ . \tag{1.42}$$

It should be noted that this result is highly ($\sim 4\sigma$) inconsistent with later results [76, 80, 74]. Additionally, [79] mentions $\sim 2\sigma$ inconsistency in the linear form factor slope with respect to the measurement of the $K^+ \to \pi^+ e^+ e^-$ decay [81]. Assuming lepton universality is true, one could argue that the observed discrepancy was caused by an unknown systematic uncertainty that was not accounted for.

E865 experiment at the BNL, 2000, [76] – was also performed on the AGS. The E865 detector was primarily designed to search for the lepton number violating process $K^+ \to \pi^+ \mu^+ e^-$. From the total sample of 402 $K_{\pi\mu\mu}$ candidate events, the $K_{\pi\mu\mu}$ branching fraction was measured to be

$$\mathcal{B}_{\mathrm{E865}}(K_{\pi\mu\mu}) = (9.22 \pm 0.60_{\mathrm{stat}} \pm 0.49_{\mathrm{syst}}) \times 10^{-8}\ , \tag{1.43}$$

The slope of the form factor in the linear parametrisation was determined to be $\delta = 2.45^{+1.30}_{-0.95}$. The experiment also measured $K_{\pi ee}$ decay form factor parameters a_{E865} and b_{E865} in the parametrisation shown in Eq. 1.35 with results

$$a^e_{\mathrm{E865}} = -0.587 \pm 0.010, \qquad b^e_{\mathrm{E865}} = -0.655 \pm 0.044, \qquad [77]. \tag{1.44}$$

HyperCP experiment (E871) at Fermilab, 2001, [80] – was carried out in the Meson Center beam line of Fermilab, primarily designed for studies of CP violation in $\Xi/\overline{\Xi}$ and $\Lambda/\overline{\Lambda}$ decays. The data taking took place in 1997 and 1999. Based on the analysis of the 1997 data, which registered a total number of 110 $K_{\pi\mu\mu}$ candidate events, the measured $K_{\pi\mu\mu}$ branching fraction was

$$\mathcal{B}_{\mathrm{E871}}(K_{\pi\mu\mu}) = (9.8 \pm 1.0_{\mathrm{stat}} \pm 0.5_{\mathrm{syst}}) \times 10^{-8}\ , \tag{1.45}$$

consistent with the E865 measurement.

NA48/2 experiment at CERN, 2011, [74] – was the preceding experiment to the current NA62 experiment. The data was taken during 2003 and 2004, and a $K_{\pi\mu\mu}$ candidate sample of 3120 events was collected (~ 4.5 times larger than all the previous experiments combined).

In order to measure the branching fraction of the $K_{\pi\mu\mu}$ decay, normalisation on a kinematically similar $K^+ \to \pi^+\pi^+\pi^-$ decay was used. The invariant mass spectra obtained after applying the corresponding event selections are showed in Fig. 1.11.

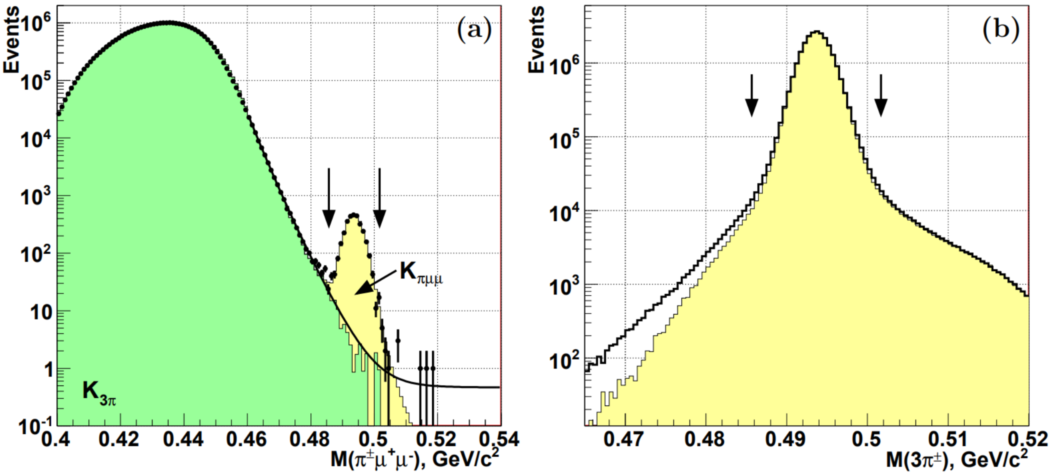

Figure 1.11: (a) Invariant mass of the reconstructed $K_{\pi\mu\mu}$ candidate events together with the remaining $K_{3\pi}$ background. (b) Invariant mass of the reconstructed $K_{3\pi}$ events used for normalisation. Arrows indicate signal regions.

The NA48/2 measured the $K_{\pi\mu\mu}$ branching fraction to be

$$\mathcal{B}_{\text{NA48/2}}(K_{\pi\mu\mu}) = (9.62 \pm 0.21_{\text{stat}} \pm 0.11_{\text{syst}} \pm 0.07_{\text{ext}}) \times 10^{-8} \ . \tag{1.46}$$

The final spectrum of the z variable defined in Eq. 1.28 and the resulting $\mathrm{d}\Gamma/\mathrm{d}z$ distribution are shown in Fig. 1.12. The remaining background contamination is at the level of $(3.3 \pm 0.7)\%$.

An extensive study of the form factor parametrisations was also performed, obtaining the slope of the linear parametrisation $\delta = 3.11 \pm 0.56_{\text{stat}} \pm 0.11_{\text{syst}}$. Parameters a and b measured by the NA48/2 experiment are shown[11] in Eq. 1.38 and Eq. 1.39.

As seen from Eq. 1.44, Eq. 1.38 and Eq. 1.39, previous measurements of $K_{\pi\mu\mu}$ and $K_{\pi ee}$ form factor parameters show consistent results between the electron-producing and muon-producing decay modes. However, there is still room for improvement, especially in the case of $K_{\pi\mu\mu}$ parameters, where the error on b^μ is 2 to 3-times larger than the

---

[11] For the values of other parameters in parametrisations listed in subsection 1.3.2, please see the original publication [74].

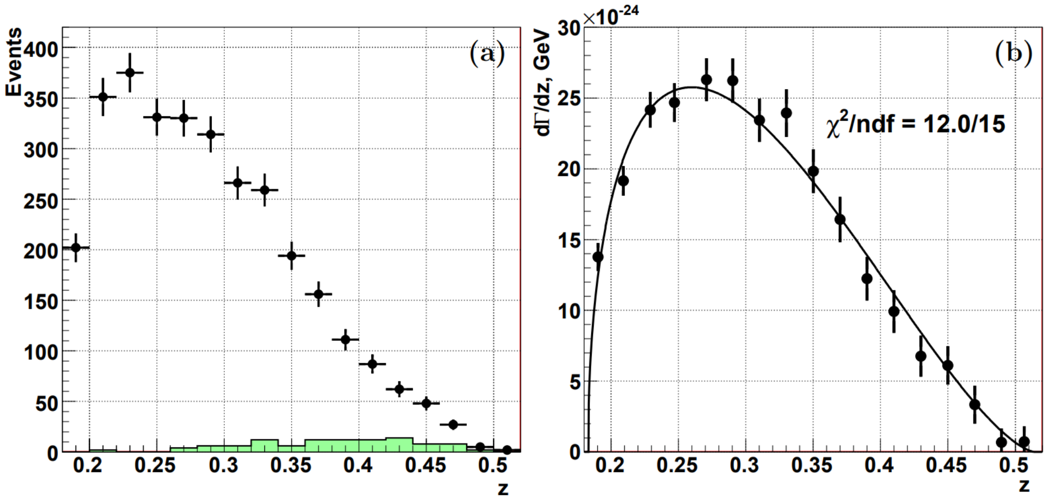

Figure 1.12: (a) Reconstructed spectrum of the kinematic variable z defined in Eq. 1.28 for $K_{\pi\mu\mu}$ candidate events together with the remaining $K_{3\pi}$ background. (b) Final $\mathrm{d}\Gamma/\mathrm{d}z$ spectrum fitted with the theoretical function.

error on b^e from $K_{\pi ee}$ decays.

The main analysis of the presented thesis can be regarded as a preliminary measurement of the $K_{\pi\mu\mu}$ form factor parameters by the NA62 experiment. Once the full dataset collected in 2017 and 2018 is analysed, the cumulative $K_{\pi\mu\mu}$ sample will be the largest one in the world – larger by at least a factor of 5 compared to the NA48/2 $K_{\pi\mu\mu}$ sample. If the final systematic uncertainties can be held reasonably low (see section 2.15 for more details), the NA62 has a potential to challenge the LFU or at least improve the previous measurements [74, 75, 77].

2 Measurement of $K^+ \to \pi^+\mu^+\mu^-$ Decay Form Factor

2.1 Analysis Strategy

The main goal of the NA62 experiment, a measurement of the $K^+ \to \pi^+\nu\bar{\nu}$ decay branching fraction, requires a high intensity kaon beam, a detector setup comprising precise particle tracking and timing and high-efficiency particle identification (PID) and photon detection. This allows for studies of other rare processes to be performed at NA62 in parallel to the main decay mode analysis.

One of the most interesting kaon decay channels is the semileptonic decay $K^+ \to \pi^+\mu^+\mu^-$ ($K_{\pi\mu\mu}$), theoretically described in section 1.3. An analysis of the $K_{\pi\mu\mu}$ decay with a measurement of the form factor parameters a and b (Eq. 1.35) is the main goal of the presented thesis and was also summarised in an NA62 internal note [82].

A measurement of both form factor parameters is equivalent to the simultaneous determination of the overall scale and shape of the differential decay width (Eq. 1.31 and Eq. 1.35). This implies that the obtained sample of $K_{\pi\mu\mu}$ decays needs to be properly normalised using another K^+ decay channel. The $K^+ \to \pi^+\pi^+\pi^-$ ($K_{3\pi}$) decay was selected as the normalisation in our analysis for two main reasons.

Firstly, the $K_{3\pi}$ decay is abundant (Table 1.1), which allows for the collection of a large $K_{3\pi}$ sample, practically eliminating the systematic uncertainty on $K_{\pi\mu\mu}$ form factor parameters arising from the normalisation.

Secondly, the $K_{3\pi}$ decay is kinematically similar to the $K_{\pi\mu\mu}$ decay — it contains three charged tracks originating from a common vertex and no other particles in the final state, which allows for minimal differences in the corresponding event selection procedures described in section 2.8, section 2.9 and section 2.10, thus reducing both the complexity of the analysis as well as various possible systematic effects.

Due to the similarity between the signal and the normalisation channels and relatively small branching fractions of other three-track decay modes, the $K_{3\pi}$ decay channel is also the most important potential source of background in the selected $K_{\pi\mu\mu}$ sample. Therefore, the PID and a small difference in decay kinematics play a crucial role in the suppression of the $K_{3\pi}$ background. The NA62 beam and sub-detectors used in our analysis are described in section 2.2.

In order to determine acceptances of the developed signal and normalisation event selections, we used simulated Monte Carlo (MC) samples of $K_{\pi\mu\mu}$ and $K_{3\pi}$ decays.

Comparisons of various distributions obtained from data and MC are made to validate the event selections and to justify the measured acceptances. We describe the MC simulation procedure in section 2.3, summarise the used MC samples in section 2.4 and show the data-MC comparison plots in section 2.11.

The data sample employed in this analysis was recorded in September and October 2017 with relatively stable data taking conditions. The collected NA62 dataset is split into smaller units called *runs*, which themselves consist of $\mathcal{O}(1\text{k})$ *bursts*. Runs represent periods of stable data taking conditions and usually span a few hours, while bursts correspond to data recorded in individual few-seconds-long SPS spills (subsection 2.2.1). A more detailed description of the used dataset is given in section 2.4.

Relatively minor variations in data taking conditions and possible systematic shifts in reconstructed quantities are accounted for by applying corrections to the reconstructed track momenta and cluster energies. Both are summarised in section 2.6.

Additionally, we use specialised tools to inject accidental hits into pure reconstructed MC events containing one single kaon decay. This is done in order to emulate the pileup observed in data, caused either by decays of other particles present in the high-intensity NA62 beam or by the presence of a muon halo accompanying the beam. The pileup generators are described in section 2.6.

In our analysis, we make use of the NA62 software framework[1] developed by the members of the Collaboration in `C++` with an extensive use of CERN `ROOT` library [83]. The whole framework consists of three packages: *NA62MC* (section 2.3), *NA62Reconstruction* (section 2.5) and *NA62Analysis* (containing tools necessary for any NA62 data analysis).

The $K_{\pi\mu\mu}$ signal and $K_{3\pi}$ normalisation data samples were collected using separate trigger streams described in subsection 2.2.11. Measurements of the underlying trigger efficiencies play a crucial role in the presented analysis since they affect both the shape and the scale of the resulting $K_{\pi\mu\mu}$ z spectrum (Eq. 1.28). In the case of the trigger stream used for collecting the $K_{3\pi}$ normalisation channel, it was possible to measure the corresponding trigger efficiencies directly from data.

However, due to the limited number of observed $K_{\pi\mu\mu}$ decays in data and non-existence of other non-rare K^+ decay producing a muon pair, it was impossible to reliably measure the trigger efficiency of the trigger stream used for collecting the $K_{\pi\mu\mu}$ signal events. To address this issue, detailed L0 and simplified L1 trigger emulators were developed, tuned and applied on MC samples on an event-by-event basis, using the accept/reject method. They are described in detail in subsection 2.6.6.

The z spectrum obtained from the $K_{\pi\mu\mu}$ data candidates is compared to the z spectrum of weighted $K_{\pi\mu\mu}$ MC events using a fitting procedure described in Appendix B. The form factor parameters a and b are determined based on the best agreement between the

---

[1] https://na62-sw.web.cern.ch/sites/na62-sw.web.cern.ch/files/doxygen/index.html

data and the weighted MC z spectra. The total $K_{\pi\mu\mu}$ branching fraction is computed by numerical integration of the $\mathrm{d}^2\Gamma/\mathrm{d}x\mathrm{d}z$ function shown in Eq. 1.31. We summarise the results of the form factor measurement in section 2.13.

Finally, systematic uncertainties on the form factor parameters and the $K_{\pi\mu\mu}$ branching fraction arising from track reconstruction efficiency, trigger efficiency, beam tuning, pileup and several other effects are estimated in section 2.15.

Final result including all systematic uncertainties and a comparison with the previous measurements is given in section 2.16.

2.2 NA62 Detector Setup in 2017

This section contains a description of the NA62 detector setup. The information presented here is based on the NA62 Technical Design Document [84] and the most recent publication describing the NA62 detector design and performance [26]. The NA62 detector is located in the CERN North Area, see Fig. 2.1. Figure 2.2 shows a simplified scheme of the NA62 detector.

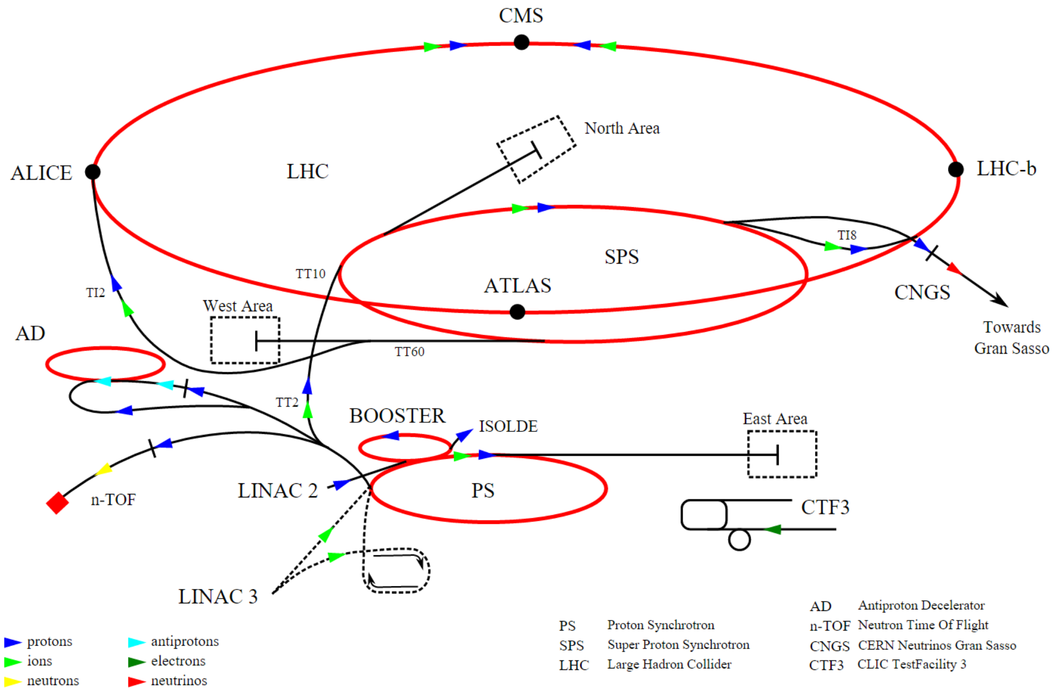

Figure 2.1: Scheme of the CERN accelerator complex. The NA62 experiment is situated in the North Area[2].

2.2.1 Beam Line

The NA62 beam is produced from a primary beam of 400 GeV/c SPS protons delivered in spills (sometimes called bursts) lasting a few seconds (3 s effective) with $\sim$ 10 seconds

---

[2] `http://en.wikipedia.org/wiki/File:Cern-accelerator-complex.svg`

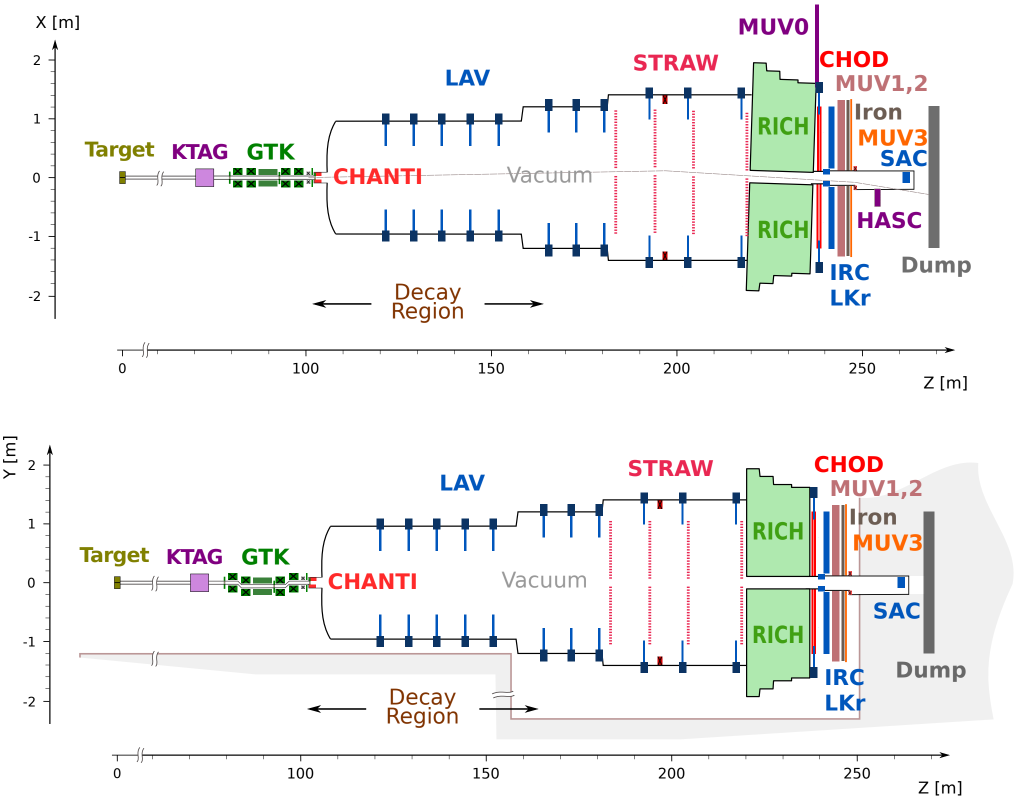

Figure 2.2: Simplified NA62 detector layout [26] in XZ (top) and YZ (bottom) views. Beam comes from the left side.

between spills. The primary SPS beam impinges on a 400 mm long and 2 mm diameter beryllium target (denoted T10 in Fig. 2.3) and produces positive secondary beam. A set of quadrupole magnets (Q1, Q2, Q3) and an achromat magnet (A1) consisting of four dipoles are used to select the beam of the mean momentum of 75 GeV/c and 1% momentum bite. Two motorised water-cooled beam-dump units (TAX1 and TAX2) are placed between the two pairs of the A1 achromat magnets in order to perform the momentum selection and absorb the unwanted particles.

The secondary beam is then refocused and stripped off of electrons by another set of quadrupole magnets (Q4, Q5, Q6) and three collimators (C1, C2, C3). Subsequently, the beam passes through three 2 m long dipole magnets with the purpose of deflecting muons. The beam is then refocused and realigned using two quadrupoles (Q7, Q8) and two collimators (C4, C5).

Afterwards, the beam enters the KTAG sub-detector designed to identify the K^+ beam component (subsection 2.2.2). After exiting the KTAG, the precise beam momentum measurement is performed using GTK sub-detector consisting of three silicon pixel stations surrounded by a set of dipole magnets denoted A2 in Fig. 2.3 (subsection 2.2.2).

The nominal rate of the secondary hadron beam entering the fiducial decay volume is $\sim$ 750 MHz. During the 2017 data taking, the average beam intensity was measured to be ≈ 60% of the nominal value. The composition of the secondary beam is: K^+ (6%), protons (23%), π^+ (71%). The beam divergence at the beginning of the decay region is 100 μrad rms with the transverse dimensions of 60×30 mm^2.

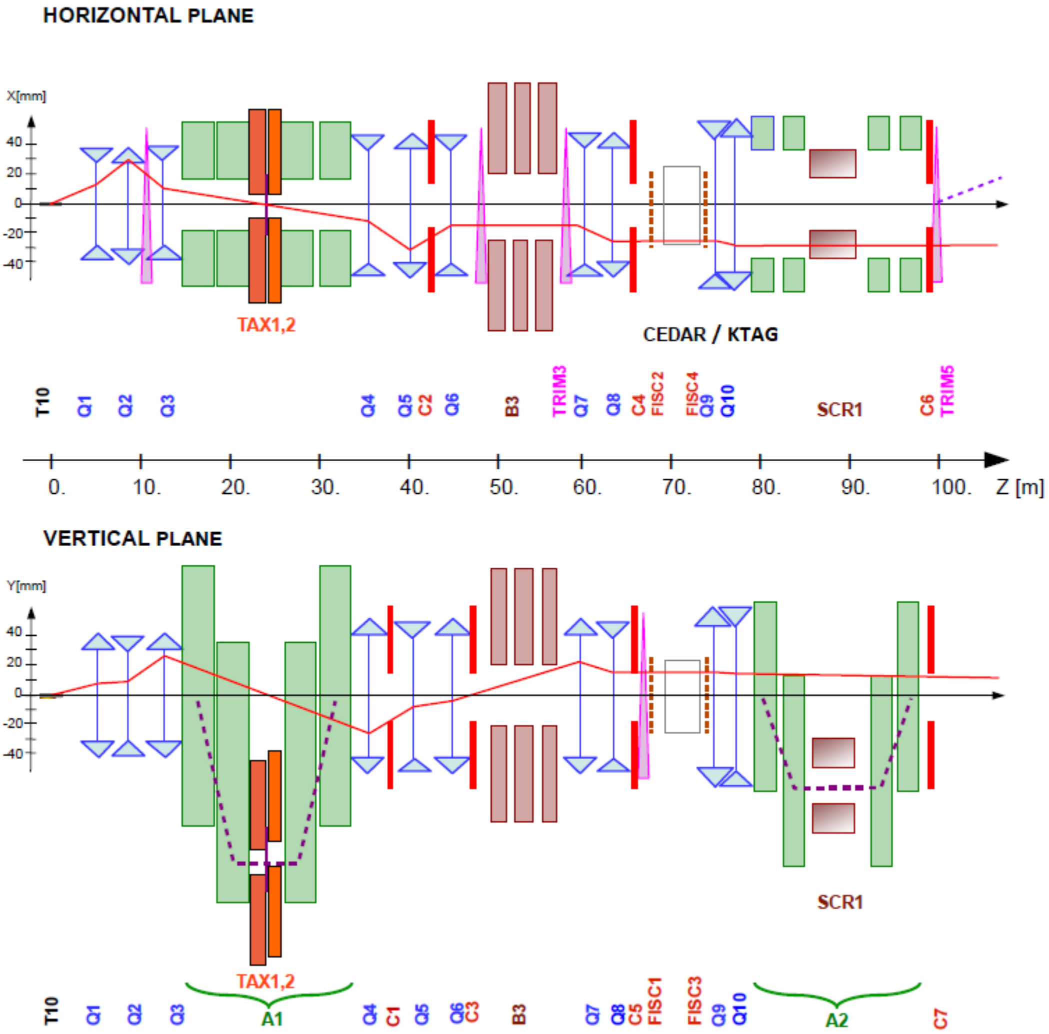

Figure 2.3: Schematic view of the K^+ beam line from the T10 target to the start of the fiducial volume, [26]. The figure has been modified by adding "/KTAG" next to the word "CEDAR" (see subsection 2.2.2 for explanation).

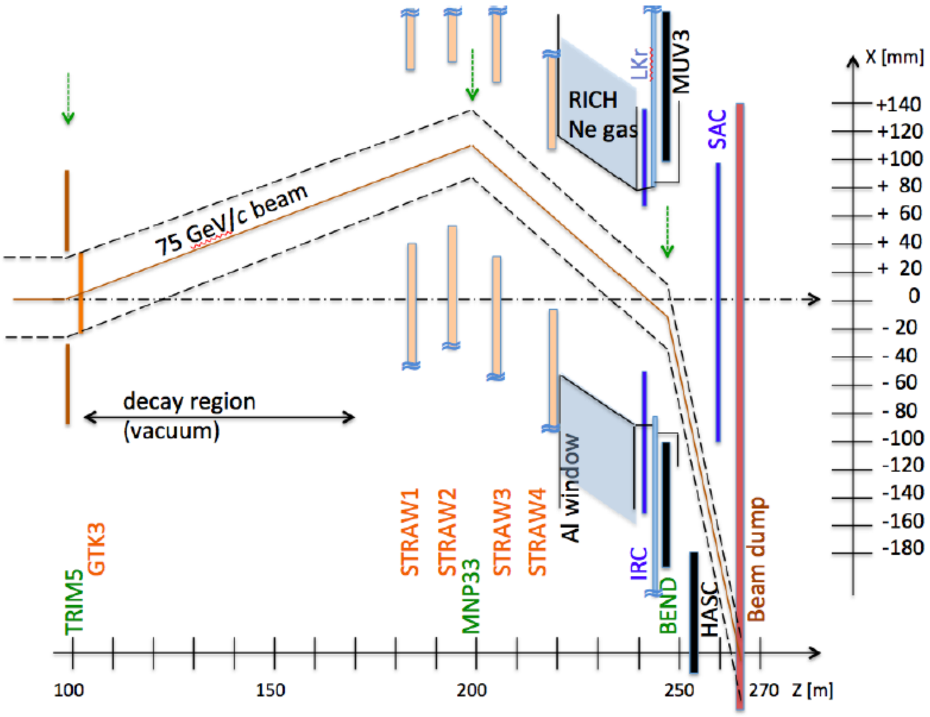

Figure 2.4: Scheme of the beam line after the last GTK station, [26].

2.2.2 Upstream Sub-detectors and Decay Volume

The Kaon Tagger (KTAG) is a differential Cherenkov counter filled with nitrogen gas at 1.75 bar and room temperature. It is used for positive identification of beam kaons amounting to about 6% of the NA62 beam. The Cherenkov light is produced inside a CERN W-type CEDAR vessel and focussed into rings using achromatic lenses. The photons are subsequently detected by photomultipliers.

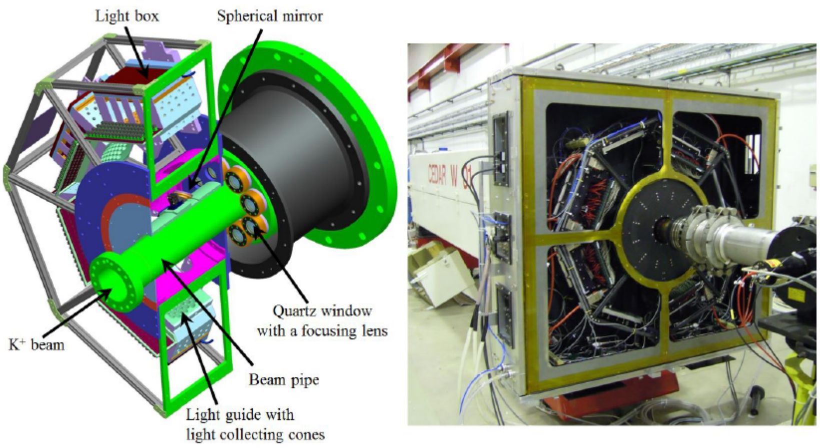

Figure 2.5: Drawing of the KTAG sub-detector with an upstream part of the CEDAR (left) and a photograph of the KTAG and CEDAR systems taken in 2012 (right), [26].

Since the original photomultipliers and readout system were insufficient for the high (∼ 45 MHz) kaon rate of the NA62 beam line, nor were they capable of reaching the required time resolution of less than 100 ps and the efficiency of 95%, an upgraded detection and readout system was developed, called KTAG. It is situated upstream of the CEDAR part of the detector, see Fig. 2.5. The pressure inside the CEDAR is chosen so that only Cherenkov light produced by charged kaons exits through an annular diaphragm and passes through eight quartz windows, corresponding to eight KTAG *sectors*, equipped with focusing lenses. The light is then reflected into eight sectors, each containing 48 photomultipliers.

The GigaTracker (GTK) is a beam spectrometer composed of three Si pixel stations separating two pairs of the last achromat A2 (subsection 2.2.1 and Fig. 2.6). The momentum of a beam particle is measured from the vertical displacement caused by A2.

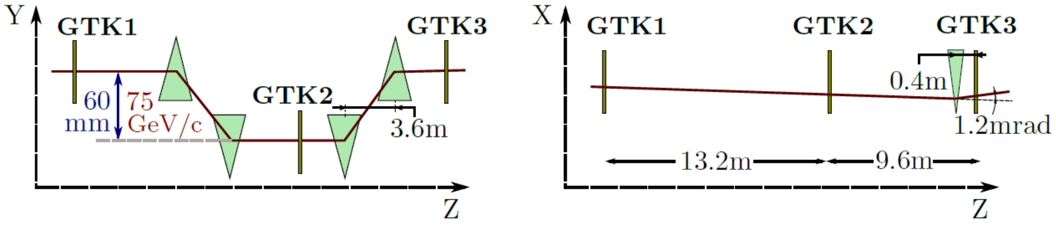

Figure 2.6: Scheme of the YZ view of the GTK stations and the achormat magnet A2 (left) and the XZ view of the GTK stations together with the 40 cm long TRIM5 magnet providing the final momentum kick of $p_T = 90$ MeV/c (right), [26].

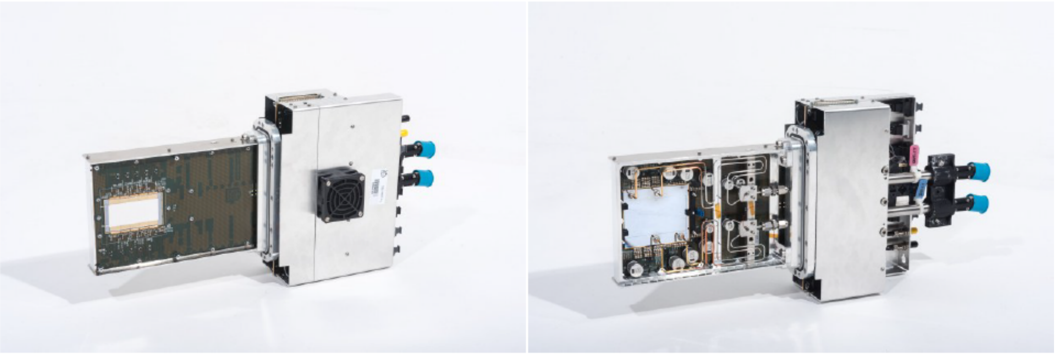

Figure 2.7: Assembled GTK station. Sensor side (left) and cooling side (right), [26].

Each GTK station has a resolution of 200×90 pixels of 300×300 μm^2, thus covering an area of 62.8×27 mm^2 (Fig. 2.7). The pixel matrix readout is provided by ten application-specific integrated circuits (ASIC) arranged in two rows by five chips.

The resolution of the momentum measurement is 0.2% and the resolution of the beam direction at the A2 exit is 16 μrad. The timing resolution is $\sigma_T \simeq 200$ ps.

The Charged Anti-coincidence detector (CHANTI) is a hodoscope placed immediately after the last GTK station. It serves as a veto to reduce the background originating from inelastic interactions of the beam particles inside the last GTK station.

It is also used as a veto for early decays of beam particles, products of which could enter the decay volume and mimic the signature of the $K_{\pi\nu\nu}$ decay.

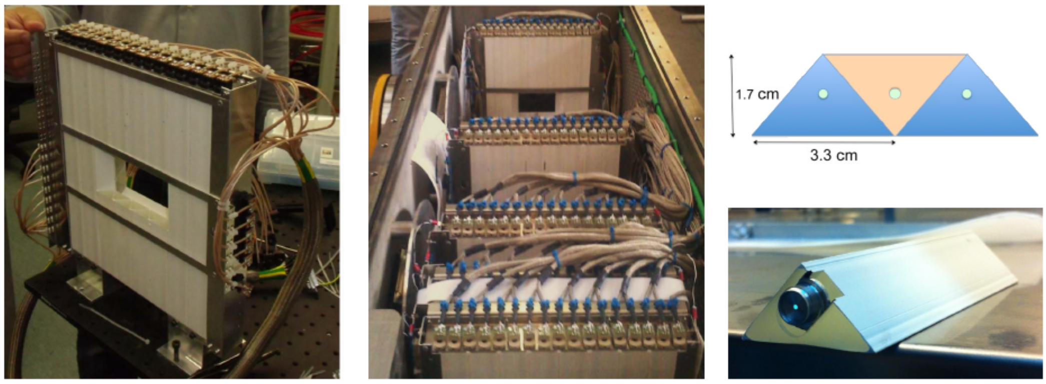

Figure 2.8: One assembled CHANTI station (left) and the first five CHANTI stations in a vacuum vessel during assembly (center). Right: schematic view of a transverse cut of three CHANTI scintillator bars (top) and a photograph of one bar with the WLS fibre in the middle (bottom), [26].

It is composed of six square stations of dimensions 300×300 mm^2 with a 95×65 mm^2 hole in the centre. Each station is composed of 48 bars of triangular cross section. The readout is provided by fast wavelength-shifting fibres (WLS) and silicon photomultipliers. Photographs and schematic view of the bars can be seen in Fig. 2.8.

The vacuum vessel and decay volume

A fraction ($\sim 10\%$) of the beam kaons decays inside a 65 m long evacuated fiducial volume consisting of several connected cylindrical parts of various diameter (Fig. 2.2), collectively called the Blue Tube (Fig. 2.9).

Figure 2.9: The NA62 vacuum vessel called the Blue Tube, [84]. The beam comes from the left. The white sections dividing the Blue Tube are individual LAV stations (subsection 2.2.5). The downstream spectrometer magnet can be seen as a light-blue square-shaped object downstream (subsection 2.2.3).

In order to minimise the interactions of the beam particles and kaon decay products with the residual gas inside the fiducial volume, the vacuum inside the vessel must be kept below the level of 10^{-6} mbar.

Magnetic field inside the Blue Tube, originating from the residual magnetisation of the cylindrical sections of the vacuum vessel as well as the Earth magnetic field, was measured and a field map was created [85]. This map is subsequently used in the offline analysis providing correction to particle momenta [26].

Products of in-flight decays of the charged kaons inside the fiducial volume are registered in several sub-detector systems described in the following subsections.

2.2.3 Momentum Spectrometer

The Spectrometer (Straw) is used for momentum and trajectory measurement of the charged downstream particles. It consists of four chambers separated in the middle by a high aperture dipole magnet (MNP33) producing a vertical magnetic field of 0.36 T, which translates into the momentum kick of 270 MeV/c (Fig. 2.4). The distance between the first and the last station is 35 m.

Each chamber is divided into four views: X, Y, U, V, each rotated by 45 degrees with respect to the previous one. The main building block of the spectrometer is an ultra-light, 2.1 m long, 9.8 mm thick drift chamber called the straw tube. Every view consists of four planes, each containing 448 straw tubes. The whole sub-detector thus contains 7168 of these tubes.

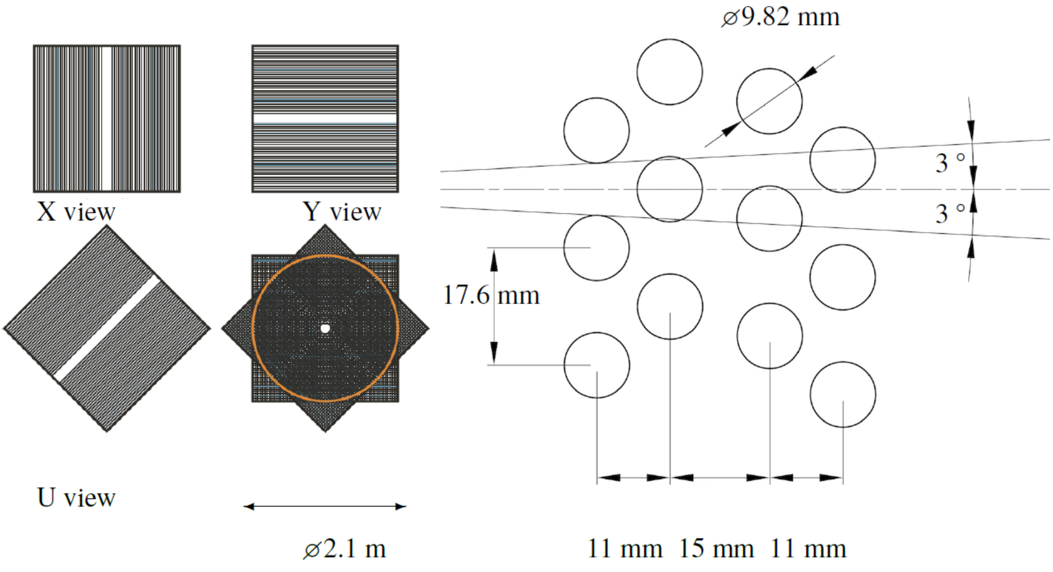

Figure 2.10: Left: individual Straw views X, Y, U and all four views in one chamber combined. Right: scheme of 12 straws in four planes of one view. The 3° angle in the figure represents the opening angle between decay products of charged kaons in the fiducial volume that are within Straw acceptance, [26].

The necessary level of kinematic suppression of the abundant charged kaon decay modes imposes strict requirements on the detector performance and resolution. The use of four views per chamber, four planes per view and the optimised individual straw positions within each plane (Fig. 2.10) provide sufficient redundancy and spatial resolution of space points. This translates into the following track momentum resolution

$$\frac{\sigma_p}{p} = 0.30\% \oplus 0.005\% \cdot p[\mathrm{GeV}/c] \ . \tag{2.1}$$

The track angular resolution varies with the track momentum from 60 μrad at 10 GeV/c to 20 μrad at 50 GeV/c. Both these values satisfy the design requirements.

2.2.4 Electromagnetic Calorimeter

The Liquid Krypton Calorimeter (LKr) was formerly used in the NA48 experiment. The inside volume is filled with 9000 litres of liquid krypton held at the temperature of 120 K. The LKr has a quasi-cylindrical cross section with an outer radius of 128 cm and a hole ($r \approx 8$ cm) for the beam pipe in the centre. The longitudinal dimension of the LKr container is 127 cm, which corresponds to $27X_0$.

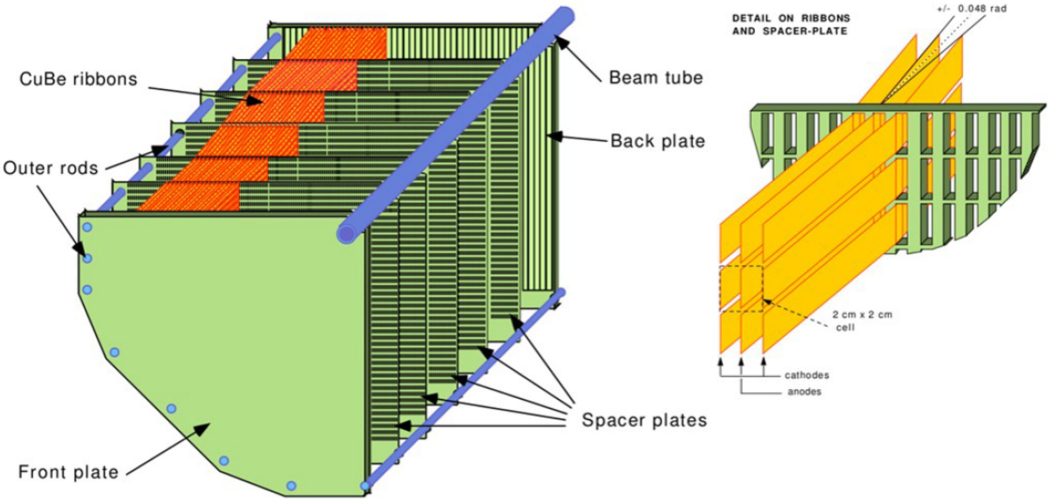

Figure 2.11: One quadrant of the LKr vessel (left) and a view of the ribbon-like Cu-Be electrodes (right), [26].

The LKr is subdivided into 13248 cells of an approximate cross section of 2×2 cm^2. The cells are defined by Cu-Be electrodes in the form of ribbons (Fig. 2.11). Particles crossing the active region of the LKr produce showers, which are then collected by the LKr electrodes. The signal is then amplified and read out by upgraded readout systems.

The energy resolution of the LKr detector was measured to be

$$\frac{\sigma_E}{E} = \frac{8.8\%}{\sqrt{E[\mathrm{GeV}]}} \oplus \frac{7.1\%}{E[\mathrm{GeV}]} \ . \tag{2.2}$$

2.2.5 Photon Veto Detectors

Several generic kaon decays produce neutral pions in their final state [18], which in majority of cases decay into two photons ($\mathcal{B}(\pi^0 \to 2\gamma) \simeq 98.8\%$, [18]). Since these abundant kaon decays could mimic the main $K^+ \to \pi^+ \nu\bar{\nu}$ signal (especially the $K^+ \to \pi^+\pi^0$, Table 1.1), it is necessary to detect these photons with an inefficiency smaller than 10^{-4}. The overall rejection factor of the photon veto system has to be of an order of 10^{-8}. Therefore, the NA62 experiment is equipped with multiple photon veto detectors placed at different positions along the beam axis to cover the wide range of possible photon emission angles: from 0 mrad to 50 mrad.

The intermediate range of angular acceptance (from 1 mrad to 8.5 mrad) is covered by the LKr described in the previous subsection 2.2.4.

The Large-Angle Veto (LAV) consists of 12 ring-shaped stations composed of lead-glass blocks connected to photomultipliers at one end (Fig. 2.12). First 11 LAV stations are placed inside the fiducial decay volume, while the last station is situated downstream on the LKr and is operated in air (Fig. 2.2). The LAV stations cover the angular acceptance from 8.5 mrad to 50 mrad.

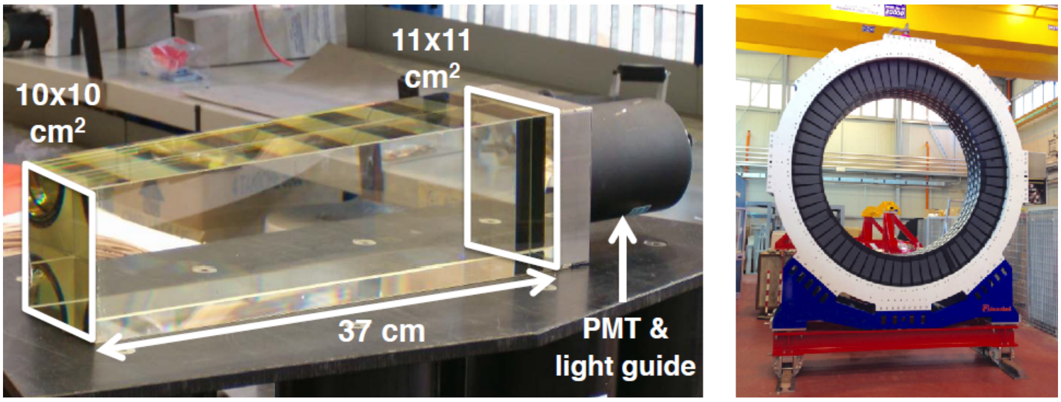

Figure 2.12: One lead-glass block used in the LAV (left) and a fully assembled LAV12 station (right), [26].

The Small-Angle Veto (SAV) covers the angular acceptance from 0 mrad to 1 mrad and is composed of two separate sub-detectors: the intermediate-ring calorimeter (IRC) and the small-angle calorimeter (SAC). The placement of the two sub-detectors is visible in Fig. 2.2 and Fig. 2.4.

2.2.6 Ring Imaging Cherenkov Detector

The Ring-Imaging Cherenkov detector (RICH) is designed to distinguish *positive* pions and muons in the momentum range from 15 GeV/c to 35 GeV/c. Rings corresponding to negative particles are usually not fully detected due to RICH tilt in the XZ-plane (Fig. 2.4) and the fact that charged particles have already been deflected by the Straw MNP33 magnet (subsection 2.2.3).

The RICH is housed in a 17.5 m long vessel filled with neon gas at atmospheric pressure and room temperature. These parameters ensure full efficiency at 15 GeV/c by placing the pion threshold at 12.5 GeV/c. The diameter of the vessel varies from 4.2 m upstream to 3.2 m downstream.

The upstream end of the detector is equipped with two arrays of photomultipliers placed outside of the active area of the detector, while the downstream part houses 18 hexagonal and 2 semi-hexagonal mirrors and their support structure (Fig. 2.13). The Cherenkov light is reflected off of the mirrors and focused on the two arrays of photomultipliers. The ring time resolution of the RICH detector is below 100 ps, which is in agreement with the design value.

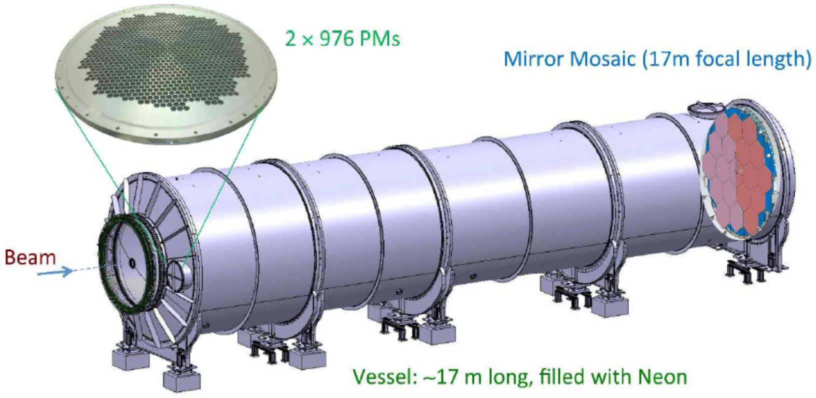

Figure 2.13: RICH vessel, beam comes from the left hand side, [26].

2.2.7 Charged Hodoscopes

The NA48 Hodoscope (NA48-CHOD) was originally used in the NA48 experiment and is now being reused for the detection of possible photo-nuclear interactions in the RICH mirrors and as a part of the L0 trigger for collecting minimum bias Control data.

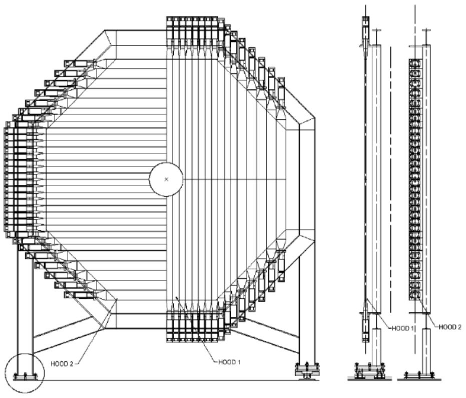

Figure 2.14: Schematic view of the NA48-CHOD detector. Only halves of the vertical and horizontal planes are shown, [26].

It consists of 64 vertical and horizontal plastic scintillator slabs. Each slab is read out at one end by a photomultiplier. The slabs are 20 mm thick and vary in width from

65 mm in the region close to the beam pipe to 99 mm in the outer regions. The outer edge of the NA48-CHOD is shaped like an octagon (Fig. 2.14). The time resolution of the NA48-CHOD is ∼ 200 ps and the spatial resolution is given by the width of the slabs.

The Hodoscope (CHOD) consists of 152 plastic scintillator tiles of various sizes and shapes (Fig. 2.15) and the thickness of 30 mm. The tiles cover the annular active area of the detector spanning from the inner radius 140 mm to the outer radius 1070 mm.

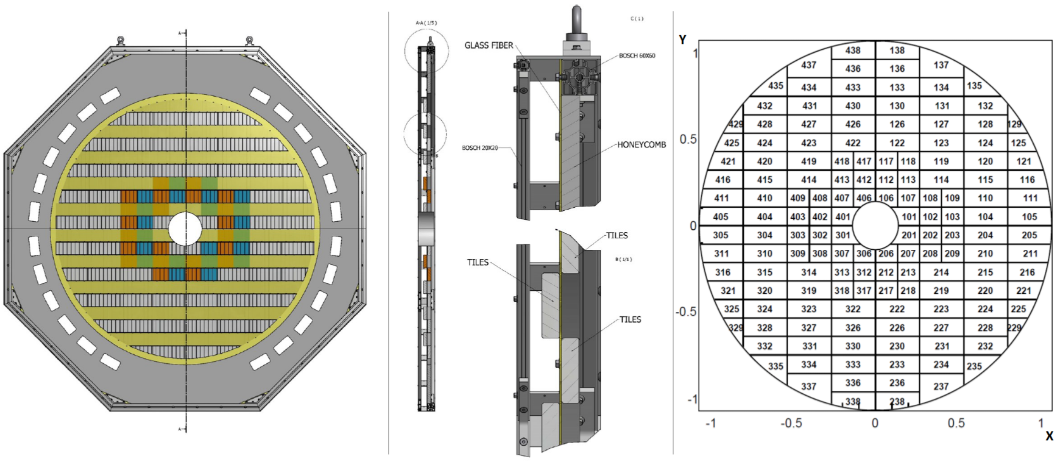

Figure 2.15: CHOD mounting on the LAV12 front face (left), the scintillator mounting and transverse cut of the support structure (centre), CHOD tile shapes and tile numbering (right)[3], [26].

Each CHOD scintillator tile is read out by a pair of photomultipliers. The time resolution of the CHOD detector is ∼ 1 ns.

2.2.8 Muon Veto System

Muon veto system consists of three separate sub-detectors: MUV1, MUV2 and MUV3. The main purpose of this system is to provide π^+/μ^+ particle identification in addition to the RICH. This is achieved by placing two hadronic calorimeters MUV1 and MUV2 in front of an 80 cm thick iron wall, with the MUV3 – a fast muon veto – placed downstream of this wall. The MUV1 and MUV2, shown in Fig. 2.16, are standard iron-scintillator sandwich calorimeters, while the MUV3 is composed of a single layer of plastic scintillator tiles.

The MUV1 consists of 24 layers of 26.8 mm thick steel plates with 23 layers of plastic scintillator strips, which are 9 mm thick and 60 mm wide. The strips in two consecutive layers are alternately aligned in the horizontal and vertical direction. The strips are read out by WLS fibres connected to photomultipliers. The outer edge of the MUV1 detector is of a rectangular shape with the dimensions of 270 × 260 cm^2.

---

[3] `https://twiki.cern.ch/twiki/pub/NA62/NewChodDetector/channelmap.PNG`, modified

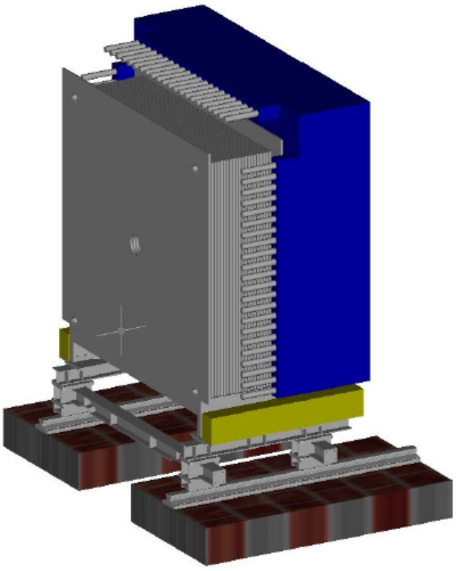

Figure 2.16: Drawing of MUV1 (grey) and MUV2 (blue) detectors, [84].

The MUV2 is an upgraded hadronic calorimeter originally used in NA48. It is composed of 24 layers of iron plates of 25 mm thickness, each followed by a layer of scintillator strips with the dimensions 1300 × 119 × 4.5 mm^3 (length × width × thickness). Each strip spans half the calorimeter, so the outer calorimeter dimensions are 260×260 cm^2. As in the MUV1 sub-detector, the strips in consecutive planes are alternately aligned in the horizontal and vertical direction. The strips are connected to photomultipliers using Plexiglas light-guides.

The MUV3 consists of a total number of 148 square-shaped plastic scintillating tiles arranged in a square of 264 × 264 cm^2 (Fig. 2.17).

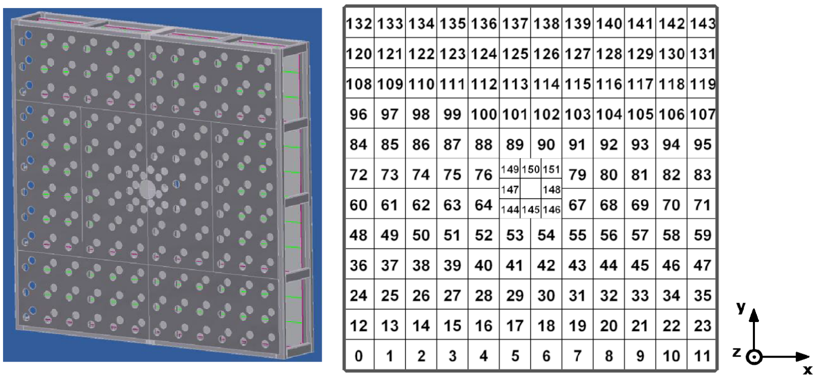

132	133	134	135	136	137	138	139	140	141	142	143
120	121	122	123	124	125	126	127	128	129	130	131
108	109	110	111	112	113	114	115	116	117	118	119
96	97	98	99	100	101	102	103	104	105	106	107
84	85	86	87	88	89	90	91	92	93	94	95
72	73	74	75	76	149 150 151 147 148 144 145 146		79	80	81	82	83
60	61	62	63	64			67	68	69	70	71
48	49	50	51	52	53	54	55	56	57	58	59
36	37	38	39	40	41	42	43	44	45	46	47
24	25	26	27	28	29	30	31	32	33	34	35
12	13	14	15	16	17	18	19	20	21	22	23
0	1	2	3	4	5	6	7	8	9	10	11

Figure 2.17: Left: MUV3 detector layout with holes indicating photomultiplier positions, [84]. Right: scheme of the MUV3 detector geometry[4]. Numbers indicate tile numbering (so called geometric tile ID).

These tiles are divided into two groups: 8 inner and 140 outer tiles. The outer (inner) tiles have dimensions 22 × 22 cm^2 (14.6 × 14.6 cm^2). All tiles have a thickness of 5 cm

---

[4] `https://twiki.cern.ch/twiki/pub/NA62/Muv3Detector/MUV3-tile-numbering.GIF`

and are read out by 2 photomultipliers housed in a light-tight box to avoid cross-talk between neighbouring tiles. There is a vertical gap of 0.8 mm separating the $x > 0$ and $x < 0$ halves of the MUV3. Since this gap is not covered by any tiles, it constitutes an inactive region of the sub-detector. The time resolution of MUV3 is ~ 0.5 ns.

2.2.9 Other Veto Detectors

Two additional detectors are used to suppress $K^+ \to \pi^+\pi^+\pi^-$ decays in which one or two of the pions escape the acceptance of Straw spectrometer: MUV0 and HASC. If not vetoed, these decays could potentially mimic the $K^+ \to \pi^+\nu\bar{\nu}$ signal. The placement of these two detectors can be seen in Fig. 2.2 and the schematic view of the detectors is shown in Fig. 2.18.

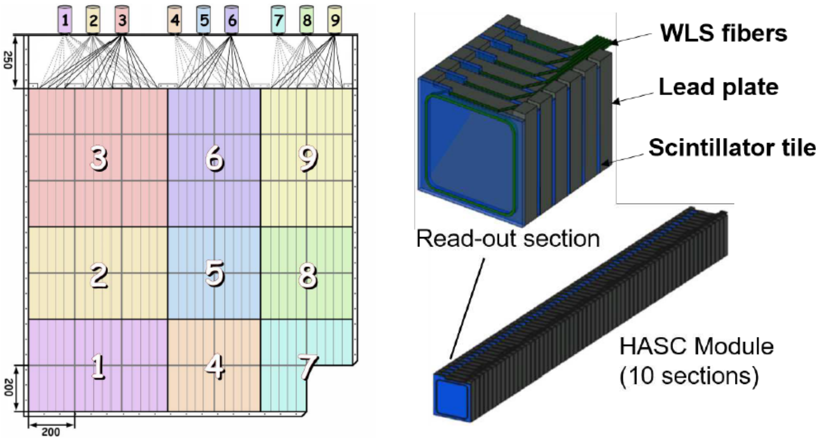

Figure 2.18: Left: schematic view of MUV0 displaying the subdivision into scintillator tiles and super-tiles. Right: six consecutive scintillators of HASC form one readout section (top), while 10 such sections form one HASC module (bottom), [26].

The Peripheral Muon Veto (MUV0) is a scintillator hodoscope placed downstream of RICH and serves for the detection of π^- from $K_{3\pi}$ decays with momenta below 10 GeV/c that escaped the Straw acceptance due to the kick of the MNP33 magnet.

The Hadronic Sampling Calorimeter (HASC) is placed downstream of MUV3 and the BEND dipole magnet used to deflect the beam from the SAC (Fig. 2.4). The primary purpose of HASC is to detect π^+ with momenta above 50 GeV/c originating from $K_{3\pi}$ decays and travelling through the beam holes in Straw chambers. The HASC consists of 9 modules composed of 10 sections. Each section, consisting of alternately placed 6 lead plates and 6 scintillator tiles, is read out by WLS optical fibres and photomultipliers.

2.2.10 Trigger and Data Acquisition Systems

High intensity beam of the NA62 experiment (750 MHz), necessary for the study of (ultra) rare kaon decays, results in a high flux ($\mathcal{O}(10)$ MHz) of secondary particles in the NA62 sub-detectors. Therefore, the NA62 Trigger and Data Acquisition Systems have to satisfy strict conditions in order to minimise system dead time and maximise the reliability of data taking.

The NA62 Trigger System consists of one hardware-implemented trigger level denoted L0 and two software trigger levels called L1 and L2 running on a PC farm. The input rate of the L0 trigger corresponds to the full rate in the NA62 sub-detector systems and is of an order of 10 MHz. The output rate of L0 trigger was designed to be 1 MHz at maximum. The limited bandwidth of 10 kHz for writing data on magnetic storage tapes imposes additional requirements on the L1 and L2 triggers. Figure 2.19 shows a simplified scheme of the NA62 trigger system.

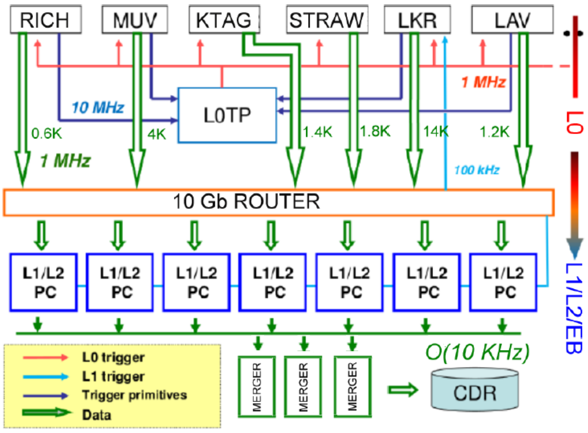

Figure 2.19: NA62 TDAQ system schematics (some sub-detectors are not shown), [26].

The L0 hardware trigger uses information from sub-detectors RICH, CHOD, MUV1, MUV2, MUV3, LKr and LAV. These detectors send compressed information in the form of L0 trigger primitives via Gigabit Ethernet links to the Level 0 Trigger Processor (L0TP). Based on the currently evaluated trigger condition, the L0TP combines and time-matches primitives from required sub-detectors and subsequently gives an appropriate L0 trigger verdict.

In case of a positive L0 trigger decision, the L0 trigger signal is sent to Local Trigger Units (LTU, see below and Fig. 2.20), which then propagate it to front-end electronics (FEE) of all sub-detectors. Each subsystem (except GTK and calorimeters) responds by sending the corresponding data to the PC farm, where the L1 and L2 software triggers are evaluated. The large data fluxes of GTK and calorimeters make readout at L0 for these systems impossible. Instead, their data is stored in local temporary buffers and is sent directly to the PC farm only if a positive L1 trigger verdict is received.

The data flow exiting L2 trigger has an event rate of around 10 kHz, which is sufficiently low for it to be stored on tape for later offline reconstruction and analysis.

The Common Signal Distribution: the NA62 uses the Time and Trigger Control (TTC) system for clock and trigger distribution. The TTC is based on a one-way signal transmission via optical fibre. It was developed at CERN and is used by all LHC experiments. The main clock with a period of ~ 25 ns is generated by a single high-quality oscillator (40.079 MHz) situated in the experimental area. During the SPS spill (subsection 2.2.1), all synchronous TDAQ systems of the NA62 experiment are fully synchronised to this clock. System of LTUs serves as an interface between the L0TP and the FEE of NA62 sub-detectors and manages distribution of the main clock signal to the sub-detector FEE. For a better visualisation of the described relations, see Fig. 2.20. The LTU module testing and programming of LTU control software were the primary responsibilities of the Bratislava NA62 group during the development phase of the NA62 experiment[5].

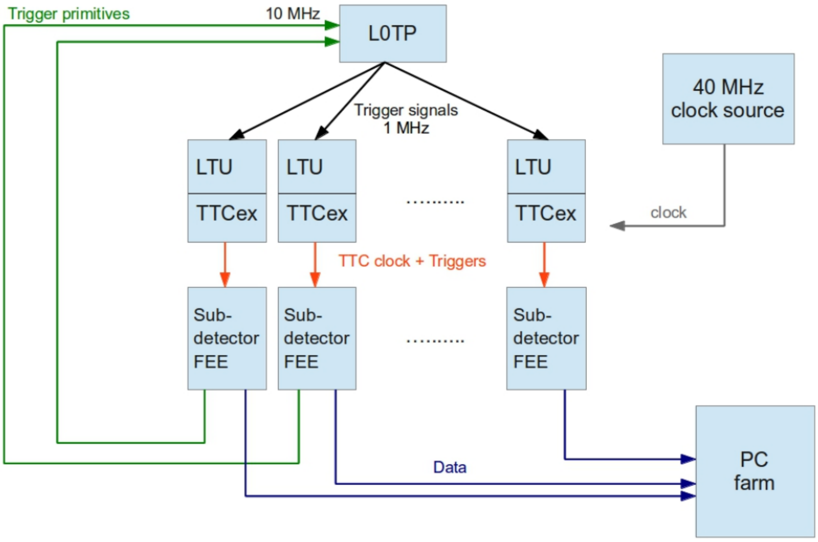

Figure 2.20: Simplified NA62 L0 trigger signal and clock distribution scheme[5].

The Data Acquisition in the NA62 experiment is provided by several systems:

- Majority of the NA62 sub-detectors (CHANTI, LAV, NA48-CHOD, CHOD, RICH, MUV3, SAC and IRC) are equipped with specialised TEL62 boards [86], initially developed for LHCb as TELL1 [87]. Each TEL62 can house up to four high-performance TDCB cards [88].

  TEL62 boards are used in online data acquisition. Additionally, TEL62 boards of sub-detectors participating in the L0 trigger also generate L0 trigger primitives.

  The purpose of the TDCBs are high-resolution time and time-over-threshold measurements. Each TDCB can process signals from up to 128 input channels.
- The GTK readout system uses custom made ASICs called TDCPix. In addition, an off-detector readout system (GTK-RO) was developped in order to bridge the TDCPix readout with the TTC system.
- The Straw spectrometer FE boards are called Covers. Each houses two CARIOCA

---

[5] http://na48.web.cern.ch/NA48/Welcome/thesis/PhDthesis_Koval.pdf

chips [89] originally developed for LHCb muon chambers. Every Cover serves 16 channels. One straw of the Straw spectrometer constitutes one channel. All channels are equipped with time-to-digital converters (TDC). The TDC measures leading and trailing edges of the signal.

The leading edge gives information about the radial distance of a particle track from the straw wire. The trailing time does not depend on the path of the particle through the straw and represents the particle crossing time, which is used to improve the offline track reconstruction.

Covers are connected to back-end (BE) electronics called Straw Readout Boards (SRB) using Ethernet cables. SRBs receive and process data from Covers, react to L0 triggers and send data to the PC farm.

- The readout from LKr, MUV1 and MUV2 calorimeters is provided by Calorimeter Readout Modules (CREAM) [90]. The CREAM is a 6U VME 64 board developed by CAEN[6], based on the specifications provided by NA62. Each CREAM consists of two boards: a daughter-board that shapes and digitises the input signals, and a motherboard that processes the data and sends it to the PC farm if the relevant trigger decision arrives.

2.2.11 Relevant Trigger Conditions

Three separate trigger streams have been used in the presented $K^+ \to \pi^+\mu^+\mu^-$ ($K_{\pi\mu\mu}$) decay form factor measurement:

1. **Di-muon** trigger stream was designed to accept events with at least two muons. This trigger stream was used to obtain the $K_{\pi\mu\mu}$ signal sample.
2. **Multi-track** trigger stream collected events compatible with the presence of multiple tracks and was used to select the $K_{3\pi}$ normalisation sample.
3. **Control** trigger stream is a multi-purpose minimum-bias trigger. Its use is described below.

Generally, trigger streams consist of several L0 conditions and L1 algorithms. The first two trigger streams mentioned above belong to a category of dedicated *physics triggers*. The Di-muon and Multi-track trigger streams share significant part of their trigger stream components. The Control trigger stream contains only one condition and was used in this analysis to measure the efficiencies of L0 conditions of the two physics triggers.

L0 conditions are evaluated using sub-detector hits. These hits are clustered in sub-detector-specific time windows by clustering algorithms described in subsection 2.6.6. Information about hits in each cluster is turned into a trigger primitive. Trigger primitive

---

[6] `http://www.caen.it`

time is defined as the average time of all cluster hits. Cumulative properties of hits in a given primitive define the type of that primitive. One trigger primitive can satisfy multiple L0 trigger conditions. Generated L0 trigger primitives from sub-detector systems that participate in L0 trigger are sent to the L0TP (subsection 2.2.10), where they are time-matched within 6.25 ns and compared to L0 trigger primitives from other sub-detectors.

Let us now describe all relevant trigger stream conditions and algorithms in more detail. The actual composition of the three trigger streams is given at the end of this section.

Control condition requires time coincidence (within 6.25 ns) of signals from at least one pair of overlapping vertical and horizontal slabs of the NA48-CHOD. The condition aims to select events with at least one charged decay product.

L0 RICH condition is met if there is a cluster consisting of at least two in-time (6.25 ns) hits registered in the RICH. The time of this cluster is defining the event *trigger time*. In the case of Control events that did not pass L0 RICH condition, the trigger time is the NA48-CHOD time.

L0 QX condition requires time coincidence (6.25 ns) between at least two hits in CHOD sub-detector situated in opposing CHOD quadrants. The condition was designed to preferably select events with multi-track signature: the fact that positive and negative particles are bent by the Straw magnet (subsection 2.2.3) in opposing directions in the XZ-plane and predominantly hit the CHOD detector in different quadrants is exploited here.

L0 MO2 condition asks for a time coincidence of at most 6.25 ns between at least two hits in outer tiles of the MUV3 sub-detector, which aims to select events with at least two muons in-time. The inner MUV3 tiles are excluded from the condition in order to reduce the otherwise significantly higher[7] trigger rate caused by beam pion decays $\pi^+ \to \mu^+\nu$.

L1 KTAG algorithm requires there are hits registered in at least five KTAG sectors within 10 ns from the trigger time defined by the L0 RICH condition. The L1 KTAG algorithm is designed to positively identify kaons.

L1 STRAW Exotics (simply STRAW$_\mathrm{e}$) algorithm uses hits from Straw sub-detector. The hits are clustered first within one view and then within one chamber. The resulting clusters serve as an input to a pattern recognition algorithm employing fast Hough transform [91], which tries to determine if their positions are compatible with a negative track traversing the detector. Only clusters with hits in at least three out of four views per chamber are considered in the L1 STRAW$_\mathrm{e}$ algorithm. This condition is a source of most of the L1 STRAW$_\mathrm{e}$ inefficiency observed in data (more details can be found in subsection 2.6.6).

---

[7] The integrated channel rates in inner (outer) MUV3 tiles are 6.0 MHz (7.7 MHz), respectively.

If a given trigger stream employs more than one L1 trigger algorithm, the algorithms run in a specific predefined order. It is always true that, for a given event, next L1 algorithm in the sequence is executed only if the previous L1 algorithm accepted the event.

In addition to the trigger conditions and algorithms described above, the NA62 trigger streams are subjected to different L0 and L1 *downscaling factors* D. The purpose of these factors is to reduce the rate from the trigger streams to manageable levels. They are chosen based on the non-downscaled rates and on the relevance of a particular trigger stream to the NA62 experiment.

Another mechanism implemented at L1 trigger is the application of *L1 autopass fraction* f: an event passing all L0 trigger conditions relevant to a given trigger stream is with a probability f accepted regardless of the decision of L1 algorithms in that trigger stream. The L1 algorithms are however evaluated and their decision is stored together with the event. This sub-sample of events is used for measuring the efficiency of L1 trigger algorithms.

The three trigger streams listed at the beginning of this section are defined in Table 2.1. The Di-muon trigger stream does not contain the L1 KTAG algorithm due to the fact that it was also used for searches of exotic particles in events not involving kaon decays.

Let us briefly mention that the acquisition of data used for the main $K_{\pi\nu\nu}$ analysis proceeds via a dedicated *non-downscaled* trigger stream, which uses different trigger stream components to the ones listed above (e.g. the LKr sub-detector). It is beyond the scope of this thesis to describe the $K_{\pi\nu\nu}$ trigger stream in detail.

In order to separate the data samples used for trigger efficiency computation and $K_{3\pi}$ and $K_{\pi\mu\mu}$ signal selection, we use the following scheme:

- The $K_{3\pi}$ ($K_{\pi\mu\mu}$) signal events are taken only from such sub-samples of data that pass the Multi-track (Di-muon) trigger streams but are accepted by *neither* the Control trigger *nor* are L1 autopass.
- Efficiency of L0 conditions (with the exception of the MO2 trigger condition) present in Multi-track and Di-muon trigger streams is measured using sub-sample of Control events. The decisions of the relevant L0 trigger conditions are saved in these events. The MO2 efficiency was measured on L1 autopass Multi-track events due to an observed correlation between QX and MO2 trigger decisions. More details are given in subsection 2.6.6.
- Efficiency of L1 algorithms is measured on Multi-track or Di-muon L1 autopass events.

Adopting this scheme reduces the statistics of $K_{3\pi}$ and $K_{\pi\mu\mu}$ signal events by $\sim 2\%$ (value mostly given by the autopass fraction f) compared to the case when Control and autopass events were not rejected from the signal sub-sample. However, separating the

Trigger stream	L0 conditions	L1 algorithms	L0 D	L1 D	f
Di-muon	RICH×QX×MO2	STRAW$_\mathrm{e}$	2	1	0.02
Multi-track	RICH×QX	KTAG→STRAW$_\mathrm{e}$	100	1	0.02
Control	Control		400		

Table 2.1: Definition of NA62 trigger streams relevant for the $K_{\pi\mu\mu}$ analysis.

signal and trigger efficiency measurement sub-samples ensures the values obtained from them are uncorrelated.

2.3 Monte Carlo Simulation

In order to evaluate acceptances of the signal and normalisation decay modes, we used the official NA62 Monte Carlo (MC) samples. The NA62 MC event generation is an integral part of the NA62 software framework[8] and is comprised of several modules described below.

Kaon Beam simulation uses ray-tracing program TURTLE [92] to propagate the kaon beam through the upstream beam optics up to the KTAG sub-detector (subsection 2.2.2), where the beam kaon is passed to Geant4 [93] which handles the rest of the simulation. The MC beam position and momentum are tuned to match the ones observed in data by building the kaon from $K^+ \to \pi^+\pi^+\pi^-$ ($K_{3\pi}$) decay products in data, back-propagating it to the third GTK station and using the resulting momentum and position distributions to appropriately modify several MC parameters. The MC samples used in our analysis have been tuned to match the beam conditions in 2016. This results in a systematic uncertainty on the final result arising from the difference in beam momentum distributions in 2016 and 2017 data samples. This is discussed in detail in section 2.15.

Decay generators constitute separate libraries developed in Fortran or `C++` mostly by members of the NA62 Collaboration and include radiative or Coulomb corrections, when applicable. The two most relevant decay generators for the presented thesis handle the $K_{3\pi}$ and $K_{\pi\mu\mu}$ decays. The theoretical description of the $K_{\pi\mu\mu}$ decay was given in section 1.3, while the $K_{3\pi}$ decay amplitude is described in [94].

Particle propagation and interactions within the NA62 detector are simulated using the Geant4 toolkit. Among the simulated interactions are Compton and multiple Coulomb scattering, pair production, $e^- - e^+$ annihilation, bremsstrahlung, Cherenkov and scintillator light emission and (with limited accuracy) hadronic and nuclear interactions. Decays of unstable kaon decay products, such as $\pi^\pm \to \mu^\pm\nu$, $\pi^0 \to \gamma\gamma$ or $\mu^\pm \to e^\pm\nu\bar{\nu}$ are simulated as well. Due to its extremely short lifetime [18], decays of π^0

---

[8] https://na62-sw.web.cern.ch/sites/na62-sw.web.cern.ch/files/doxygen/index.html

are usually handled at the level of generators and Geant4 receives only the π^0 decay products.

Detector response simulation involves Cherenkov light production inside KTAG and RICH sub-detectors, generation of electromagnetic and hadronic showers inside LKr and emission of scintillation light in scintillator-based detectors.

Output of the MC generation phase is a `ROOT` [83] file containing non-digitised MC hits as well as true information about kaons and their decay products.

GRID production [95] is used to generate the large ($\mathcal{O}$(10M) events) MC samples necessary for most of the analyses performed by the NA62 Collaboration.

2.4 Data and Monte Carlo Samples

The following centrally generated and reconstructed MC samples have been used in the presented analysis: $K_{\pi\mu\mu}$, $K_{3\pi}$, $K_{3\pi}$ upstream and $K^+ \to \pi^+\pi^-\mu^+\nu$ ($K_{\mu4}$). The numbers of reconstructed events from these MC samples entering our analysis and the branching fractions of the decays are summarised in Table 2.2.

MC sample	Reconstructed events	Branching fraction [18]
$K_{\pi\mu\mu}$	$9,811,801$	$(9.4 \pm 0.6) \times 10^{-8}$
$K_{3\pi}$	$44,553,712$	$(5.583 \pm 0.024)\%$
$K_{3\pi}$ upstream	$93,927,389$	$(5.583 \pm 0.024)\%$
$K_{\mu4}$	$76,387,969$	$(1.4 \pm 0.9) \times 10^{-5}$

Table 2.2: MC samples used in the presented $K_{\pi\mu\mu}$ analysis.

The $K_{3\pi}$ upstream sample was generated by forcing the kaons to decay between 96.95 m and 102.425 m from the beryllium target and was produced to understand an upstream background observed in $K_{\pi\mu\mu}$ event candidates in data. It is discussed in more detail in section 2.10.

In the remaining MC samples the kaons were forced to decay between 102.425 m and 180 m from the beryllium target.

The data used in our analysis was recorded between September 21st and October 23rd 2017 with relatively stable data taking conditions, and is internally referred to as *2017 Sample A*. The collected NA62 dataset is split into smaller units with almost constant data taking conditions, called *runs*, which themselves consist of *bursts* corresponding to data recorded in individual SPS spills.

In order to ensure sufficient quality of the analysed data, we required that each burst was *not* marked as bad (chapter 3) by any of the following subsystems: KTAG, NA48-CHOD, CHOD, MUV3, Straw and Processing. More details can be found in section 2.8. The remaining good bursts constitute

$$N_{\mathrm{K}} = (5.17 \pm 0.01_{\mathrm{stat}} \pm 0.43_{\mathrm{syst}}) \times 10^{11} \tag{2.3}$$

kaon decays. N_{K} was measured from data events passing our $K_{3\pi}$ selection described in section 2.8 and section 2.9 with the selection acceptance obtained from the $K_{3\pi}$ MC sample described above. The systematic uncertainty is calculated from all relevant contributions listed in section 2.15 and is dominated by Straw track reconstruction efficiency.

2.5 Event Reconstruction

A separate software package included in the NA62 framework manages both data and MC event reconstruction. When run on raw MC files, the non-digitised MC hits from all sub-detectors first undergo digitisation, followed by a full event reconstruction. The data is only subjected to the latter.

The actual event reconstruction is performed by individual modules specifically designed for each sub-detector. Most of the modules use sub-detector information in the form of reconstructed hits to form sub-detector *candidates*. Each candidate should represent registration of a single particle by a given sub-detector. Following paragraphs give simplified description of reconstruction algorithms employed in sub-detectors most important for this thesis.

KTAG reconstruction time-corrects and subsequently clusters KTAG hits close in time (within 2 ns). Each cluster represents one reconstructed KTAG candidate. KTAG hits associated to a given candidate define the number of sectors that have been hit by the Cherenkov light produced by a passing kaon (subsection 2.2.2). A cut on the candidate time and its number of sectors is used at the analysis level to positively identify kaons.

Straw reconstruction employs several stages designed to reconstruct Straw tracks from Straw hits. Hit time and position information is used in the process. Leading time of a hit defines the closest distance of a line segment representing particle crossing path through a straw tube from the corresponding straw wire, while the trailing time gives information about the particle crossing time. Straw hits in a given event are first clustered within planes, views and chambers and subsequently a track is fitted to resulting cluster positions using Kalman filter algorithm [96]. Hits from three Straw chambers are sufficient to reconstruct a Straw track.

NA48-CHOD reconstruction builds NA48-CHOD candidates by time-matching hits from vertical and horizontal slabs from the same quadrant and within 25 ns from the trigger time. The time difference between a pair of hits considered for a candidate is set to 10 ns. Individual hit times are corrected for time of light propagation in each slab and slewing corrections involving hit time-over-threshold are applied.

LKr reconstruction is a complex tool originally written in Fortran for the NA48 experiment and is described in an NA62 internal note[9]. It builds clusters (LKr candidates) from energy deposited in neighbouring cells. Several sub-routines and fitting procedures are used to improve the accuracy of the estimate of the deposited energy, particularly if there are shower overlaps.

CHOD and MUV3 reconstruction use similar algorithms to reconstruct CHOD and MUV3 candidates. These candidates can be of either *loose* or *tight* type. Loose candidates are created from only one photomultiplier (PMT) hit in a given tile due to either there being no other hit in the second PMT or the second hit being outside a predefined time window set to 5 ns (10 ns) in the case of MUV3 (CHOD). Tight candidates are created if there is a time coincidence between hits from two PMTs in the same tile. In our analysis, we used both loose and tight candidates.

The reconstructed events are saved in `ROOT` [83] files and written to a storage accessible by the whole NA62 Collaboration.

2.6 Applied Corrections

Reconstructed data and MC events are subjected to several additional corrections applied at the analysis level. In case of data, this is done to correct for varying data taking conditions such as currents in GTK or Straw magnets, sub-detector misalignment, etc. On the other hand, MC corrections are mostly (with the exception of LKr corrections) applied to fine-tune parameters already present in the MC simulation. The most important corrections for the presented analysis are Straw track corrections and LKr cluster corrections described in subsection 2.6.1 and subsection 2.6.2, respectively.

Apart from application of the corrections mentioned above, we used two pileup generators, MUV3 sub-detector efficiency tool (section 3.1) and a set of trigger emulators on MC. The purpose of pileup generators is to inject additional hits or candidates to the original MC event in order to simulate accidental activity inside the detector, which is inherently present in data. The necessity to apply MUV3 sub-detector efficiency on MC is discussed in subsection 2.6.5. The main reason for the development and use of trigger emulators was an estimation of Di-muon trigger efficiency (subsection 2.2.11), which can't be directly measured from data due to low number of observed $K_{\pi\mu\mu}$ events. All these tools are described in detail in the following subsections.

---

[9] https://na62.web.cern.ch/NA62/restricted/NotesDoc/NA62_15_02.pdf

2.6.1 Straw Track Corrections

Magnitudes p_{old} of momenta of reconstructed Straw tracks are corrected according to relation

$$p_{\text{new}} = p_{\text{old}} \cdot (1 + \beta) \cdot (1 + \alpha q p_{\text{old}}), \tag{2.4}$$

where q is the track charge (± 1), p_{new} is the corrected momentum magnitude, and α and β are run-dependent parameters of the correction. Parameter β corrects for variations of the MNP33 (subsection 2.2.3) magnetic field integral, while α represents residual misalignment of Straw spectrometer.

In the case of data, both parameters are fitted on a run-by-run basis during the reprocessing stage and their values are stored in a central database. For MC, there is only one set of α and β values and it is stored in the database as well.

The α and β are obtained by comparing the invariant mass of reconstructed $K_{3\pi}$ decays passing a standard $K_{3\pi}$ selection (slightly different than the one presented in section 2.8 and section 2.9) to the nominal kaon mass [18]. Similarly to data, standard $K_{3\pi}$ MC sample was used to obtain α and β parameters applicable to MC.

In addition to α and β, corrections to positions and momenta of Straw tracks propagated through the Blue Tube (subsection 2.2.2) need to be applied in order to account for non-zero magnetic field present in the vacuum vessel. The total magnetic field integral is ~ 0.003 Tm, dominated by the magnetic field of Earth with a smaller contribution from residual magnetisation of the vacuum vessel material. The field was measured in 2013 and the results and implementation of relevant corrections are summarised in an internal note[10].

2.6.2 LKr Cluster Corrections

Clusters built by the LKr reconstruction software described in section 2.5 are subjected to additional set of energy scale, non-linearity, mis-alignment and energy loss corrections applied to both data and MC at the analysis level.

Additionally, a pair of run-dependent (constant) fine calibration parameters A and B is used to fine-tune the reconstructed data (MC) cluster energies using relation

$$E_{\text{new}} = \frac{E_{\text{old}}}{A + B/E_{\text{old}}} \ . \tag{2.5}$$

The fine calibration is designed so that the distribution of corrected LKr cluster energy divided by Straw track momentum (E/p) associated to electrons from $K^+ \to \pi^0 e^+ \nu$ decays centers at 1, since electrons deposit all of their energy in the LKr.

---

[10] https://na62.web.cern.ch/NA62/restricted/NotesDoc/NA62_15_06.pdf

2.6.3 Upstream Pileup Generator

Upstream pileup generator is a tool used to inject accidental GTK hits into MC events based on a pre-defined beam intensity spectrum shown in Fig. 2.21, measured from data. The tool was developed for the purposes of the main $K_{\pi\nu\nu}$ analysis (described in chapter 4).

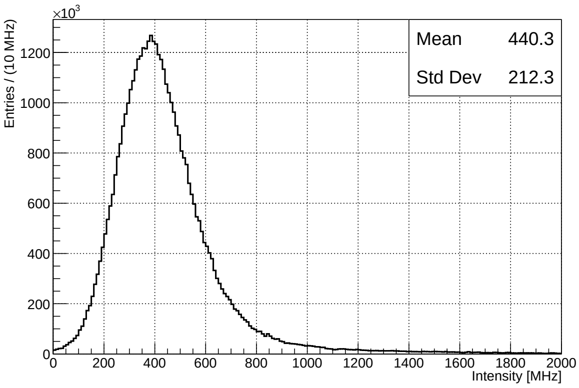

Figure 2.21: Beam intensity profile used to generate accidental GTK hits. The profile corresponds to the integrated beam intensity spectrum of the dataset on which the presented analysis was done.

As discussed in section 2.8, the presented analysis does not use the GTK sub-detector. It however still uses the upstream pileup generator to randomly generate the value of instantaneous beam intensity for MC events using the spectrum in Fig. 2.21. This value is then used in MUV3 pileup generator (subsection 2.6.4) and trigger emulators (subsection 2.6.6).

2.6.4 MUV3 Pileup Generator

MUV3 pileup generator is a tool developed by the author of this thesis. Similarly to the upstream pileup generator, it injects hits and candidates to MUV3 MC event based on distributions obtained from data. Control trigger data sample is used to acquire these distributions since it does not contain any MUV3-related trigger condition and so no trigger-related bias is introduced.

The tool is initially run over the analysed dataset in order to determine the spatial distribution and number of accidental candidates registered out-of-time from the trigger in order to avoid counting muons from triggered kaon decays. Both distributions are shown in Fig. 2.22. The number of accidental candidates in data is obtained from two time intervals with total length of 50 ns shown in Fig. 2.23.

When the MUV3 pileup generator is applied on MC events, accidental candidates are generated with times distributed uniformly between −100 ns and 100 ns. This time interval is four times greater than the one used to extract accidental rates in data,

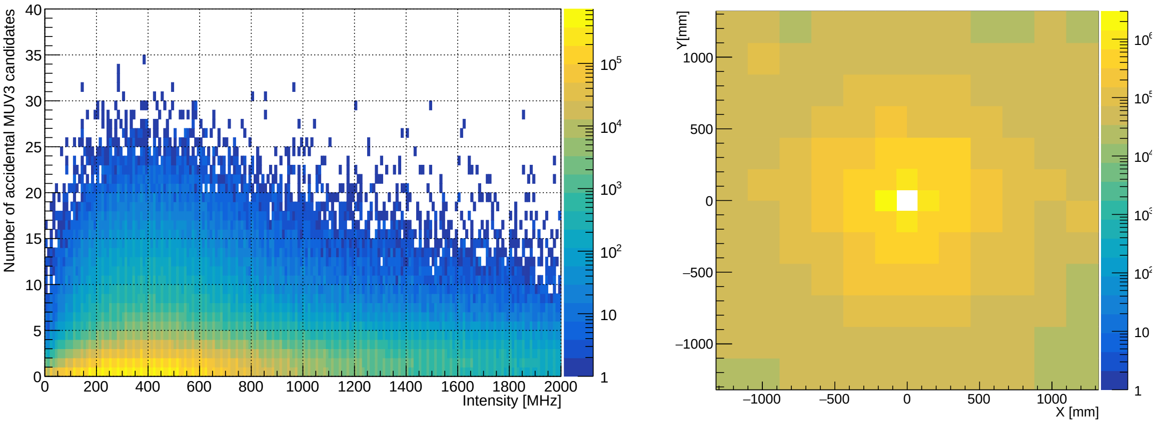

Figure 2.22: Left: the number of accidental MUV3 candidates versus instantaneous beam intensity as measured from data. Right: spatial distribution of accidental MUV3 candidates in data (arbitrary units).

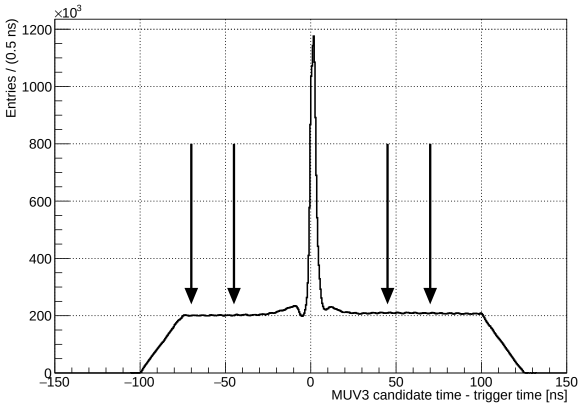

Figure 2.23: Distribution of time difference between times of reconstructed MUV3 candidates and trigger times in data. The two pairs of arrows to the left and right of the central peak denote two 25 ns intervals used to obtain the rate of accidentals.

which needs to be accounted for in the random generation of the number of accidentals in MC.

The first step in the algorithm generating the number of accidentals for a particular MC event is a request of the value of instantaneous beam intensity given for each event by the upstream pileup generator. Subsequently, the number of accidental candidates is determined by sampling the corresponding slice of the two-dimensional histogram shown in Fig. 2.22 (left) four times. This ensures that the mean and variance of the number of accidentals in MC scale correctly with respect to the values in data. Tile ID (Fig. 2.17) of each accidental candidate is chosen randomly according to the hit-map shown in Fig. 2.22 (right). Every accidental candidate is assigned a pair of new MUV3 hits in both PMTs corresponding to a given tile. For simplicity, hit times are chosen equal to the candidate time.

The generated MUV3 accidental hits and candidates are finally saved to the MC event.

The user can also ask the tool to return the number of generated accidentals, which allows for determination if a particular MUV3 hit or candidate is accidental or real.

2.6.5 MUV3 Efficiency

Contrary to efficiencies of other sub-detectors used in $K_{3\pi}$ and $K_{\pi\mu\mu}$ event selections described in section 2.8, section 2.9 and section 2.10, the efficiency of MUV3 sub-detector needs to be carefully taken into account in the analysis. This is implied by the fact that the MUV3 sub-detector is used only in the $K_{\pi\mu\mu}$ event selection and *not* in the $K_{3\pi}$ selection, which causes that any non-zero MUV3 efficiency in data is not cancelled out between the signal and normalisation channels.

Therefore, we first measured MUV3 efficiency on data and MC (section 3.1) and subsequently rejected 0.14% of real (i.e. not pileup, since the pileup properties were read from data events that have the MUV3 efficiency already applied) MUV3 candidates in any MC sample on which we ran our $K_{\pi\mu\mu}$ event selection. The value 0.14% represents a difference between MUV3 efficiencies measured on MC and data, computed from Eq. 3.4 and Eq. 3.5. We discuss the systematic effects on $K_{\pi\mu\mu}$ measurement coming from MUV3 inefficiency in subsection 2.15.3.

For completeness let us mention that we assumed that all other sub-detector efficiencies contribute with the same amount to the signal and normalisation channels and therefore cancel exactly in the ratio. We consider this being a reasonable first-order approximation with a neglected second-order effect coming from possible kinematic and particle type efficiency dependencies.

2.6.6 Trigger Emulators

As already mentioned, the small number of the available $K_{\pi\mu\mu}$ decay candidates ($\mathcal{O}(10^3)$ in the Di-muon sample, $\mathcal{O}(10)$ in the Control sample) is insufficient to measure the Di-muon trigger efficiency directly using the $K_{\pi\mu\mu}$ signal sample. Moreover, for a successful fit of the $K_{\pi\mu\mu}$ form factor parameters, one needs to know the dependence of the Di-muon trigger efficiency as a function of the kinematic variable z defined in Eq. 1.28.

Therefore, we tested two different approaches of including the Di-muon trigger efficiency as a function of z (denoted ε(Di-muon)(z) in the following text) in the $K_{\pi\mu\mu}$ form factor measurement:

1. The first option involved using specialised software tools called *trigger emulators* at the analysis level. These tools are designed to emulate the generation of RICH, CHOD and MUV3 L0 primitives, which can be used to emulate RICH, QX and MO2 trigger conditions present in the Di-muon trigger stream (subsection 2.2.11). Since at the time the presented analysis was performed it was not possible to

run L1 trigger algorithms on MC events, the author developed a simplified L1 STRAW_e and L1 KTAG emulators.

The L0 and L1 trigger emulators were run as parts of both $K_{3\pi}$ and $K_{\pi\mu\mu}$ event selections on MC samples and their responses were used to accept/reject MC events. This way the trigger efficiencies are translated into $K_{3\pi}$ and $K_{\pi\mu\mu}$ selection acceptances.

2. The second approach involved measuring $\varepsilon(\text{Di-muon}, z)$ on low-invariant-mass background events to $K_{\pi\mu\mu}$ signal sample in data. This background sample is dominated by $K_{3\pi}$ decays with two of the pions decaying into muons and is discussed in more detail in section 2.10.

However, due to the different kinematics of the $K_{\pi\mu\mu}$ signal and the background from $K_{3\pi}$ with two pion decays, we chose the first approach to obtain the final result presented in section 2.13. The individual trigger emulators are described in detail in the rest of this subsection.

L0 RICH emulator implements the behaviour of the hardware clustering algorithm used in the RICH data-acquisition electronics. Accidental hits are injected to MC events uniformly in a 400 ns-wide interval centred at zero, with their mean number $\overline{N^{\text{RICH}}_{\text{accidentals}}}$ given by the instantaneous beam intensity I from the upstream pileup generator

$$\overline{N^{\text{RICH}}_{\text{accidentals}}} = \frac{I}{4\ \text{MHz}}\ . \tag{2.6}$$

Equation 2.6 is an approximate relation derived from accidental rates in RICH observed in data at the average beam intensity ($\sim$ 440 MHz) across the whole analysed dataset and assuming zero average accidental rate at $I = 0$. For any given event the number of injected accidentals is drawn from Poisson distribution with mean $\overline{N^{\text{RICH}}_{\text{accidentals}}}$.

All RICH hits are split into 25 ns slots and subsequently clustered within each slot using 6.25 ns time window. The clustering is performed on both emulated PP and SL modules of RICH TEL62 boards [86]. At each clustering stage, clusters with less than 2 hits are deleted. The remaining clusters are converted to emulated RICH primitives and stored in the event.

L0 CHOD emulator is a detailed tool designed and tuned to best match the CHOD accidentals observed in data and shown in Fig. 2.24 and to emulate the CHOD L0 trigger primitive generation. The number of accidentals injected into an MC event is sampled from a two-dimensional map obtained from data, see Fig. 2.25. The accidentals are generated in one hundred 4 ns-wide windows, which helps replicating the non-uniform time-structure (Fig. 2.24) of accidentals caused by high-hit-multiplicity events.

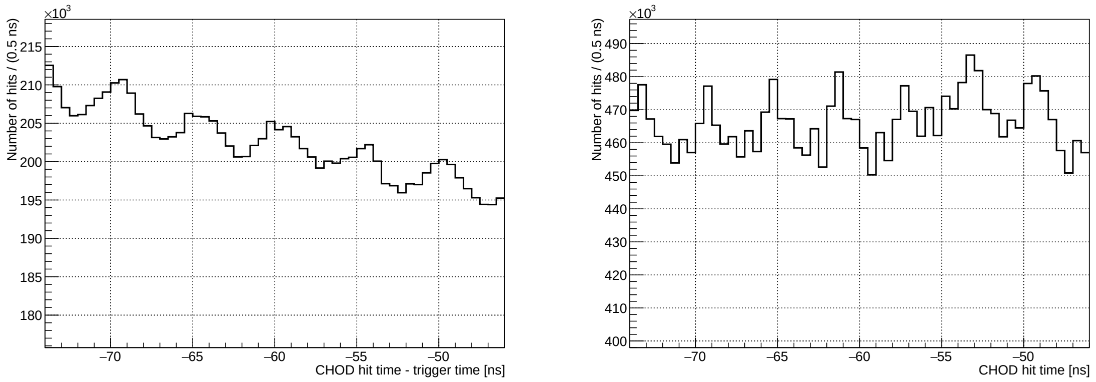

Figure 2.24: The 4 ns time-structure of the number of hits in out-of-time side-bands for data (left) and MC (right). The counts on the y axes are arbitrary and correspond only to the size of the sample used to produce the plots. The slope observed in data is not emulated in MC.

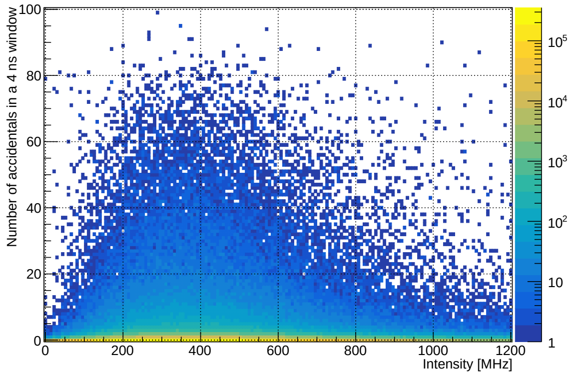

Figure 2.25: Two-dimensional map of the number of CHOD accidentals in a 4 ns time window as a function of instantaneous beam intensity, taken from data.

The CHOD primitive generation is also based on clustering the real and injected MC hits. The hits are first separated into 6.4 μs frames, each consisting of 64 splits of 100 ns. Inside each split the hits are shuffled and then clustered by comparing their times to a distributor cluster time. Each hit can either merge with an existing distributor cluster if it is within 6.25 ns time window, be directly added to the list of existing clusters, or become a new distributor cluster.

During the 2017 data taking, a bug in the L0 CHOD primitive generating firmware was causing high-hit-multiplicity events with at least 32 hits in one 100 ns split to be inefficient. This behaviour was emulated as well and is the reason for the strong dependence of QX efficiency on the beam intensity, shown in Fig. D.13.

L0 MUV3 emulator uses equivalent mechanism for generating emulated MUV3 primitives as the L0 CHOD emulator. The exception in this case is that the default accidentals injection mechanism implemented in L0 MUV3 emulator is disabled and the hits injected by the MUV3 pileup generator described in subsection 2.6.4 are used instead.

L1 KTAG emulator constitutes a trivial tool that randomly rejects $1 - \varepsilon(\text{KTAG})$ of MC events regardless of event properties. The value of $\varepsilon(\text{KTAG})$ (Table 2.5) was measured on data and seems to be completely independent of the kinematics of beam kaons and their decay products (Appendix D). It is expected that the final NA62 $K_{\pi\mu\mu}$ analysis will use the full L1 KTAG algorithm efficiency obtained by running the algorithm on MC events.

L1 STRAW$_\mathbf{e}$ emulator was also developed by the author of this thesis. This was done because a non-trivial kinematic and spatial inefficiency of the L1 STRAW$_\text{e}$ algorithm was found in $K_{3\pi}$ event sample (passing our $K_{3\pi}$ selection described in section 2.8 and section 2.9) in data. The inefficiency was traced to events with *negative* tracks crossing Straw chambers in regions covered by only three out of four views. As a consequence, our approach of emulating the algorithm efficiency $\varepsilon(\text{STRAW}_\text{e})$ in MC involved first extracting a two-dimensional map of $\varepsilon(\text{STRAW}_\text{e})$ observed in $K_{3\pi}$ data events and shown in Fig. 2.26, and subsequently rejecting MC events based on this map.

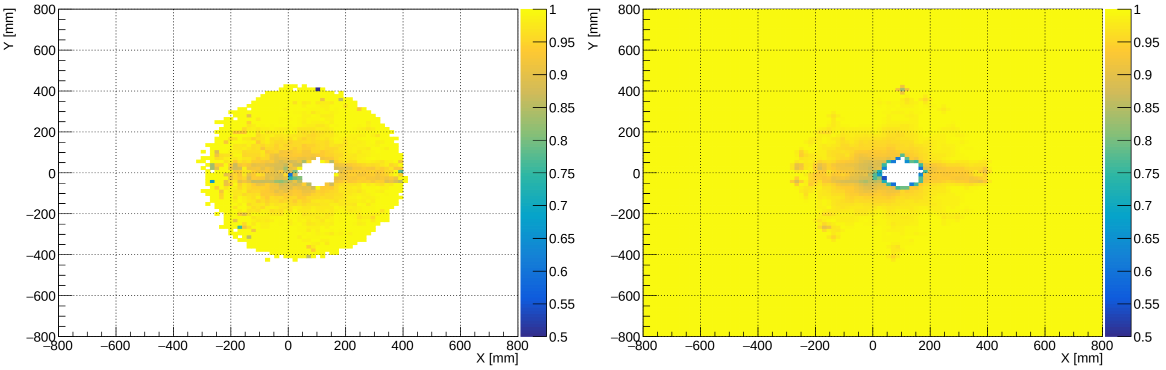

Figure 2.26: Left: $\varepsilon(\text{STRAW}_\text{e})$ map as a function of negative $K_{3\pi}$ pion position in the first Straw station, extracted from data events passing our $K_{3\pi}$ selection. Right: $\varepsilon(\text{STRAW}_\text{e})$ obtained by extrapolating the map on the left with $\varepsilon(\text{STRAW}_\text{e}) = 1$ outside the measured area and smoothing the result. This map was used in the L1 STRAW$_\text{e}$ emulator.

2.7 Association of Straw Tracks to Other Sub-detector Candidates

The presented $K_{3\pi}$ and $K_{\pi\mu\mu}$ event selections, described in the following sections, rely on associating reconstructed Straw tracks to candidates in downstream sub-detectors (RICH, NA48-CHOD, CHOD, LKr and MUV3) needed for particle identification and timing measurement.

Specialised tools unique for each sub-detector are used to match Straw tracks to downstream sub-detector candidates. Most of the tools are purely geometrical with each user imposing timing cuts suitable for their analysis.

Each tool loops over reconstructed Straw tracks in a given event, extrapolates each track to front-plane of a particular downstream sub-detector and looks for reconstructed candidates geometrically compatible with the Straw track. Unless specified otherwise, more than one candidate in any given downstream sub-detector can be associated to any given Straw track.

Spectrometer–RICH association is an algorithm that builds rings of four different radii around a track-seeded centre-point in the RICH PMT plane (subsection 2.2.6). The sizes of the four radii depend on the Straw track momentum and correspond to different charged particles detectable by RICH: kaons (K^+), pions ($\pi^\pm$), muons ($\mu^\pm$) and electrons/positrons ($e^\pm$), see Fig. 2.27. The relation for the expected ring radius is

$$R_{\mathrm{RICH}}(p,m) = f \cdot \mathrm{acos}\frac{1}{n\beta(p,m)}, \tag{2.7}$$

where $f = 17.02$ m is the focal length of RICH mirrors, n is a refractive index of the neon gas and $\beta = v/c$ is the particle velocity factor computed from the Straw track momentum p and a particular mass hypothesis m

$$\beta(p,m) = \frac{pc}{\sqrt{p^2c^2 + m^2c^4}} \; . \tag{2.8}$$

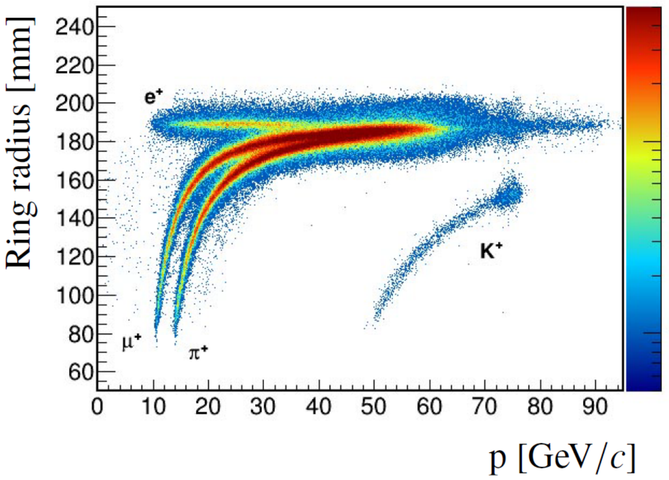

Figure 2.27: Measured RICH ring radius in the PMT plane for different particles as a function of the Straw track momentum, [26].

Five hypothesis are tested for each Straw track using the four expected rings and a background region corresponding to an infinitely light particle. Likelihoods for these five hypothesis are computed based on the observed RICH hits and can be used to identify the type of a particle corresponding to the track.

Spectrometer–NA48-CHOD association extrapolates reconstructed Straw tracks to the NA48-CHOD horizontal (vertical) planes in order to determine the expected y (x) track positions in the NA48-CHOD planes measuring the two perpendicular position coordinates (subsection 2.2.7).

A track is considered to be associated to a given NA48-CHOD candidate if a 2 cm circle (determined from an analysis of minimum-bias data) drawn around the extrapolated track position even partially intersects a “tile” defined by the overlapping parts of the horizontal and vertical slabs corresponding to the NA48-CHOD candidate.

Spectrometer–CHOD association works similarly to the Straw–NA48-CHOD association. A momentum-dependent circle with radius $R_{\text{CHOD}}(p)$ constructed around an extrapolated track point in the CHOD plane is checked for intersection with tiles (subsection 2.2.7) corresponding to reconstructed CHOD candidates. If a CHOD candidate is found in a tile having non-empty overlap with the search circle, it is associated to the track.

The relation $R_{\text{CHOD}}(p)$ was computed by fitting the widths of the distributions of coordinate differences $\Delta X(p)$ and $\Delta Y(p)$ between true and reconstructed particle positions in the CHOD plane using official $K_{\mu 2}$ MC sample. The relation is expected to take into account possible multiple Coulomb scattering of charged particles in material between the last Straw chamber and the CHOD sub-detector.

Considering the established approximation of the angle of deflection for charged particles showed in [18], it was found that the optimal $R_{\text{CHOD}}(p)$ has the form

$$R_{\text{CHOD}}(p) = 4 \times \left(0.07 + \frac{47.3\ \text{GeV}/c}{p}\right)\ \text{mm}\ . \tag{2.9}$$

The constants in parentheses come from the fits to the widths of the measured and *identical* $\Delta X(p)$ and $\Delta Y(p)$ distributions obtained from the MC sample mentioned above, while the factor 4 constitutes a tuning parameter chosen to maximise the probability of a correct association and to minimise the probability of associating multiple CHOD candidates to one Straw track.

Spectrometer–LKr association tool associates at most one LKr cluster to a Straw track. LKr clusters are searched for within a 5 cm distance from the track impact point in the LKr front-plane (chosen to be at 241.093 m) and within 10 ns from the corrected track time.

The Straw track time correction is performed using either the time of the geometrically closest NA48-CHOD association, the time of the geometrically closest CHOD association, or the Straw leading time in this order of preference.

Spectrometer–MUV3 association employs an algorithm equivalent to the one used in the Straw–CHOD association with the candidate search radius $R_{\text{MUV3}}(p)$ computed using similar MC-based approach and equal to

$$R_{\mathrm{MUV3}}(p) = 4 \times \left(\frac{530\ \mathrm{GeV}/c}{p}\right)\ \mathrm{mm}, \tag{2.10}$$

where the larger fit constant with respect to the one in the momentum-dependent term in Eq. 2.9 originates from additional material between the hodoscopes and the MUV3, mainly the calorimeters (LKr, MUV1, MUV2) and the 80 cm iron wall preceding MUV3 [26].

2.8 Common Part of $K_{3\pi}$ and $K_{\pi\mu\mu}$ Event Selections

Due to the very similar masses of charged pions and muons [18], the kinematics of the $K_{\pi\mu\mu}$ signal and $K_{3\pi}$ normalisation channels is also similar. For this reason, the underlying event selections share significant part of the cuts with only one kinematic cut and a particle identification procedure being specific for the $K_{\pi\mu\mu}$ event selection. In this section, we describe the common part of our $K_{3\pi}$ and $K_{\pi\mu\mu}$ event selections, while section 2.10 discusses the cuts specifically applied to select $K_{\pi\mu\mu}$ event candidates.

In the current section, we show plots comparing relevant spectra obtained from data and MC simulation. Unless stated otherwise, these plots contain events passing full $K_{3\pi}$ or $K_{\pi\mu\mu}$ event selections *without* cutting on the plotted variable. We consider this worth mentioning, as the $K_{\pi\mu\mu}$-related plots shown in this section have the $K_{\pi\mu\mu}$-specific cuts already applied.

Event cleaning

In order to ensure the analysed data is of a sufficient quality for the form factor measurement, we require that all events and bursts in the our data sample have *not* been marked as “bad” by the following subsystems:

- **KTAG**, used as a L1 trigger detector in the Multi-track trigger stream and for kaon tagging in both $K_{3\pi}$ and $K_{\pi\mu\mu}$ event selections;
- **Straw**, used in both L1 trigger and offline analysis to reconstruct tracks;
- **NA48-CHOD**, used for time-corrections of Straw tracks and for measurement of L0 trigger efficiencies;
- **CHOD**, used in the L0 trigger and as an assisting sub-detector to the NA48-CHOD in track time-corrections;
- **MUV3**, used as a L0 trigger detector in the Di-muon trigger stream and as a particle identification detector in the $K_{\pi\mu\mu}$ event selection;

- **Processing**, which constitutes a special category of bad bursts, in which a problem in the evaluation of data quality occurred during the reprocessing stage and the quality of the reconstructed data cannot be determined. We conservatively treat such bursts as bad.

An event or burst is marked as bad due to a given sub-detector if the offending sub-system is not time-aligned with other sub-detectors or if the measured sub-detector efficiency is insufficient. The creation of bad burst lists is done during the data reprocessing stage by specialised tools. Two such tools (measuring CHOD and MUV3 sub-detector efficiencies) are described in chapter 3. Bad bursts constitute $\approx 6\%$ of all bursts in the dataset used for our analysis (section 2.4).

Three track vertex fitting

Both $K_{3\pi}$ and $K_{\pi\mu\mu}$ decays produce three charged particles in the final state with a total charge of $+1$ (in units of elementary charge e). The trajectories of these decay products are measured using Straw spectrometer (subsection 2.2.3 and section 2.5). By default, we also accept Straw tracks reconstructed from hits in only *three* Straw chambers.

Since no other particles are created in these decays, the decay vertex is determined using trajectories of the three decay products. Our analysis makes use of an official multi-track vertex fitting tool described in an internal note[11]. The tool is based on a least-square vertex fitting method developed by Billoir, Frühwirth and Regler [97].

Inputs to this algorithm constitute reconstructed Straw track fit parameters (track slopes, positions and momenta in the first Straw station) and their covariance matrices. The tool checks all combinations of n (by default $n = 3$) tracks in an event for compatibility with a hypothesis that they originate from the same interaction point. If the quality of the underlying least-square fit, represented by a χ^2 value, is reasonably high and the fitted vertex lies inside a relaxed volume enveloping the fiducial decay region (subsection 2.2.2), the tool outputs the obtained vertex. Track momenta at the position of the decay vertex are corrected for the non-zero magnetic field present in the decay region (subsection 2.6.1) as well.

In our selection we impose these additional criteria on the output of the vertex fitting tool:

- In order to reduce combinatorial background arising from pileup Straw tracks in data, which are not present in MC, we require exactly one (from now on only *the vertex*) three-track vertex to be fitted in an event. Possible systematic effects caused by this requirement are discussed in subsection 2.15.7.
- Positive kaon beam motivates the cut on the total charge Q of the tracks forming

---

[11] https://na62.web.cern.ch/NA62/restricted/NotesDoc/NA62-16-05.pdf

the vertex: $Q = +1$.

- Vertex fit quality cut $\chi^2 < 20$ is imposed, see Fig. 2.28.

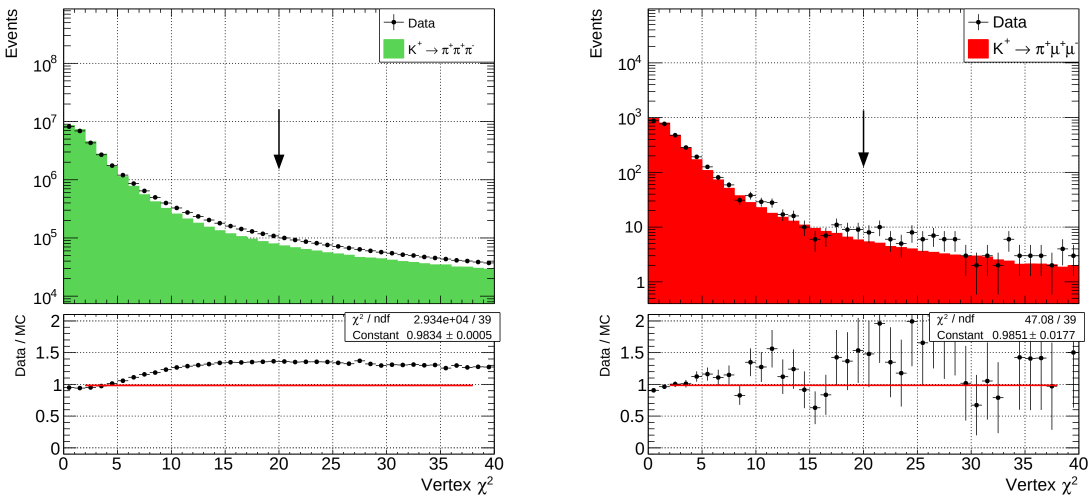

Figure 2.28: Vertex fit χ^2 for events passing our $K_{3\pi}$ (left) and $K_{\pi\mu\mu}$ (right) event selections. Arrows indicate cut values.

- We further require that the Z-position of the fitted vertex lies between 110 m and 180 m from the beryllium target (subsection 2.2.1). The upper cut is motivated by the position of the first Straw station and the upper limit on the position of the kaon decay in MC. The lower cut is chosen to reduce background observed in events passing our $K_{\pi\mu\mu}$ event selection (Fig. 2.29) originating from upstream ($Z < 102.425$ m) $K_{3\pi}$ decays whose decay products are affected by the TRIM5 magnet (Fig. 2.3) distorting their kinematics.

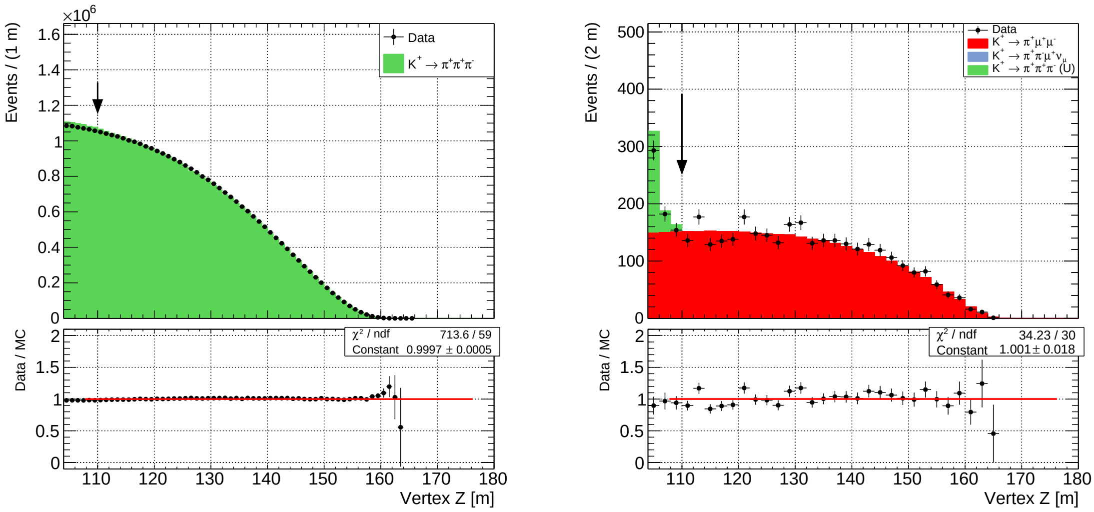

Figure 2.29: Vertex Z-position for events passing our $K_{3\pi}$ (left) and $K_{\pi\mu\mu}$ (right) event selections. Arrows indicate cut values. Green component of the MC stack histogram on the right corresponds to upstream $K_{3\pi}$ decays (section 2.4). No $K_{\mu 4}$ MC events (blue) pass our $K_{\pi\mu\mu}$ event selection.

- Compatibility of the fitted vertex with a beam kaon decay is also performed in the momentum space by requiring (Fig. 2.30)

$$|p_{\text{vertex}} - p_{\text{beam}}| < 2.5 \text{ GeV}/c, \tag{2.11}$$

  where p_{vertex} is the magnitude of the sum of the Straw track momenta forming the vertex, and p_{beam} is a magnitude of an average run-dependent beam momentum $\mathbf{p}_{\text{beam}}$ determined at the reprocessing stage using official $K_{3\pi}$ event selection (slightly looser than our selection presented here). The observed discrepancy between data and MC spectra in Fig. 2.30 (and Fig. 2.31) is addressed in our systematic studies in subsection 2.15.4.

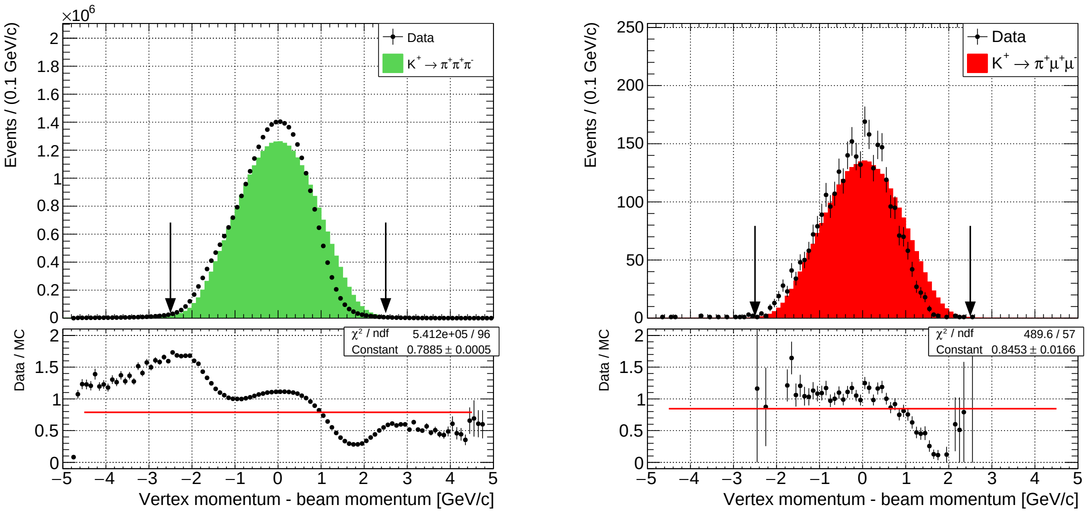

Figure 2.30: $p_{\text{vertex}} - p_{\text{beam}}$ for events passing our $K_{3\pi}$ (left) and $K_{\pi\mu\mu}$ (right) event selections. Arrows indicate cut values.

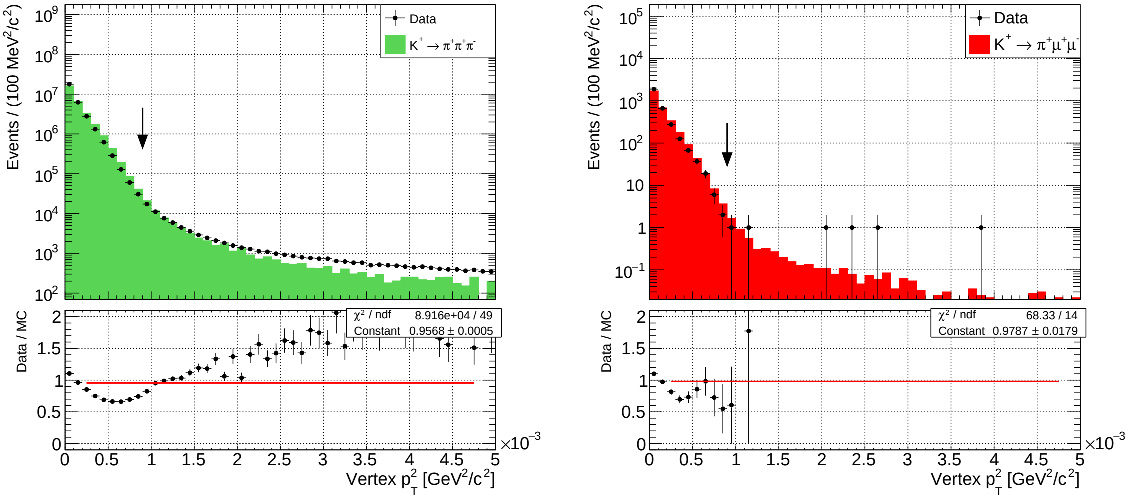

Figure 2.31: Vertex p_T^2 for events passing our $K_{3\pi}$ (left) and $K_{\pi\mu\mu}$ (right) event selections. Arrows indicate cut values.

- In addition to the cut on total momentum magnitude, a cut on the magnitude of the squared vertex transverse momentum $p_T^2 < 900$ MeV$^2/c^2$ with respect to $\mathbf{p}_{\text{beam}}$ is imposed and shown in Fig. 2.31.

Geometrical acceptance cuts

In order to use reconstructed candidates from downstream sub-detectors, the decay products have to be in their geometrical acceptance. Reconstructed vertex tracks are extrapolated to different Z-planes, corresponding to individual front-planes of downstream sub-detectors, and are required to be inside their active regions defined in the following way:

- Straw, all four chambers, to ensure the fitted particle trajectory overlaps with the area covered by at least two Straw views in each chamber. An additional cut of 1 m on the distance of a track point in each station from the centre of that station is made.
- CHOD, for which the extrapolated track position in the CHOD front-plane has to lie between 140 mm and 1070 mm from the centre of the CHOD beam hole.
- NA48-CHOD, where the track is required to lie between 130 mm and 1100 mm from the point of intersection between the beam line and the NA48-CHOD front-plane.
- LKr, for which the inner radial cut requires the extrapolated track point in the LKr front-plane to be outside a 150 mm circle centred at beam line. Additionally, the track point has to lie inside an octagon with an apothem of 1130 mm.

Timing cuts

To reduce the probability of incorrect matching of Straw tracks to downstream sub-detector candidates, caused by accidental activity in the sub-detectors (mostly related to the pileup), strict cuts are imposed between the trigger time, (average) track times and the time of a kaon (defined below).

The *trigger time* t_{trigger} is assigned to the event by the time-reference sub-detector. For events accepted by a physics trigger (subsection 2.2.11), this is the RICH sub-detector, while for events accepted only by the Control trigger, the reference sub-detector is NA48-CHOD.

The resolution of Straw track time, defined by trailing edges of hits corresponding to the track, is ~ 6 ns, which is several times larger than time resolutions of most other sub-detectors involved in our analysis. We therefore define a *track time* t^i_{track} as a time of the best NA48-CHOD (or CHOD if NA48-CHOD is not present) geometric association (section 2.7). All three vertex tracks have to be time-corrected, meaning they are all required to have either a NA48-CHOD or a CHOD association.

We define *vertex time* t_{vertex} as an average of the corrected track times.

The following timing cuts are then imposed:

- there has to be at least one reconstructed KTAG candidate with hits in at least five sectors and the time t_{KTAG} within 3 ns from both t_{vertex} and t_{trigger};
- $|t_{\text{trigger}} - t_{\text{vertex}}| < 3$ ns;
- $|t_{\text{vertex}} - t^i_{\text{track}}| < 3$ ns for all vertex tracks.

Suppression of $e^{\pm}$ background

During the development of our $K_{\pi\mu\mu}$ event selection, non-negligible background was found to be present in the final sample when the LKr sub-detector was not used. It was later identified to be caused by an $e^{\pm}$ contamination of the sample, discussed in section 2.10. Since $e^{\pm}$ contamination is undesirable also in the $K_{3\pi}$ event sample, we use the LKr in the $K_{3\pi}$ event selection as well.

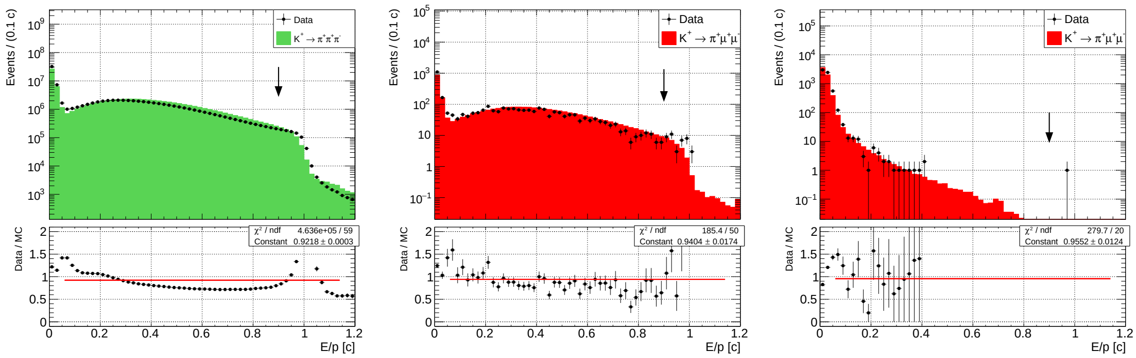

Figure 2.32: $E^i_{\text{cluster}}/p^i_{\text{track}}$ spectrum of $K_{3\pi}$ ($K_{\pi\mu\mu}$) pions is shown in the left (centre) plot. $E^i_{\text{cluster}}/p^i_{\text{track}}$ spectrum of $K_{\pi\mu\mu}$ muons is plotted on the right. Arrows indicate cut values.

The cut used to suppress $e^{\pm}$-like tracks involves $E^i_{\text{cluster}}/p^i_{\text{track}}$ variable, where E^i_{cluster} is the energy of the cluster associated to a vertex track i (section 2.7) and p^i_{track} is the momentum of the same track measured by the Straw spectrometer

$$E^i_{\text{cluster}}/p^i_{\text{track}} < 0.9c, \tag{2.12}$$

where c is the light velocity in vacuum. The $E^i_{\text{cluster}}/p^i_{\text{track}}$ spectra for pions from $K_{3\pi}$ as well as pions and muons from $K_{\pi\mu\mu}$ are shown in Fig. 2.32.

Due to a highly non-trivial simulation of hadronic showers in LKr, we observe significant disagreement between data and MC $E^i_{\text{cluster}}/p^i_{\text{track}}$ spectra in Fig. 2.32. This discrepancy is taken into account by modifying the $K_{3\pi}$ selection acceptance obtained from MC with a factor $f = (1 - 0.0013)$, derived in Appendix C. Further studies of data and MC disagreement related to LKr are discussed in subsection 2.15.9.

Track separation in Straw and LKr

To reduce the probability of a pair of vertex tracks to share the same Straw clusters, which would be an indication of one of the tracks being fake, we require track separation of at least 15 mm (Fig. 2.33) between each pair of the vertex tracks in the first Straw station. As the tracks are generally closer to each other in the first Straw station than in the remaining three, no cuts on track separation in downstream Straw chambers is made.

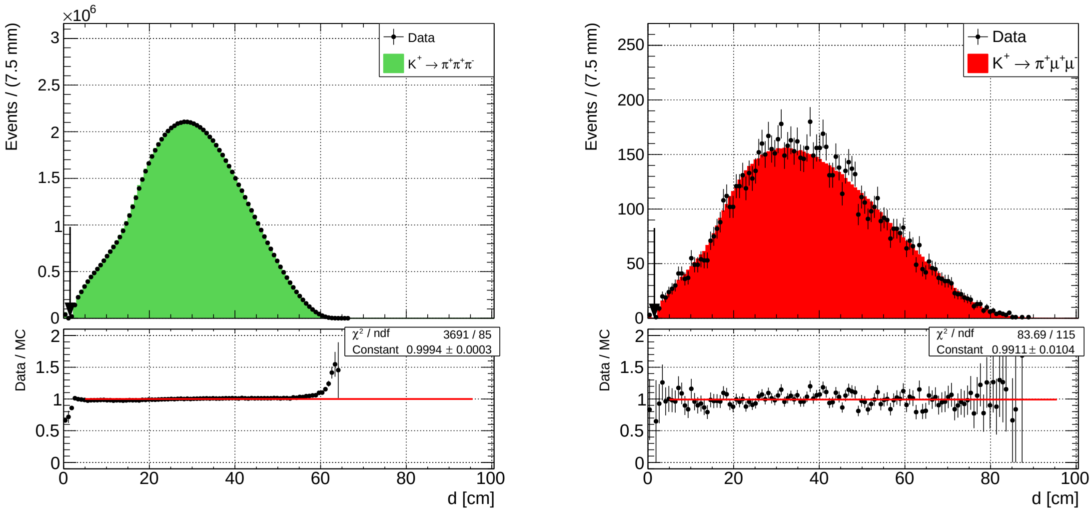

Figure 2.33: Track separation in the first Straw station for events passing our $K_{3\pi}$ (left) and $K_{\pi\mu\mu}$ (right) event selections. Arrows indicate cut values.

Similarly, to reduce the number of accepted events with overlaps and mergers of LKr clusters corresponding to different particles, we also require each pair of the three vertex tracks to be separated by at least 20 cm in the LKr front-plane (Fig. 2.34).

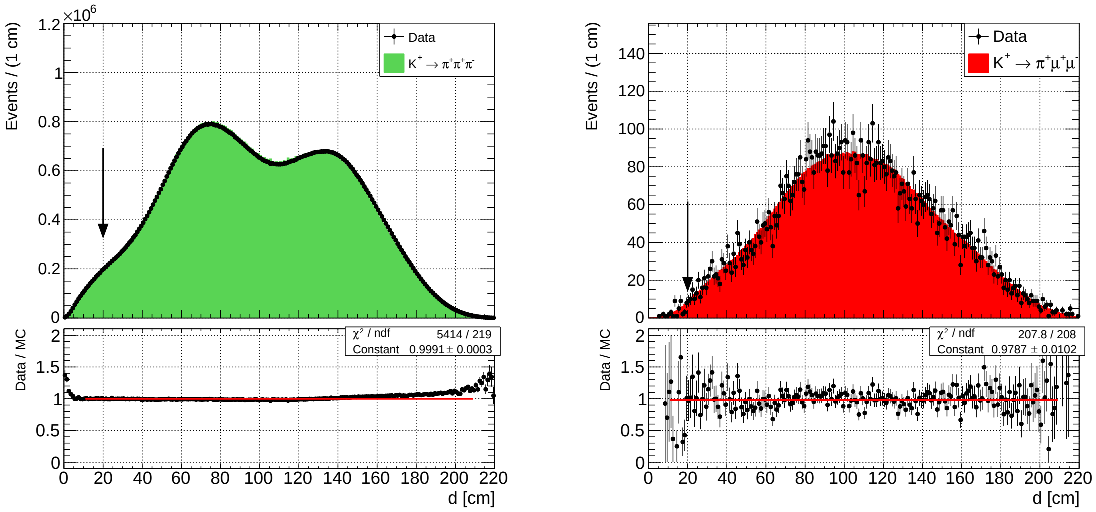

Figure 2.34: Track separation in the LKr front-plane for events passing our $K_{3\pi}$ (left) and $K_{\pi\mu\mu}$ (right) event selections. Arrows indicate cut values.

Offline trigger conditions

The $K_{3\pi}$ and $K_{\pi\mu\mu}$ data samples used in our analysis were collected using Multi-track and Di-muon trigger streams described in subsection 2.2.11, respectively. In general, L0 trigger conditions and L1 trigger algorithms affect both scales and shapes of spectra of physical quantities, e.g. track momenta or angles, vertex position, etc.

In order to compare spectra obtained from data and MC, these effects have to be properly accounted for. One of the commonly used ways is to introduce cuts in event selections designed to imitate (or even be stronger than) the online trigger conditions. Residual differences between the online and offline conditions are then taken into account by measuring trigger efficiencies, which may also depend on kinematics.

Due to the limited statistics of the $K_{\pi\mu\mu}$ event candidates observed in data, it is not possible to measure the Di-muon trigger efficiencies directly on $K_{\pi\mu\mu}$ events. Therefore, a slightly modified approach was used in our analysis:

- We introduced event selection cuts designed to reflect the online trigger conditions. Most of these cuts, relevant for both $K_{3\pi}$ and $K_{\pi\mu\mu}$ event selections, are described below. The remaining condition regarding L0 MO2 trigger, present only in the Di-muon trigger stream, is explained in section 2.10.
- When running on MC samples, we employed trigger emulators described in subsection 2.6.6 to imitate the response of triggering system used during NA62 data taking. The emulators are used to accept or reject events based on the presence (or lack thereof) of emulated trigger primitives. Comparison of measured and emulated trigger efficiencies is shown in section 2.12.

The selection cuts designed to reflect the online trigger conditions are:

- L0 RICH: at least 2 reconstructed RICH hits within 5 ns from t_{trigger};
- L0 QX: at least two CHOD associations to vertex tracks within 5 ns from t_{trigger} placed in opposing CHOD quadrants;
- L1 KTAG: $|t_{\text{trigger}} - t_{\text{KTAG}}| < 3$ ns cut mentioned above;
- L1 STRAW$_{\text{e}}$: one negative vertex track satisfying the timing cuts above.

2.9 $K_{3\pi}$ Event Selection

Signal region definition

The $K_{3\pi}$ event selection used to obtain the sample of $K_{3\pi}$ normalisation events employs all cuts mentioned in section 2.8. The final cut involves the invariant mass $M(3\pi)$ of the three vertex tracks under the charged pion hypotheses:

$$M(3\pi) = \frac{1}{c}\sqrt{\left(\sum_{i=1}^{3} P_i\right)^2}, \tag{2.13}$$

where $P_i = \left(\sqrt{m_\pi^2 c^2 + (p^i_{\text{track}})^2}, \mathbf{p}^i_{\text{track}}\right)$, with track momenta reconstructed at the decay vertex. The resulting $M(3\pi)$ spectrum for data and MC samples is shown in Fig. 2.35. We define the $K_{3\pi}$ signal region by selecting events with

$$|M(3\pi) - M_K| < 5\ \text{MeV}/c^2, \tag{2.14}$$

where M_K is the nominal charged kaon mass ($M_K \simeq 493.7\ \text{MeV}/c^2$, [18]).

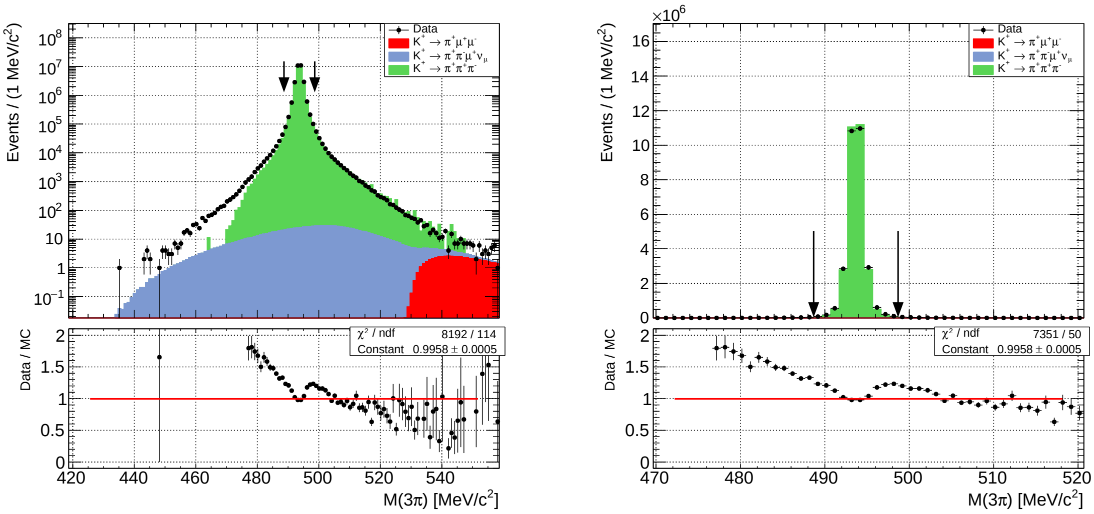

Figure 2.35: $M(3\pi)$ spectrum in logarithmic (left) and linear (right) scales for data and most important MC contributions. Arrows indicate the $K_{3\pi}$ invariant mass signal region.

The selected data sample of $K_{3\pi}$ decay candidates in Fig. 2.35 contains

$$N(K_{3\pi}) \approx 2.93 \times 10^7 \tag{2.15}$$

events used for normalisation. The $K_{3\pi}$ selection acceptance is

$$A(K_{3\pi}) = (10.14 \pm 0.01_{\text{stat}})\%, \tag{2.16}$$

defined as a ratio of the number of $K_{3\pi}$ MC events with reconstructed vertex Z-position between 110 m and 180 m and the number of generated $K_{3\pi}$ MC decays in this region.

The $K_{\mu4}$ background contamination in the selected $K_{3\pi}$ sample was estimated using MC to be ≈ 300 events, which is negligible in comparison to the $K_{3\pi}$ sample size.

Due to limited statistics of the simulated $K_{3\pi}$ MC sample, the left tail visible in the logarithmic plot in Fig. 2.35 is not populated by MC events. To populate such far tail would require a factor $\mathcal{O}(10^2)$ more $K_{3\pi}$ MC events, which is not feasible to achieve using standard MC simulation. This problem is currently being addressed in the NA62 Collaboration by developing a simplified "fast" MC simulation, in which some downstream sub-detectors are not simulated in Geant4 [93], but their response is emulated in the analysis.

2.10 $K_{\pi\mu\mu}$ Event Selection

The key difference between the $K_{3\pi}$ and $K_{\pi\mu\mu}$ event selections is the pion and muon particle identification (PID). The main sub-detector used for this purpose is the MUV3 (subsection 2.2.8).

MUV3 geometrical acceptance cut

All three vertex tracks extrapolated to the MUV3 front-plane are required to fall inside the MUV3 geometrical acceptance. The extrapolated track point has to be further than 103 mm from the centre of the beam pipe and has to lie inside a square with a side of 2640 mm centred on the Z-axis.

Particle identification

The MUV3-based PID is done in two steps:

1. A track is identified as a pion if it has *no* MUV3 association (inner or outer) within 3 ns from both t_{vertex} and t_{trigger}. To accept the event, it is required that *exactly one* of the two positive tracks is identified as π^+.
2. The two remaining vertex tracks are considered as $\mu^\pm$ candidates and both are required to have an *outer* MUV3 association within 3 ns from t_{vertex} and t_{trigger}. To account for multiple Straw–MUV3 associations to a single track and two tracks sharing the same MUV3 candidate, additional requirements are imposed on the muon candidate tracks:
    - If a muon candidate track has more than one in-time outer MUV3 association, the one with the smallest

      $$\delta t = \sqrt{(t_{\text{MUV3}} - t_{\text{vertex}})^2 + (t_{\text{MUV3}} - t_{\text{trigger}})^2}, \tag{2.17}$$

      where t_{MUV3} is the time of a given MUV3 candidate, is chosen to be the "correct" MUV3 association to the track.
    - If the two muon candidate tracks have their "correct" MUV3 associations in the same MUV3 tile, the event is rejected. This condition reduces the possibility of a positive μ PID of both muon candidate tracks based on the

presence of only one muon. Moreover, it reflects the online L0 MO2 trigger condition (as was done for other trigger conditions in section 2.8), which required hits in two *different* outer MUV3 tiles (subsection 2.2.11).

Definition of $M(\pi^+\mu^+\mu^-)$

Once the three vertex tracks have been identified as π^+, μ^+ and μ^-, we define their invariant mass $M(\pi^+\mu^+\mu^-)$ as

$$M(\pi^+\mu^+\mu^-) = \frac{1}{c}\sqrt{\left(\sum_{i=1}^{3} P_i\right)^2}, \tag{2.18}$$

where $P_i = \left(\sqrt{m_i^2c^2 + (p^i_{\text{track}})^2}, \mathbf{p}^i_{\text{track}}\right)$, with track momenta reconstructed at the decay vertex and m_i being the nominal muon or charged pion mass [18], depending on the result of the PID procedure.

Suppression of background from early $K_{3\pi}$ decays

As mentioned in section 2.8, kaon decays before the last GTK station, particularly those happening before or inside TRIM5 (Fig. 2.3) have the kinematics of their decay products affected by the TRIM5 magnetic field ($\Delta p_X = \pm 90$ MeV/c integrated over the full TRIM5 length).

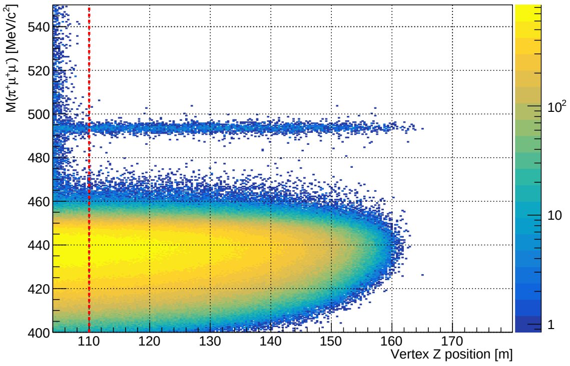

Figure 2.36: $M(\pi^+\mu^+\mu^-)$ spectrum versus Z-position of the reconstructed vertex for data events passing our full $K_{\pi\mu\mu}$ event selection without the cut on the vertex Z-position. Dashed red line indicates the cut position. Upstream $K_{3\pi}$ decays excluded by this cut are clearly visible in the $Z < 110$ m region.

Distorted trajectories of $K_{3\pi}$ decay products can cause the reconstructed vertex to be inside the decay region, since the vertex fitting tool does not consider the possibility of a kaon decay happening before the last GTK station.

Cut on the vertex Z-position discussed in section 2.8 and shown in Fig. 2.36 helps to reduce this background to a minimum: from ≈ 93 million generated upstream $K_{3\pi}$

decays only 18 survive our full $K_{\pi\mu\mu}$ event selection without the vertex Z cut and *none* of them have their vertex reconstructed above the default cut at 110 m. This fact together with a good agreement between data and MC shown in Fig. 2.29 (right) gives us confidence that the low-Z background is understood and negligible in our final $K_{\pi\mu\mu}$ event sample.

In addition to the cut on the Z-position of the decay vertex, we require the angle Θ computed at the reconstructed vertex between each *muon track* and the run-dependent beam direction (section 2.8) to be smaller than 9 mrad.

Suppression of $e^{\pm}$ background

A cut (Fig. 2.37) on the $E^i_{\text{cluster}}/p^i_{\text{track}}$ variable defined in Eq. 2.12 reduces the $e^{\pm}$ background originating from $K_{\pi ee}$ decays (Table 1.1) and $\pi^{\pm}$ or $\mu^{\pm}$ decays into $e^{\pm}$.

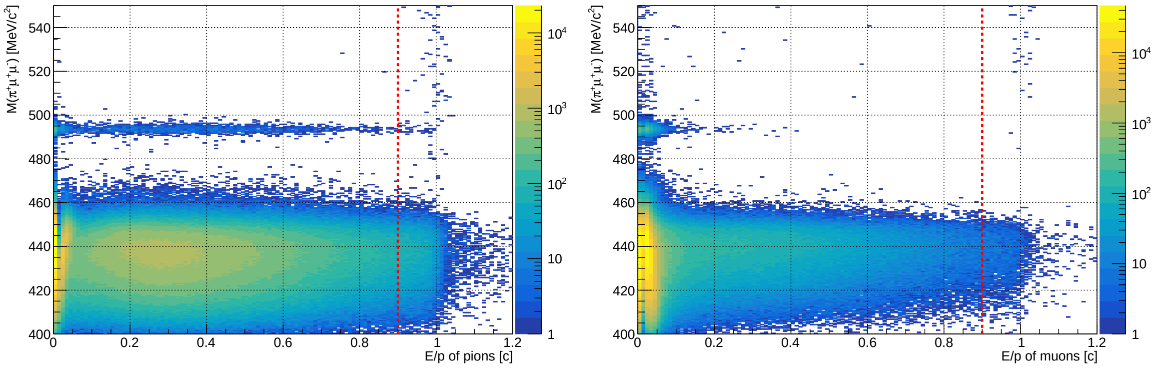

Figure 2.37: $M(\pi^+\mu^+\mu^-)$ spectrum versus $E^i_{\text{cluster}}/p^i_{\text{track}}$ of the pion (left) and muon (right). Dashed red lines indicate the cut designed to remove residual $e^{\pm}$ tracks with $E^i_{\text{cluster}}/p^i_{\text{track}} \approx 1$.

Definition of signal and low-mass regions

The same half-size (5 MeV/c^2 around M_K) of the signal window in the invariant mass $M(\pi^+\mu^+\mu^-)$ was chosen as the final cut in our $K_{\pi\mu\mu}$ event selection. The data and MC $M(\pi^+\mu^+\mu^-)$ spectra are shown in Fig. 2.38. We observe

$$N(K_{\pi\mu\mu}) = 3074 \tag{2.19}$$

data events in the $K_{\pi\mu\mu}$ signal window. The $K_{\pi\mu\mu}$ signal acceptance $A(K_{\pi\mu\mu})$, measured from the $K_{\pi\mu\mu}$ MC sample as a ratio of the number of events with the reconstructed vertex Z-position between 110 m and 180 m and the number of $K_{\pi\mu\mu}$ decays generated in this region, is equal to

$$A(K_{\pi\mu\mu}) = (12.77 \pm 0.02_{\text{stat}})\% \ . \tag{2.20}$$

This acceptance result does *not* enter the $K_{\pi\mu\mu}$ form factor fitting procedure directly, since it is only valid for a particular choice of form factor parameters used in the MC generator. A detailed description of the fitting procedure is given in Appendix B.

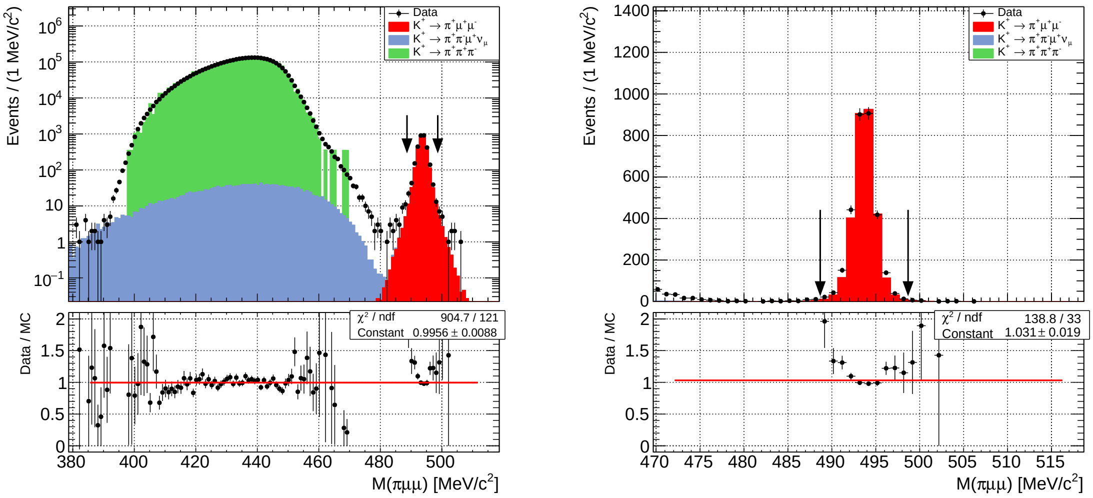

Figure 2.38: $M(\pi^+\mu^+\mu^-)$ spectrum in logarithmic (left) and linear (right) scales for data and most important MC contributions. Arrows indicate the $K_{\pi\mu\mu}$ invariant mass signal region.

The dominant contribution to the bulk of events below $M(\pi^+\mu^+\mu^-) = 480$ MeV/c^2 in Fig. 2.38 corresponds to $K_{3\pi}$ decays with two pions decaying into muons, with a smaller contribution ($\approx 10\%$) from random pileup muons associated to $K_{3\pi}$ pions and $K_{\mu 4}$ decays. These low-mass events are labelled $K_{3\pi} \to 2\mu$ in later text and are used to measure the real and emulated Di-muon trigger efficiencies (subsection 2.6.6).

As already mentioned in section 2.9, the limited size of the available $K_{3\pi}$ MC sample does not allow to fill the tails in the invariant mass distributions. This can be seen in Fig. 2.38 (left) as well, where the green area should extend well beyond the current limits. The new fast MC algorithm will provide necessary sample size to fill these gaps.

Due to the limited size of the $K_{3\pi}$ MC sample, we see no MC background events entering the $K_{\pi\mu\mu}$ signal region indicated by black arrows in Fig. 2.38. The $K_{3\pi}$ background contamination in the selected $K_{\pi\mu\mu}$ decay sample and the related systematic uncertainty is discussed in subsection 2.15.11.

2.11 Data and Monte Carlo Comparison

In this section, we show data–MC comparison plots of variables that were not directly used in our $K_{3\pi}$ and $K_{\pi\mu\mu}$ event selections. We include all data events but only $K_{3\pi}$ ($K_{\pi\mu\mu}$) MC events passing the $K_{3\pi}$ ($K_{\pi\mu\mu}$) event selections. Unless stated otherwise, the plotted events pass *full* event selections.

The largest discrepancies are seen in Fig. 2.42, Fig. 2.43 and Fig. 2.44, corresponding to vertex momentum components. They arise from the fact that the beam parameters used to generate the MC samples employed in our analysis were tuned for 2016 instead of the 2017 data sample. We address these discrepancies in our beam tuning systematic studies described in subsection 2.15.4.

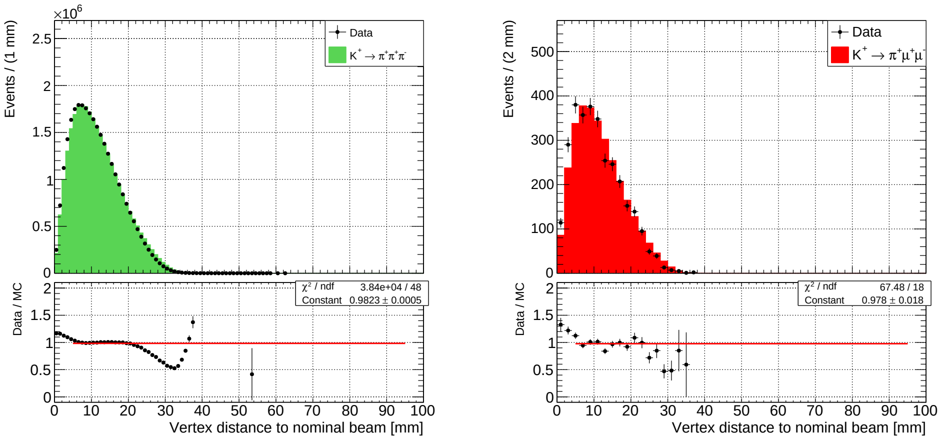

Figure 2.39: Vertex distance to run-dependent beam axis for events passing the $K_{3\pi}$ (left) and $K_{\pi\mu\mu}$ (right) event selections.

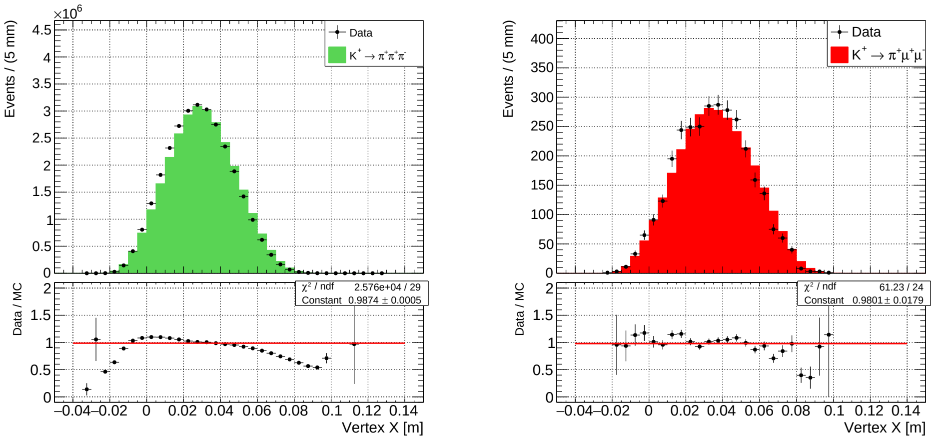

Figure 2.40: Vertex X-position for events passing the $K_{3\pi}$ (left) and $K_{\pi\mu\mu}$ (right) event selections.

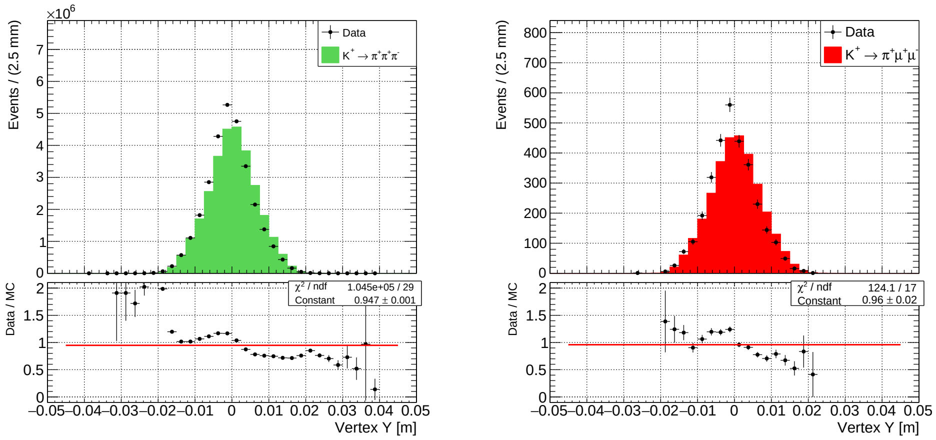

Figure 2.41: Vertex Y-position for events passing the $K_{3\pi}$ (left) and $K_{\pi\mu\mu}$ (right) event selections.

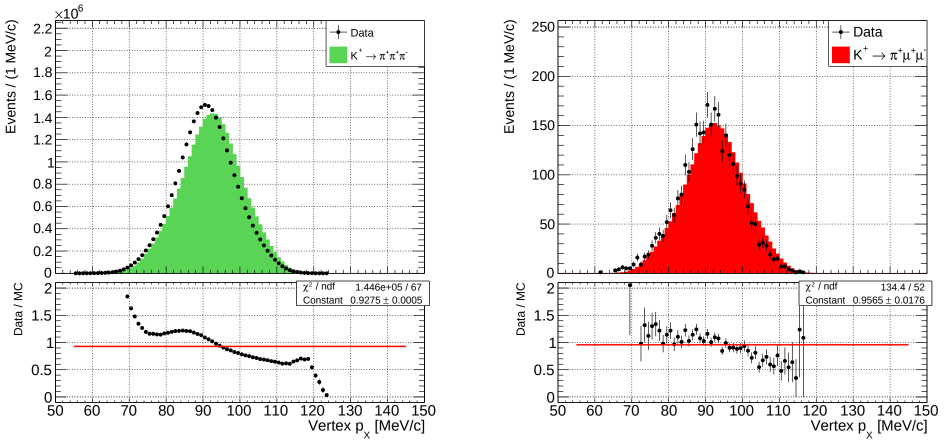

Figure 2.42: Vertex p_X for events passing the $K_{3\pi}$ (left) and $K_{\pi\mu\mu}$ (right) event selections. Vertex momentum cut from Eq. 2.11 is not applied.

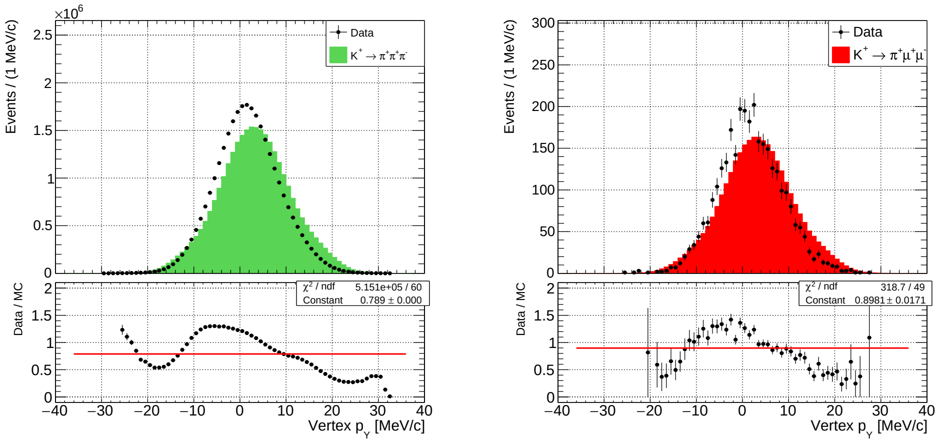

Figure 2.43: Vertex p_Y for events passing the $K_{3\pi}$ (left) and $K_{\pi\mu\mu}$ (right) event selections. Vertex momentum cut from Eq. 2.11 is not applied.

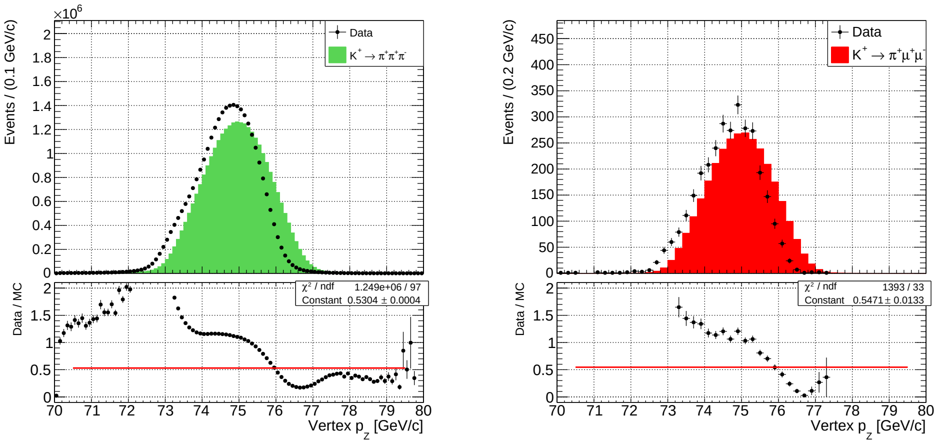

Figure 2.44: Vertex p_Z for events passing the $K_{3\pi}$ (left) and $K_{\pi\mu\mu}$ (right) event selections. Vertex momentum cut from Eq. 2.11 is not applied.

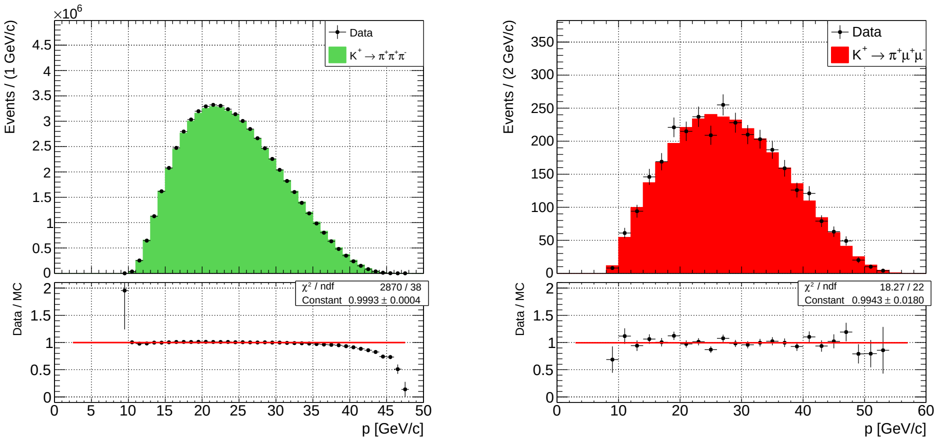

Figure 2.45: Momentum of *positive pions* for events passing the $K_{3\pi}$ (left) and $K_{\pi\mu\mu}$ (right) event selections.

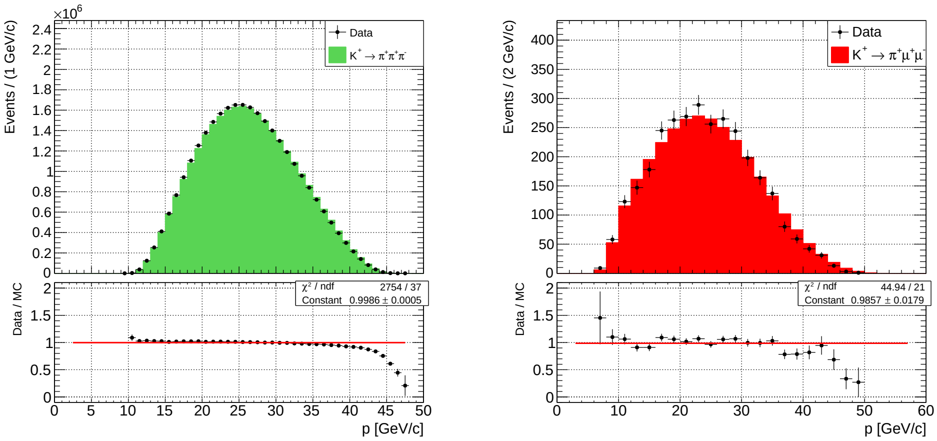

Figure 2.46: Momentum of *negative* $K_{3\pi}$ *pions* and $K_{\pi\mu\mu}$ *muons* for events passing the $K_{3\pi}$ (left) and $K_{\pi\mu\mu}$ (right) event selections.

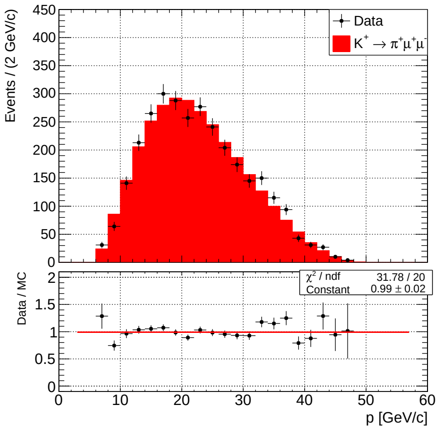

Figure 2.47: Momentum of *positive* $K_{\pi\mu\mu}$ *muons* for events passing the $K_{\pi\mu\mu}$ event selection.

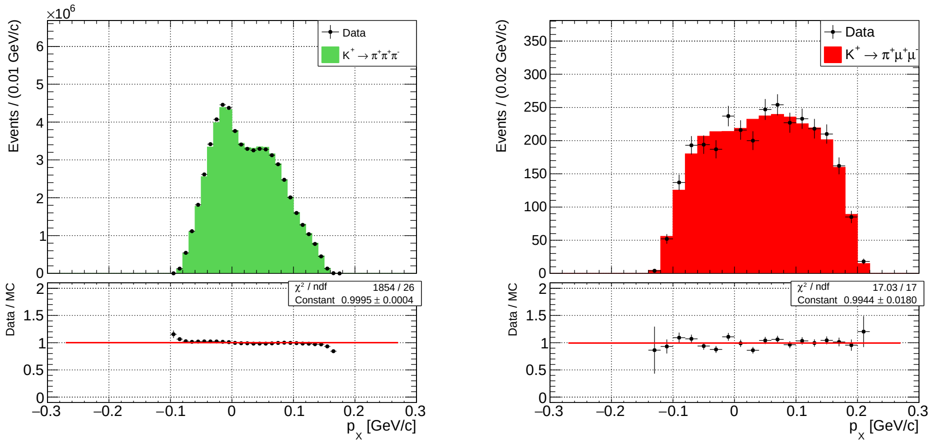

Figure 2.48: p_X of *positive pions* for events passing the $K_{3\pi}$ (left) and $K_{\pi\mu\mu}$ (right) event selections.

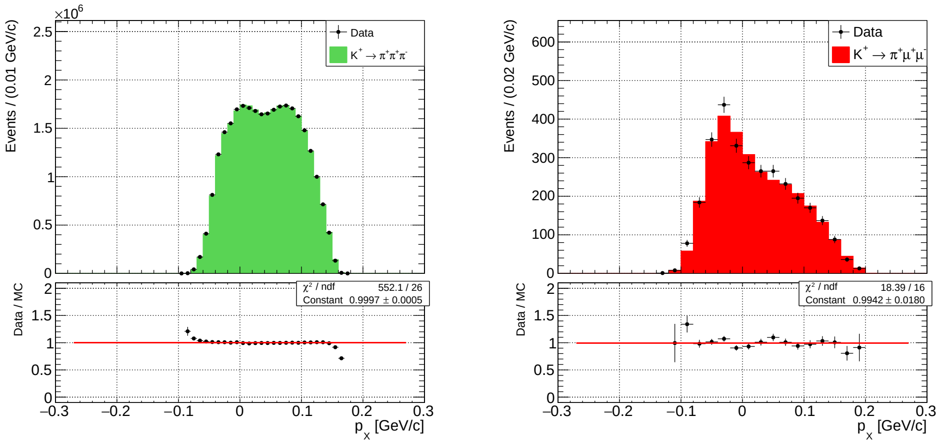

Figure 2.49: p_X of *negative* $K_{3\pi}$ *pions* and $K_{\pi\mu\mu}$ *muons* for events passing the $K_{3\pi}$ (left) and $K_{\pi\mu\mu}$ (right) event selections.

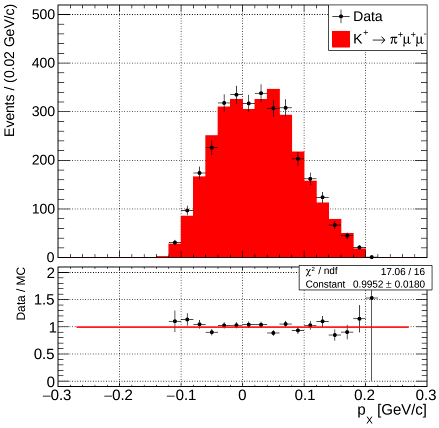

Figure 2.50: p_X of *positive* $K_{\pi\mu\mu}$ *muons* for events passing the $K_{\pi\mu\mu}$ event selection.

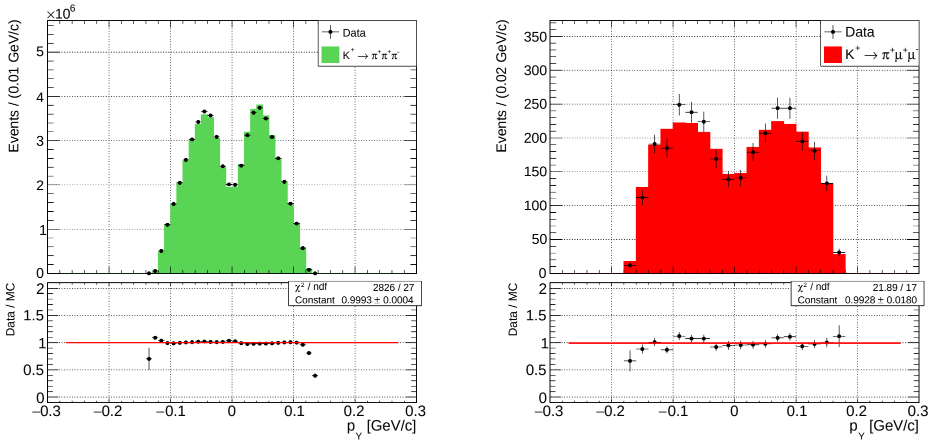

Figure 2.51: p_Y of *positive pions* for events passing the $K_{3\pi}$ (left) and $K_{\pi\mu\mu}$ (right) event selections.

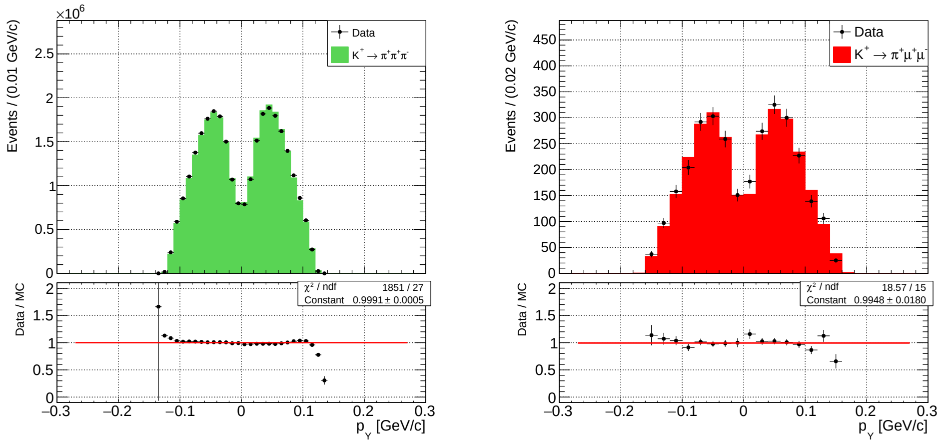

Figure 2.52: p_Y of *negative* $K_{3\pi}$ *pions* and $K_{\pi\mu\mu}$ *muons* for events passing the $K_{3\pi}$ (left) and $K_{\pi\mu\mu}$ (right) event selections.

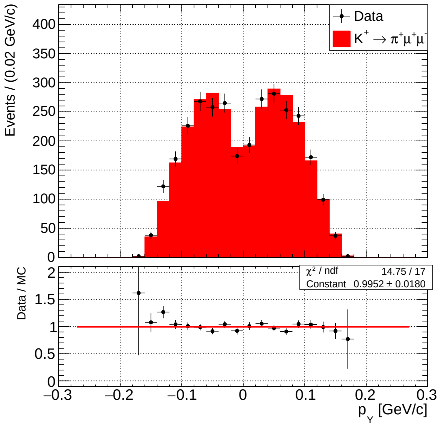

Figure 2.53: p_Y of *positive* $K_{\pi\mu\mu}$ *muons* for events passing the $K_{\pi\mu\mu}$ event selection.

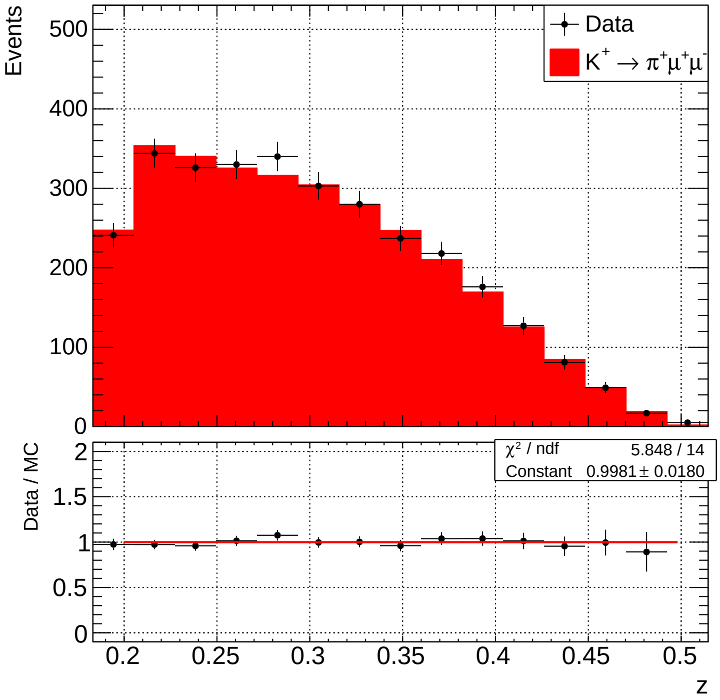

Figure 2.54: z spectrum of events passing the *full* $K_{\pi\mu\mu}$ event selection.

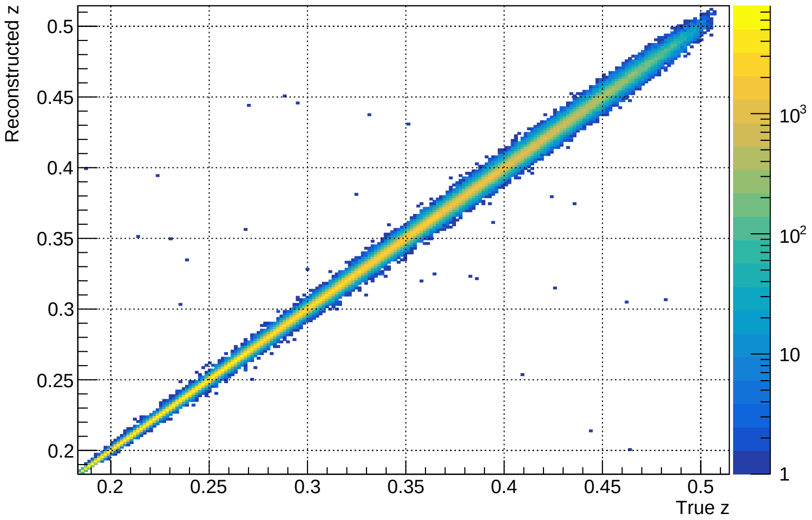

Figure 2.55: Correlation of reconstructed and true z variable for $K_{\pi\mu\mu}$ MC events passing the $K_{\pi\mu\mu}$ event selection. Outlier events are discussed in subsection 2.15.10.

The final z spectrum of data and MC events passing our full $K_{\pi\mu\mu}$ event selection is shown in Fig. 2.54. The exceptionally good agreement between data and MC z spectra suggests the values of $K_{\pi\mu\mu}$ form factor parameters used in the NA62 MC generator (Eq. 1.40) should not be far from the ones obtained after the fitting procedure.

The resolution on the reconstructed z variable is shown in Fig. 2.55 as a function of the true z for $K_{\pi\mu\mu}$ MC events passing the $K_{\pi\mu\mu}$ event selection. The resolution can be parametrised as

$$\sigma(z) = -0.0015 + 0.0096 \cdot z, \tag{2.21}$$

which returns values from 0.0003 for lower kinematic bound of z to 0.0034 for the upper bound (Eq. 1.27).

2.12 Trigger Efficiencies

In this section, a comparison of *measured* (data) and *emulated* (MC) trigger efficiencies obtained from the selected $K_{3\pi}$, $K_{3\pi} \to 2\mu$ and $K_{\pi\mu\mu}$ samples, is presented.

Since the results shown in this section are primarily used to validate the performance of trigger emulators described in subsection 2.6.6, we first present the comparison of measured and emulated Multi-track (Di-muon) trigger efficiencies obtained using $K_{3\pi}$ ($K_{3\pi} \to 2\mu$) events.

The emulated trigger efficiencies acquired from the $K_{\pi\mu\mu}$ MC events passing the $K_{\pi\mu\mu}$ event selection are shown afterwards.

As already mentioned in subsection 2.2.11, the trigger efficiencies are measured on Control or L1 autopass events passing the $K_{3\pi}$ or $K_{\pi\mu\mu}$ event selections described in section 2.8, section 2.9 and section 2.10. The emulated trigger efficiencies are computed from MC events passing the $K_{3\pi}$ or $K_{\pi\mu\mu}$ event selections with the cut on the decision of trigger emulators *removed* from the selections.

Plots in Fig. 2.56 show comparison between measured and emulated efficiencies of Multi-track trigger components as functions of track momenta for data and $K_{3\pi}$ MC events passing the $K_{3\pi}$ selection. Additional plots comparing measured and emulated trigger efficiencies can be found in Appendix D.

	Measured	Emulated
$1 - \varepsilon(\mathrm{RICH})$	0.023(1)	0.001(1)
$1 - \varepsilon(\mathrm{QX})$	1.631(6)	1.685(6)
$1 - \varepsilon(\mathrm{KTAG})$	0.166(5)	0.163(2)
$1 - \varepsilon(\mathrm{STRAW_e})$	4.375(26)	4.740(10)
Total inefficiency	6.112(27)	6.499(12)

Table 2.3: Measured and emulated trigger inefficiencies (in %) of Multi-track trigger components obtained from $K_{3\pi}$ events. The quoted errors are statistical only.

As seen from Fig. 2.56 and Table 2.3, the measured and emulated L0 RICH, L0 QX and L1 KTAG trigger efficiencies agree within 0.06% and are flat with respect to the pion track momenta, while the L1 $\mathrm{STRAW_e}$ trigger efficiencies show significant

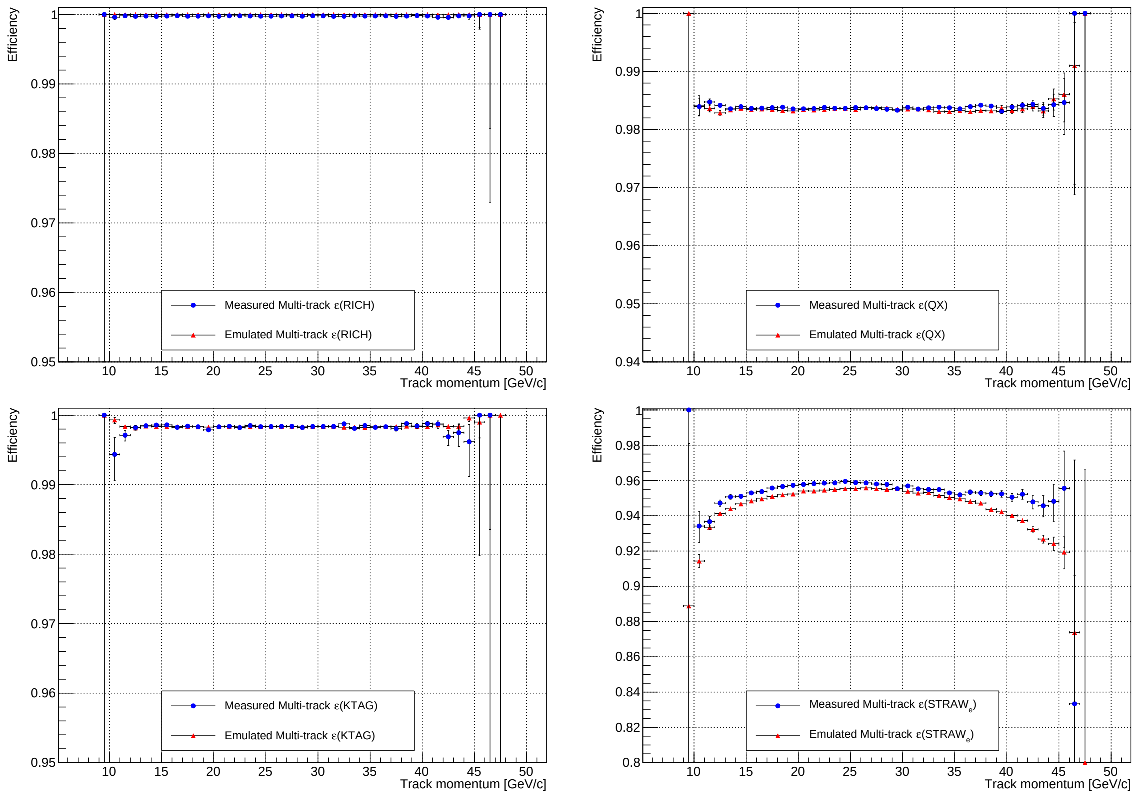

Figure 2.56: Measured and emulated efficiencies of Multi-track trigger conditions versus decay products momenta for data and $K_{3\pi}$ MC events passing the $K_{3\pi}$ event selection.

dependence on track momenta. Additionally, we observe $\sim 0.4\%$ shift between the measured and emulated $\varepsilon(\mathrm{STRAW_e})$, which is a limitation of the simplified L1 $\mathrm{STRAW_e}$ emulator introduced in subsection 2.6.6. We postpone further discussion about origins of discrepancies between the measured and emulated trigger efficiencies to the end of this section.

In Fig. 2.57 we plot the measured (on $K_{3\pi} \to 2\mu$ events only) and emulated (on $K_{3\pi} \to 2\mu$ and $K_{\pi\mu\mu}$ events) efficiencies of Di-muon trigger components as functions of the z variable defined in Eq. 1.28.

The sizes and slopes of measured and emulated trigger efficiencies agree reasonably well. As in the Multi-track case above, the largest difference is seen in $\varepsilon(\mathrm{STRAW_e})$ and is caused by the simplicity of the used L1 $\mathrm{STRAW_e}$ emulator. One can also observe that the $K_{3\pi} \to 2\mu$ events do not reach as high z values as the $K_{\pi\mu\mu}$ events, which is a result of their different kinematic properties.

The inefficiencies of individual Di-muon trigger components averaged over z as well as the total measured and emulated Di-muon trigger inefficiencies are shown in Table 2.4.

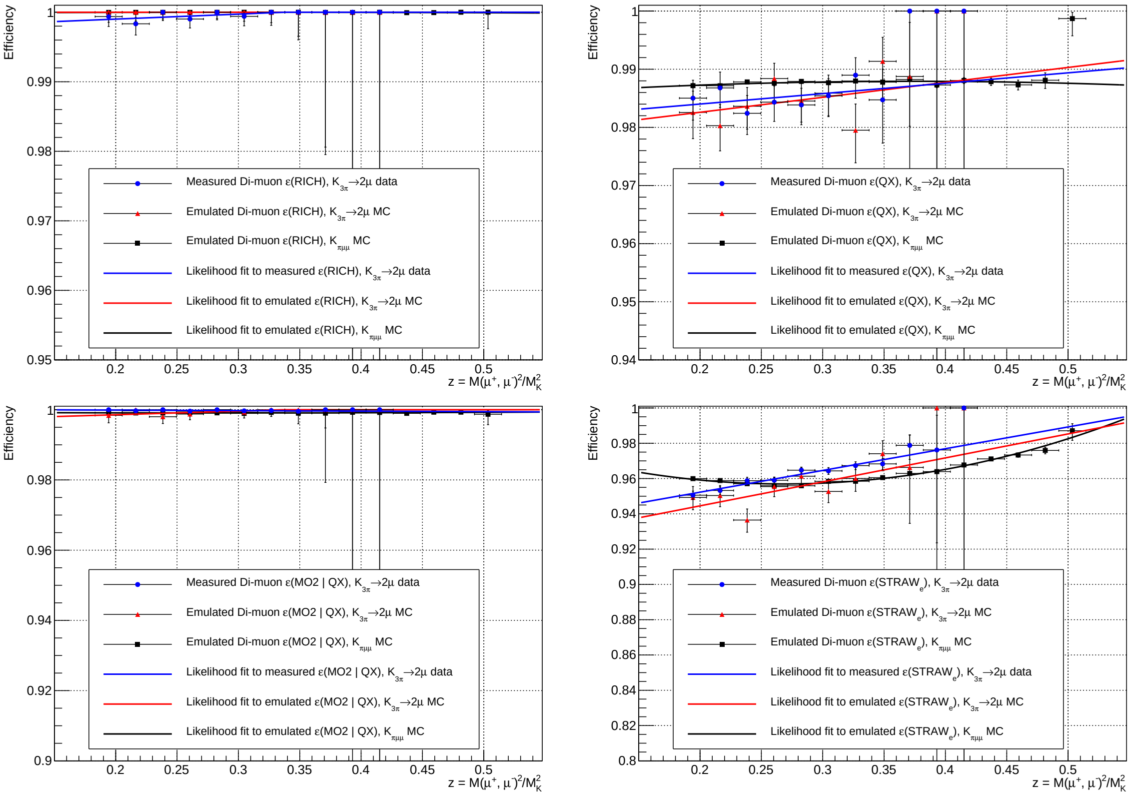

Figure 2.57: Measured and emulated efficiencies of Di-muon trigger conditions versus the kinematic z variable for data, $K_{\pi\mu\mu}$ MC and $K_{3\pi} \to 2\mu$ MC decays for events passing our $K_{\pi\mu\mu}$ selection.

	Measured	Emulated
$1 - \varepsilon(\text{RICH})$	0.054(29)	0.001(1)
$1 - \varepsilon(\text{QX})$	1.486(117)	1.747(136)
$1 - \varepsilon(\text{MO2} \mid \text{QX})$	0.020(9)	0.076(37)
$1 - \varepsilon(\text{STRAW}_\text{e})$	3.988(74)	4.606(212)
Total inefficiency	5.485(137)	6.345(248)

Table 2.4: Measured and emulated trigger inefficiencies (in %) of Di-muon trigger components obtained from $K_{3\pi} \to 2\mu$ events. The quoted errors are statistical only.

The Di-muon trigger efficiencies displayed in Fig. 2.57 have been fitted with functions

$$\varepsilon(i, z) = \max(0, \min(1, c_i + d_i z + e_i z^2)) \tag{2.22}$$

using binned maximum likelihood fit, where index i stands for RICH, QX, MO2 and STRAW_e trigger conditions.

For $K_{3\pi} \to 2\mu$ data and MC event samples (shown in blue and red in Fig. 2.57), parameter e_i was fixed to zero as the shapes of individual efficiencies do not require a quadratic fit. This is not valid for the $\varepsilon(\text{STRAW}_\text{e})$ emulated on $K_{\pi\mu\mu}$ MC events (showed in black), therefore the quadratic term is included in the fit function.

The fit is performed by computing a product of bin-by-bin binomial probabilities for obtaining n events in each bin of the numerator histogram out of N events in the same bin of the denominator histogram, taking the average value of $\varepsilon(i,z)$ in each bin as the binomial probability parameter. The individual bin probabilities are assumed to be independent and multiplied together. The resulting value is a likelihood for the particular choice of parameters c_i, d_i and e_i, given the observed numerator and denominator histograms. Maximising the likelihood as a function of c_i, d_i and e_i gives the fitted $\varepsilon(i,z)$ function.

The fit described in the previous paragraph is done using a dedicated binomial fitting tool contained in the `ROOT` software package [83]. In addition to the optimal values of c_i, d_i and e_i, the fitting tool also returns the fit parameters covariance matrix.

Functions $\varepsilon(i,z)$ are used to obtain the total Di-muon trigger efficiency function

$$\varepsilon(\text{Di-muon},z) = \varepsilon(\text{RICH},z)\cdot\varepsilon(\text{QX},z)\cdot\varepsilon(\text{MO2}\mid\text{QX},z)\cdot\varepsilon(\text{STRAW}_\text{e},z)\ . \tag{2.23}$$

The presence of the term $\varepsilon(\text{MO2}\mid\text{QX},z)$ instead of $\varepsilon(\text{MO2},z)$ is motivated by the fact that the QX and MO2 trigger decisions were found to be correlated. The correlation arises from the fact that the MUV3 and CHOD primitive generation firmwares are essentially identical (subsection 2.6.6), which implies that their efficiencies as functions of beam intensity (which was found to be the primary source of the inefficiency) correlate as well. No correlation between decisions of other Di-muon L0 trigger conditions was found. The efficiency of the L1 STRAW_e algorithm factorises by definition, since it is computed on events passing the L0 trigger.

Using the fit functions $\varepsilon(i,z)$ and covariance matrices for parameters c_i, d_i and e_i, *approximate* 1σ bands around the total measured and emulated Di-muon trigger efficiencies $\varepsilon(\text{Di-muon},z)$ are evaluated using the formula Eq. 2.23

$$\begin{aligned}\sigma^2_{\varepsilon(\text{Di-muon},z)} = \sum_i \left(\frac{\varepsilon(\text{Di-muon},z)}{\varepsilon(i,z)}\right)^2 \cdot \\ \cdot\Big[C_i^2(z)\sigma^2_{c_i} + D_i^2(z)\sigma^2_{d_i} + E_i^2(z)\sigma^2_{e_i} + \\ + 2\left(C_i(z)D_i(z)\sigma_{c_id_i} + C_i(z)E_i(z)\sigma_{c_ie_i} + D_i(z)E_i(z)\sigma_{d_ie_i}\right)\Big]\,,\end{aligned} \tag{2.24}$$

where $C_i(z)$, $D_i(z)$ and $E_i(z)$ are partial derivatives of $\varepsilon(i,z)$ with respect to fit parameters c_i, d_i and e_i, respectively, and σ^2_X and σ_{XY} come from the covariance matrix. If $\varepsilon(i,z) = 1$ or $\varepsilon(i,z) = 0$ for a given z, functions $C_i(z)$, $D_i(z)$ and $E_i(z)$ return 0 for this value of z.

The total Di-muon trigger efficiency functions with $\pm 1\sigma$ bands are presented in Fig. 2.58.

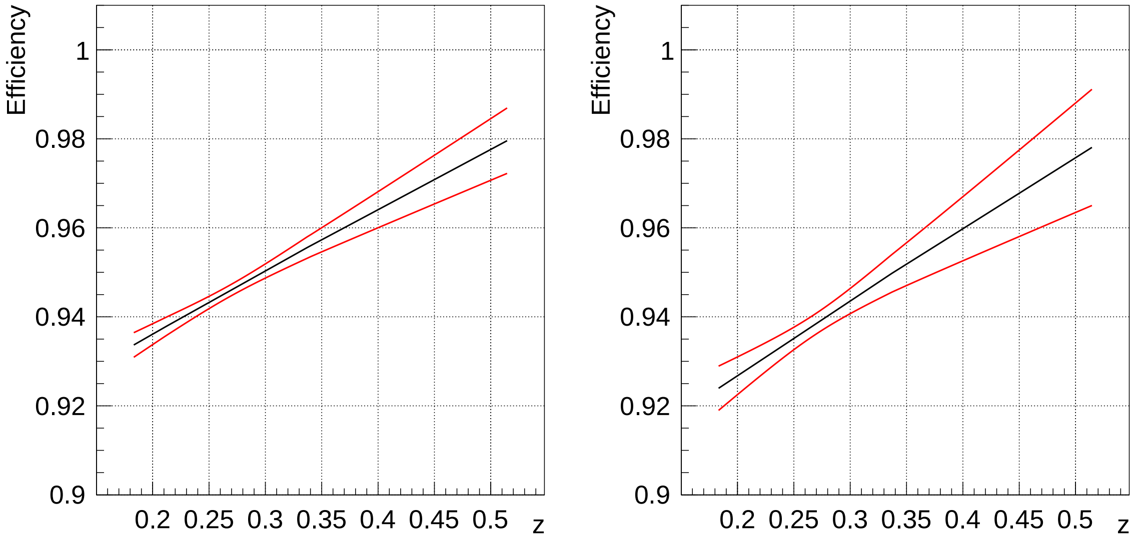

Figure 2.58: Total measured (left) and emulated (right) Di-muon trigger efficiencies computed using $K_{3\pi} \to 2\mu$ events as functions of the kinematic variable z are shown as black lines. Red curves define *approximate* 1σ (stat.) regions around the central lines. The lines start and end at kinematic boundaries of z defined below Eq. 1.27.

The functions are *not* used in the $K_{\pi\mu\mu}$ form factor fitting procedure. Instead, we plot them to test the compatibility of the measured and emulated trigger responses of the Di-muon trigger conditions. A reasonably good agreement between the measured and emulated $\varepsilon(\text{Di-muon}, z)$ on $K_{3\pi} \to 2\mu$ data and MC event candidates is achieved.

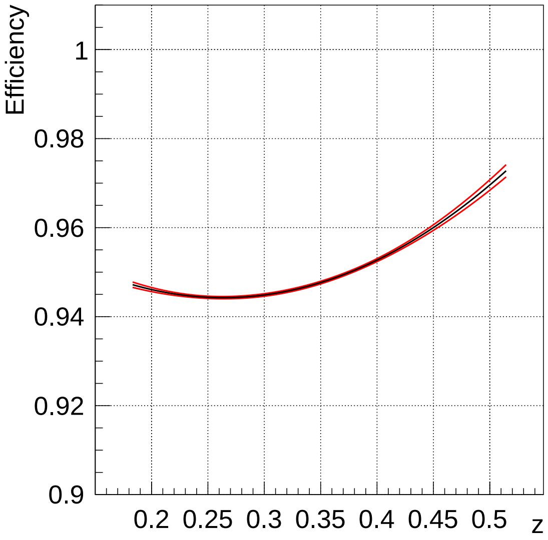

Figure 2.59: Total emulated Di-muon trigger efficiency for $K_{\pi\mu\mu}$ MC events shown as a function of the kinematic variable z. See Fig. 2.58 for more details.

Once the trigger emulators used in the $K_{3\pi}$ and $K_{\pi\mu\mu}$ event selections to reject MC events have been validated, we investigated the Di-muon trigger efficiencies on $K_{\pi\mu\mu}$ MC samples. The obtained z-dependencies of individual Di-muon trigger components have already been presented in Fig. 2.57, while the total Di-muon trigger efficiency obtained using Eq. 2.23 is shown in Fig. 2.59.

Comparing Fig. 2.58 and Fig. 2.59, a slight rise in the emulated Di-muon trigger efficiency on $K_{\pi\mu\mu}$ events is observed in low-z region. This is a result of the quadratic term introduced in the fit function to account for the non-linearities observed in the emulated $\varepsilon(\mathrm{STRAW_e}, z)$ on $K_{\pi\mu\mu}$ events, shown in Fig. 2.57.

Sample	$K_{3\pi}$		$K_{3\pi} \to 2\mu$		$K_{\pi\mu\mu}$
Type	Measured	Emulated	Measured	Emulated	Emulated
$1 - \varepsilon(\mathrm{RICH})$	0.023(1)	0.001(1)	0.054(29)	0.001(1)	0.001(1)
$1 - \varepsilon(\mathrm{QX})$	1.631(6)	1.685(6)	1.486(117)	1.747(136)	1.224(10)
$1 - \varepsilon(\mathrm{MO2} \mid \mathrm{QX})$	–	–	0.020(9)	0.076(37)	0.089(3)
$1 - \varepsilon(\mathrm{KTAG})$	0.166(5)	0.163(2)	–	–	–
$1 - \varepsilon(\mathrm{STRAW_e})$	4.375(26)	4.740(10)	3.988(74)	4.606(212)	4.025(18)
Total inefficiency	6.112(27)	6.499(12)	5.485(137)	6.345(248)	5.285(20)

Table 2.5: Measured and emulated trigger inefficiencies (in %) of Multi-track and Di-muon trigger components. The quoted errors are statistical only.

Table 2.5 summarises the individual measured and emulated inefficiencies of separate L0 trigger conditions and L1 trigger algorithms for events passing the $K_{3\pi}$ and $K_{\pi\mu\mu}$ selections presented in section 2.8, section 2.9 and section 2.10. The reasons for observed discrepancies between measured and emulated trigger efficiencies depend on trigger conditions:

- Both measured and emulated L0 RICH efficiencies are close to 100%. In data, the $\varepsilon(\mathrm{RICH})$ is measured on Control events with a CHOD primitive in-time with the trigger time. If an event was triggered by a physics trigger, the RICH primitive is present by definition and the event is efficient. If however the event was only triggered by the Control trigger, the trigger time is defined as the NA48-CHOD time and there is a possibility of not finding the corresponding RICH primitive in-time with the trigger, which causes the observed inefficiency in data.

  The inefficiency in MC is caused by events in which the L0 RICH clustering algorithm fails to produce a cluster with at least two hits in the 6.25 ns time window around the trigger time (equal to zero in MC). The fraction of such events is negligible.

- Measured and emulated QX trigger efficiencies agree reasonably well in $K_{3\pi}$ and $K_{3\pi} \to 2\mu$ events. The QX inefficiency is caused by high-hit-multiplicity events which were affected by a bug in the primitive generation firmware present during the 2017 data taking (subsection 2.6.6), causing events with high number of CHOD hits to be inefficient. This behaviour was emulated in the L0 CHOD emulator. However, due to the difficulties of properly simulating inelastic hadronic interactions of pions in RICH mirrors, there is a remaining discrepancy between the measured and emulated $K_{3\pi}$ QX efficiencies. Since the $K_{\pi\mu\mu}$ decay has only one pion in the final state compared to three pions in $K_{3\pi}$, the probability of an inelastic interaction occurring inside RICH mirrors is ~ 3 times lower, which reduces the number of high-multiplicity events and increases the QX efficiency measured on the $K_{\pi\mu\mu}$ MC event sample.

- The disagreement between measured and emulated MO2 efficiencies for $K_{3\pi} \to 2\mu$ is most probably caused by residual run-dependent differences between the rates of MUV3 pileup hits in data and the constant rate set in MC (obtained as an average rate in data over the full analysed dataset). We observe up to 10% run-dependent variation of the MUV3 accidental rates in data caused by a similar variation of the run-averaged beam intensity. Further improvements of the MUV3 pileup generator (e.g. making the generation maps run-dependent) should describe the pileup in data with a higher accuracy, which could improve the agreement between the measured and emulated MO2 efficiencies.
- The measured and emulated KTAG efficiencies agree within 1σ, which is expected since the value measured on $K_{3\pi}$ data sample was directly applied to the L1 KTAG emulator described in subsection 2.6.6.
- The observed discrepancies between measured and emulated $\mathrm{STRAW_e}$ efficiencies are given by the simplicity of the used L1 $\mathrm{STRAW_e}$ emulator. For example, as seen in Fig. D.9 and Fig. D.13, the emulator does not reproduce the beam intensity and vertex Z-position efficiency dependencies observed in data.

Future analyses will benefit from the possibility of running the L1 trigger algorithms directly on MC events without the necessity to use L1 emulators. The bug present in the CHOD primitive generation firmware affecting high-hit-multiplicity events was fixed before the 2018 data taking started.

Systematic uncertainties originating from the treatment of trigger efficiencies are discussed in detail in subsection 2.15.1.

2.13 $K_{\pi\mu\mu}$ Form Factor Measurement

In this section we present the results of the $K_{\pi\mu\mu}$ form factor fitting procedure (described in Appendix B) on the selected $K_{\pi\mu\mu}$ event sample.

The fitting proceeded as follows:

1. When running on data, the $K_{\pi\mu\mu}$ signal and $K_{3\pi}$ normalisation events were selected using the $K_{\pi\mu\mu}$ and $K_{3\pi}$ event selections.
2. The number of $K_{3\pi}$ decays was corrected for the Multi-track trigger downscaling (factor 100).
3. An equipopulous histogram (Fig. 2.60) of 15 bins in variable z, containing $K_{\pi\mu\mu}$ data events weighted by the Di-muon trigger downscaling (factor 2), was filled. The number of bins was chosen based on the resolution on the reconstructed z variable, shown in Fig. 2.55. The widths of z bins in the equipopulous histogram span from ≈ 0.01 to ≈ 0.1.

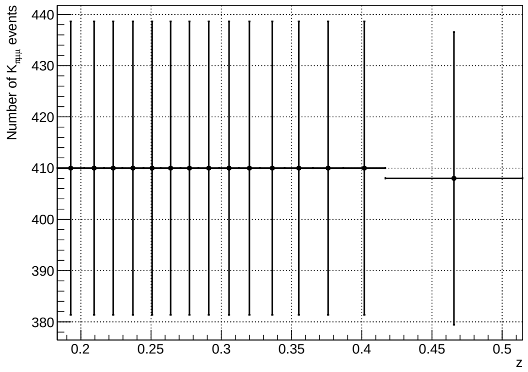

Figure 2.60: Equipopulous histogram filled with 3074 weighted $K_{\pi\mu\mu}$ data events.

4. The $K_{3\pi}$ and $K_{\pi\mu\mu}$ selection acceptances are shown in Eq. 2.16 and Eq. 2.20, respectively. The $K_{\pi\mu\mu}$ acceptance as a function of z is shown in Fig. B.1 (right). The number of kaon decays used for normalisation was given in Eq. 2.3.
5. The form factor fitting procedure gives the following result

$$\begin{aligned} a &= -0.564 \pm 0.034_{\text{stat}}, & b &= -0.797 \pm 0.118_{\text{stat}}, \\ \chi^2/\text{ndf} &= 11.61/13, & p\text{-value} &= 0.56, \end{aligned} \tag{2.25}$$

   with the model-dependent $K_{\pi\mu\mu}$ branching fraction

$$\mathcal{B}(K_{\pi\mu\mu}) = (9.32 \pm 0.17_{\text{stat}}) \times 10^{-8}, \tag{2.26}$$

   and the correlation coefficient $\rho(a,b) = -0.973$.

2.14 Result Stability With Respect to Selection Cut Variations

In this section we show plots displaying the values and errors of $K_{\pi\mu\mu}$ form factor parameters a (left) and b (right) when individual selection cuts are modified. The scans are meant to verify the stability of our results.

Full and uncorrelated statistical errors are shown. The uncorrelated errors between the *nominal* result (marked by dashed green lines in the plots below) and an i-th result, obtained by modifying some selection cut, are estimated using formula[12]

$$\sigma_{\mathrm{uncorr}} \simeq \sqrt{|\sigma^2_{\mathrm{nominal}} - \sigma^2_{\mathrm{i}}|}, \tag{2.27}$$

where $\sigma_{\mathrm{nominal}}$ and σ_{i} are full statistical errors (shown in red) of the nominal and i-th results, respectively. Equation 2.27 is a reasonably good estimation of uncorrelated errors between two results obtained using the same dataset in the cases where a set of events passing one of the events selections is a subset of events passing the second event selection[13].

Further discussion of the plots below is given at the end of this section.

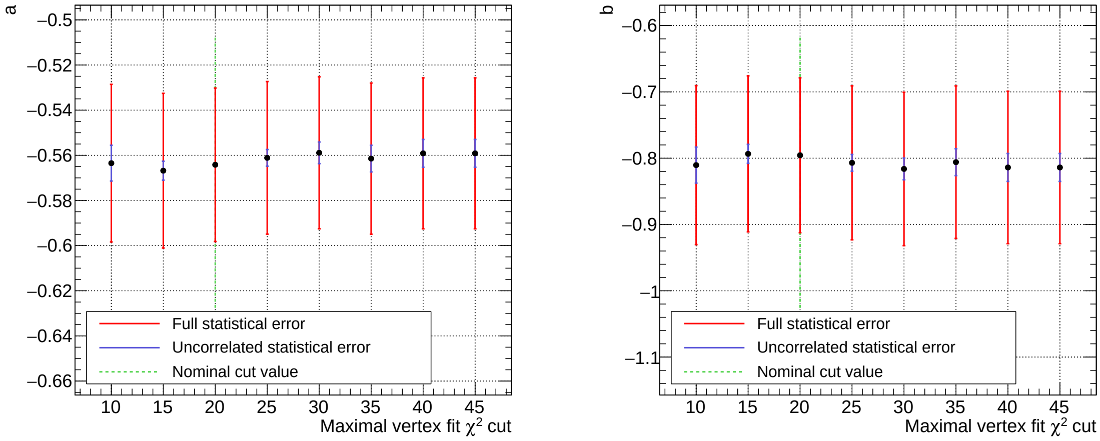

Figure 2.61: Vertex χ^2 cut scan.

---

[12] http://www-group.slac.stanford.edu/sluo/Lectures/stat_lecture_files/sluolec5.pdf, page 10

[13] This is satisfied for most of the following scans, with the exception being the plot in Fig. 2.69, showing the MUV3-related timing cuts. Due to the interplay between the π^+ and $\mu^\pm$ PID conditions, increasing or decreasing the MUV3-related timing cuts can result in both inclusion and exclusion of additional events, which results in one set of the events no longer being a subset of the other. Nevertheless, we observe almost no dependence of the results on the used MUV3 timing cuts.

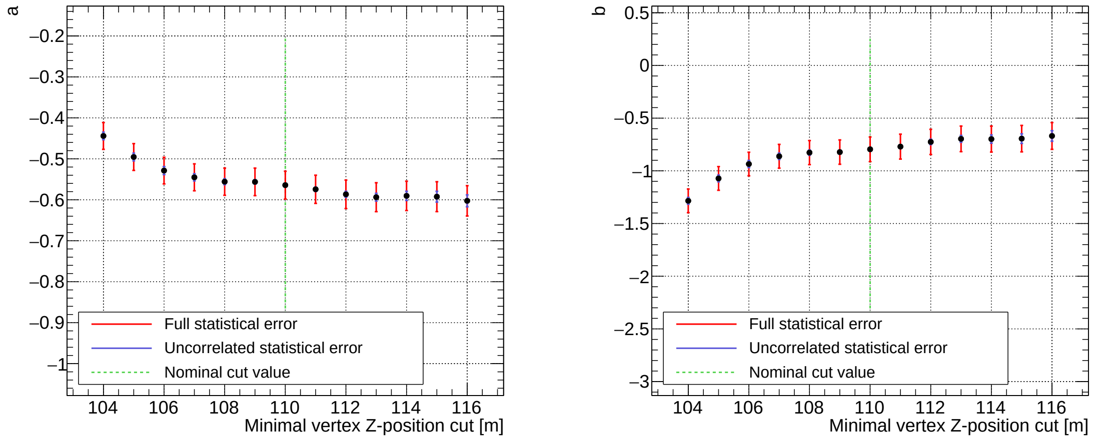

Figure 2.62: Vertex Z-position cut scan.

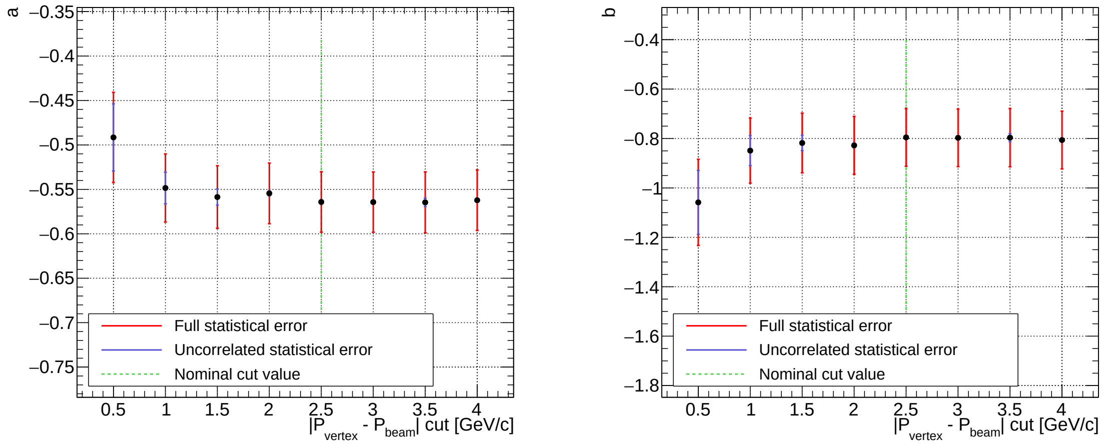

Figure 2.63: $|p_{\text{vertex}} - p_{\text{beam}}|$ cut scan.

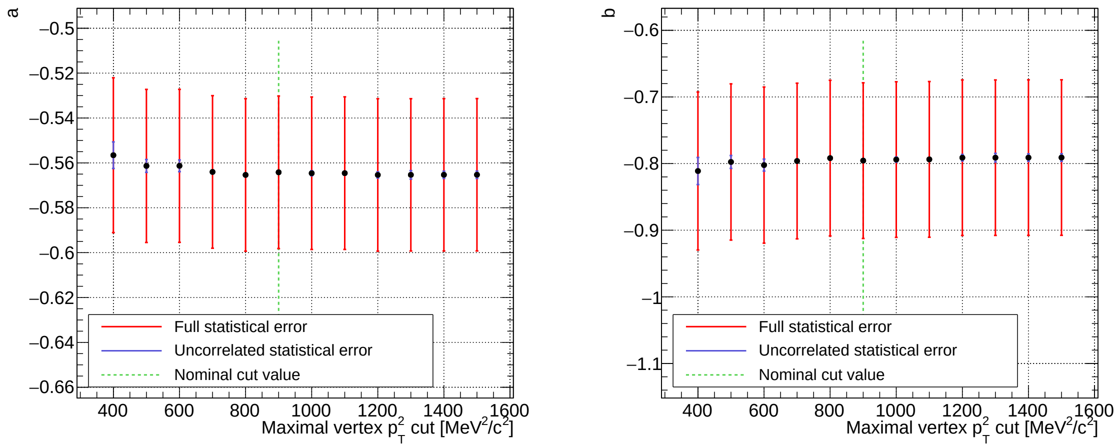

Figure 2.64: Vertex p_T^2 cut scan.

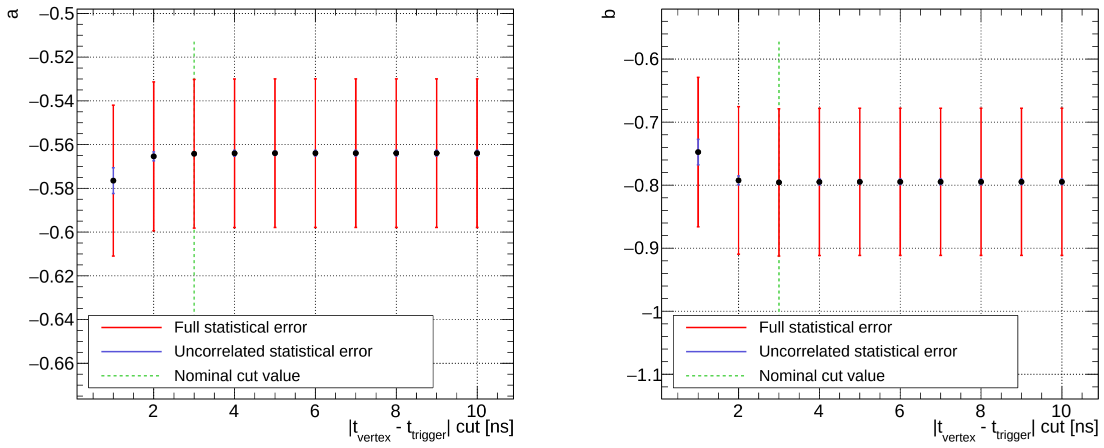

Figure 2.65: $|t_{\text{vertex}} - t_{\text{trigger}}|$ cut scan.

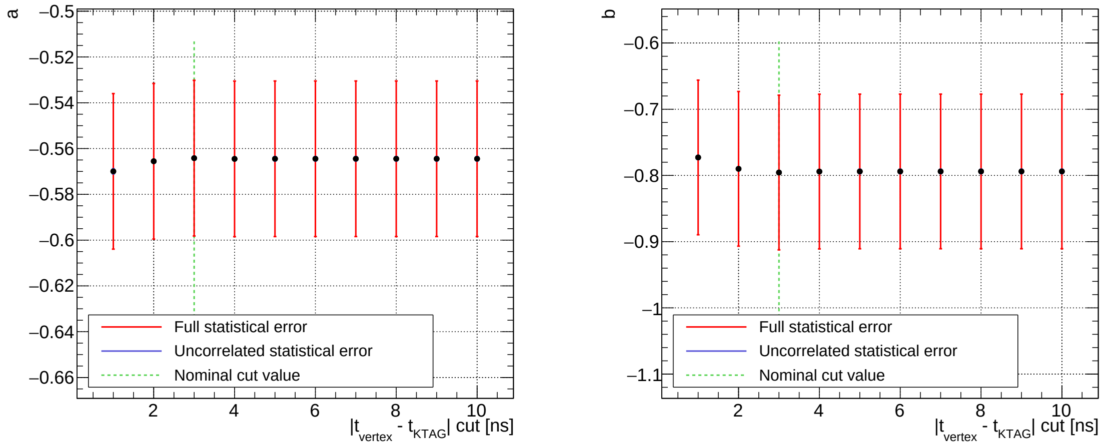

Figure 2.66: $|t_{\text{vertex}} - t_{\text{KTAG}}|$ cut scan.

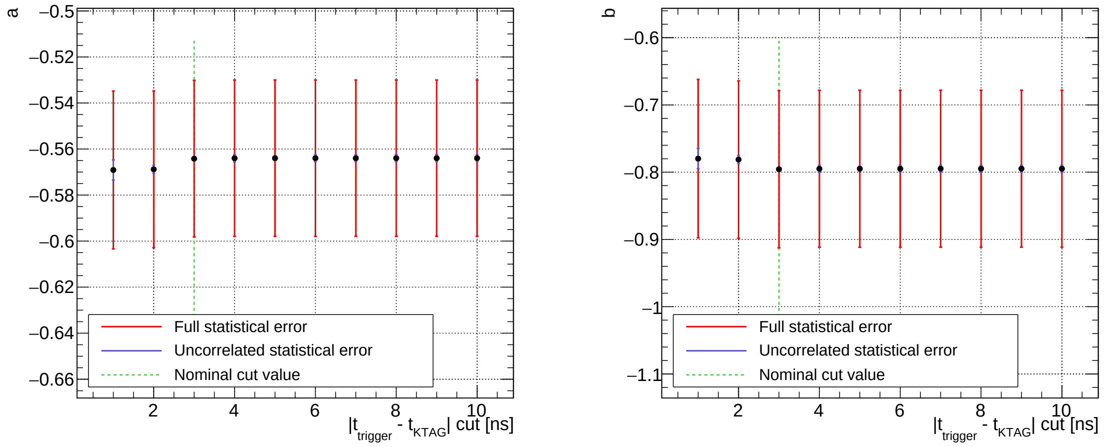

Figure 2.67: $|t_{\text{trigger}} - t_{\text{KTAG}}|$ cut scan.

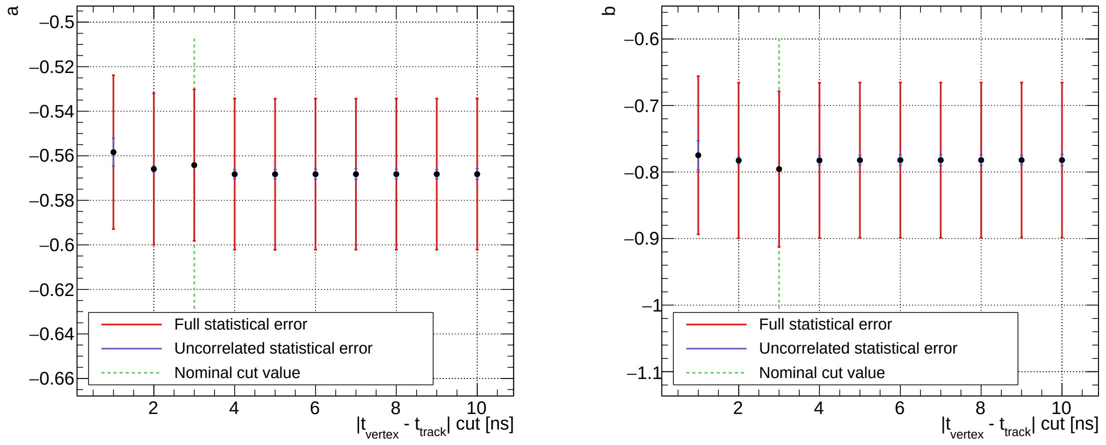

Figure 2.68: $|t_{\text{vertex}} - t_{\text{track}}|$ cut scan.

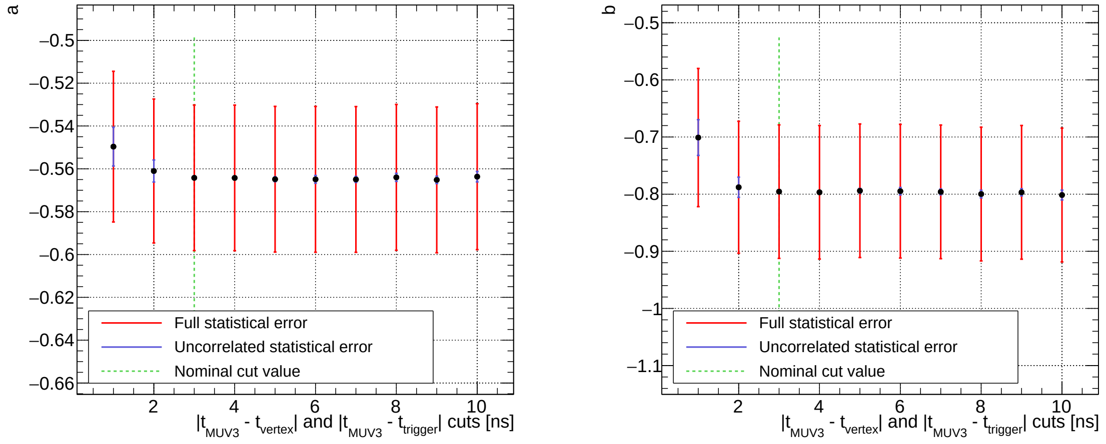

Figure 2.69: $|t_{\text{MUV3}} - t_{\text{vertex}}|$ and $|t_{\text{MUV3}} - t_{\text{trigger}}|$ cuts scan.

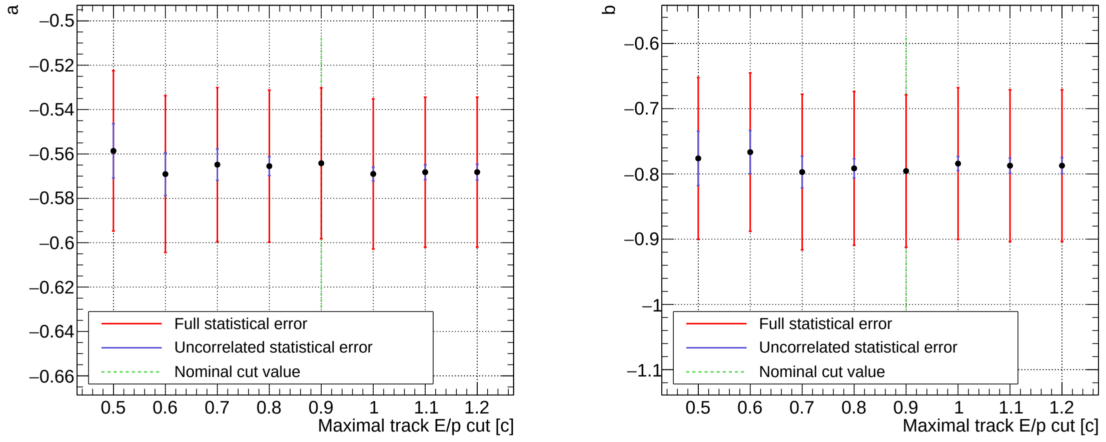

Figure 2.70: $E^{i}_{\text{cluster}}/p^{i}_{\text{track}}$ cut scan.

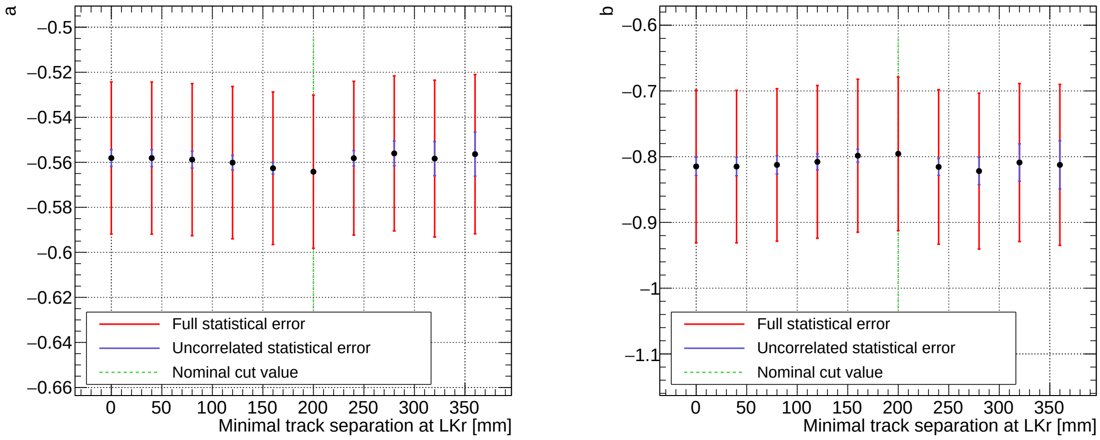

Figure 2.71: Track separation at LKr cut scan.

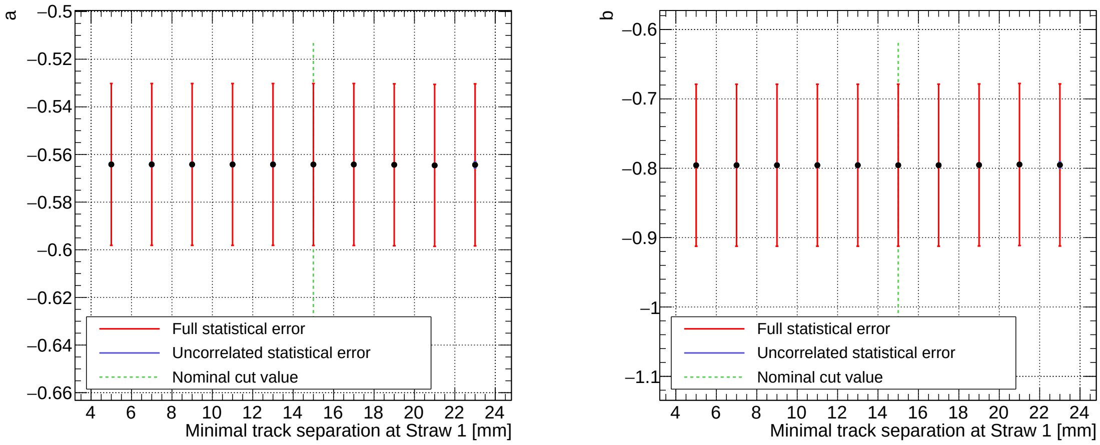

Figure 2.72: Track separation at Straw 1 cut scan.

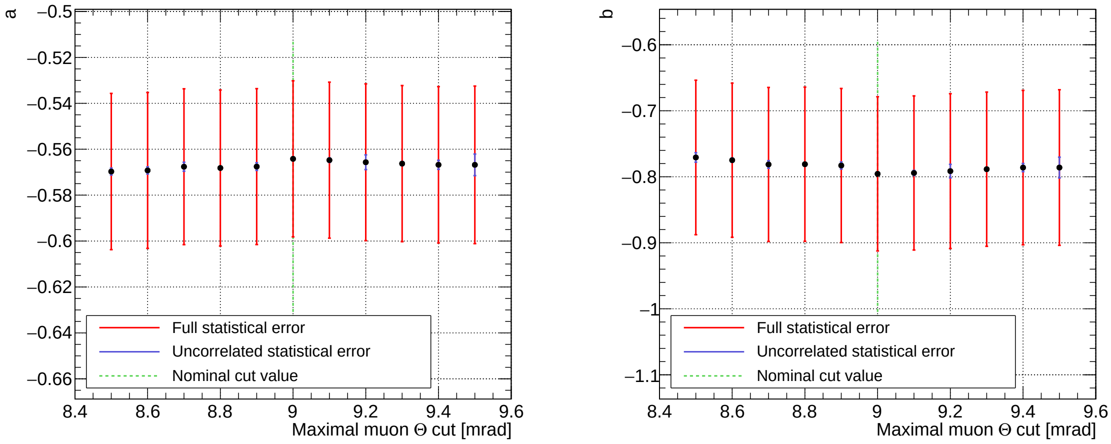

Figure 2.73: Muon track Θ cut scan.

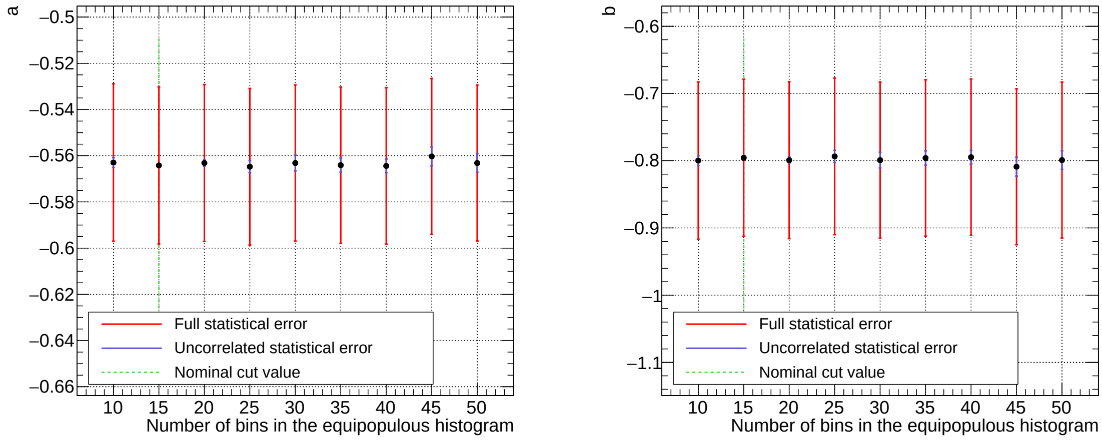

Figure 2.74: Number of equipopulous bins scan (Appendix B).

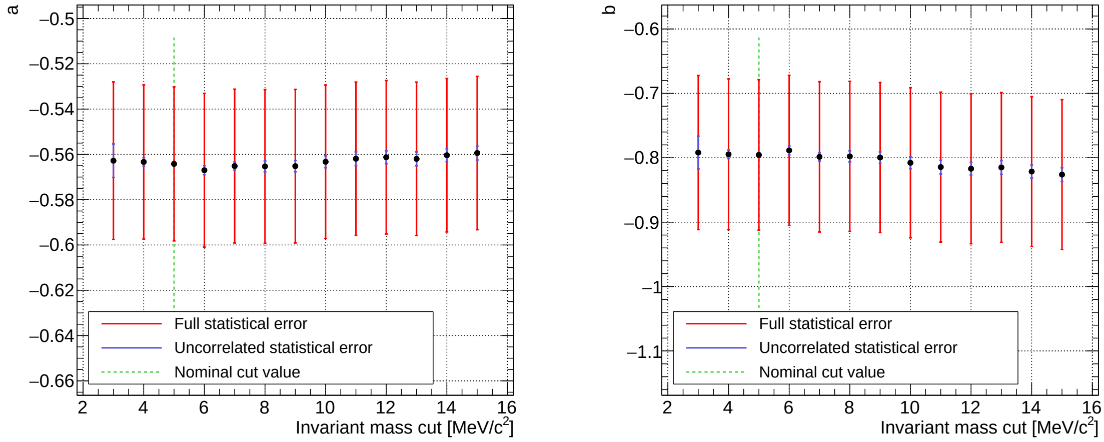

Figure 2.75: Invariant mass cut scan.

In all of the above plots with the exception of vertex Z-position (Fig. 2.62), the nominal result lies within 1 or 2 uncorrelated errors of the remaining results. The increasing discrepancies in fitted parameters a and b visible for vertex Z-position cut below 108 m are caused by introducing TRIM5-affected $K_{3\pi}$ background events discussed in section 2.10 and seen in Fig. 2.29 or Fig. 2.36.

2.15 Study of Systematic Effects

This section describes relevant systematic effects affecting the results of the presented analysis. Each subsection deals with a single systematic effect and contains the description of the effect and the estimation of the resulting uncertainties. The final result and all uncertainties are summarised in section 2.16.

In tables shown in the following subsections, form factor parameters with all significant digits obtained from the fitting algorithm are listed, since they are used to evaluate the final systematic uncertainty.

2.15.1 Trigger Efficiency

From the early stages of our analysis, we suspected trigger efficiency to be a significant contribution to the overall systematic uncertainty. This was mainly caused by the fact that the limited statistics of the $K_{\pi\mu\mu}$ signal sample makes it impossible to measure the Di-muon trigger efficiency (subsection 2.2.11) directly on $K_{\pi\mu\mu}$ data events. Therefore, we either had to rely on the $K_{3\pi} \to 2\mu$ background events described in section 2.10, or use trigger emulators on $K_{\pi\mu\mu}$ MC samples (subsection 2.6.6) to emulate the behaviour of the online trigger. As discussed in subsection 2.6.6, we chose the latter approach for our final result. However, fully describing the behaviour of online triggers using software emulators has proven to be challenging.

The main contribution ($\sim$ 4.5%) to the overall Multi-track and Di-muon trigger inefficiencies was found to be the L1 $\mathrm{STRAW_e}$ algorithm (Table 2.5). Its efficiency also showed non-trivial z-dependence (Fig. 2.57). Since at the time our analysis was performed, it was not possible to run the actual L1 $\mathrm{STRAW_e}$ algorithm on MC events, we had to rely on our own simplified emulator described in subsection 2.6.6.

The second most important contribution ($\sim$ 1.5%) to the total trigger inefficiencies was the L0 QX condition. The inefficiency was mostly caused by high-hit-multiplicity events, strongly correlated to the beam intensity (Fig. D.13 in Appendix D).

We decided to use a conservative approach for estimating systematic uncertainties on the $K_{\pi\mu\mu}$ form factor parameters. The approach consisted of *disabling* the L0 and L1 trigger emulators when the $K_{3\pi}$ and $K_{\pi\mu\mu}$ selections were applied on MC samples. Since the emulators were disabled for both $K_{\pi\mu\mu}$ and $K_{3\pi}$ MC samples simultaneously, any shift in the fitted values of form factor parameters should be caused solely by the difference in the behaviour of trigger emulators on $K_{\pi\mu\mu}$ and $K_{3\pi}$ MC samples. Table 2.6 summarises the results obtained when L0 and/or L1 emulators are disabled.

	a	b	$\mathcal{B}(K_{\pi\mu\mu}) \times 10^8$
Nominal result	-0.564499	-0.796607	9.31905
L0 emulators disabled	-0.564807	-0.800619	9.35053
L1 emulators disabled	-0.561125	-0.822422	9.40943
L0 and L1 emulators disabled	-0.561496	-0.826314	9.44163

Table 2.6: $K_{\pi\mu\mu}$ form factor and branching fraction results obtained when L0 and/or L1 trigger emulators are disabled.

We choose the difference between the "Nominal result" and "L0 and L1 emulators disabled" as our estimate of systematic uncertainties originating from trigger efficiencies, namely $\delta a \approx 0.003$, $\delta b \approx 0.030$ and $\delta\mathcal{B}(K_{\pi\mu\mu}) \approx 0.12 \times 10^{-8}$.

2.15.2 MUV3 Pileup

Accidental muons originating from either genuine kaon decays (Table 1.1) or from muon halo accompanying the NA62 hadron beam could spoil particle identification (PID) in our $K_{\pi\mu\mu}$ event selection described in section 2.10. Additionally, the accidental rate in MUV3 sub-detector electronics causes small ($\sim 0.1\%$) MO2 trigger inefficiencies (subsection 2.2.11 and section 2.12).

To address these issues, we developed and tuned a software tool called MUV3 pileup generator, described in subsection 2.6.4, which injects accidental MUV3 hits and candidates to MC events in order emulate pileup in MUV3 sub-detector. The accidental hits are then used inside L0 MUV3 emulator (subsection 2.6.6) to emulate MO2 trigger response, while the accidental MUV3 candidates are added to the already reconstructed genuine MUV3 candidates in the MC event (section 2.5) and are treated as real muons in our $K_{\pi\mu\mu}$ selection.

It is therefore necessary to estimate systematic uncertainties originating from inaccuracies in MUV3 pileup generator tuning. The effect on L0 MO2 trigger efficiency has already been accounted for in subsection 2.15.1 by disabling L0 trigger emulators. Once the L0 MUV3 emulator is disabled (MC events are not rejected based on its decisions), the injected pileup hits are not used anymore, only the pileup candidates are used in the PID algorithm of the $K_{\pi\mu\mu}$ event selection.

In order to asses the remaining effect on PID, we first decided to run the selection in a mode in which it ignores pileup MUV3 candidates in PID. We obtained $K_{\pi\mu\mu}$ form factor and branching fraction results shifted by $\delta a < 0.001$, $\delta b \approx 0.004$ and $\delta\mathcal{B}(K_{\pi\mu\mu}) \approx 0.03 \times 10^{-8}$, as is seen from Table 2.7.

	a	b	$\mathcal{B}(K_{\pi\mu\mu}) \times 10^8$
Nominal result	-0.564499	-0.796607	9.31905
MUV3 pileup not used in PID	-0.564392	-0.792938	9.29399

Table 2.7: $K_{\pi\mu\mu}$ form factor and branching fraction results obtained when MUV3 pileup was not used in PID.

Due to the smallness of these errors compared to those associated with other systematic effects, we opted to not investigate the accuracy of the MUV3 pileup generator further and assign the quoted shifts in central fit values as systematics due to MUV3 accidentals.

2.15.3 MUV3 Sub-detector Efficiency

As already discussed in subsection 2.6.5, the efficiency difference of MUV3 sub-detector measured on data and MC samples needs to be properly taken into account, since only the $K_{\pi\mu\mu}$ selection (and not the $K_{3\pi}$ selection) uses MUV3 for PID.

It was found that the difference between MC and data efficiencies is 0.14%, which is accounted for by rejecting real (not pileup) MUV3 candidates when applying the $K_{\pi\mu\mu}$ event selection on MC samples.

Since we neglected differences in individual tile inefficiencies seen in Fig. 3.6, we assigned 100% relative uncertainty to our knowledge of the inefficiency and obtained form factor fits for the central nominal value ($\varepsilon = 99.86\%$) and upper ($\varepsilon = 100\%$) and lower ($\varepsilon = 99.72\%$) edges of 1σ interval of the MUV3 efficiency estimate. The results are summarised in Table 2.8.

	a	b	$\mathcal{B}(K_{\pi\mu\mu}) \times 10^8$
Nominal result	-0.564499	-0.796607	9.31905
Upper edge ($\varepsilon = 100\%$)	-0.564112	-0.794256	9.29633
Lower edge ($\varepsilon = 99.72\%$)	-0.565294	-0.798702	9.34877

Table 2.8: $K_{\pi\mu\mu}$ form factor and branching fraction results obtained for different MUV3 sub-detector efficiency values.

We choose the difference between the “Nominal result” and “Lower edge” as our systematics estimate due to MUV3 sub-detector efficiency: $\delta a \approx 0.001$, $\delta b \approx 0.002$ and $\delta\mathcal{B}(K_{\pi\mu\mu}) \approx 0.03 \times 10^{-8}$.

2.15.4 Beam Tuning

The beam parameters used to generate MC samples employed in our analysis have been tuned to match the properties of the NA62 beam present during 2016 data taking. As already shown in Fig. 2.42, Fig. 2.43 or Fig. 2.44, there is substantial disagreement between data and MC spectra of reconstructed vertex momenta.

Different vertex momentum spectra could in principle lead to distortions of the $K_{\pi\mu\mu}$ z spectrum due to kinematic dependence of $K_{\pi\mu\mu}$ acceptance: variable z depends on opening angles between the muon pair in the LAB frame as well as magnitudes of muon momenta; changes in vertex momenta affect opening angles of kaon decay products. This could, for example, cause a portion of events with certain z to miss sub-detector acceptances in data, but not in MC (or vice-versa).

To estimate the systematic effect on our results coming from inaccurate MC beam tuning for the 2017 data sample used in our analysis, we decided to use an MC reweighting technique, in which every MC event is assigned its own weight based on the true kaon momentum and all subsequent manipulation of this event carries this weight. We describe the full procedure in the following points:

1. We first apply our $K_{3\pi}$ event selection *without* the vertex momentum and vertex p_T^2 cuts applied.

2. We fill spectra of vertex p_X, p_Y and p_Z for data and MC events passing the modified $K_{3\pi}$ event selection. The MC spectra are filled with weights equal to one. Average (across events) beam momentum components $p_X^{\rm avg}$, $p_Y^{\rm avg}$ and $p_Z^{\rm avg}$ are evaluated from the data sample.
3. Once the data and MC spectra are filled, we normalise the MC spectra to data, divide them and fit each result with a function

$$f(p) = \min(10, \max(0, \mathrm{Pol6}(p - p_0))), \tag{2.28}$$

where $\mathrm{Pol6}(p - p_0)$ is a 6-th order polynomial in variable $p - p_0$ with parameter p_0 representing mean value of p. The obtained weight functions are shown in Fig. 2.76.

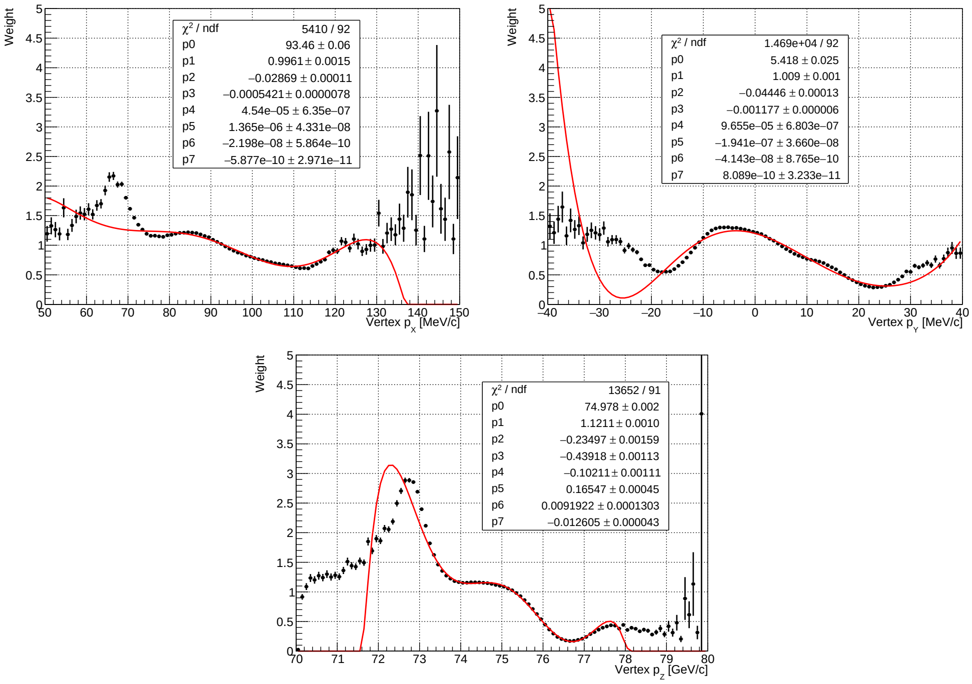

Figure 2.76: Functions used to reweight MC events.

4. We then proceed with our analysis in almost the same way as we would if no MC reweighting was applied, with the following modifications:
   - Every MC event carries weight

$$w = f_X(p_X^{\rm true}) \cdot f_Y(p_Y^{\rm true}) \cdot f_Z(p_Z^{\rm true}), \tag{2.29}$$

     where $p_i^{\rm true}$ is an i-th component of the true kaon momentum in that event.
   - The original average MC beam momentum $\mathbf{p}_{\rm beam}$ used in the $p_{\rm vertex}$ and p_T^2

cuts (section 2.8) is substituted with the average data beam momentum

$$\mathbf{p}_{\text{beam}}^{\text{new}} = (p_X^{\text{avg}}, p_Y^{\text{avg}}, p_Z^{\text{avg}}) \tag{2.30}$$

since the average weighted MC vertex momentum should be *approximately* equal to $\mathbf{p}_{\text{beam}}^{\text{new}}$.

- During the $K_{\pi\mu\mu}$ form factor fitting described in Appendix B, the reweighting of MC z template is done with a product of weight w from Eq. 2.29 and weight $w_i(a,b)$ from Eq. B.1.

The comparison of reconstructed vertex p_X, p_Y, p_Z and p_T^2 spectra before and after MC reweighting are shown in Fig. 2.77, Fig. 2.78, Fig. 2.79 and Fig. 2.80, respectively. We observe significantly improved agreement between data and MC spectra in all plots where the above weights are applied.

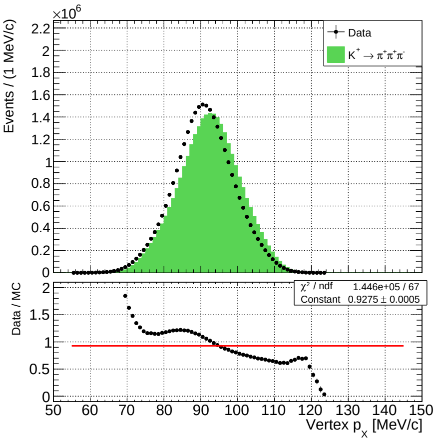

Figure 2.77: Vertex p_X of $K_{3\pi}$ events before (left) and after (right) MC reweighting.

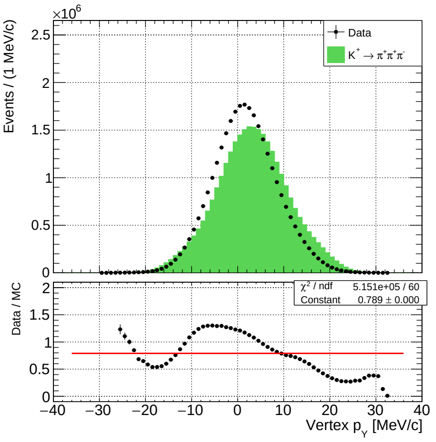

Figure 2.78: Vertex p_Y of $K_{3\pi}$ events before (left) and after (right) MC reweighting.

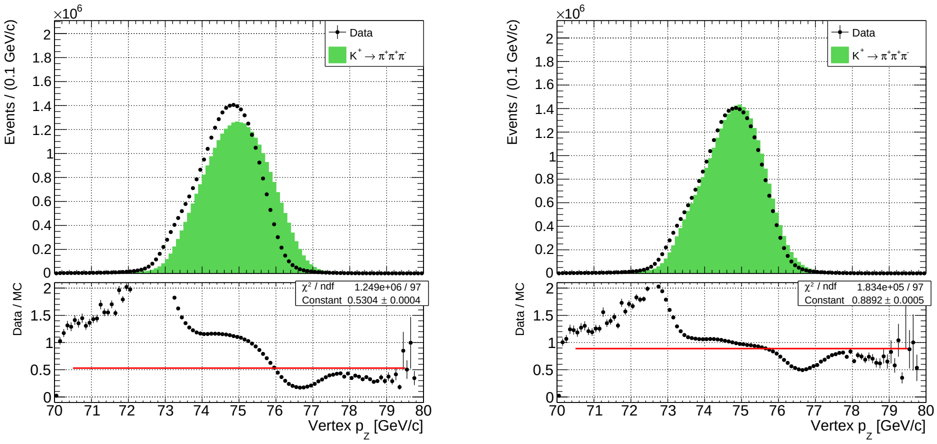

Figure 2.79: Vertex p_Z of $K_{3\pi}$ events before (left) and after (right) MC reweighting.

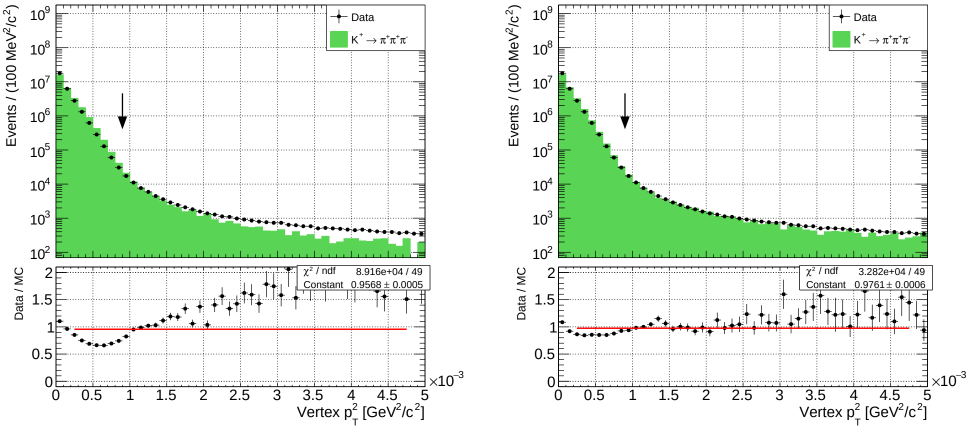

Figure 2.80: Vertex p_T^2 of $K_{3\pi}$ events before (left) and after (right) MC reweighting.

	a	b	$\mathcal{B}(K_{\pi\mu\mu}) \times 10^8$
Nominal result	-0.564499	-0.796607	9.31905
With MC reweighting	-0.565295	-0.801592	9.36681

Table 2.9: $K_{\pi\mu\mu}$ form factor and branching fraction results obtained when we do (not) reweight MC.

The $K_{\pi\mu\mu}$ form factor parameters and branching fractions we obtain with and without the application of MC reweighting are summarised in Table 2.9. We assign the full difference of these results as a systematic uncertainty due to the limited accuracy of MC beam parameters: $\delta a \approx 0.001$, $\delta b \approx 0.005$ and $\delta\mathcal{B}(K_{\pi\mu\mu}) \approx 0.05 \times 10^{-8}$.

2.15.5 Straw Track Reconstruction Efficiency

The efficiency of Straw reconstruction algorithm described in section 2.5 is another source of systematic uncertainties on the $K_{\pi\mu\mu}$ form factor parameters and branching fraction. If the reconstruction efficiency in data does not reach 100%, it lowers the number of observed $K_{\pi\mu\mu}$ signal and $K_{3\pi}$ normalisation events. If it does not reach 100% in MC, it reduces the measured $K_{\pi\mu\mu}$ and $K_{3\pi}$ acceptances. The effect of the inefficiency needs to be simulated with a high precision in order to not bias the measurement by a wrong acceptance estimate.

The inefficiency of Straw reconstruction for three-track kaon decays has two main components:

- The first one is the inherent inefficiency of the reconstruction algorithm, which was primarily optimised to reconstruct single-track events for the purposes of the main $K_{\pi\nu\nu}$ analysis. Tightly positioned hits from multi-track kaon decays, especially in the first Straw chamber, increase the probability of track mis-reconstruction. This is related to the second point.
- A major contribution to Straw reconstruction inefficiency is caused by pileup hits from decays of un-triggered kaon decays, products of upstream beam interactions or muon halo. None of these effects is simulated in MC and currently there is no available Straw pileup generator that could be used to inject pileup hits into Straw. The presence of pileup increases the probability of matching hits produced by two different particles to a single track, which worsens the track momentum resolution and overall reconstruction performance. Moreover, it also causes reconstruction of additional fake tracks.

Obtaining Straw reconstruction efficiency from MC samples is relatively straight-forward: for events in which kaons decayed inside the fiducial decay region and all charged decay products are inside Straw acceptance, check if there are reconstructed Straw tracks compatible in position and momentum with the decay products. A tool designed to measure the Straw reconstruction efficiency on MC events using this approach was developed in the NA62 software framework and its results from $K_{3\pi}$ and $K_{\pi\mu\mu}$ MC samples are shown in Fig. 2.81 and Fig. 2.82, respectively. The measurement was done for two cases:

- Requiring tracks to be reconstructed from hits in all four Straw chambers, shown in maroon in Fig. 2.81 and Fig. 2.82.
- Accepting also Straw tracks reconstructed from hits in only three Straw chambers (default option), shown in blue in Fig. 2.81 and Fig. 2.82.

The full event (i.e. all tracks are reconstructed) reconstruction efficiencies measured on $K_{3\pi}$ and $K_{\pi\mu\mu}$ MC samples are summarised in Table 2.10.

	3 or 4-chamber tracks	Only 4-chamber tracks
$K_{3\pi}$ MC	88.7 ± 0.2	68.1 ± 0.2
$K_{\pi\mu\mu}$ MC	92.9 ± 0.2	74.1 ± 0.3

Table 2.10: Full event Straw efficiencies (in %). Errors are purely statistical.

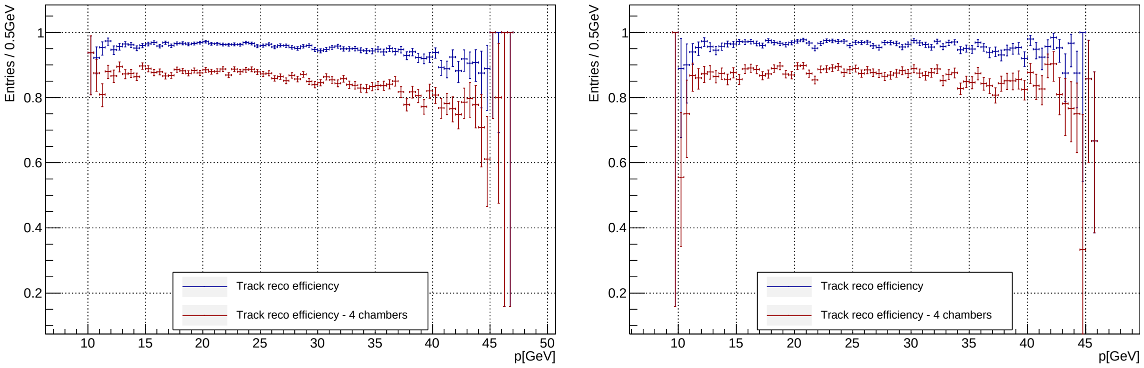

Figure 2.81: π^+ (left) and π^- (right) track reconstruction efficiency as a function of true particle momentum measured on $K_{3\pi}$ MC sample.

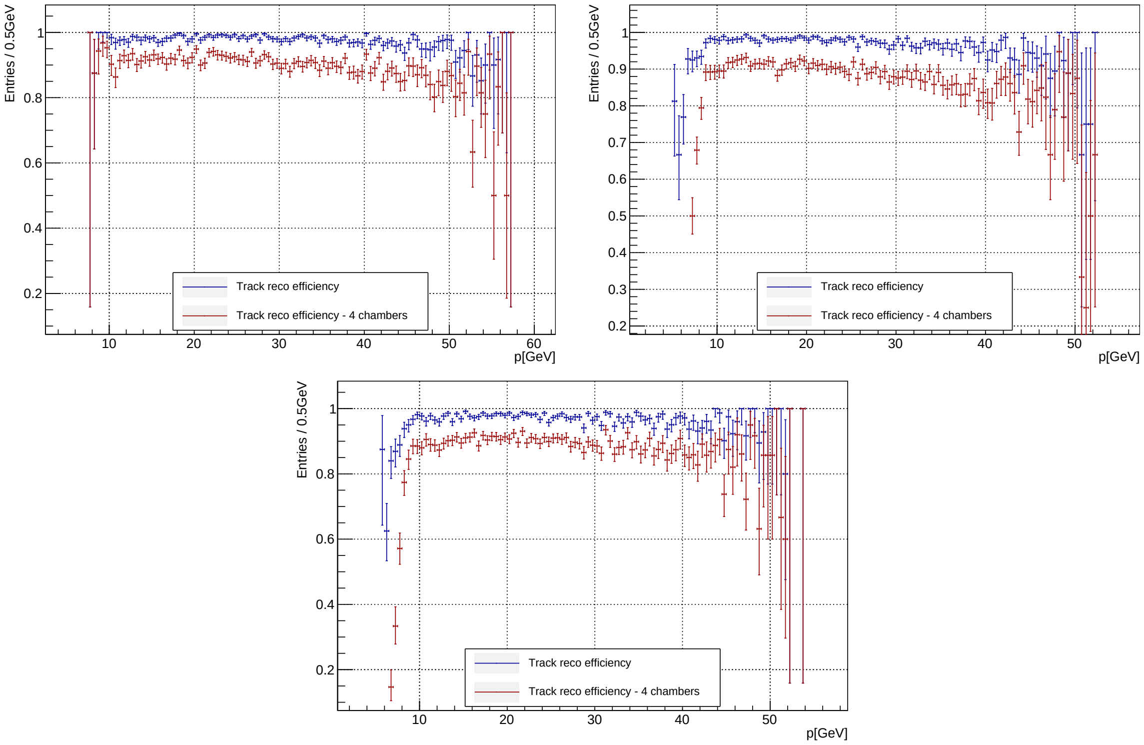

Figure 2.82: From top to bottom and left to right, we show π^+, μ^+ and μ^- track reconstruction efficiency as a function of true particle momentum measured on $K_{3\pi}$ MC sample.

Unfortunately, the measurement of Straw track reconstruction efficiency on data is highly non-trivial. Due to the obvious fact that true particle trajectories are unknown, the approach used for MC cannot be applied in data.

One possible approach is to vary the parameters used in the Straw reconstruction software to firstly optimise the reconstruction efficiency and then to estimate the residual systematic effect. This, however, would require a specialised tool allowing to modify the reconstruction parameters at the analysis level, which was still under development at the time the presented analysis was finalised.

Another approach would be to select a sample of $K_{3\pi}$ events by building the kaon four-momentum P_K (using the run-dependent beam momentum and nominal kaon mass [18]) and two pion four-momenta P_π^i (from momenta of two reconstructed Straw tracks forming a vertex in the fiducial volume, assigned charged pion mass). By requiring that the missing mass variable

$$M_{\text{miss}} = \frac{1}{c}\sqrt{(P_K - P_\pi^1 - P_\pi^2)^2}, \tag{2.31}$$

is close to the nominal charged pion mass, a “probe” can be built from the three-momenta of the kaon and the two pions. Extrapolating this probe to Straw chambers and making sure it lies in their geometrical acceptances, allows for subsequent test whether there is a third reconstructed Straw track (not chosen in the creation of the probe) compatible with the probe.

The two problems with this approach are the following:

- It cannot deal with events where two or three of the $K_{3\pi}$ decay products are not reconstructed in Straw. This leaves the user with the necessity to assume that the full event reconstruction efficiency factorises into the three track reconstruction efficiencies.
- More importantly, since this measurement has to be done on a minimum-bias Control sample (subsection 2.2.11), there is not enough available statistics of $K_{\pi\mu\mu}$ events to measure the Straw reconstruction efficiency for $K_{\pi\mu\mu}$ data events.

Due to the unavailability of the first approach and limitations of the second approach, we decided to proceed differently. For our estimate of the systematic uncertainty on $K_{\pi\mu\mu}$ form factor parameters and branching fraction originating from Straw track reconstruction efficiency, we compared the results obtained *with* and *without* the requirement that all Straw tracks forming the vertex were reconstructed from hits in all four Straw chambers.

This approach required re-evaluation of the L1 STRAW_e efficiency map shown in Fig. 2.26 using only $K_{3\pi}$ events with all three tracks reconstructed from hits in four Straw chambers (instead of three *or* four chambers, which is the default option). This resulted in $\approx 0.5\%$ increase in the measured (and subsequently emulated) L1 STRAW_e efficiencies, which increased the $K_{3\pi}$ and $K_{\pi\mu\mu}$ acceptances by similar ($\approx 0.5\%$) relative amounts. The difference between the fit results obtained using the default L1 STRAW_e efficiency map and the map from only “four-chamber events” is at a 0.1% level.

The results from default selection configuration and the results obtained from selection accepting only four-chamber tracks with the four-chamber L1 STRAW_e efficiency map, are shown in Table 2.11.

Not knowing which of the two approaches is less biased, we choose to take their

	a	b	$\mathcal{B}(K_{\pi\mu\mu}) \times 10^8$
Nominal result (3 or 4 chambers)	-0.564499	-0.796607	9.31905
Only 4-chamber tracks	-0.584647	-0.697452	9.13892

Table 2.11: $K_{\pi\mu\mu}$ form factor and branching fraction results obtained with and without the cut on the number of Straw chambers.

full difference as the systematic uncertainty: $\delta a \approx 0.020$, $\delta b \approx 0.099$ and $\delta\mathcal{B}(K_{\pi\mu\mu}) \approx 0.18\times10^{-8}$, which constitutes the largest individual contribution to the overall systematic uncertainty in the presented analysis. The relative error on $\mathcal{B}(K_{\pi\mu\mu})$ is $\approx 2\%$. Future improvement of this systematic uncertainty is crucial for a competitive measurement.

2.15.6 Straw Resolution

Resolution of the reconstructed Straw track momenta and angles, discussed in subsection 2.2.3, is given by the precision on particle space point measurements, the accuracy of the MNP33 magnetic field model and multiple Coulomb scattering in the material of straws.

However, the resolution of the reconstructed z variable parametrised in Eq. 2.21 and the sizes of z bins in the equipopulous data histogram presented in Fig. 2.60 suggest only minor bin migration and consequently z spectrum distortion. Therefore, we expect almost negligible systematic effects coming from Straw resolution.

In data, potential Straw misalignment and variations in the MNP33 magnetic field are corrected for using the Straw track correction procedure described in subsection 2.6.1. In MC, the same procedure is also applied, but the resulting corrections do not come from Straw misalignment or variations of magnetic field, but from slight differences in the MNP33 magnetic field integral used in the MC simulation and in the Straw reconstruction (section 2.5).

Even with the corrections applied, the residual resolution differences between data and MC have to be accounted for since the Straw track resolution directly affects the resolution on the $K_{\pi\mu\mu}$ z variable (measured for MC as Eq. 2.21), which in turn distorts the reconstructed z spectrum.

In order to quantify the disagreement between data and MC Straw resolutions, we extracted (Fig. 2.83 (right)) the width of the $K_{3\pi}$ invariant mass distribution as a function of run number (ID) from the data sample and a constant value from the full $K_{3\pi}$ MC sample.

We observe $\approx 5\%$ relative difference between data and MC mass resolutions, which we take into account by running the $K_{\pi\mu\mu}$ form factor fitting procedure several times for different values of parameter K defining the “new” reconstructed z value for filling the

MC template

$$z' = z_{\text{true}} + K \cdot (z_{\text{reco}} - z_{\text{true}}), \tag{2.32}$$

where z_{reco} and z_{true} are the original reconstructed and true values of z for $K_{\pi\mu\mu}$ MC events and z' is the new resolution-corrected reconstructed z.

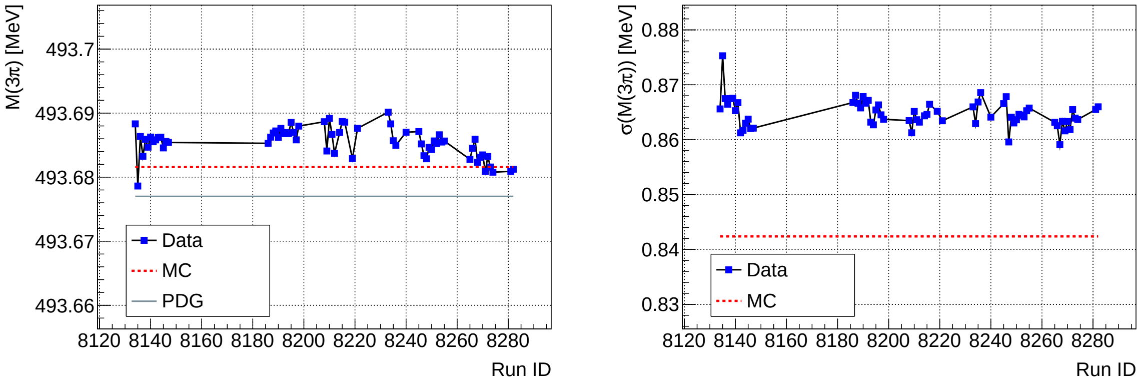

Figure 2.83: Central value (left) and width (right) of $K_{3\pi}$ invariant mass for data and $K_{3\pi}$ MC events passing our $K_{3\pi}$ event selection.

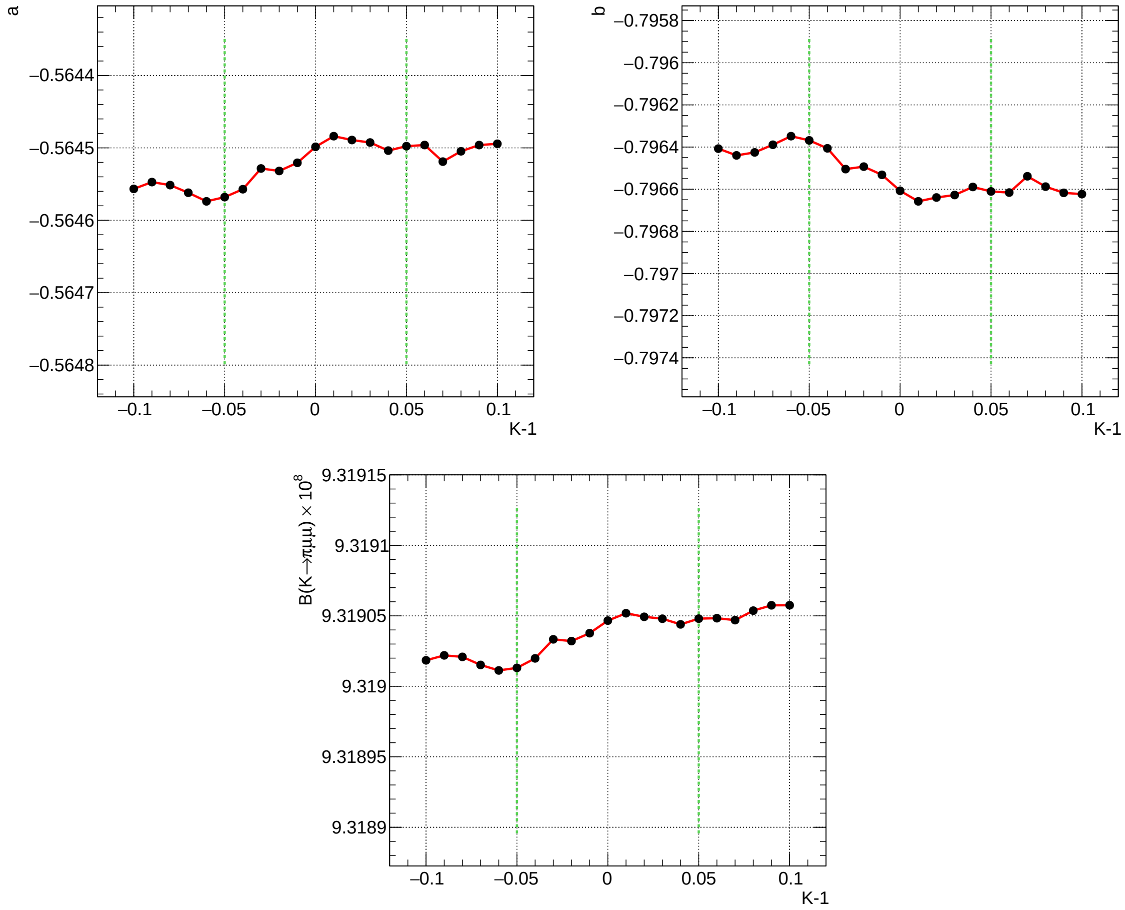

Figure 2.84: $K_{\pi\mu\mu}$ form factor parameters and branching fraction for different values of K. The vertical green lines mark $\pm 5\%$ relative scaling of MC resolution.

Setting $K = 1$ gives the nominal result, while values of $K \neq 1$ scale the MC resolution $\sigma(z)$ given in Eq. 2.21. The a- and b-dependent weights are still computed according to the z_{true} values (Appendix B). The results for different values of K are shown in Fig. 2.84.

Due to the small changes in a, b and $\mathcal{B}(K_{\pi\mu\mu})$ with respect to K, we choose to take the difference between the highest and lowest points in interval $|K - 1| < 0.05$ in each graph in Fig. 2.84 as systematic uncertainties on the results. The value 0.05 aims to reflect the maximal relative difference between widths of $K_{3\pi}$ invariant mass peaks in data and MC described above. The systematic uncertainties on a, b and $\mathcal{B}(K_{\pi\mu\mu})$ due to Straw resolution are therefore negligible: $\delta a < 0.001$, $\delta b < 0.001$ and $\delta\mathcal{B}(K_{\pi\mu\mu}) < 0.01 \times 10^{-8}$.

2.15.7 Straw Pileup Tracks

As discussed in more detail in subsection 2.15.5, the presence of Straw pileup affects the efficiency of the track reconstruction software. In addition to this effect, the presence of more than three reconstructed Straw tracks could cause the vertex fitting algorithm to find multiple three-track vertices: even if there is only one additional reconstructed Straw track accidentally passing close to the genuine three-track vertex, the fitting algorithm will find (up to) four 3-track vertices purely from combinatorics.

To estimate the systematic uncertainty we introduce with our selection requirement of *exactly one* reconstructed three-track vertex in an event (section 2.8), we disable this cut in our selection and substitute it with the following requirement:

- For each event, select the reconstructed 3-track vertex with the lowest fit χ^2 and treat it as *the vertex*. Ignore the remaining vertices.

The nominal and modified (“best vertex”) selections give the results shown in Table 2.12.

	a	b	$\mathcal{B}(K_{\pi\mu\mu}) \times 10^8$
Nominal result	-0.564499	-0.796607	9.31905
Best vertex result	-0.576622	-0.749694	9.28083

Table 2.12: $K_{\pi\mu\mu}$ form factor and branching fraction results obtained when (not) allowing multiple three-track vertices to be reconstructed in an event.

We conservatively take the difference of the two results in Table 2.12 as an estimate of the systematic uncertainty caused by the presence of pileup tracks in data: $\delta a \approx 0.012$, $\delta b \approx 0.047$ and $\delta\mathcal{B}(K_{\pi\mu\mu}) \approx 0.04 \times 10^{-8}$.

Modifying the default vertex selection cut from the current *exactly one vertex* to *exactly one good vertex*, where *good* corresponds to χ^2, charge and momentum conditions discussed in section 2.8, could potentially reduce this systematic uncertainty in future analyses. This is implied by the fact that the latter selection cut should be less sensitive to pileup tracks, i.e. fewer events are rejected due to combinatorics.

2.15.8 Straw Track Corrections

The Straw track momentum correcting procedure described in subsection 2.6.1 uses two run-dependent parameters α and β obtained by comparing nominal kaon mass [18] with the reconstructed $K_{3\pi}$ mass. The values of α and β for 2017 runs used in our analysis are shown in Fig. 2.85. The MC values are $\alpha = 7.6 \times 10^{-9} \cdot (\mathrm{MeV}/c)^{-1}$ and $\beta = -0.00087$ in all MC samples.

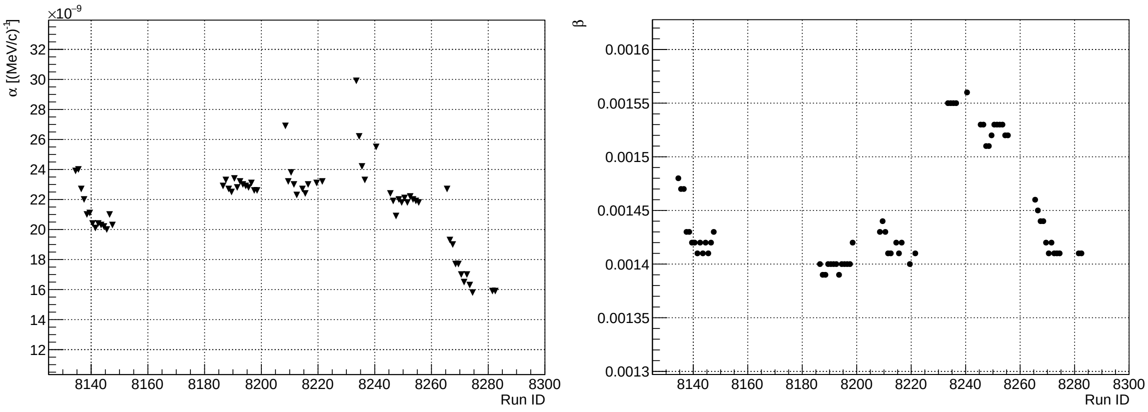

Figure 2.85: Values of α (left) and β (right) corrections for runs used in our analysis.

As already stated in subsection 2.15.6, the MC corrections account for small discrepancies between the MNP33 magnetic field integrals (subsection 2.2.3) used in the MC simulation and Straw track reconstruction software.

In data, however, the α and β parameters correct for actual physical changes in the detector caused by chamber misalignment and variations in the MNP33 magnetic field. At the time our analysis was performed, the fitting algorithm used to measure α and β did not provide errors on the fitted parameters, which consequently did not allow to estimate the systematic effects by varying each fitted value within its error.

We therefore proceeded in the following way:

- We found the maximal and minimal values of both α and β in the whole dataset

$$\begin{aligned}
\alpha_{\mathrm{min}} &= 15.9 \times 10^{-9} \cdot (\mathrm{MeV}/c)^{-1}, \\
\alpha_{\mathrm{max}} &= 29.9 \times 10^{-9} \cdot (\mathrm{MeV}/c)^{-1}, \\
\beta_{\mathrm{min}} &= 0.00139, \\
\beta_{\mathrm{max}} &= 0.00156 \ .
\end{aligned} \tag{2.33}$$

- We re-run the whole analysis four times, each time setting α or β to one of the values from Eq. 2.33, while keeping the MC corrections intact.

We compare the four results with the nominal result in Table 2.13. As the parameters α and β correct for different phenomena, we separate the systematic uncertainty into two

	a	b	$\mathcal{B}(K_{\pi\mu\mu}) \times 10^8$
Nominal result	-0.564499	-0.796607	9.31905
$\alpha \equiv \alpha_{\text{min}}$	-0.564962	-0.794845	9.31778
$\alpha \equiv \alpha_{\text{max}}$	-0.564810	-0.795775	9.32038
$\beta \equiv \beta_{\text{min}}$	-0.565202	-0.794032	9.31773
$\beta \equiv \beta_{\text{max}}$	-0.563913	-0.798800	9.32045

Table 2.13: $K_{\pi\mu\mu}$ form factor and branching fraction results obtained with different hard-coded Straw track correction parameters.

components: one due to α and one due to β. Since the overall changes to the results are minimal in all cases shown in Table 2.13, we decided to be once again conservative and take the maximal differences between nominal and extremal results as systematic uncertainties due to α and β corrections:

- Systematic uncertainties due to α:
  $\delta a \approx 0.001$, $\delta b \approx 0.002$ and $\delta\mathcal{B}(K_{\pi\mu\mu}) < 0.01 \times 10^{-8}$.
- Systematic uncertainties due to β:
  $\delta a \approx 0.001$, $\delta b \approx 0.003$ and $\delta\mathcal{B}(K_{\pi\mu\mu}) < 0.01 \times 10^{-8}$.

2.15.9 LKr Cluster Corrections

As discussed in subsection 2.6.2, energies of reconstructed LKr clusters are modified using complex position and energy-dependent corrections and subsequently tuned by additional run-dependent fine calibration constants.

Unless corrected for, the discrepancies between data and MC $E_{\text{cluster}}/p_{\text{track}}$ (E/p) spectra shown in Fig. 2.32 would result in a systematic bias of the measured $K_{\pi\mu\mu}$ form factor parameters and branching fraction. We describe the treatment of this discrepancy in Appendix C and section 2.8. To summarise the procedure, we compute a correction factor $f = (1 - 0.0013)$ to the $K_{3\pi}$ selection acceptance (Eq. C.7) based on the probabilities P_{DT} and P_{MC} of a pion having $E/p < 0.9$, the nominal cut value.

However, even with the correction applied, we observe different dependencies of P_{DT} and P_{MC} on the pion momentum p, see Fig. 2.86. The relative variation of MC with respect to data is ≈ 30%. We decided to assign a systematic uncertainty of 30% on the correction factor f and estimate the resulting error on $K_{\pi\mu\mu}$ form factor parameters and branching fraction by running the fitting procedure with

$$\begin{aligned} f_{\text{up}} &= f + 0.3 \cdot (1 - f) = 1 - 0.0009, \\ f_{\text{down}} &= f - 0.3 \cdot (1 - f) = 1 - 0.0017\ . \end{aligned} \tag{2.34}$$

The obtained results are given in Table 2.14. As systematic uncertainties on $K_{\pi\mu\mu}$

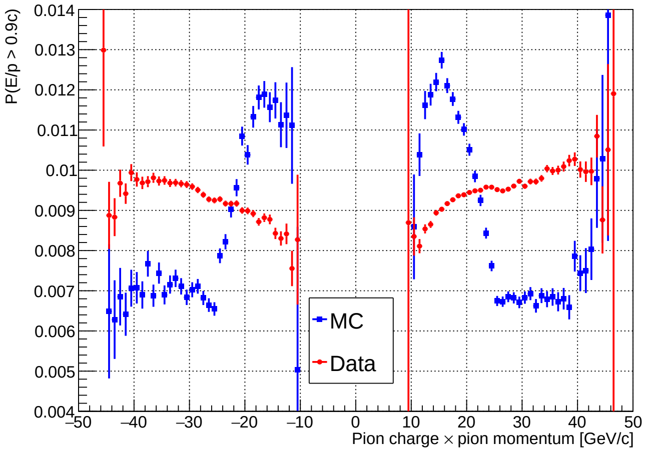

Figure 2.86: $1 - P_{\mathrm{DT}}$ and $1 - P_{\mathrm{MC}}$ for data and MC as functions of pion charge × momentum.

	a	b	$\mathcal{B}(K_{\pi\mu\mu}) \times 10^8$
Nominal result (using $f = 1 - 0.0013$)	-0.564499	-0.796607	9.31905
Using $f_{\mathrm{up}} = 1 - 0.0009$	-0.564798	-0.797111	9.32845
Using $f_{\mathrm{down}} = 1 - 0.0017$	-0.564603	-0.796463	9.32033

Table 2.14: $K_{\pi\mu\mu}$ form factor and branching fraction results obtained with different $K_{3\pi}$ acceptance correction factors f.

form factor parameters and branching fraction originating from LKr cluster corrections and the differences between data and MC related to LKr cluster energies, we take the difference between results obtained with the nominal correction factor f and those obtained using f_{up}: $\delta a < 0.001$, $\delta b \approx 0.001$ and $\delta\mathcal{B}(K_{\pi\mu\mu}) \approx 0.01 \times 10^{-8}$.

2.15.10 Particle Identification

Our $K_{3\pi}$ event selection described in section 2.8 and section 2.9 involves no PID. We pay for this fact with an $\mathcal{O}(10^{-5})$ contamination from $K_{\mu4}$ decays entering our $K_{3\pi}$ signal region (Fig. 2.35). The estimated number of such $K_{\mu4}$ events is ≈ 300, an order of magnitude less than the poissonian error on the number of $K_{3\pi}$ decays in the signal region, discussed in subsection 2.15.12.

On the other hand, the $K_{\pi\mu\mu}$ event selection described in section 2.8 and section 2.10 relies strongly on PID based on the MUV3 sub-detector (subsection 2.2.8) in order to distinguish π^+ from $\mu^\pm$. There are two ways how an event selection can fail to properly identify $K_{\pi\mu\mu}$ decay products:

- $\pi^+ \leftrightarrow \mu^-$ mis-ID: this option is highly unlikely, as in addition to incorrect PID discussed in the second point, it requires two Straw tracks to have incorrectly reconstructed charges: true π^+ needs to be assigned a negative charge and true

μ^- a positive charge.

- $\pi^+ \leftrightarrow \mu^+$ mis-ID: in this option a true π^+ is identified as a μ^+ and vice-versa. The two misidentifications involved could happen in the following way:
  - The $\pi^+ \to \mu^+$ mis-ID occurs if the π^+ decays into a muon and a neutrino and the muon produces a MUV3 candidate in outer tiles geometrically associated to the π^+. Additionally, a pileup muon, originating from either a muon halo accompanying the hadron beam or from other kaon decay, that happens to be in-time with the $K_{\pi\mu\mu}$ kaon can also result in an outer MUV3 candidate assigned to the π^+.
  - The $\mu^+ \to \pi^+$ mis-ID requires the MUV3 candidate that should be associated to the μ^+ to be either out-of-time, outside the association radius (section 2.7), or completely non-existent.

    To address the first point, MUV3 timing scan in Fig. 2.69 shows practically no dependence of the fitted $K_{\pi\mu\mu}$ form factor parameters on the MUV3 timing cuts, which indicates no PID systematic effect related to timing.

    The Straw-MUV3 association algorithm takes into account multiple Coulomb scattering and the search radius is chosen to achieve maximal association efficiency. The remaining systematic effect coming from the true μ^+ scattering outside the association radius of its track is discussed below.

    The non-existence of the MUV3 candidate can be either caused by MUV3 inefficiency (emulated for MC, see subsection 2.6.5) or the true μ^+ scattering outside the MUV3 acceptance (even though its reconstructed track was extrapolated inside it).

One obvious way to assess the probability of misidentifying $K_{\pi\mu\mu}$ decay products is to modify the total charge requirement of the two tracks identified as muons (requiring $Q = +2$ instead of $Q = 0$), thus selecting the LNV mode $K^+ \to \pi^-\mu^+\mu^+$ forbidden in the SM. Counting the number of data events surviving in the default invariant mass signal window could serve as an estimate on the number of misidentified $K_{\pi\mu\mu}$ data events. Unfortunately, since a separate analysis focusing on searches of LNV decays using the same dataset is currently ongoing in the NA62 Collaboration, the LNV signal region is blinded for all members of the Collaboration.

Therefore, we proceeded differently in our efforts to estimate the systematic uncertainties coming from particle mis-ID. Thanks to the MUV3 efficiency (section 3.1 and subsection 2.6.5), MUV3 pileup generator (subsection 2.6.4) and L0 MUV3 emulator (subsection 2.6.6) tools, we decided to use an MC-based technique to assess the probability of misidentifying $K_{\pi\mu\mu}$ decay products. It is highly likely that such misidentification will cause the true and reconstructed z values (Eq. 1.28) to differ by a noticeable amount. We therefore plotted their difference as a function of z_{true}

(Fig. 2.87) and counted the number of outlying events. Out of the total number of 1123565 $K_{\pi\mu\mu}$ MC events passing our $K_{\pi\mu\mu}$ event selection, there are:

- 28 events outside a $|z_{\text{reco}} - z_{\text{true}}| < 0.02$ band marked by dashed red lines in Fig. 2.87, and
- 2542 events lying further than $5\sigma(z)$ from z_{true}, with $\sigma(z)$ given in Eq. 2.21.

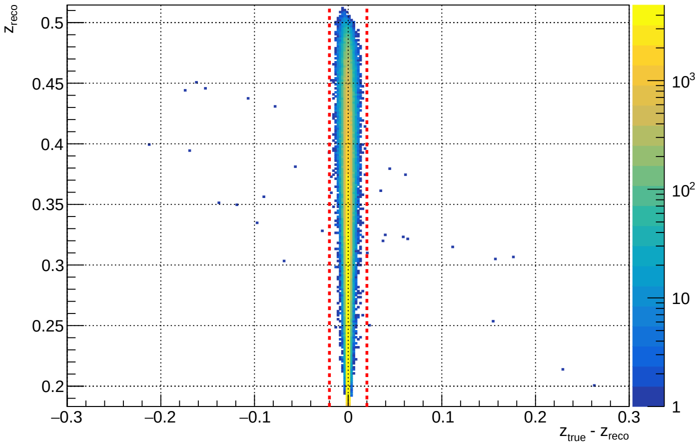

Figure 2.87: $z_{\text{true}} - z_{\text{reco}}$ as a function of z_{reco} for $K_{\pi\mu\mu}$ MC events passing our $K_{\pi\mu\mu}$ event selection. The purpose of the red lines is discussed in the text.

The two points above place the probability $P_{\text{mis-ID}}$ of misidentifying $K_{\pi\mu\mu}$ decay products in a way the true and reconstructed values of z differ by a significant amount somewhere between $P_{\text{mis-ID}} \approx 2.5 \cdot 10^{-5}$ and $P_{\text{mis-ID}} \approx 2.3 \cdot 10^{-3}$. The two values suggest that the number of misidentified $K_{\pi\mu\mu}$ events in our sample of 3074 $K_{\pi\mu\mu}$ decay candidates observed in data is between 0 and 7.

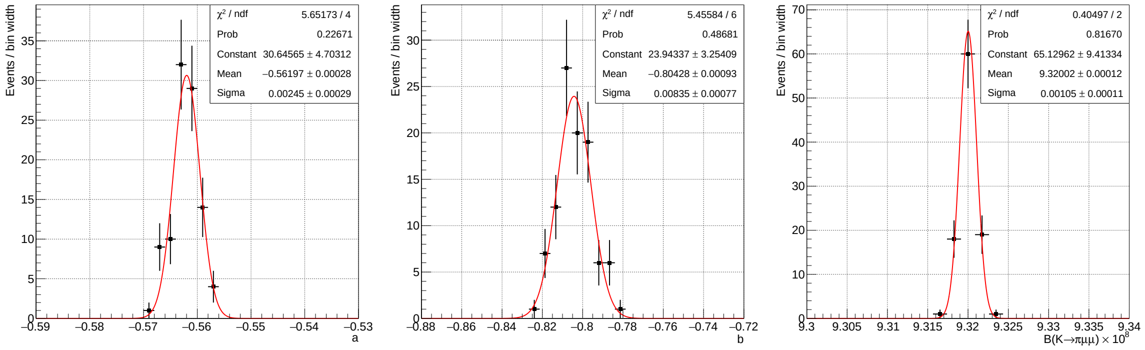

Figure 2.88: Distributions of fitted a, b and $\mathcal{B}(K_{\pi\mu\mu})$ obtained from 100 fits with different subset of 7 $K_{\pi\mu\mu}$ data events treated as misidentified. Details are in the text.

Assuming the upper limit as a conservative estimate of the number of misidentified $K_{\pi\mu\mu}$ events in data, we ran the fitting procedure 100 times, each time choosing a different subset of 7 $K_{\pi\mu\mu}$ data events for which we replace their reconstructed z value by a uniformly randomly chosen value from anywhere in the available kinematic interval

(Eq. 1.27). The obtained distributions of the fitted $K_{\pi\mu\mu}$ form factor parameters and branching fraction are shown in Fig. 2.88.

We take the difference between the nominal result and the central values of the fits in Fig. 2.88 as systematic uncertainties on the $K_{\pi\mu\mu}$ form factor parameters and branching fraction coming from possible misidentification of $K_{\pi\mu\mu}$ decay products: $\delta a \approx 0.003$, $\delta b \approx 0.008$ and $\delta\mathcal{B}(K_{\pi\mu\mu}) < 0.01 \times 10^{-8}$.

2.15.11 Background Events

In addition to misidentifying $K_{\pi\mu\mu}$ decay products between themselves, other three-track kaon decays could mimic the $K_{\pi\mu\mu}$ signal and enter the signal invariant mass region. As was mentioned in section 2.10 and is visible from Fig. 2.38, there is not enough available statistics in our full $K_{3\pi}$ MC sample to fill the tails of the $K_{3\pi} \to 2\mu$ bulk to the left of the $K_{\pi\mu\mu}$ signal, which makes the MC-based estimation of background impossible at this stage.

We therefore decided to estimate the background by fitting the tails of the data spectrum with an empirical function used also in the NA48/2 and E865 analyses [74, 77]: a constant plus an exponentiated cubic polynomial. Resulting fits obtained for different sizes of the excluded signal region (±13 MeV/c^2 (blue), ±11 MeV/c^2 (red) and ±10 MeV/c^2 (green)) around the nominal kaon mass M_K [18] are shown in Fig. 2.89.

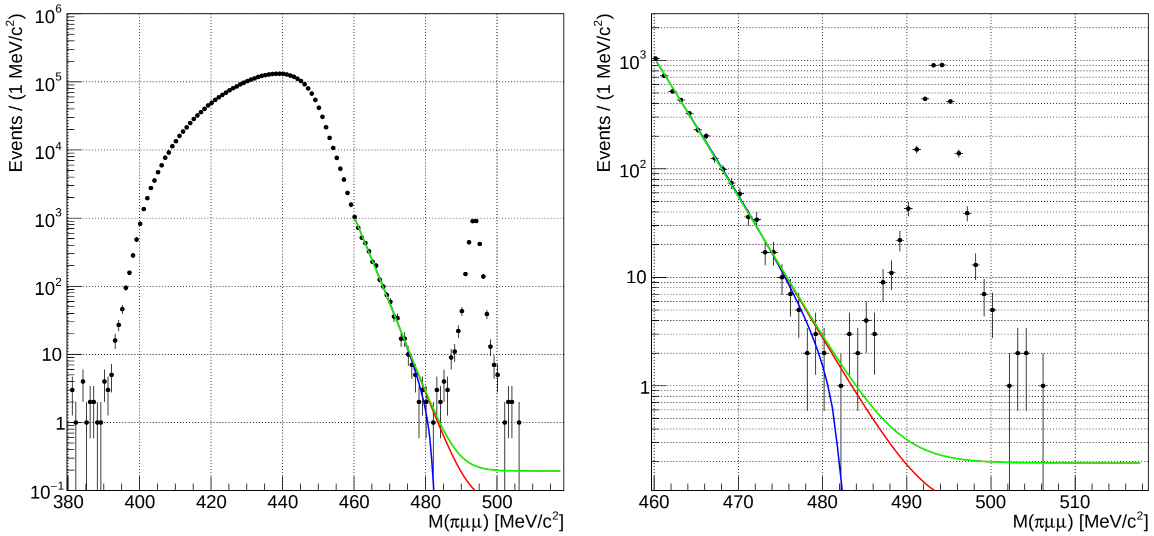

Figure 2.89: Full (left) and zoomed (right) final spectrum of data events passing our $K_{\pi\mu\mu}$ event selection together with the three background fits described in the text.

The expected number of background events, computed as integrals of the blue, red and green curves in Fig. 2.89 inside the 10 MeV/c^2-wide $K_{\pi\mu\mu}$ signal region centred at M_K, are 0, 1.2 and 2.5, respectively.

We therefore expect the number of background events inside the $K_{\pi\mu\mu}$ signal region to be “at most” 3. From this, we estimated the effect on the $K_{\pi\mu\mu}$ form factor parameters and branching fraction by running the fitting procedure 100 times, each time discarding a different subset of 3 $K_{\pi\mu\mu}$ data events. The distributions of the fitted form factor parameters and the resulting branching fraction are shown in Fig. 2.90. The central values of the fits are summarised in Table 2.15.

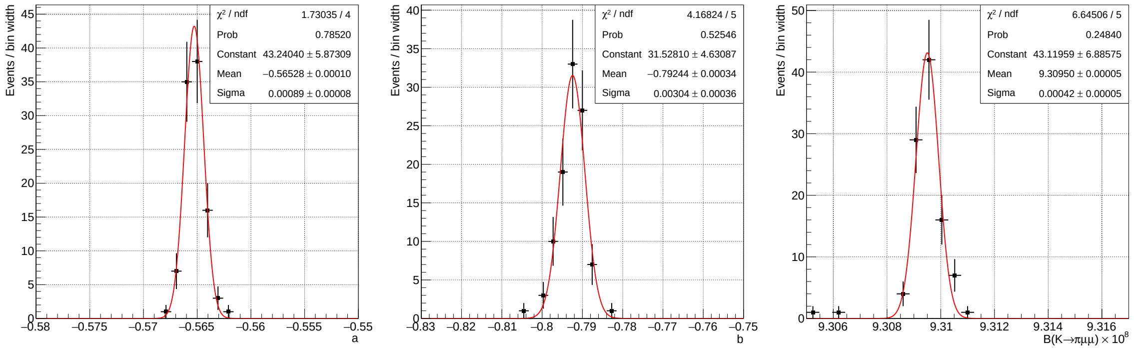

Figure 2.90: Distributions of fitted a, b and $\mathcal{B}(K_{\pi\mu\mu})$ obtained from 100 fits with different subset of 3 $K_{\pi\mu\mu}$ data events discarded.

	a	b	$\mathcal{B}(K_{\pi\mu\mu}) \times 10^8$
Nominal result	-0.564499	-0.796607	9.31905
Discarding expected background	-0.565280	-0.792440	9.30950

Table 2.15: $K_{\pi\mu\mu}$ form factor parameters and branching fraction results obtained when the expected number of background events is (not) discarded from the $K_{\pi\mu\mu}$ data sample.

We would like to emphasise here the improved resolution ($\sigma = 1.2$ MeV$/c^2$) on the $K_{\pi\mu\mu}$ invariant mass peak (Fig. 2.89) in our analysis compared to the resolution ($\sigma = 2.5$ MeV$/c^2$) achieved in the NA48/2 analysis (Fig. 1.11). Moreover, the expected number of background events in our selected $K_{\pi\mu\mu}$ sample is $\sim$ 10-times smaller than the number of background events contaminating the NA48/2 $K_{\pi\mu\mu}$ sample.

In addition to $K_{3\pi}$ decays entering the $K_{\pi\mu\mu}$ signal region through pion decays or particle misidentification, there are other three-track charged kaon decays (for example $K^+ \to \pi^+\pi^-e^+\nu_e$ or $K^+ \to \mu^+\nu_\mu\mu^+\mu^-$) that could enter the $K_{\pi\mu\mu}$ signal region through particle mis-ID or pion decays. These are however suppressed by their small branching fractions (Table 1.1).

We estimate the systematic uncertainties on the $K_{\pi\mu\mu}$ form factor parameters and branching fraction due to accidental inclusion of background events to the $K_{\pi\mu\mu}$ signal sample as the difference between the two results in Table 2.15: $\delta a \approx 0.001$, $\delta b \approx 0.004$ and $\delta\mathcal{B}(K_{\pi\mu\mu}) \approx 0.01 \times 10^{-8}$.

2.15.12 Poissonian error on $N(3\pi)$

Another systematic uncertainty comes from the number of observed $K_{3\pi}$ normalisation decays $N(K_{3\pi})$, given in Eq. 2.15. To estimate the systematic effect coming from the size of the $K_{3\pi}$ normalisation sample, we ran the fitting procedure with substituting $N(K_{3\pi})$ by the 1σ-interval boundaries: $N(K_{3\pi}) \pm \sqrt{N(K_{3\pi})}$. The results are shown in Table 2.16 and the overall systematic uncertainties are *negligible*, since in our final result we round a, b and $\mathcal{B}(K_{\pi\mu\mu})$ to three significant digits.

	a	b	$\mathcal{B}(K_{\pi\mu\mu}) \times 10^8$
Nominal result	-0.564499	-0.796607	9.31905
$N(K_{3\pi}) \mapsto N(K_{3\pi}) + \sqrt{N(K_{3\pi})}$	-0.564457	-0.796470	9.31733
$N(K_{3\pi}) \mapsto N(K_{3\pi}) - \sqrt{N(K_{3\pi})}$	-0.564540	-0.796745	9.32077

Table 2.16: $K_{\pi\mu\mu}$ form factor parameters and branching fraction results obtained for different values of $N(K_{3\pi})$.

2.15.13 Error on $\mathcal{B}(3\pi)$

Finally, since the $K_{3\pi}$ decay branching fraction $\mathcal{B}(3\pi)$ enters into the fitting procedure as an external parameter, the statistical error on its value (Table 1.1) translates into systematic uncertainties on the fitted $K_{\pi\mu\mu}$ form factor parameters and the resulting branching fraction.

	a	b	$\mathcal{B}(K_{\pi\mu\mu}) \times 10^8$
Nominal result	-0.564499	-0.796607	9.31905
$\mathcal{B}(K_{3\pi}) \mapsto \mathcal{B}(K_{3\pi}) + \delta\mathcal{B}(K_{3\pi})$	-0.565460	-0.799803	9.35911
$\mathcal{B}(K_{3\pi}) \mapsto \mathcal{B}(K_{3\pi}) - \delta\mathcal{B}(K_{3\pi})$	-0.563535	-0.793405	9.27899

Table 2.17: $K_{\pi\mu\mu}$ form factor parameters and branching fraction results obtained for different values of $\mathcal{B}(K_{3\pi})$.

We ran the fitting procedure with both extremal (1σ) values of $\mathcal{B}(3\pi)$ and obtained results summarised in Table 2.17. The estimated systematic (external) uncertainty on our results was taken as a difference between the values obtained with nominal and extremal values of $\mathcal{B}(3\pi)$: $\delta a \approx 0.001$, $\delta b \approx 0.003$ and $\delta\mathcal{B}(K_{\pi\mu\mu}) \approx 0.04 \times 10^{-8}$.

2.16 Final Result of the $K_{\pi\mu\mu}$ Form Factor Measurement

2.16.1 Error budget

The measured $K_{\pi\mu\mu}$ form factor parameters a and b obtained using the fitting procedure described in Appendix B and the model-dependent $\mathcal{B}(K_{\pi\mu\mu})$ calculated as a numerical integral of Eq. 1.31 are summarised in Table 2.18 together with the full error budget. We show the individual errors rounded to three significant digits, but the total errors are calculated from all available digits and rounded to three significant digits at the end. The partial errors are assumed to be independent and are summed in quadrature.

	a	b	$\mathcal{B}(K_{\pi\mu\mu}) \times 10^8$
Central values	-0.564	-0.797	9.32
Errors	δa	δb	$\delta\mathcal{B}(K_{\pi\mu\mu}) \times 10^8$
Statistical	0.034	0.118	0.17
Systematic			
Straw reconstruction efficiency	0.020	0.099	0.18
Trigger efficiency	0.003	0.030	0.12
Beam tuning	0.001	0.005	0.05
Straw pileup tracks	0.012	0.047	0.04
MUV3 pileup	< 0.001	0.004	0.03
MUV3 efficiency	0.001	0.002	0.03
LKr cluster corrections	< 0.001	0.001	0.01
Background	0.001	0.004	0.01
Straw track corrections, α	0.001	0.002	< 0.01
Straw track corrections, β	0.001	0.003	< 0.01
Particle identification	0.003	0.008	< 0.01
Error on $N(K_{3\pi})$	< 0.001	< 0.001	< 0.01
Straw resolution	< 0.001	< 0.001	< 0.01
Total systematic	0.024	0.114	0.23
External			
Error on $\mathcal{B}(K_{3\pi})$	0.001	0.003	0.04
TOTAL	0.042	0.164	0.29

Table 2.18: Final error budget of the $K_{\pi\mu\mu}$ form factor and branching fraction measurement.

The statistical and systematic uncertainties contribute almost equally to the total error budget. The systematic uncertainties are dominated by contributions from Straw reconstruction and trigger efficiencies discussed in subsection 2.15.5 and subsection 2.15.1, respectively. Future improvements of the estimates of these systematic uncertainties are crucial to achieve better precision than the measurements from previous experiments (see Eq. 1.44, Eq. 1.38, Eq. 1.39 and the following subsection 2.16.2).

2.16.2 Comparison to Previous Results and Future Prospects

The $\mathcal{B}(K_{\pi\mu\mu}) = 9.32 \pm 0.29_{\text{total}}$ measured in the presented analysis agrees within 1 to 2σ with both the world average value [18] shown in Table 1.1 as well as with the previous measurement performed by the NA48/2 Collaboration [74], displayed in Eq. 1.46.

In Fig. 2.91, we show comparison of the $K_{\pi\mu\mu}$ form factor parameters a and b obtained in this analysis and in the previous experiments E865 (Eq. 1.44, [77]) and NA48/2 (Eq. 1.39, Eq. 1.38, [75], [74]).

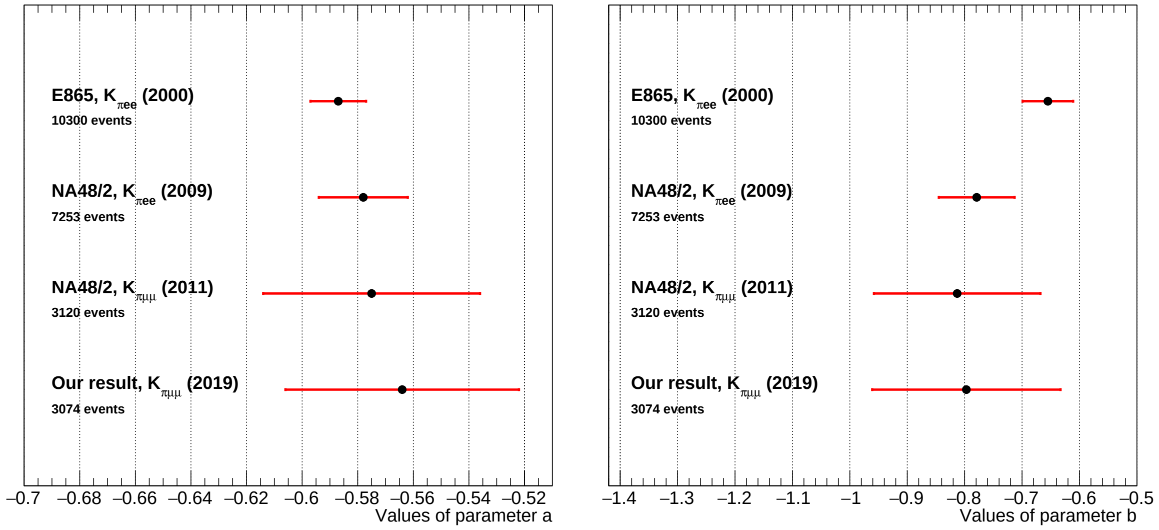

Figure 2.91: Comparison of world data on $K^{\pm} \to \pi^{\pm} l^{+} l^{-}$ form factor parameters. Combined statistical and systematic uncertainties are shown.

The $K_{\pi\mu\mu}$ sample size of 3074 candidate events used in the presented analysis was collected in one month of data taking in 2017 and already constitutes comparable sample to the NA48/2 (Fig. 2.91).

Once the full available NA62 dataset from 2017 and 2018 is analysed, we expect to observe at least 5-times more $K_{\pi\mu\mu}$ event candidates than in the presented analysis, which will reduce the statistical error by approximately a factor of two. Future analyses will also benefit from tools and methods currently under development that should resolve the major systematic effects present in our analysis.

After the remaining issues are addressed and the full available dataset is analysed, the NA62 experiment has a clear potential to provide world-leading result on the $K_{\pi\mu\mu}$ form factor parameters and branching fraction.

3 MUV3 and CHOD Efficiency Studies

In order to ensure high quality of the collected data necessary for a successful fulfilment of the NA62 physics plan, several online tools have been developed by members of the Collaboration to monitor the data taking. However, even with these tools in place, the quality of the acquired data needs to be evaluated offline as well and possible problems in any sub-detector system have to be identified.

This process is currently performed automatically as one of the several stages of data reconstruction. Each sub-system involved in data taking uses specialised tools that read the reconstructed data and monitor its quality. In case a problem in the data has been spotted, the corresponding event or burst (spill, subsection 2.2.1) is marked as “bad”, remembering the offending sub-system.

Sub-detector efficiency and timing are the two monitored quantities that determine the quality of the collected data. Time mis-alignment or low sub-detector efficiency can cause the collected data to be of insufficient quality for analysis.

Author of the presented thesis developed tools for monitoring efficiency of MUV3 and CHOD sub-detectors (section 2.2). The following sections describe these tools and show examples of their outputs obtained on Monte Carlo simulation (MC) and Control data samples (subsection 2.2.11) corresponding to 2017 runs used in the main analysis of this thesis (section 2.4).

3.1 MUV3 Efficiency Measurement

The basic principle of the MUV3 efficiency tool involves extrapolation of Straw tracks identified as muons by RICH, LKr, MUV1 and MUV2 sub-detectors to the MUV3 front-plane and checking if a reconstructed MUV3 candidate compatible in both time and space is present in the event.

A combination of two different samples for measuring MUV3 efficiency is used by default: halo muons accompanying the hadron beam, and muons from $K^+ \to \mu^+\nu_\mu$ decays (Table 1.1). One of the advantages of using both samples is the fact that the muon halo, consisting of both positive and negative muons, covers almost full MUV3 acceptance. This is not true for muons produced in the $K_{\mu2}$ decays which, due to their positive charge, are swept in the negative-X direction by the Straw magnet (subsection 2.2.3) and so do not cover some MUV3 tiles.

The default setting of using both muon samples ensures sufficiently high number of muon tracks hitting the MUV3 sub-detector in one SPS spill, which allows for the identification of problems with the resolution of one spill.

The choice between the halo and $K_{\mu 2}$ selections is done automatically for each event, creating a combined muon sample on which the MUV3 efficiency is estimated. The following subsection describes the algorithm in detail.

3.1.1 Event Selection

When running on reconstructed data, the event selection starts with a requirement that a given event was accepted by a Control trigger (subsection 2.2.11). This condition ensures that the obtained MUV3 efficiency will not be biased by the choice of the trigger stream. If the tool runs on MC, this requirement is skipped since MC events are not triggered.

The main goal of the event selection is to select a well-reconstructed muon track without using the MUV3 sub-detector. This track is then extrapolated to the MUV3 front-plane and a check for compatible reconstructed muon candidate in MUV3 is performed.

Since NA62 is a high-intensity experiment, any given event could contain several tracks reconstructed in the Straw spectrometer originating from generic beam kaon and pion decays, muon halo, particles created in inelastic interactions in upstream detectors, etc.

First step in the event selection involves the decision whether the current event will be analysed as a $K^+ \to \mu^+ \nu_\mu$ event or a muon halo event. The algorithm first looks for a track compatible with particle originating from a kaon decay. This is done by looping over all tracks and checking the distance of the closest approach (DCA) between the Straw track and the run-dependent beam axis:

- If exactly one track has DCA smaller than 5 cm, the event will be considered a $K_{\mu 2}$ event candidate.
- Otherwise, if there is at least one track with DCA larger than 15 cm, the event will be analysed as a muon halo event. If more than one track satisfies this DCA condition, the selection chooses the last such track for further analysis.
- If none of the above two points is satisfied, the event is rejected.

At this point of the selection, the tool has identified one Straw track as a potential muon candidate that all subsequent selection criteria will be imposed on. All remaining Straw tracks are completely ignored from now on. The selected track will be called simply *the track*.

The following kinematic cuts are applied to the track:

1. The track momentum p, shown in Fig. 3.1, has to lie between 5 GeV/c and 100 GeV/c. Tracks with momentum below 5 GeV/c are not well reconstructed by the Straw reconstruction algorithm. The 100 GeV/c cut is made to have a well-defined upper momentum limit in the measurement.
2. The χ^2 returned by the Straw track fitting algorithm (section 2.5) for the track

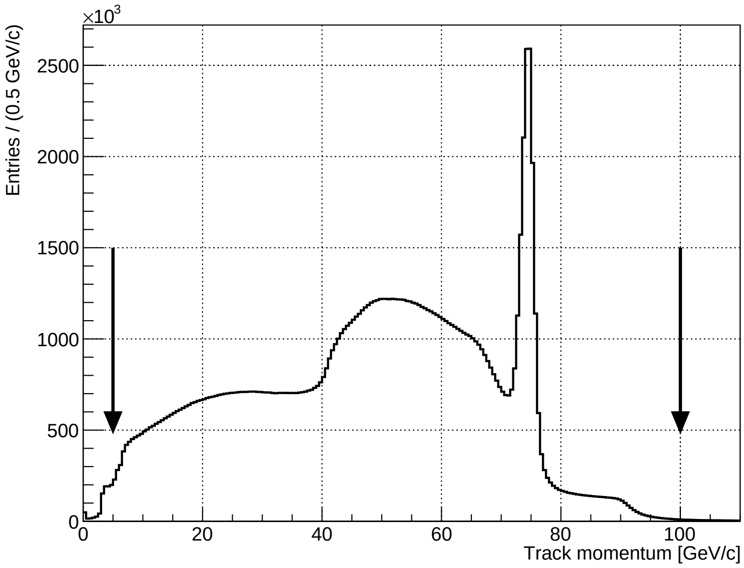

Figure 3.1: Track momentum distribution. Clearly visible peak at 75 GeV/c corresponds to scattered and peripheral beam particles detected by Straw close to the inner acceptance boundary (subsection 2.2.3).

has to be less than 10 to ensure sufficient quality of the fit.

3. The track is also required to be inside the geometrical acceptance of all Straw chambers, the NA48-CHOD, the LKr calorimeter and the MUV3 sub-detector. Since muons reaching the MUV3 sub-detector could undergo multiple Coulomb scattering inside the detector material preceding MUV3, it is required that the point obtained by linear extrapolation of the track to the MUV3 front-plane is sufficiently far from the inner and outer edges of the active region of MUV3. The required distance $R_{\mathrm{MUV3}}(p)$ depends on the track momentum and was described in more detail in section 2.7.
4. There has to be at least one reconstructed NA48-CHOD candidate in the event geometrically associated (section 2.7) to the track.
5. The closest NA48-CHOD candidate associated to the track has to be within 5 ns from the trigger time. This is done to ensure that the reconstructed Straw track, the trigger and the NA48-CHOD candidate are compatible.

Next step is the particle identification performed using MUV1, MUV2, LKr and RICH sub-detectors:

1. It is required that there are no clusters with energy above 5 GeV closer than 10 cm to the extrapolated track in MUV1 or MUV2 calorimeters, see Fig. 3.2, in order to suppress pions in the sample.

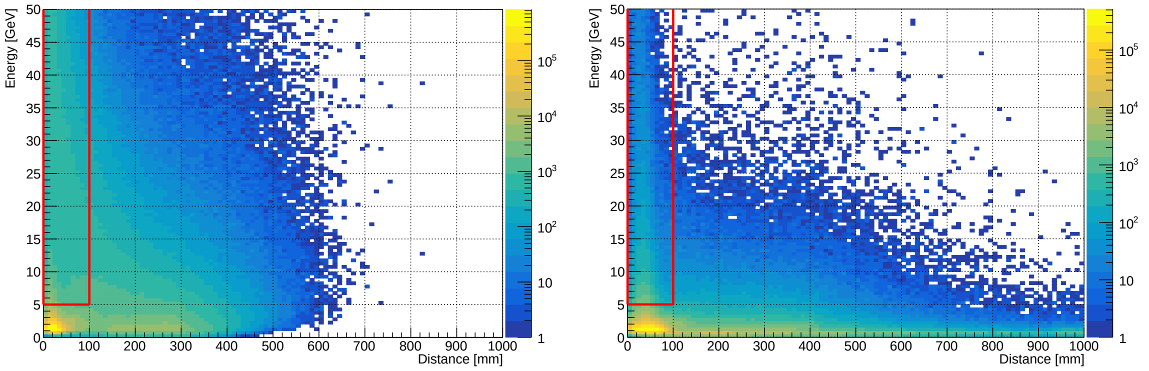

Figure 3.2: MUV1 (left) and MUV2 (right) cuts in energy–distance planes. Red lines define regions containing events that are rejected in the selection.

2. A cut $E/p < 0.1c$, shown in Fig. 3.3 (left), is imposed, where E is the energy of the closest LKr cluster geometrically associated to the track (see section 2.7 for description of the association algorithm) and p is the Straw track momentum. If no such LKr cluster exists, the event is rejected. This cut is motivated by the fact that muons are minimally ionising particles (MIPs) and so loose very little energy ($\mathcal{O}$(500 MeV)) in the LKr.

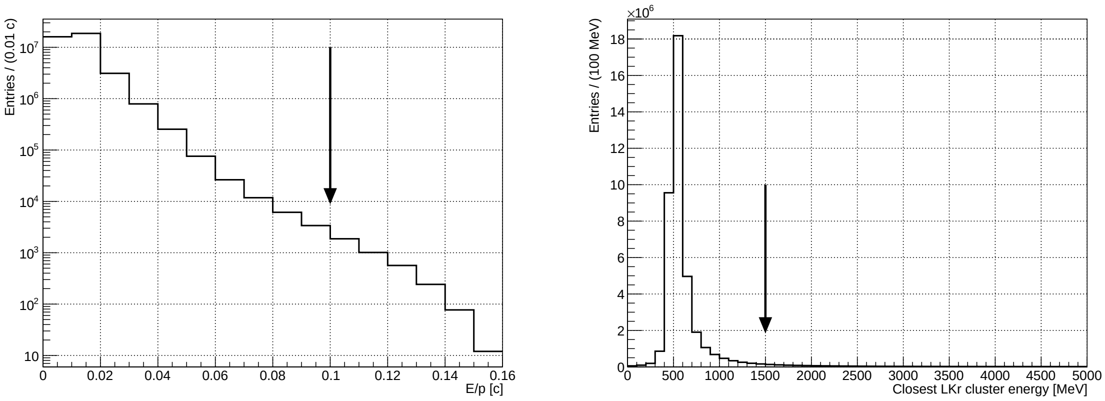

Figure 3.3: Left: E/p distribution of muon candidates. Right: E distribution of the closest LKr cluster to the track.

3. To further ensure the LKr cluster associated to the muon candidate track is compatible with a MIP, it has to:
    - have energy $E < 1.5$ GeV, as shown in Fig. 3.3 (right),
    - be within 10 ns from the trigger time, and
    - be within 3 cm from the extrapolated track point.
4. If the track momentum is below 40 GeV/c, RICH particle identification criteria are applied to further reduce pion contamination. The reason why the RICH condition is applied only in the limited momentum range is the fact that RICH sub-detector cannot reliably distinguish pions and muons with momenta above

40 GeV/c. This can be seen from the pion and muon bands in Fig. 2.27. The conditions for positive muon identification are:

- The RICH time, defined as an average of hits associated to the ring with the diameter corresponding to a muon hypothesis (section 2.7), has to be within 5 ns from the trigger time.
- Electron, muon and pion likelihoods $\mathcal{L}(e)$, $\mathcal{L}(\mu)$ and $\mathcal{L}(\pi)$ are computed based on the numbers and times of hits associated to rings under the three hypotheses. A cut

  $$\mathcal{L}_{\text{Ratio}} \equiv \mathcal{L}(\mu)/\max(\mathcal{L}(e), \mathcal{L}(\pi)) > 1.2 \tag{3.1}$$

  is imposed, illustrated in Fig. 3.4 (left).

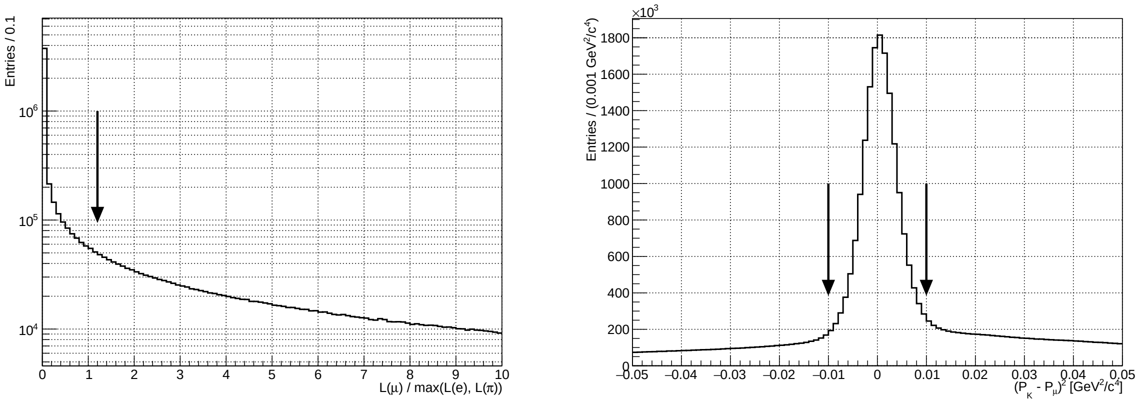

Figure 3.4: Left: distribution of $\mathcal{L}_{\text{Ratio}}$ for tracks with $p > 40$ GeV/c. Events *below* the value denoted by the arrow are rejected. This constitutes $\sim 25\%$ of all events entering the plot. Right: distribution of M^2_{miss} for $K_{\mu 2}$ candidate events.

5. If the current event is being selected as a $K_{\mu 2}$ event candidate, a cut on the squared missing mass M^2_{miss} is made

   $$M^2_{\text{miss}} = \frac{1}{c^2}(P_K - P_\mu)^2 \in [-0.01, 0.01] \text{ GeV}^2/c^4, \tag{3.2}$$

   where P_K is the four-momentum of the beam kaon and P_μ is the four-momentum of the track under the muon mass hypothesis. The distribution together with the applied cut is shown in Fig. 3.4 (right).

Finally, once the muon candidate track is selected, we can proceed to the evaluation of MUV3 sub-detector efficiency:

1. Events passing the previous selection criteria enter the denominator in the efficiency measurement.
2. If there is a MUV3 candidate geometrically associated to the track within 10 ns from the trigger time, the event also enters the numerator.

3.1.2 Results

The MUV3 efficiency measurement tool outputs a list of bursts with the total efficiency lower than a predefined threshold, set to 96% by default. This list is then used in user analyses to automatically skip MUV3-inefficient bursts. Relevant plots in the form of a `pdf` file are also created, which helps in visualisation of the measured quantities.

Figure 3.5 (left) displays how the efficiency measured on data depends on the muon momentum, while Fig. 3.6 contains two-dimensional maps of MUV3 inefficiency observed in data. The total MUV3 efficiency measured in the analysed data sample is

$$\varepsilon(\text{MUV3, data, full } p \text{ range}) = (99.701 \pm 0.001_{\text{stat}} \pm 0.027_{\text{syst}})\,\%, \tag{3.3}$$

where the systematic uncertainty was estimated as a difference between the results obtained when the tool is forced to measure the efficiency only on $K_{\mu2}$ or halo muons.

We also computed the total MUV3 efficiency for track momenta below 60 GeV/c, which is a limit of the momenta of $K_{\pi\mu\mu}$ decay products (section 2.10). The total MUV3 efficiency in this momentum range was measured to be

$$\varepsilon(\text{MUV3, data, } p \text{ below 60 GeV}/c) = (99.813 \pm 0.001_{\text{stat}} \pm 0.002_{\text{syst}})\,\%, \tag{3.4}$$

with the efficiency increase with respect to Eq. 3.3 caused by discarding the inefficient events with tracks extrapolated to inner MUV3 tiles and track momenta around 75 GeV/c (Fig. 3.5 (left)).

To test whether the measured MUV3 efficiency in MC is close to unity, the presented tool has also been run on an official $K_{\mu2}$ MC sample with the total efficiency

$$\varepsilon(\text{MUV3, MC, } p \text{ below 60 GeV}/c) = (99.953 \pm 0.001_{\text{stat}})\,\% \;. \tag{3.5}$$

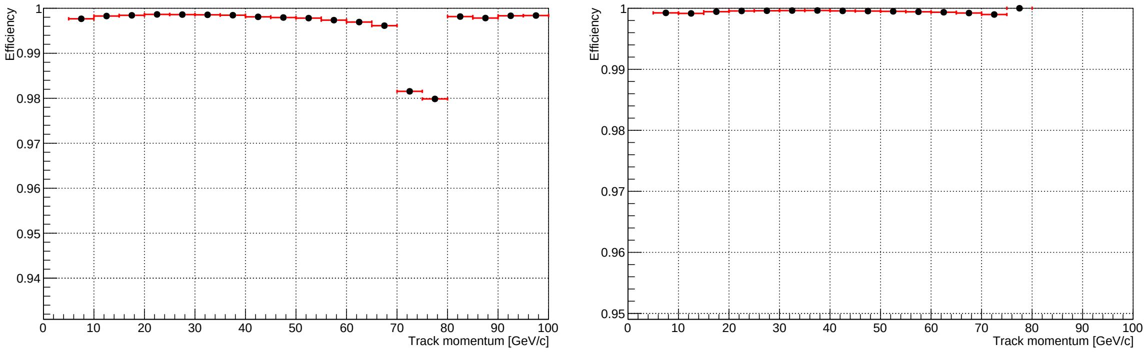

Figure 3.5: MUV3 efficiency as a function of muon momentum from data (left) and $K_{\mu2}$ MC (right). Clearly visible efficiency drop can be seen around 75 GeV/c in data originating from beam pions close to the beam pipe that are extrapolated to the MUV3 acceptance but in reality miss the MUV3, thus creating an artificial inefficiency.

The tile-by-tile and muon momentum (in)efficiency dependences for $K_{\mu 2}$ MC events are shown in Fig. 3.7 and Fig. 3.5 (right), respectively.

The above results from Eq. 3.4 and Eq. 3.5 are used in the $K^+ \to \pi^+\mu^+\mu^-$ decay form factor measurement to emulate MUV3 sub-detector inefficiency on MC samples. The procedure is described in subsection 2.6.5.

Both data and MC inefficiency plots in Fig. 3.6 and Fig. 3.7 show a vertical band of inefficient tiles on both sides of the $x = 0$ axis. This is a consequence of the 0.8 mm vertical gap separating the $x < 0$ and $x > 0$ halves of the MUV3 (subsection 2.2.8).

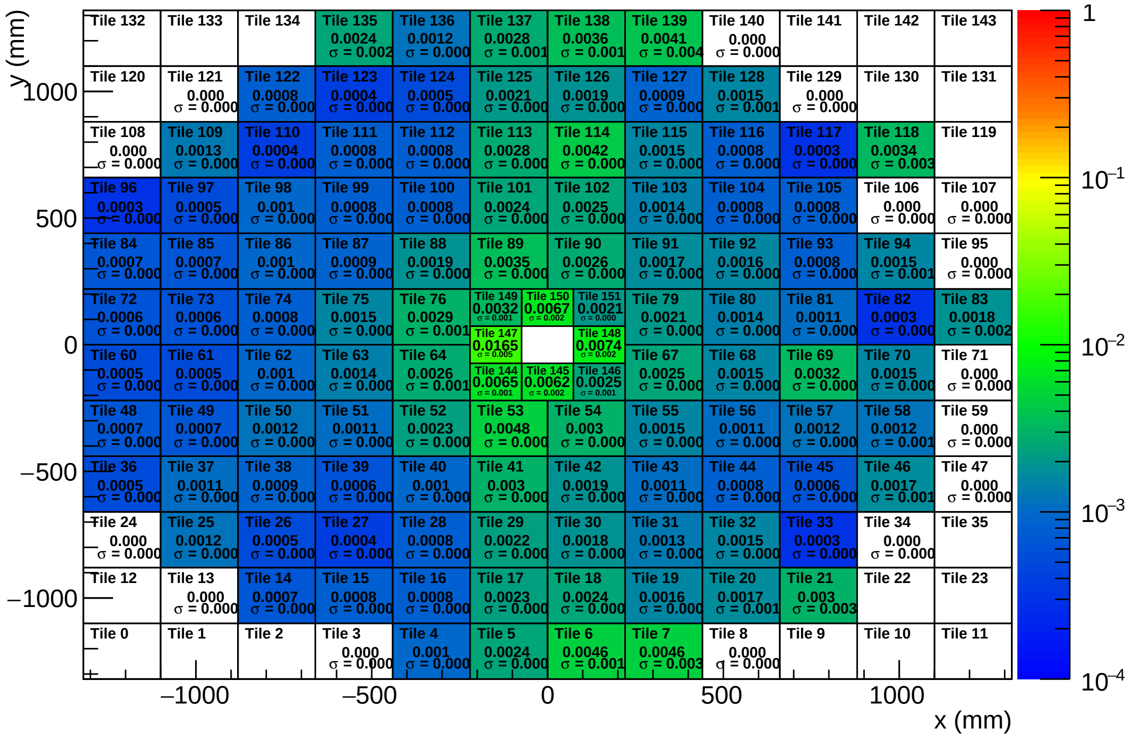

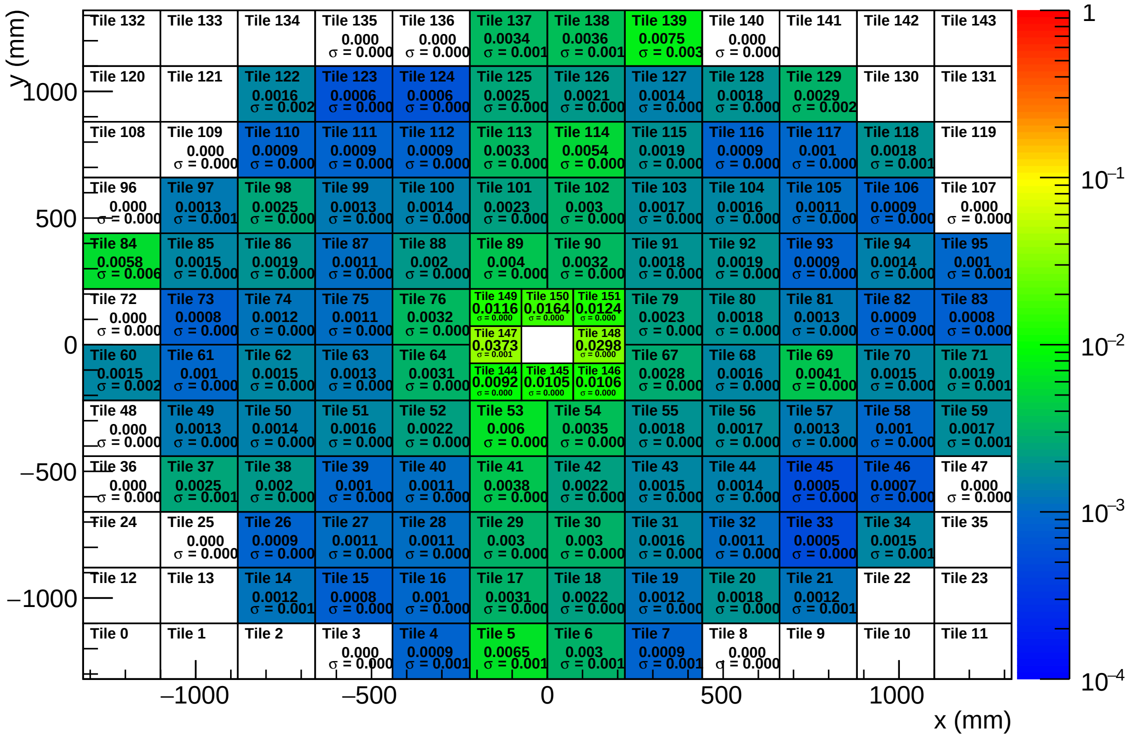

Figure 3.6: MUV3 inefficiency maps from data for muon momenta in intervals $[5, 40]$ GeV/c (top) and $[40, 150]$ GeV/c (bottom).

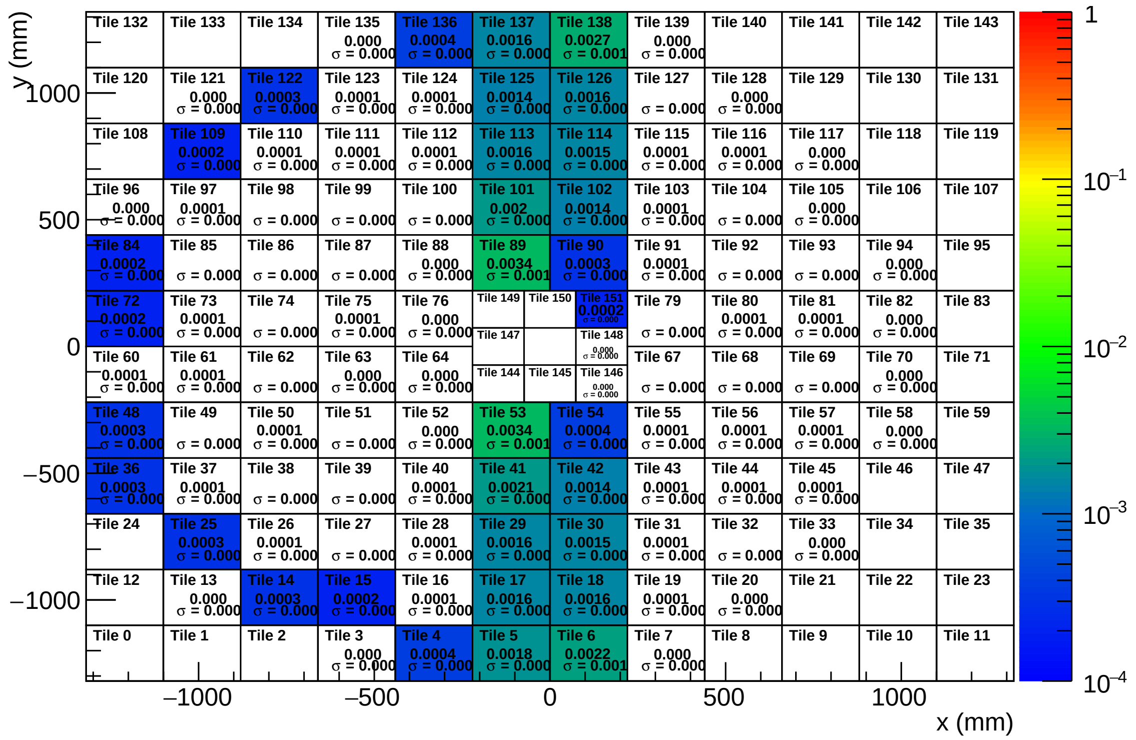

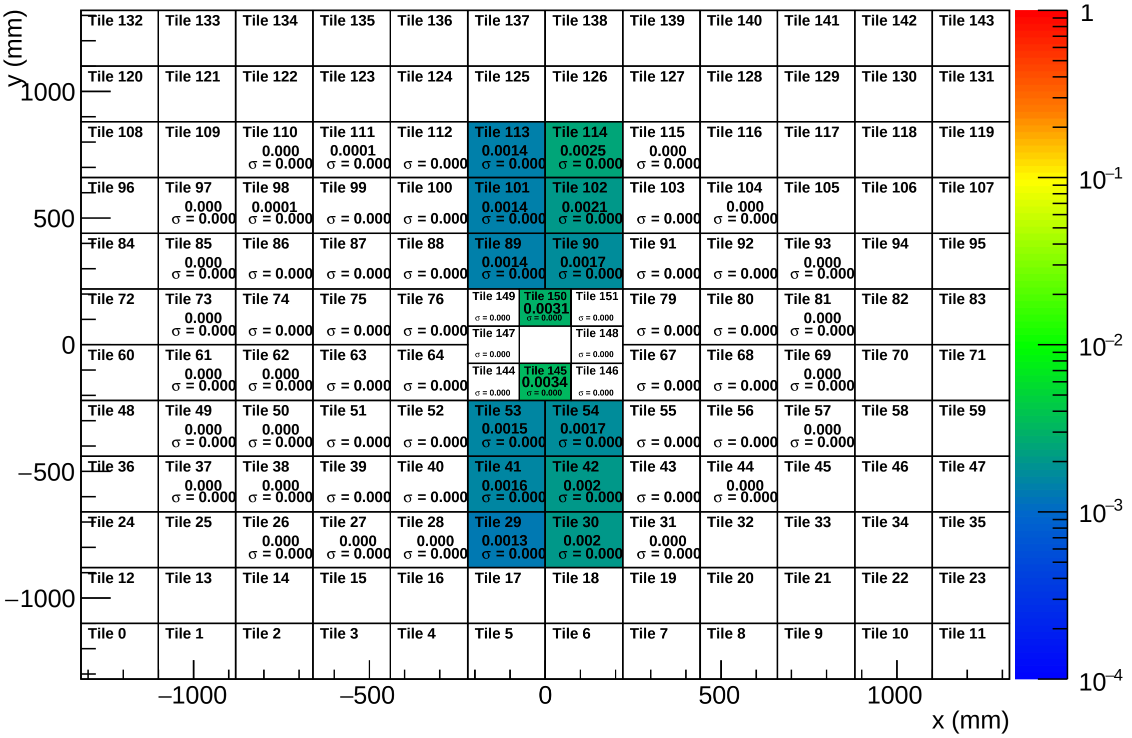

Figure 3.7: MUV3 inefficiency maps from $K_{\mu 2}$ MC for muon momenta in intervals $[5, 40]$ GeV/c (top) and $[40, 150]$ GeV/c (bottom).

3.2 CHOD Efficiency Measurement

The tool used for CHOD efficiency measurement is also based on track-seeded checks for the presence of a compatible CHOD candidate.

Since the MUV3 and CHOD sub-detectors have a similar design involving scintillator tiles (section 2.2), the tool used for the CHOD efficiency measurement was derived from the one used for the MUV3 efficiency evaluation.

However, since the CHOD should see all charged particles in its acceptance, no particle identification has to be made, which makes the CHOD tool significantly simpler.

3.2.1 Event Selection

As in the MUV3 efficiency tool, the event selection on data begins by the Control trigger requirement. On MC, this condition is skipped. The following cuts are then applied:

1. Exactly one Straw track reconstructed in the event is required.
2. The track fit $\chi^2 < 10$ cut is imposed.
3. Track momentum p has to be larger than 5 GeV/c^2 and smaller than 100 GeV/c^2.
4. The geometrical acceptance cuts only involve Straw, CHOD and NA48-CHOD. Using the same argument as in the MUV3 efficiency tool, the inner and outer CHOD acceptance cut is adjusted with the $R_{\text{CHOD}}(p)$ function defined in Eq. 2.9.
5. The number of reconstructed NA48-CHOD candidates has to be exactly one. This candidate has to be geometrically associated to the track and within 5 ns from the trigger time.

Finally, we proceed with the CHOD efficiency evaluation:

1. Events passing the above criteria enter the denominator in the CHOD efficiency measurement.
2. A check for the existence of a CHOD association to the track is performed (section 2.7). If more than one such association exists, the one closest to the trigger time is chosen. Additional timing cut of 5 ns on the difference between the NA48-CHOD candidate time and the time of the chosen CHOD candidate is imposed. If the CHOD candidate survives this cut, the event is considered efficient.

3.2.2 Results

The tool produces a list of inefficient (“bad”) bursts which can then be skipped later at the analysis stage. A burst is defined as bad by the CHOD efficiency tool if the overall burst efficiency integrated over all CHOD tiles drops below 96%.

As in the case of the MUV3 efficiency tool, the CHOD efficiency tool also exports the measured efficiency spectra in the form of a `pdf` file which helps visualising possible inefficiencies. An example of the output obtained from the same Control sample as described in chapter 3 is shown in Fig. 3.8.

The overall CHOD efficiency is

$$\varepsilon(\text{CHOD, data}) = (99.459 \pm 0.001_{\text{stat}})\,\%. \tag{3.6}$$

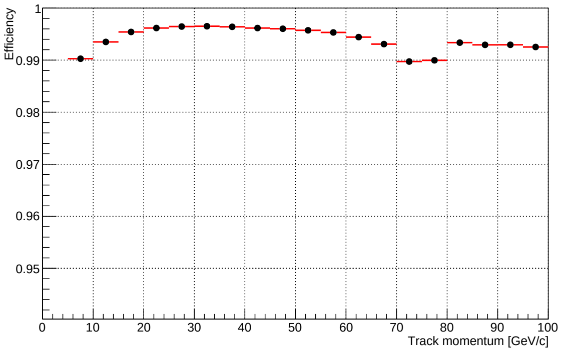

Figure 3.8: CHOD efficiency as a function of muon momentum, integrated over all tiles. The drop in the efficiency at 75 GeV/c momentum is caused by the beam particles passing the selection cuts but missing the actual CHOD acceptance. Similarly, the decrease in efficiency for low momenta is mostly caused by the track extrapolating to outer CHOD tiles, but in reality missing the CHOD acceptance.

4 $K^+ \to \pi^+ \nu \bar{\nu}$ Decay Analysis at NA62

The main goal of the NA62 experiment is the measurement of the branching fraction of an ultra-rare charged kaon decay $K^+ \to \pi^+ \nu \bar{\nu}$ ($K_{\pi\nu\nu}$) at the precision comparable to the Standard Model prediction (section 1.2). The NA62 detector setup is described in section 2.2.

This chapter summarises the measurement of $K_{\pi\nu\nu}$ branching fraction performed on 2016 data sample and presented in the NA62 publication [41]. Although the author did not develop the underlying event selection, he participated in the data taking and introduced tools that helped ensuring high quality of the acquired data, namely the algorithms for measuring the efficiency of MUV3 and CHOD sub-detectors (chapter 3).

4.1 2016 Event Selection

The general signature of the $K_{\pi\nu\nu}$ decay in the NA62 experiment is a detection of an incoming kaon by the KTAG and GTK sub-detectors and registration of an outgoing Straw track identified as a pion. The pair of a neutrino and an anti-neutrino escape undetected.

As it can be seen in Table 1.1, there are several abundant kaon decays that could mimic the signature of $K_{\pi\nu\nu}$ signal if the decay products were not properly identified or if some of the decay products missed the detector acceptance.

Consequently, the $K_{\pi\nu\nu}$ event selection relies on three types of background suppression: kinematic rejection, particle identification and photon veto.

The kinematic suppression involves selecting the $K_{\pi\nu\nu}$ signal in two intervals named *region* 1 (R1) and *region* 2 (R2) of a kinematic variable m^2_{miss} called *squared missing mass*, defined as

$$\begin{aligned} m^2_{\text{miss}} &\equiv \frac{1}{c^2}(P_K - P_\pi)^2, \\ \text{R1: } m^2_{\text{miss}} &\in [0, 0.010]\ \text{GeV}^2/c^4, \\ \text{R2: } m^2_{\text{miss}} &\in [0.026, 0.068]\ \text{GeV}^2/c^4, \end{aligned} \tag{4.1}$$

where P_K is the four-momentum of the decaying kaon and P_π is the four-momentum of the charged decay product under the π^+ mass hypothesis. The theoretical spectrum of the m^2_{miss} for the signal and the main background decay channels as well as regions 1 and 2 used for the $K_{\pi\nu\nu}$ signal search are shown in Fig. 4.1. The signal regions are bounded by the abundant charged kaon decays, namely $K^+ \to \mu^+ \nu_\mu(\gamma)$, $K^+ \to \pi^+ \pi^0(\gamma)$ and $K^+ \to \pi^+ \pi^+ \pi^-$.

During the development of the $K^+ \to \pi^+\nu\bar{\nu}$ decay selections, the signal regions 1 and 2 were blinded together with a neighbouring *control regions* defined in [41]. This was done to ensure the final selection is unbiased.

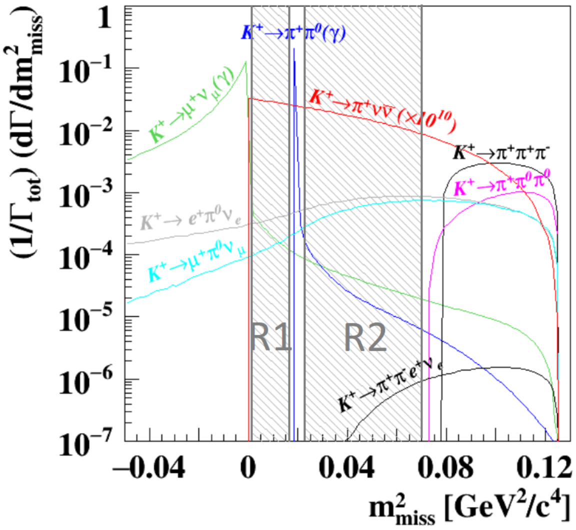

Figure 4.1: Theoretical distributions of m^2_{miss} variable for the signal and the main background decay channels ([41], modified). Charged pion mass [18] hypothesis is assumed for the charged decay product. The signal spectrum is multiplied by 10^{10} for better visibility. The two shaded areas represent the $K_{\pi\nu\nu}$ signal regions.

Radiative components of the $K^+ \to \mu^+\nu_\mu(\gamma)$ and $K^+ \to \pi^+\pi^0(\gamma)$ decay modes as well as the spectra of $K^+ \to \pi^0\mu^+\nu_\mu$, $K^+ \to \pi^0 e^+\nu_e$ and $K^+ \to \pi^+\pi^- e^+\nu_e$ decays enter the signal regions (Fig. 4.1), which poses stringent requirements on the background suppression. Moreover, possible muon-pion misidentification, track momentum mis-reconstruction and accidental activity within the detector could mimic the signal decay if the underlying effects were not properly accounted for.

The main selection criteria used to identify the signal sample are

- At most two reconstructed Straw tracks can be present in the event. If one of them is negative or if the two tracks form a vertex, the event is rejected.
- One well-reconstructed positive Straw track in the geometrical acceptances of RICH, CHOD, NA48-CHOD, LKr, MUV1, MUV2 and MUV3 sub-detectors is required.
- This track has to be geometrically associated to reconstructed candidates in RICH, CHOD, NA48-CHOD and LKr.
- The track momentum is required to be within 15 GeV/c and 35 GeV/c:
  - The lower cut is chosen so the track is well-reconstructed by the Straw and to ensure that the track momentum is above the RICH pion threshold, which allows the use of RICH for positive π^+ identification (Fig. 2.27).
  - The upper cut maximises the π^0 rejection by leaving ~ 40 GeV of energy to

  the π^0 from abundant $K_{2\pi}$ decays (Table 1.1). The photons from $\pi^0 \to \gamma\gamma$ can then be detected with high efficiency.
  - The upper cut also ensures sufficient π^+–μ^+ separation in the RICH (Fig. 2.27) which lowers the probability of $\mu^+ \to \pi^+$ misidentification.

- Signals from downstream detectors are used to compute the π^+ time with the precision of 100 ps.
- KTAG sub-detector is used to verify that the reconstructed π^+ originated from a kaon by requiring there is a well-reconstructed KTAG candidate in-time with the π^+.
- Matching of a GTK track in-time with the KTAG candidate to the Straw track corresponding to π^+ is done using a specialised discriminant dependent on the distance of the closest approach of the two tracks and the π^+ and GTK track times.
- The decay vertex is defined as a midpoint of a line segment spanning the shortest distance between the two lines defined by the GTK and π^+ tracks.
- A two-dimensional cut on the radial distance of the π^+ from the beam line in the first Straw station and the Z position of the decay vertex is performed in order to suppress background originating from early kaon decays and interactions in the material of the GTK sub-detector.
- Pion identification is done with LKr, MUV1, MUV2, MUV3 and RICH sub-detectors:
  - A multivariate classifier using information from LKr, MUV1 and MUV2 detectors was developed to distinguish pions from muons.
  - Hits in the RICH and π^+ momentum measured by the Straw are used to determine the likelihood of different mass hypotheses for the π^+ track.
  - Additionally, RICH hits are fitted with a single ring and the obtained radius is used together with the momentum measured by the Straw to determine the mass of the π^+ candidate. A cut on this mass is applied to improve the π^+ identification further.
  - Presence of no reconstructed MUV3 candidate in-time with the π^+ is required.
- Photon veto detectors LAV, IRC, SAC and LKr are used to suppress background from decays producing photons either as primary decay products, from π^0 decays or as radiative photons.
- Events with photon interactions upstream of the LKr are identified by the multiplicity rejection, which correlates the activity in downstream sub-detectors unrelated to the π^+.

The overall π^+ identification efficiency is measured to be 64%, while the probability of $\mu^+ \to \pi^+$ misidentification is $\mathcal{O}(10^{-8})$.

Figure 4.2 shows two-dimensional distribution of the m^2_{miss} as a function of the π^+ momentum (under the π^+ mass hypothesis) for events passing the described selection without applying the π^+ identification and photon rejection [41]. Signal regions are shown using red boxes. The regions corresponding to the three main background sources are indicated by black boxes. Control regions are bounded by dashed lines.

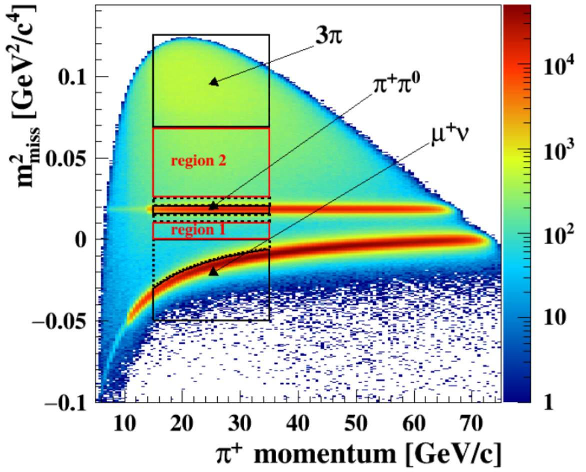

Figure 4.2: m^2_{miss} as a function of the π^+ momentum for events defined in the text.

4.2 Result from 2016 Data Sample

The number of kaon decays N_K registered in the analysed data sample, collected in approximately one month of data taking in 2016, was computed using the number $N(K_{2\pi})$ of selected events from the normalisation channel $K_{2\pi}$

$$N_K = \frac{N(K_{2\pi}) \cdot D}{A(K_{2\pi}) \cdot \mathcal{B}(K_{2\pi})} = (1.21 \pm 0.04_{\text{syst}}) \times 10^{11}, \tag{4.2}$$

where D is the downscaling factor of the trigger used to select the normalisation sample (Control trigger, see subsection 2.2.11), $A(K_{2\pi})$ is the acceptance of the $K_{2\pi}$ selection evaluated using $K_{2\pi}$ MC sample and $\mathcal{B}(K_{2\pi})$ is the $K_{2\pi}$ branching fraction [18]. The quoted systematic uncertainty comes mainly from error on $A(K_{2\pi})$ and dependence of N_K on the π^+ momentum.

The single event sensitivity SES, defined as

$$SES = \frac{1}{N_K \cdot \varepsilon(K_{\pi\nu\nu})},$$
$$\varepsilon(K_{\pi\nu\nu}) = A(K_{\pi\nu\nu}) \cdot \varepsilon_{\text{trigger}} \cdot \varepsilon_{\text{RV}}, \tag{4.3}$$

where $A(K_{\pi\nu\nu})$ is the acceptance of the $K_{\pi\nu\nu}$ selection evaluated on $K_{\pi\nu\nu}$ MC sample,

$\varepsilon_{\text{trigger}}$ is the efficiency of a trigger dedicated to select $K_{\pi\nu\nu}$ events and $1-\varepsilon_{\text{RV}}$ is the probability of signal events being discarded by photon and multiplicity rejections due to accidental activity in the detector (see [41] for more details), is equal to

$$SES = (3.15 \pm 0.01_{\text{stat}} \pm 0.24_{\text{syst}}) \times 10^{-10} \ . \tag{4.4}$$

Assuming the most recent Standard Model prediction for the $K_{\pi\nu\nu}$ branching fraction (Eq. 1.7), the expected number of signal $N^{\text{expected, SM}}_{\pi\nu\nu}$ and background $N^{\text{expected}}_{\text{background}}$ events in signal regions R1 and R2 combined, is

$$\begin{aligned} N^{\text{expected, SM}}_{\pi\nu\nu} &= 0.267 \pm 0.001_{\text{stat}} \pm 0.020_{\text{syst}} \pm 0.032_{\text{ext}}, \\ N^{\text{expected}}_{\text{background}} &= 0.152^{+0.092}_{-0.033}|_{\text{stat}} \pm 0.013_{\text{syst}}, \end{aligned} \tag{4.5}$$

where the dominant background contribution comes from the $K^+ \to \pi^+\pi^0(\gamma)$ and upstream kaon decays.

After unblinding the signal regions, *one event* is observed in region 2 with the π^+ momentum equal to 15.3 GeV/c and RICH hits clearly compatible with the pion hypothesis, as shown in Fig. 4.3.

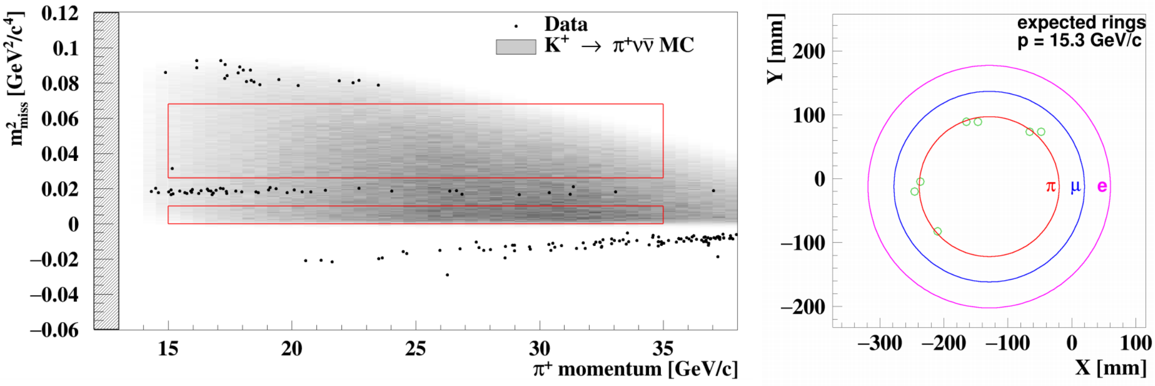

Figure 4.3: Left: m^2_{miss} as a function of the π^+ momentum for events passing the final $K_{\pi\nu\nu}$ selection. Signal regions are shown using red rectangles. One signal event is observed in region 2. Right: RICH rings corresponding to different mass hypotheses (red, blue, magenta) and positions of RICH hits associated to the π^+ track, [41].

The observed upper limit of the $K_{\pi\nu\nu}$ branching fraction at 95% confidence level is

$$\mathcal{B}(K^+ \to \pi^+\nu\bar{\nu}) < 14 \times 10^{-10} \ . \tag{4.6}$$

4.3 Prospects for the Future

The presented $K^+ \to \pi^+\nu\bar{\nu}$ analysis was performed on $\sim 2\%$ of the overall NA62 data sample collected in years 2016 to 2018. It is expected that further improvements to the detector performance and design, especially the installation of shielding in 2017 and an upstream collimator in 2018 will allow for certain cuts in the selection to be revised in order to increase the signal acceptance without decreasing the signal over background ratio.

The current result can be viewed as a validation of the new technique of $\mathcal{B}(K^+ \to \pi^+\nu\bar{\nu})$ measurement using kaon decays in-flight. The NA62 Collaboration has high hopes in achieving the initial goal of measuring the $K_{\pi\nu\nu}$ branching fraction to $\mathcal{O}(10\%)$ precision.

Conclusions

The presented thesis focused on the measurement of form factor parameters and branching fraction of a rare charged kaon decay $K^+ \to \pi^+\mu^+\mu^-$ ($K_{\pi\mu\mu}$) at the NA62 experiment at CERN using a subset of 2017 data sample.

In chapter 2, we have given a description of the NA62 detector setup, discussed our event selections used to collect $K_{\pi\mu\mu}$ signal and $K^+ \to \pi^+\pi^+\pi^-$ normalisation events, and presented results of the $K^+ \to \pi^+\mu^+\mu^-$ analysis motivated in chapter 1. The $K^+ \to \pi^+\mu^+\mu^-$ form factor can be described in terms of two low energy constants a and b, which were measured to be

$$\begin{aligned} a &= -0.564 \pm 0.034_{\text{stat}} \pm 0.024_{\text{syst}} \pm 0.001_{\text{ext}} = -0.564 \pm 0.042, \\ b &= -0.797 \pm 0.118_{\text{stat}} \pm 0.114_{\text{syst}} \pm 0.003_{\text{ext}} = -0.797 \pm 0.164, \end{aligned}$$

which gives the model-dependent $K_{\pi\mu\mu}$ branching fraction equal to

$$\mathcal{B}(K_{\pi\mu\mu}) \times 10^8 = 9.32 \pm 0.17_{\text{stat}} \pm 0.23_{\text{syst}} \pm 0.04_{\text{ext}} = 9.32 \pm 0.29\ .$$

The statistical errors are dominated by the limited $K_{\pi\mu\mu}$ signal sample of 3074 event candidates. The largest contributions to systematic uncertainties are estimates of Straw reconstruction and trigger efficiency effects. The obtained results are in agreement with the previous measurement performed at the NA48/2 and with the world average.

The presented analysis was performed on the dataset collected in a period of one month and the selected $K_{\pi\mu\mu}$ signal sample is comparable in size to the total NA48/2 $K_{\pi\mu\mu}$ sample. Additionally, approximately 10-times lower background in our $K_{\pi\mu\mu}$ sample compared to the NA48/2, is observed. Once the full available dataset, collected in 2017 and 2018, is analysed we estimate that the total $K_{\pi\mu\mu}$ sample will be more than 5-times larger than in the current analysis. The two most important systematic effects are currently being studied. After they are resolved, the NA62 experiment should produce a world-leading $K_{\pi\mu\mu}$ results.

In addition to the theoretical description of the rare $K_{\pi\mu\mu}$ decay, chapter 1 also explained the motivation for the primary NA62 measurement of the branching fraction of an ultra-rare charged kaon decay $K^+ \to \pi^+\nu\bar{\nu}$ ($K_{\pi\nu\nu}$). Chapter 4 summarises the first published result of the $K_{\pi\nu\nu}$ analysis on 2016 data sample, in which one $K_{\pi\nu\nu}$ candidate event was observed and an upper limit on the $K_{\pi\nu\nu}$ branching fraction, compatible with the Standard Model predictions, was given.

Chapter 3 summarised the measurements of MUV3 and CHOD sub-detector efficiencies performed during the first two years of author's PhD studies. The obtained efficiencies are above 99%.

A CKM Matrix and Unitarity Triangle

The CKM matrix V_{CKM} was proposed by Kobayashi and Maskawa [33] in 1973. Being a 3×3 unitary matrix, it can be parametrised with three real angles and one complex phase (Eq. A.2) and is responsible for the mixing between the strong (mass) quark eigenstates d, s, b and the weak eigenstates d', s', b'

$$\begin{bmatrix} d' \\ s' \\ b' \end{bmatrix} = V_{\text{CKM}} \begin{bmatrix} d \\ s \\ b \end{bmatrix} = \begin{bmatrix} V_{ud} & V_{us} & V_{ub} \\ V_{cd} & V_{cs} & V_{cb} \\ V_{td} & V_{ts} & V_{tb} \end{bmatrix} \begin{bmatrix} d \\ s \\ b \end{bmatrix} . \tag{A.1}$$

In terms of the three Euler angles $\theta_{12}, \theta_{23}, \theta_{13}$ and a complex phase δ, the CKM matrix reads ($c_{ij} = \cos(\theta_{ij})$ and $s_{ij} = \sin(\theta_{ij})$) [18]

$$V_{\text{CKM}} = \begin{bmatrix} c_{12}c_{13} & s_{12}c_{13} & s_{13}e^{-i\delta} \\ -s_{12}c_{23} - c_{12}s_{23}s_{13}e^{i\delta} & c_{12}c_{23} - s_{12}s_{23}s_{13}e^{i\delta} & s_{23}c_{13} \\ s_{12}s_{23} - c_{12}c_{23}s_{13}e^{i\delta} & -c_{12}s_{23} - s_{12}c_{23}s_{13}e^{i\delta} & c_{23}c_{13} \end{bmatrix} . \tag{A.2}$$

The unitarity of the CKM matrix leads to the following 12 relations

$$\begin{aligned} \sum_{j\in\{d,s,b\}} V_{ij}V_{kj}^* &= \delta_{ik}, & i,k &\in \{u,c,t\}, \\ \sum_{j\in\{u,c,t\}} V_{ji}^*V_{jk} &= \delta_{ik}, & i,k &\in \{d,s,b\} . \end{aligned} \tag{A.3}$$

One of the vanishing relations,

$$V_{ud}V_{ub}^* + V_{cd}V_{cb}^* + V_{td}V_{tb}^* = 0, \tag{A.4}$$

is usually used to draw the CKM unitarity triangle. This triangle is obtained from Eq. A.4 by dividing the whole equation by $V_{cd}V_{cb}^*$, thus obtaining

$$\frac{V_{ud}V_{ub}^*}{V_{cd}V_{cb}^*} + 1 + \frac{V_{td}V_{tb}^*}{V_{cd}V_{cb}^*} = 0 . \tag{A.5}$$

One can then introduce new real parameters $\overline{\rho}$ and $\overline{\eta}$ defined from Eq. A.5

$$1 + \frac{V_{td}V_{tb}^*}{V_{cd}V_{cb}^*} = -\frac{V_{ud}V_{ub}^*}{V_{cd}V_{cb}^*} \equiv \overline{\rho} + i\overline{\eta} . \tag{A.6}$$

Magnitude of parameter $\overline{\eta}$ fully determines the amount of direct CP violation. Equation A.6 represents a triangle in the complex plane with vertices (0, 0), (1,

0) and $(\overline{\rho}, \overline{\eta})$, see Fig. A.1. The corresponding angles α, β and γ are

$$\alpha = \arg\left(-\frac{V_{td}V_{tb}^*}{V_{cd}V_{cb}^*}\right), \qquad \beta = \arg\left(-\frac{V_{cd}V_{cb}^*}{V_{cd}V_{cb}^*}\right), \qquad \gamma = \arg\left(-\frac{V_{ud}V_{ub}^*}{V_{cd}V_{cb}^*}\right) \,. \tag{A.7}$$

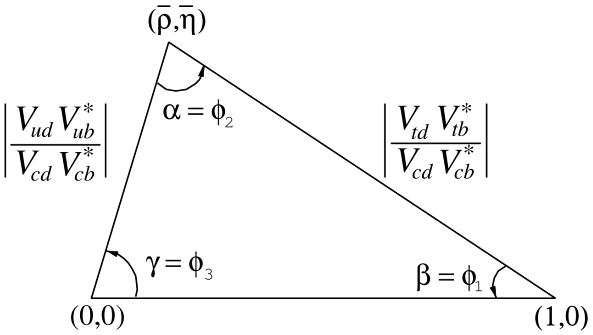

Figure A.1: CKM unitarity triangle [18].

Experimental measurements of the CKM matrix elements and verification of its unitarity are of great interest to current particle physics. The results of the most recent fit are shown in Fig. A.2.

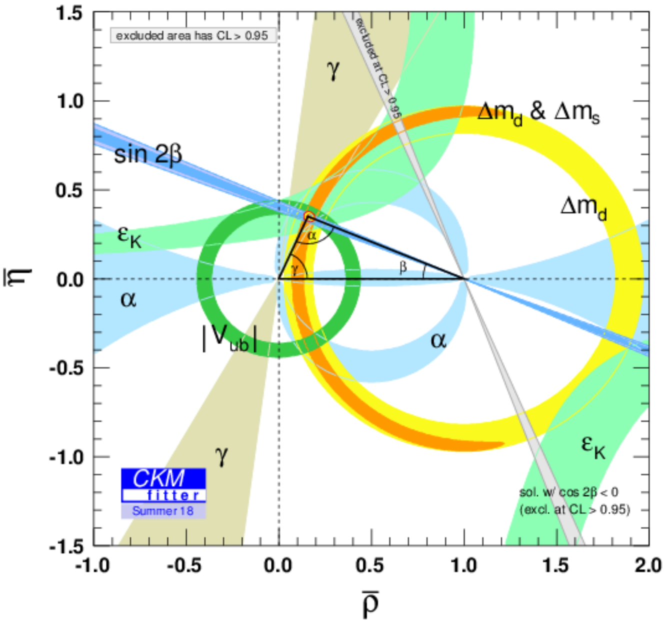

Figure A.2: Experimental constraints on the CKM unitarity triangle [98].

B Form Factor Fitting Procedure

B.1 Motivation

In this appendix a fitting procedure used to determine the form factor parameters a and b of the $K^+ \to \pi^+\mu^+\mu^-$ ($K_{\pi\mu\mu}$) decay is described. Both parameters are evaluated simultaneously using a χ^2-like test statistic based on the Pearson's χ^2 test presented in [99] and expanded in [100]. However, the test statistics used in the cited literature are not sensitive to the overall normalisation of the two histograms being compared, since the used "consistency checks" are based solely on probabilities of events falling into various bins in the two histograms, disregarding the overall normalisations of the compared histograms.

Our aim is to determine both form factor parameters in a single fit. Therefore, the test statistic derived for the presented form factor fitting procedure has to be sensitive to the shape as well as the normalisation of the two compared histograms, since the $K_{\pi\mu\mu}$ form factor parameters determine both shape of the $\mathrm{d}\Gamma/\mathrm{d}z$ and the total $K_{\pi\mu\mu}$ branching fraction.

B.2 Description of the Procedure

Since the form factor $W(z)$ does not depend on the kinematic variable x defined in subsection 1.3.2, the fitting involves only one-dimensional histograms in the kinematic variable z.

The following quantities are needed as an input to the fitting procedure:

- Vectors z_{DATA} and d_{DATA} for all events passing the $K_{\pi\mu\mu}$ selection criteria, containing a total number of $N_{\pi\mu\mu}^{\mathrm{DATA}}$ reconstructed values of z and their corresponding trigger downscale factors, respectively.
- Vector z_{MC} ($z_{\mathrm{MC}}^{\mathrm{truth}}$), which is an equivalent vector containing reconstructed (true) z values of all MC events passing the selection, generated at an arbitrary point in the $a-b$ plane: $(a_{\mathrm{NA62\ MC}}, b_{\mathrm{NA62\ MC}})$.
- The total number of $K_{\pi\mu\mu}$ MC events generated in the fiducial decay region defined in the standard selection is $N_{\pi\mu\mu}^{\mathrm{generated}}$.
- The total $K_{3\pi}$ acceptance $A(K_{3\pi})$.
- Each $K_{3\pi}$ data event is weighted by the downscale factor of the Multi-track trigger chain. The sum of these weights is $N(K_{3\pi})$. The $K_{3\pi}$ branching fraction is $\mathcal{B}(K_{3\pi})$ (Table 1.1).

- The $K_{\pi\mu\mu}$ decay branching fraction $\mathcal{B}(K_{\pi\mu\mu})(a, b)$ for any tested values of a and b is computed as a numerical integral of Eq. 1.31 divided by the total K^+ decay width [18].

The vector z_{DATA} of data events is used to fill a weighted histogram h_{DATA}, with the weights equal to the downscale factor of the Di-muon trigger stream. It can be seen from Fig. 1.9 and Fig. B.1 that both the differential decay width and the signal acceptance approach zero for high z values. This implies that if all bins of h_{DATA} were of equal size, some bins in high-z region would contain low statistics[1]. However, the χ^2 tests assume Gaussian errors on bin contents, which is not satisfied for bins with low number of events.

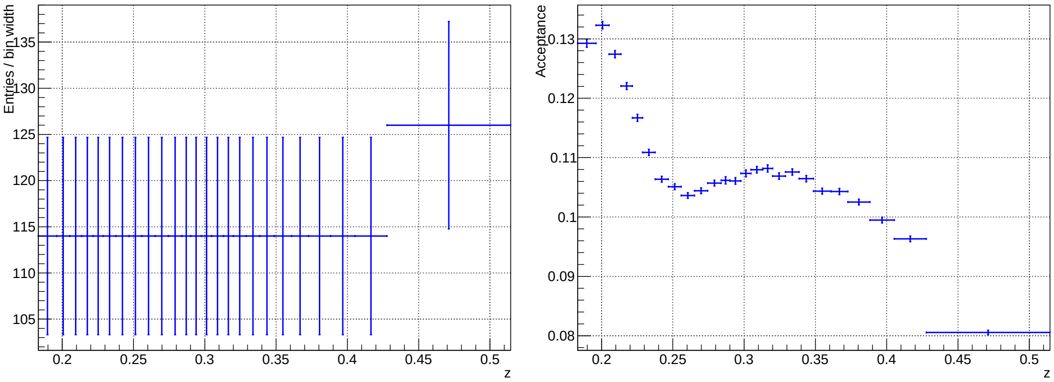

Figure B.1: *Example* of an (almost) equipopulous DATA histogram h_{DATA} (left) and the $K_{\pi\mu\mu}$ signal acceptance displayed in the same binning as h_{DATA} (right).

We correct for this by splitting the z_{DATA} vector into r sub-sets of (almost) equal size and setting the bin edges of h_{DATA} so that each bin contains one of these sub-sets. This way we obtain histogram h_{DATA} with (almost) equipopulous bins, similar to the one showed in Fig. B.1. The information about the shape of the underlying distribution is thus translated into the positions of bin edges.

The role of the $K_{\pi\mu\mu}$ MC sample in the form factor fitting procedure is discussed in the rest of this section. As it is not feasible to generate sufficiently large MC samples for every conceivable point in the $a - b$ plane, we use the reweighting technique: at every step of the minimisation of our test statistic (for each tested a and b) another histogram $h_{\mathrm{MC}}(a, b)$ of the same binning as h_{DATA} is filled with weighted events from the MC vector z_{MC} containing *reconstructed* MC z values. The aim of the discussed procedure is to find such values of a and b, in which both the shape and normalisation of the h_{DATA} and $h_{\mathrm{MC}}(a, b)$ histograms are consistent.

The reweighting of the MC histogram $h_{\mathrm{MC}}(a, b)$ is done event-by-event using the weight function

$$w_i(a, b) = \frac{\mathrm{d}\Gamma({z^{\mathrm{truth}}_{\mathrm{MC}}}_i, a, b)}{\mathrm{d}\Gamma({z^{\mathrm{truth}}_{\mathrm{MC}}}_i, a_{\mathrm{NA62\ MC}}, b_{\mathrm{NA62\ MC}})}, \tag{B.1}$$

---

[1] Of course, the expression "low statistics" is a little ambiguous, since it depends on the size of bins.

where ${z_{\mathrm{MC}}^{\mathrm{truth}}}_i$ is the i-th component of the $z_{\mathrm{MC}}^{\mathrm{truth}}$ vector.

In order to speed up the fitting as much as possible, the denominator in Eq. B.1 is precomputed for every ${z_{\mathrm{MC}}^{\mathrm{truth}}}_i$ before the actual fitting begins, since it does not depend on the tested (a, b) point. Additionally, the numerator can be rewritten as

$$\mathrm{d}\Gamma({z_{\mathrm{MC}}^{\mathrm{truth}}}_i, a, b) = \frac{\alpha^2 M_K}{8\pi(4\pi)^4} \left[\int\limits_{x_{\min}(z)}^{x_{\max}(z)} f(x,z)\mathrm{d}x \right] \times |W(z,a,b)|^2 \Bigg|_{z={z_{\mathrm{MC}}^{\mathrm{truth}}}_i}, \tag{B.2}$$

where $x_{\min}(z)$ and $x_{\max}(z)$ are minimal and maximal values of kinematic variable x for a particular value of z (see Fig. 1.8 for illustration). Function $f(x, z)$ is equal to

$$f(x,z) = \eta(x,z) \prod_{\substack{i,j=1,2,3 \\ i\neq j}} \Omega(s_{ij}(x,z)), \tag{B.3}$$

with $\eta(x, z)$ and $\Omega(s_{ij}(x, z))$ defined in Eq. 1.30 and Eq. 1.32, respectively. The squared norm $|W(z, a, b)|^2$ of the $K_{\pi\mu\mu}$ form factor is written as

$$|W(z,a,b)|^2 = g_0(a) + g_1(a,b)z + g_2(b)z^2, \tag{B.4}$$

where

$$\begin{aligned} g_0(a) &= W_{\mathrm{Re}}^2(z) + W_{\mathrm{Im}}^2(z) + 2aW_{\mathrm{Re}}(z)G_F M_K^2 + a^2 G_F^2 M_K^4, \\ g_1(a,b) &= 2bW_{\mathrm{Re}}(z)G_F M_K^2 + 2abG_F^2 M_K^4, \\ g_2(b) &= b^2 G_F^2 M_K^4, \end{aligned} \tag{B.5}$$

with $W_{\mathrm{Re}}(z)$ and $W_{\mathrm{Im}}(z)$ being real and imaginary parts of $W^{\pi\pi}(z)$ defined in Eq. 1.36, respectively.

The integral of $f(x, z)$ in Eq. B.2 is also evaluated for each element in the $z_{\mathrm{MC}}^{\mathrm{truth}}$ vector before the fitting. Using these steps, the weight $w_i(a, b)$ can be obtained by simple (and computationally fast) multiplication and division instead of multiple time-consuming numerical integrations.

Final step that needs to be performed before h_{DATA} and $h_{\mathrm{MC}}(a, b)$ can be compared is the scaling of $h_{\mathrm{MC}}(a, b)$. At this stage, the integral of $h_{\mathrm{MC}}(a, b)$ is equal to the sum of all event weights $w_i(a, b)$, which is generally a large number, comparable to the size of the $K_{\pi\mu\mu}$ MC sample.

Our goal however, is to normalise $h_{\mathrm{MC}}(a, b)$ to the number of $K_{\pi\mu\mu}$ events one would expect based on the tested (a, b) point and the number of $K_{3\pi}$ events observed in data $(N(K_{3\pi}))$. This can be achieved by first calculating:

- the number of kaon decays in data using $N(K_{3\pi})$, $\mathcal{B}(K_{3\pi})$ and $A(K_{3\pi})$:

$$N_K^{\mathrm{DATA}} = \frac{N(K_{3\pi})}{\mathcal{B}(K_{3\pi}) \cdot A(K_{3\pi})}, \tag{B.6}$$

- the number of kaon decays corresponding to the generated $K_{\pi\mu\mu}$ decays $N_{\pi\mu\mu}^{\mathrm{generated}}$ using $\mathcal{B}(K_{\pi\mu\mu})(a_{\mathrm{MC}}, b_{\mathrm{MC}})$:

$$N_K^{\mathrm{MC}} = N_{\pi\mu\mu}^{\mathrm{generated}} / \mathcal{B}(K_{\pi\mu\mu})(a_{\mathrm{MC}}, b_{\mathrm{MC}}) \ . \tag{B.7}$$

Next we define the MC scaling factor

$$s = N_K^{\mathrm{DATA}} / N_K^{\mathrm{MC}}, \tag{B.8}$$

which is then used to scale the $h_{\mathrm{MC}}(a, b)$ histogram

$$\int h_{\mathrm{MC}}(a, b) \to s \times \int h_{\mathrm{MC}}(a, b) \ . \tag{B.9}$$

Taking these precise steps to normalise $h_{\mathrm{MC}}(a, b)$ takes care of the fact that different (a, b) points change kinematics of the $K_{\pi\mu\mu}$ decay, which consequently changes the overall signal acceptance. Normalising to the number of kaons decaying in the fiducial region ensures that any change in acceptance is automatically taken into account by the previously described MC reweighting technique.

B.3 Derivation of the X^2 Test Statistic

In this subsection we will derive the χ^2-like test statistic denoted X^2 used for testing the hypothesis that the histograms h_{DATA} and $h_{\mathrm{MC}}(a, b)$ come from the same distribution and are consistent in normalisation.

Let the sum of weights in the j-th bin of the h_{DATA} histogram with r bins be n_j, the sum of squares in the same bin be s_j^2, the total sum of weights in all of the bins in h_{DATA} be N and the total sum of squares of weights in all of the bins in h_{DATA} be S^2.

Furthermore, for a particular currently tested pair of values a and b, let the sum of weights in j-th bin of the $h_{\mathrm{MC}}(a, b)$ histogram be m_j, the sum of squares of weights in the same bin be q_j^2, the total sum of weights in all of the bins in $h_{\mathrm{MC}}(a, b)$ be M and the total sum of squares of weights in all of the bins in $h_{\mathrm{MC}}(a, b)$ be Q^2.

If the hypothesis that h_{DATA} and $h_{\mathrm{MC}}(a, b)$ are from the same distribution and are consistent in normalisation is true, there exists a r-dimensional vector $\mathbf{p}$ of constants

p_j, for which $\sum\limits_{j=1}^{r} p_j = 1$, and a number $K \in \mathbb{R}^+$ such that

$$\begin{aligned}
P(n_j|p_j, N) &= \frac{1}{\sqrt{2\pi s_j^2}} \exp\left[-\frac{(n_j - Np_j)^2}{2s_j^2}\right], \\
P(m_j|p_j, M) &= \frac{1}{\sqrt{2\pi q_j^2}} \exp\left[-\frac{(m_j - Mp_j)^2}{2q_j^2}\right], \\
P(N|K) &= \frac{1}{\sqrt{2\pi S^2}} \exp\left[-\frac{(N - K)^2}{2S^2}\right], \\
P(M|K) &= \frac{1}{\sqrt{2\pi Q^2}} \exp\left[-\frac{(M - K)^2}{2Q^2}\right], \qquad \text{(B.10)}
\end{aligned}$$

where we assumed normal distributions for the sum of weights in h_{DATA} and h_{MC}.

We can write the total probability of observing sum of weights n_j in j-th bin in h_{DATA} and simultaneously obtaining the sum of weights m_j in j-th bin in $h_{\text{MC}}(a, b)$ as

$$\begin{aligned}
P(n_j, m_j|p_j, K) &= P(n_j|p_j, K) \cdot P(m_j|p_j, K) \\
&= [P(n_j|p_j, N)P(N|K)] \cdot [P(m_j|p_j, M)P(M|K)] \,.
\end{aligned}$$

Multiplying over all bins while keeping the $P(N|K)$ and $P(M|K)$ probabilities out of the product, one gets the probability of observing all the values $\mathbf{n}$ in h_{DATA} and $\mathbf{m}$ in $h_{\text{MC}}(a, b)$

$$P(\mathbf{n}, \mathbf{m}|\mathbf{p}, K) = \left[\prod_{j=1}^{r} P(n_j|p_j, N)P(m_j|p_j, M)\right] P(N|K)P(M|K). \qquad \text{(B.11)}$$

Using Eq. B.11, the likelihood for parameters $\mathbf{p}$ and K given the observed values $\mathbf{n}$ and $\mathbf{m}$ is

$$\mathcal{L}(\mathbf{p}, K|\mathbf{n}, \mathbf{m}) = P(\mathbf{n}, \mathbf{m}|\mathbf{p}, K). \qquad \text{(B.12)}$$

Taking the natural logarithm of Eq. B.12 and differentiating with respect to p_j and K, one obtains maximum likelihood estimators $\hat{p_j}$ and $\hat{K}$ equal to

$$\hat{p_j} = \frac{Nn_jq_j^2 + Mm_js_j^2}{N^2q_j^2 + M^2s_j^2} \xrightarrow[q_j^2 \to 0]{} \frac{m_j}{M}, \qquad \hat{K} = \frac{N\sum\limits_{j=1}^{r} q_j^2 + M\sum\limits_{j=1}^{r} s_j^2}{\sum\limits_{j=1}^{r} q_j^2 + \sum\limits_{j=1}^{r} s_j^2} \xrightarrow[q_j^2 \to 0]{} M, \qquad \text{(B.13)}$$

where the limit $q_j^2 \to 0$ is equivalent to the limit of *large* $K_{\pi\mu\mu}$ MC sample: scaling $h_{\text{MC}}(a, b)$ filled with large number of events down to the value similar to N causes the bin errors q_j to approach zero. The obtained limits on on $\hat{p_j}$ and $\hat{K}$ are dominated by MC contributions m_j and M, which is intuitively sensible.

It is worth noting that the estimator $\hat{p_j}$ is the same as in [100] and is the one used in the `TH1::Chi2Test(...)` in the `ROOT` library [83]. By doing this calculation however, we gained the additional estimator $\hat{K}$ for the normalisation. Following the example of [100], we may propose a test statistic

$$X^2 = \sum_{j=1}^{r} \left[\frac{(n_j - N\hat{p_j})^2}{s_j^2} + \frac{(m_j - M\hat{p_j})^2}{q_j^2} \right] + \frac{(N - \hat{K})^2}{S^2} + \frac{(M - \hat{K})^2}{Q^2} \ , \qquad \text{(B.14)}$$

which should approximately follow the $\chi^2_{(r-2)}$ distribution.

The minimisation of X^2 is done using `ROOT` class `TMinuit`, which is a C++ implementation of the Fortran `MINUIT` package developed by Fred James [101].

B.4 Validating the X^2 Test Statistic

The proposed X^2 test statistic was validated on the official NA62 $K_{\pi\mu\mu}$ and $K_{3\pi}$ MC samples. Acceptances of both $K_{\pi\mu\mu}$ and $K_{3\pi}$ selections were calculated from these samples. For the purpose of this test, all relevant trigger efficiencies were assumed to be equal to unity[2].

The fitting algorithm was checked for bias using 10k pseudo-experiments. In each pseudo-experiment, the $K_{\pi\mu\mu}$ MC events passing the standard $K_{\pi\mu\mu}$ selection were randomly split into 2 sub-samples:

- A sub-sample of N_D events was selected and treated as “data” events with which the h_DATA histogram was filled. The value of N_D was chosen randomly from a Poisson distribution with mean 3000, which represented a good estimate of the number of $K_{\pi\mu\mu}$ events expected in the anlyzed NA62 data sample.
- The rest of the events were treated as a real MC sample used for filling the $h_\text{MC}(a, b)$ histogram during fitting.

In order to emulate the fact that the *true* form factor parameters given by Nature differ from those used in the MC sample generation, we randomly selected a_true and b_true for each pseudo-experiment. Both parameters were drawn independently (disregarding correlations) from Gaussian distributions with means and standard deviations equal to the values measured by NA48/2 [74] and shown in Eq. 1.38.

All events in the “data” sub-sample of size N_D were then reweighted using Eq. B.1 to match the chosen parameters a_true and b_true. The number of equipopulous bins of h_DATA was chosen to be 15, which implies the test statistic X^2 should follow the χ^2_{13} distribution. The sum of weights of h_DATA was equal to N.

---

[2] This does not affect the validation of the fitting procedure, since in the actual fit of NA62 data, the trigger efficiencies were applied on MC using trigger-emulator-based accept/reject method, which means they are parts of the $K_{\pi\mu\mu}$ and $K_{3\pi}$ acceptances.

The number of observed $K_{3\pi}$ events ($N(K_{3\pi})$), which comes to our actual analysis of the NA62 $K_{\pi\mu\mu}$ data sample as a separate normalisation input, had to be computed for each pseudo-experiment using N, $\mathcal{B}(K_{3\pi})$, $A(K_{\pi\mu\mu})(z)$, $A(K_{3\pi})$ and $\mathrm{d}\Gamma(z, a_{\mathrm{true}}, b_{\mathrm{true}})/\mathrm{d}z$. To achieve this, some approximations were necessary. Remembering our assumption that all trigger efficiencies are equal to unity, $N(K_{3\pi})$ is precisely equal to

$$N(K_{3\pi}) = \mathcal{B}(K_{3\pi}) \cdot A(K_{3\pi}) \cdot N_K, \tag{B.15}$$

where N_K is the number of kaon decays obtainable from N, $A(K_{\pi\mu\mu})(z)$ and $\mathrm{d}\Gamma/\mathrm{d}z$ in the following way

$$N_K = \frac{N}{\int A(K_{\pi\mu\mu})(z) \cdot \frac{1}{\Gamma_K} \cdot \frac{\mathrm{d}\Gamma(z, a_{\mathrm{true}}, b_{\mathrm{true}})}{\mathrm{d}z} \mathrm{d}z} \equiv \frac{N}{\int A(K_{\pi\mu\mu})(z) \cdot \mathcal{B}(z, a_{\mathrm{true}}, b_{\mathrm{true}}) \mathrm{d}z}, \tag{B.16}$$

with Γ_K being the total K^+ decay width [18].

The integral in Eq. B.16 is the place where approximations need to be made. Since the acceptance function is only known in bins of z as shown in Fig. B.1 and *not* as a continuous function, the integral cannot be evaluated precisely. Instead, we computed it as a sum over bins in z

$$\int A(K_{\pi\mu\mu})(z) \cdot \mathcal{B}(z, a_{\mathrm{true}}, b_{\mathrm{true}}) \mathrm{d}z = \sum_{j=1}^{r} \left[A_j \cdot \int\limits_{z_j^{\mathrm{low}}}^{z_j^{\mathrm{high}}} \mathcal{B}(z, a_{\mathrm{true}}, b_{\mathrm{true}}) \mathrm{d}z \right], \tag{B.17}$$

where z_j^{low} and z_j^{high} are positions of j-th bin edges, and A_j is the value of the $K_{\pi\mu\mu}$ acceptance histogram (Fig. B.1) in bin j.

The obtained number $N(K_{3\pi})$ was then smeared using Poisson distribution to simulate random fluctuations of the number of observed $K_{3\pi}$ decays around the expected value.

For each pseudo-experiment, the fitting started at point $(a, b) = (-2, -2)$. This point was chosen because it lies several standard deviations from the central (a, b) point given by Eq. 1.38 and so it also lies sufficiently far from the chosen point $(a_{\mathrm{true}}, b_{\mathrm{true}})$ (which should be the local minimum of X^2), thus mitigating the risk of introducing bias by starting too close to the minimum.

The fitting algorithm was validated by investigating several quantities plotted in Figs. B.2, B.3, B.4 and Fig. B.5:

- The difference between the fitted values a_{fit} and b_{fit} and the true values a_{true} and b_{true} was examined and is shown in Fig. B.2.
- Parameter pulls[3], shown in Fig. B.3, were used to test for bias in fit error estimation,

---

[3] Pull of a parameter fit is defined as the difference between the fitted and the true value of the parameter, divided by the parameter fit error.

since the pull of an unbiased fit should follow the $\mathcal{N}(0,1)$ distribution.

- Normalisation of $h_{\mathrm{MC}}(a,b)$ at the fitted (a,b) point was computed and compared to the h_{DATA} normalisation equal to N (Fig. B.4). The aim of this step was to verify that, on average, the fitting converges to such point in the $a-b$ plane, in which the data and MC histograms have similar normalisations.
- Values of the X^2 statistic at the acquired minima for each pseudo-experiment are shown in Fig. B.5. The resulting spectrum was fitted with the χ^2_{ndf} function. As expected, the X^2 test statistic is compatible with a χ^2_{13} distribution.

Overall, we found the proposed X^2 test statistic to be reasonably unbiased and suitable for the use in the actual fitting of the $K^+ \to \pi^+\mu^+\mu^-$ form factor parameters.

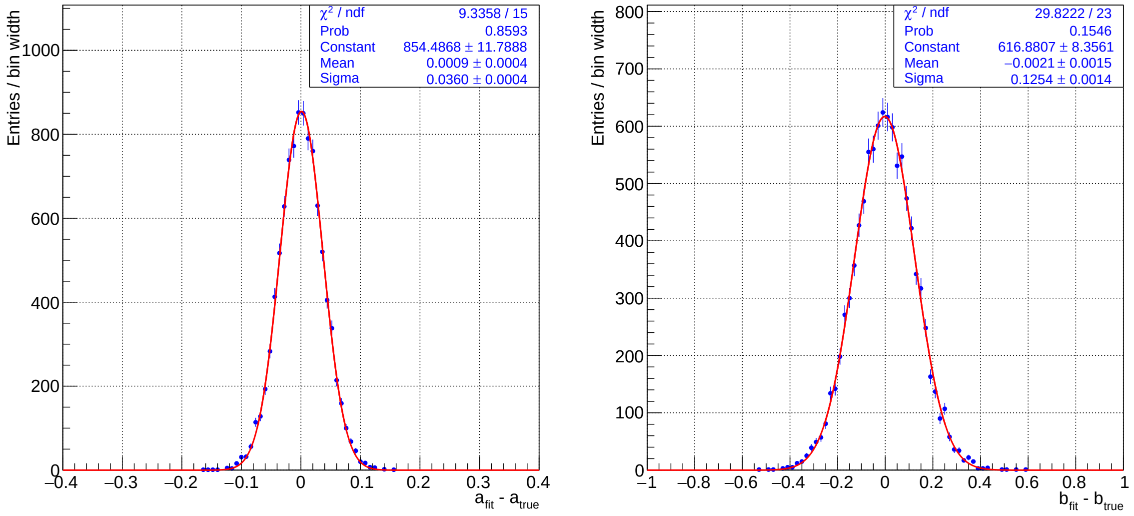

Figure B.2: Distribution of the difference between the fitted and real a (left) and b (right) form factor parameters.

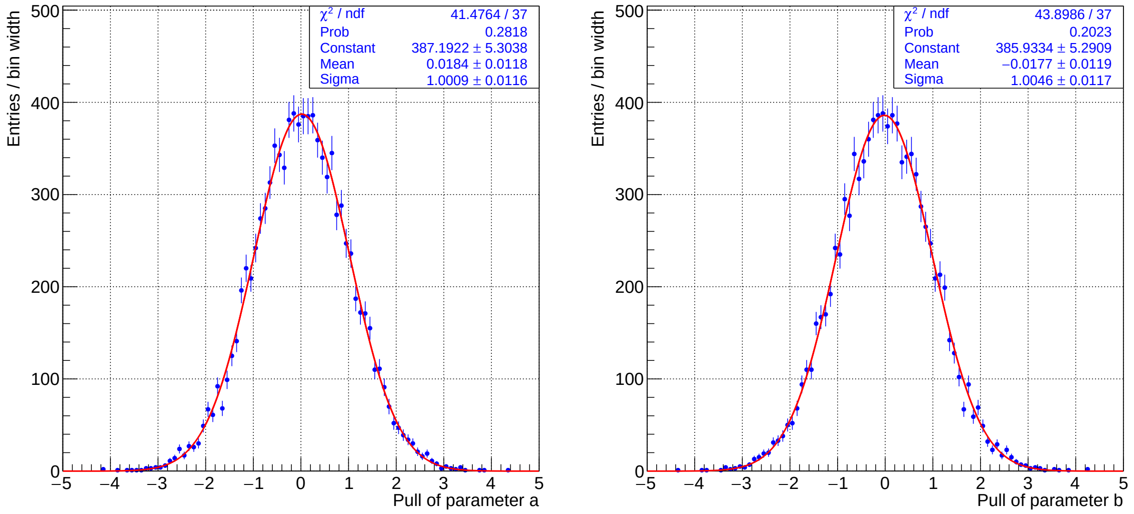

Figure B.3: Pull distribution for parameter a (left) and b (right).

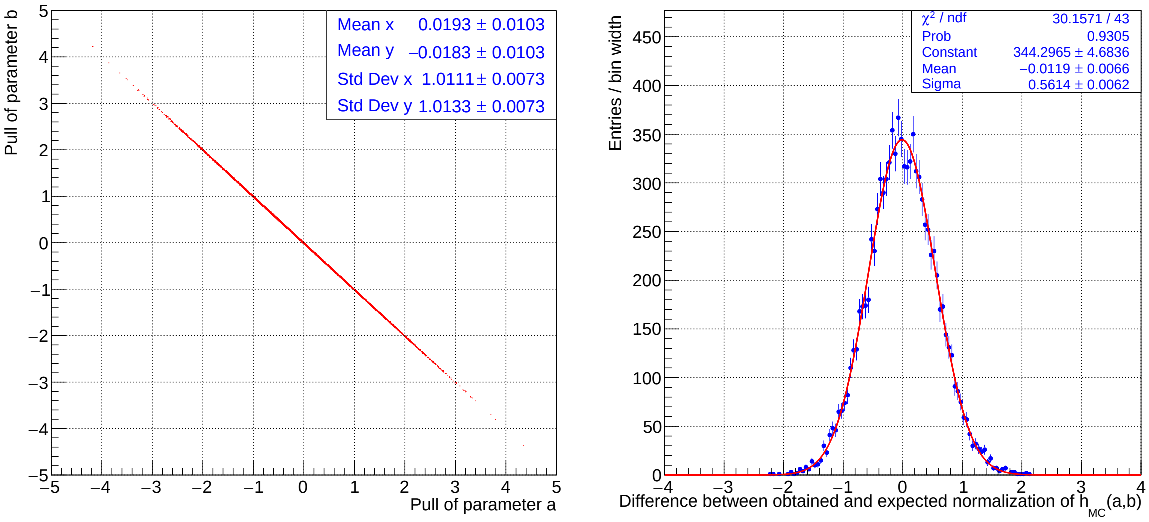

Figure B.4: Left: correlation of a and b pull distributions: almost complete anticorrelation of the parameters can be seen. Right: difference between the expected and obtained normalisation of the $h_{\mathrm{MC}}(a, b)$ histogram at the fitted $(a_{\mathrm{fit}}, b_{\mathrm{fit}})$ point.

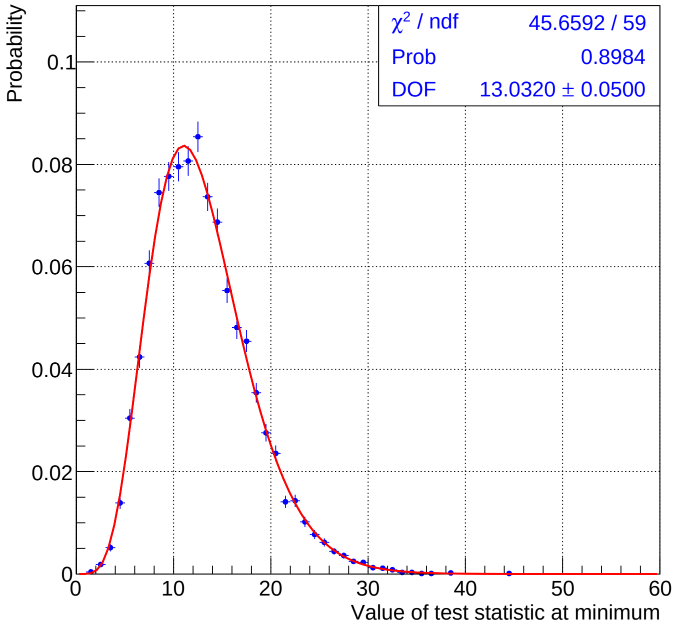

Figure B.5: Distribution of the X^2 test statistic for 10k pseudo-experiments and the fit to a χ^2 distribution. The X^2 distribution is compatible with a χ^2_{13} distribution.

For completeness, let us mention that the fitting procedure was also tested using the X^2 test statistic in the limit case of large MC sample mentioned above ($q_j^2 \to 0$) as well as using a simplistic test statistic

$$X_1^2 = \sum_{j=1}^{r} \frac{(n_j - m_j)^2}{s_j^2} \ . \tag{B.18}$$

These more approximate methods give slightly different central values and larger error estimates on a and b. We consider the three methods to be in reasonable agreement. However, due to its robustness and proper treatment of statistical errors arising from finite MC samples, we chose to use the X^2 test statistic for all results presented in this thesis.

C Treatment of discrepancies in data and MC E/p spectra

Generally speaking, any data–MC disagreement causes selection acceptances obtained from MC samples to not be applicable to data samples. The cut on the $E^i_{\text{cluster}}/p^i_{\text{track}}$ (from now only E/p) variable shown in Eq. 2.12 results in different percentage of surviving data and MC events, which alters the data and MC selection acceptances by different relative amounts.

In this appendix we describe the treatment of discrepancies between data and MC E/p spectra of pion tracks shown in Fig. 2.32. Let us firstly define several necessary variables:

- Let the $K_{3\pi}$ and $K_{\pi\mu\mu}$ selection acceptances for *data* events with (without) the E/p cut applied be $A^{\text{w/}}_{\text{DT}}(K_{\pi\mu\mu})$ ($A^{\text{w/o}}_{\text{DT}}(K_{\pi\mu\mu})$) and $A^{\text{w/}}_{\text{DT}}(K_{3\pi})$ ($A^{\text{w/o}}_{\text{DT}}(K_{3\pi})$), respectively.
- Let the $K_{3\pi}$ and $K_{\pi\mu\mu}$ selection acceptances for *MC* events with (without) the E/p cut applied be $A^{\text{w/}}_{\text{MC}}(K_{\pi\mu\mu})$ ($A^{\text{w/o}}_{\text{MC}}(K_{\pi\mu\mu})$) and $A^{\text{w/}}_{\text{MC}}(K_{3\pi})$ ($A^{\text{w/o}}_{\text{MC}}(K_{3\pi})$), respectively.
- Let the probability of a *pion* having E/p *smaller* than the default cut value in data (MC) be P_{DT} (P_{MC}).
- Let the probability of a *muon* having E/p *larger* than the default cut value in both data and MC be *negligible*. This assumption is supported by the right-most plot in Fig. 2.32.

The following relations are obvious

$$\begin{aligned}
A^{\text{w/}}_{\text{DT}}(K_{3\pi}) &= (P_{\text{DT}})^3 \cdot A^{\text{w/o}}_{\text{DT}}(K_{3\pi}),\\
A^{\text{w/}}_{\text{MC}}(K_{3\pi}) &= (P_{\text{MC}})^3 \cdot A^{\text{w/o}}_{\text{MC}}(K_{3\pi}),\\
A^{\text{w/}}_{\text{DT}}(K_{\pi\mu\mu}) &= (P_{\text{DT}})^1 \cdot A^{\text{w/o}}_{\text{DT}}(K_{\pi\mu\mu}),\\
A^{\text{w/}}_{\text{MC}}(K_{\pi\mu\mu}) &= (P_{\text{MC}})^1 \cdot A^{\text{w/o}}_{\text{MC}}(K_{\pi\mu\mu}),
\end{aligned} \tag{C.1}$$

where the powers of P_{DT} and P_{MC} are given by the number of pions produced in each decay mode. The obvious problem is that neither of the data acceptances is directly measurable. However, assuming the data and MC acceptances without the E/p cut applied are the same, namely

$$\begin{aligned}
A^{\text{w/o}}_{\text{DT}}(K_{3\pi}) &= A^{\text{w/o}}_{\text{MC}}(K_{3\pi}),\\
A^{\text{w/o}}_{\text{DT}}(K_{\pi\mu\mu}) &= A^{\text{w/o}}_{\text{MC}}(K_{\pi\mu\mu}),
\end{aligned} \tag{C.2}$$

one can rewrite Eq. C.1 in the following form

$$A_{\mathrm{DT}}^{\mathrm{w/}}(K_{3\pi}) = \left(\frac{P_{\mathrm{DT}}}{P_{\mathrm{MC}}}\right)^3 \cdot A_{\mathrm{MC}}^{\mathrm{w/}}(K_{3\pi}),$$

$$A_{\mathrm{DT}}^{\mathrm{w/}}(K_{\pi\mu\mu}) = \left(\frac{P_{\mathrm{DT}}}{P_{\mathrm{MC}}}\right)^1 \cdot A_{\mathrm{MC}}^{\mathrm{w/}}(K_{\pi\mu\mu}), \tag{C.3}$$

with the MC acceptances with the E/p cut applied easily measurable.

The final step is to realise that the $K_{3\pi}$ and $K_{\pi\mu\mu}$ acceptances enter the $\mathcal{B}(K_{\pi\mu\mu})$ computation in ratio

$$\mathcal{B}(K_{\pi\mu\mu}) = \mathcal{B}(K_{3\pi})\frac{N(K_{\pi\mu\mu})}{N(K_{3\pi})}\frac{A_{\mathrm{DT}}^{\mathrm{w/}}(K_{3\pi})}{A_{\mathrm{DT}}^{\mathrm{w/}}(K_{\pi\mu\mu})} = \mathcal{B}(K_{3\pi})\frac{N(K_{\pi\mu\mu})}{N(K_{3\pi})}\frac{A_{\mathrm{MC}}^{\mathrm{w/}}(K_{3\pi})}{A_{\mathrm{MC}}^{\mathrm{w/}}(K_{\pi\mu\mu})}\left(\frac{P_{\mathrm{DT}}}{P_{\mathrm{MC}}}\right)^2, \tag{C.4}$$

with the measured (emulated) trigger efficiencies included as parts of the data (MC) acceptances.

Since the $K_{\pi\mu\mu}$ acceptance is dependent on the values of $K_{\pi\mu\mu}$ form factor parameters, it does not enter the $K_{\pi\mu\mu}$ form factor fitting procedure directly (Appendix B). However, the $K_{3\pi}$ acceptance enters as an external parameter (together with $N(K_{3\pi})$ and $\mathcal{B}(K_{3\pi})$), which allows us to view Eq. C.4 as a necessary modification of the $A_{\mathrm{MC}}^{\mathrm{w/}}(K_{3\pi}) \equiv A_{\mathrm{old}}(K_{3\pi})$ acceptance

$$A_{\mathrm{new}}(K_{3\pi}) = \left(\frac{P_{\mathrm{DT}}}{P_{\mathrm{MC}}}\right)^2 \cdot A_{\mathrm{old}}(K_{3\pi}) \equiv f \cdot A_{\mathrm{old}}(K_{3\pi}) \ . \tag{C.5}$$

Taking the values of P_{DT} and P_{MC} from Fig. 2.32 (left), one obtains

$$P_{\mathrm{DT}} = 99.001\%, \qquad P_{\mathrm{MC}} = 99.065\%, \tag{C.6}$$

which gives

$$f = 1 - 0.0013 \ . \tag{C.7}$$

We observe that P_{DT} and P_{MC} depend differently on track momenta. This difference is discussed in subsection 2.15.9 and is treated as a systematic uncertainty.

D Trigger efficiency plots

In this appendix, measured and emulated efficiencies of Multi-track and Di-muon trigger conditions are shown.

Multi-track trigger efficiencies start with Fig. D.1 and end with Fig. D.13. They are shown for data and $K_{3\pi}$ MC events passing our $K_{3\pi}$ selection described in section 2.8 and section 2.9 as functions of various relevant variables.

Di-muon trigger efficiencies start with Fig. D.14 and end with Fig. D.27. They are shown for data, $K_{3\pi}$ MC with two $\pi \to \mu\nu$ decays and $K_{\pi\mu\mu}$ MC events passing our $K_{\pi\mu\mu}$ selection described in section 2.10 as functions of various relevant variables.

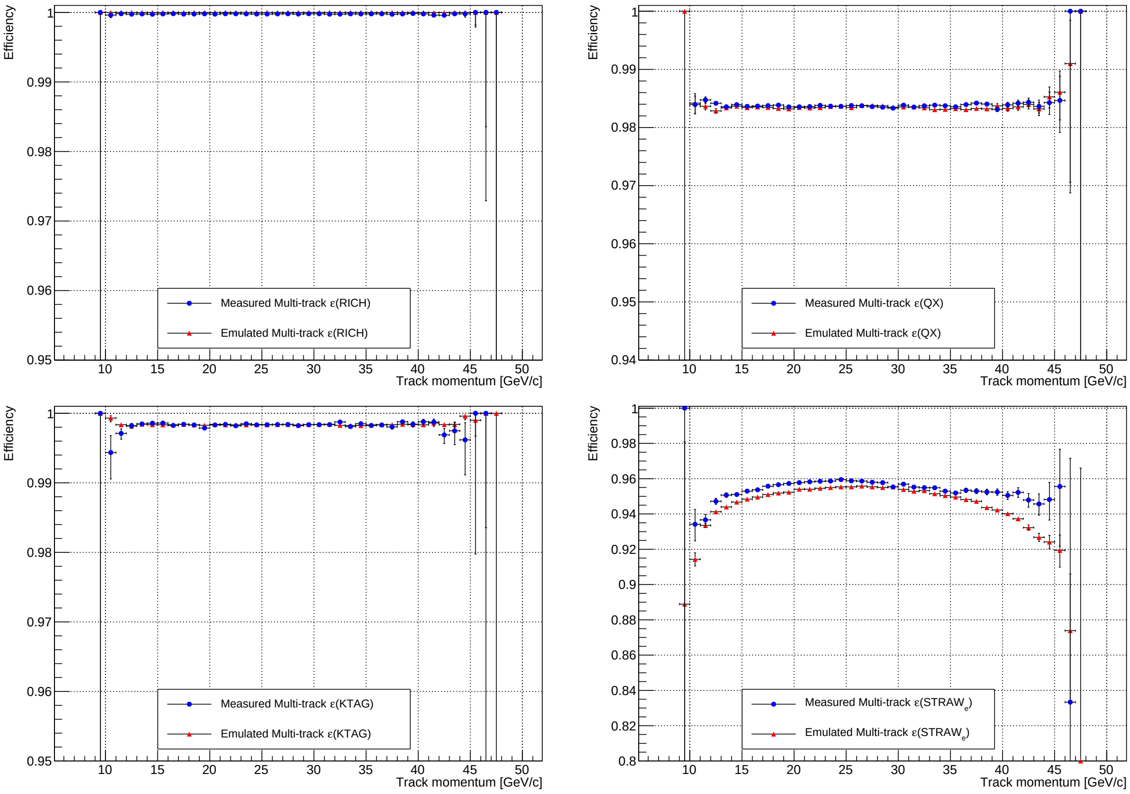

Figure D.1: ε(Multi-track) versus track momenta.

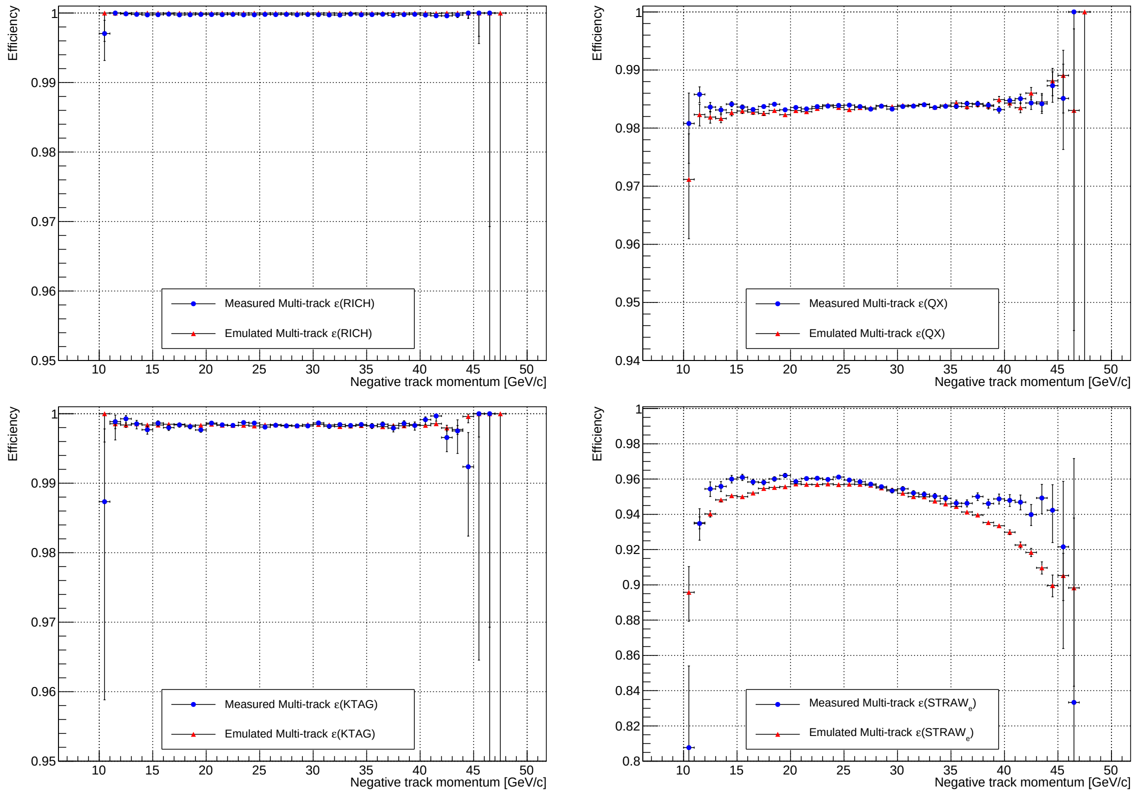

Figure D.2: ε(Multi-track) versus negative track momenta.

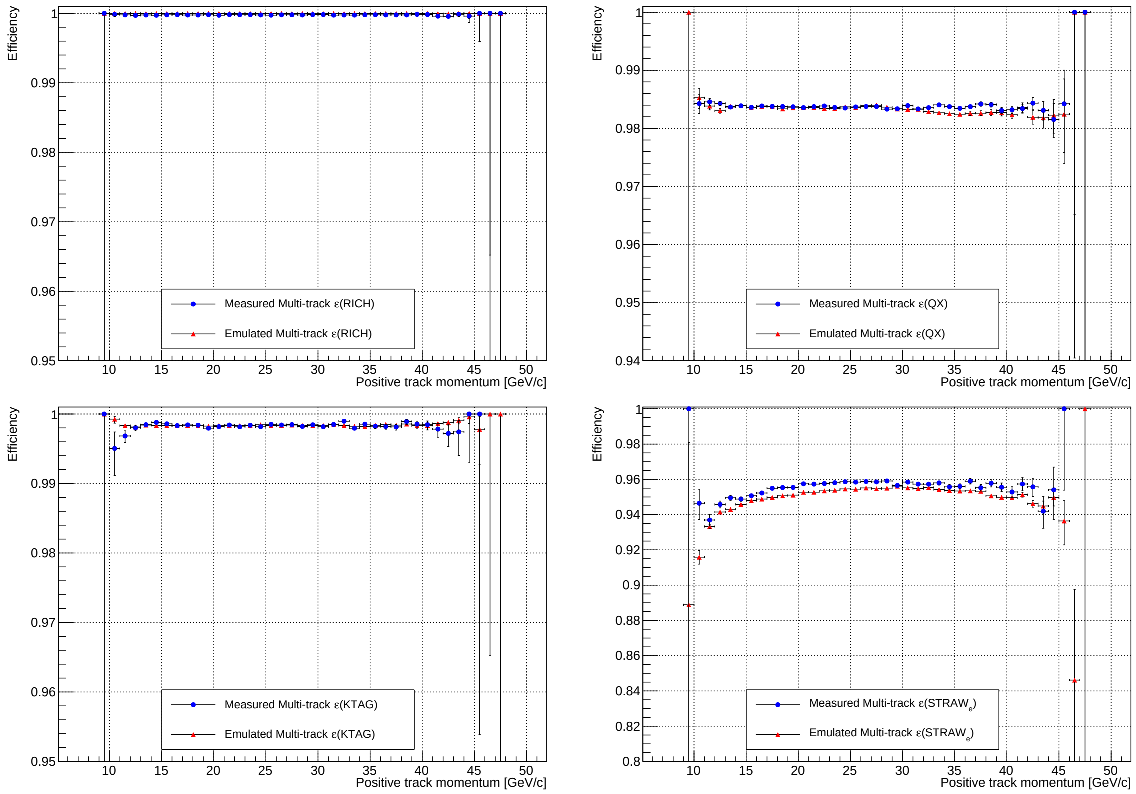

Figure D.3: ε(Multi-track) versus positive track momenta.

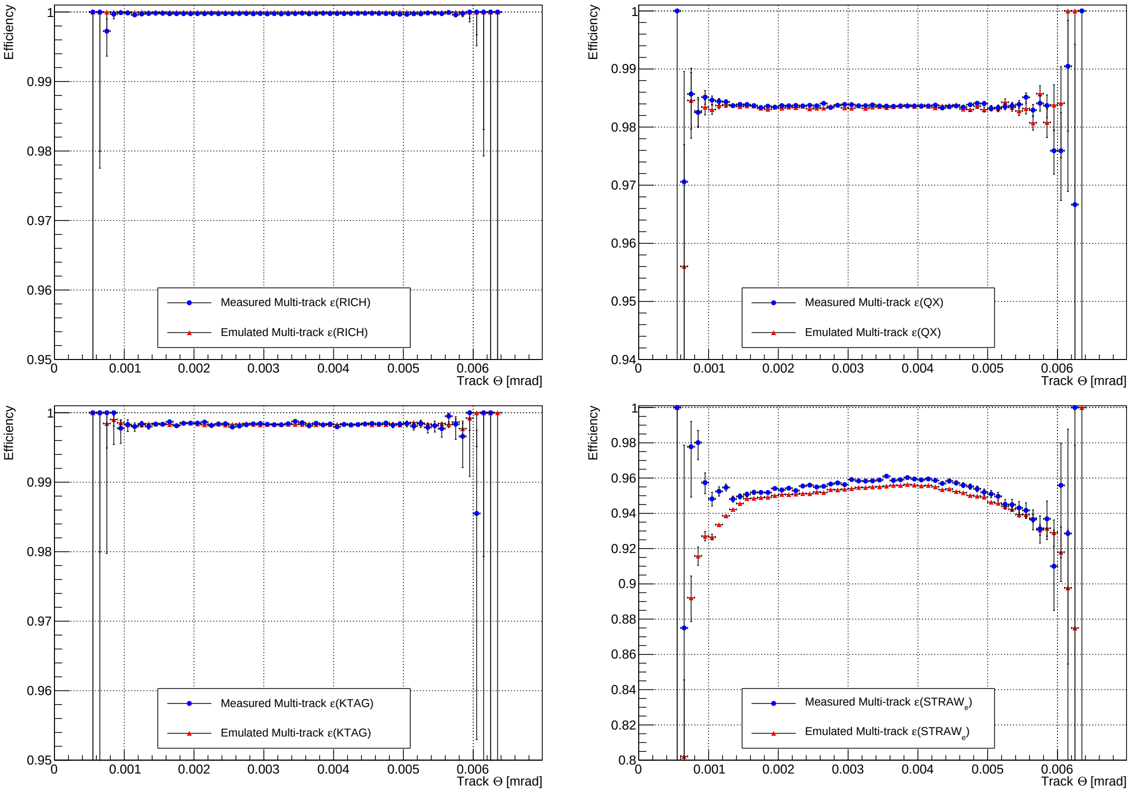

Figure D.4: ε(Multi-track) versus track Θ, defined in section 2.8.

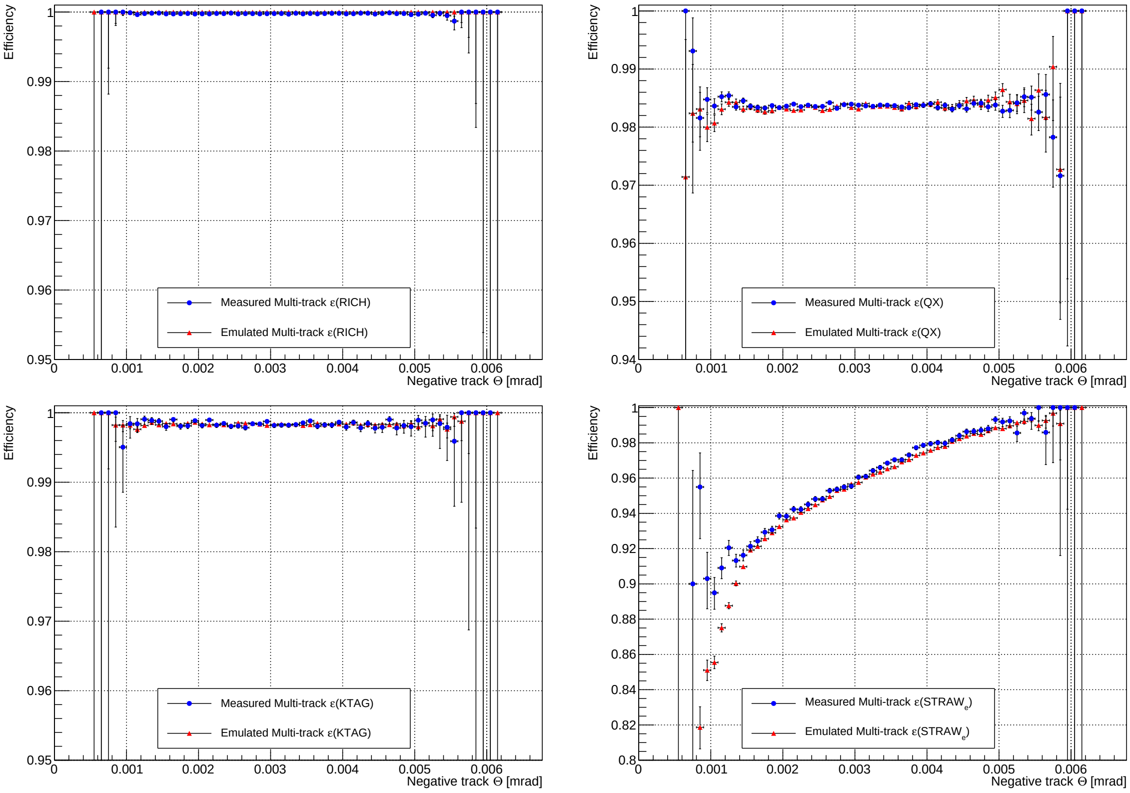

Figure D.5: ε(Multi-track) versus negative track Θ, defined in section 2.8.

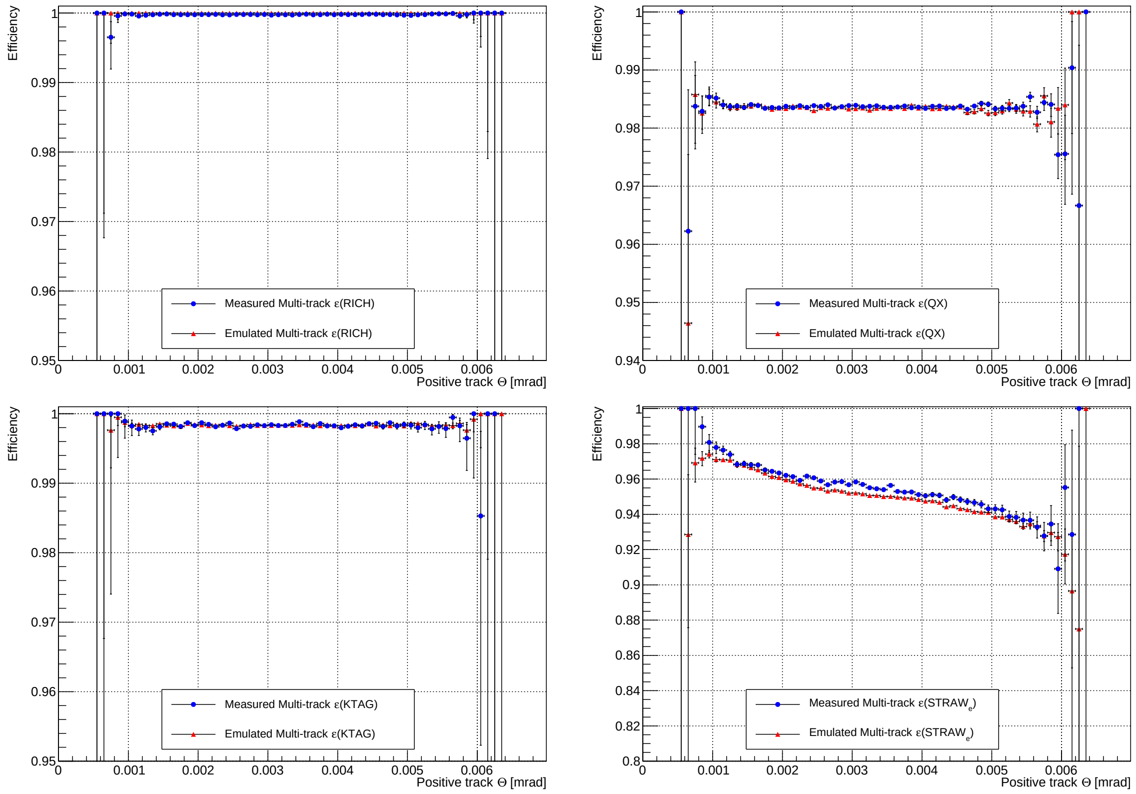

Figure D.6: ε(Multi-track) versus positive track Θ, defined in section 2.8.

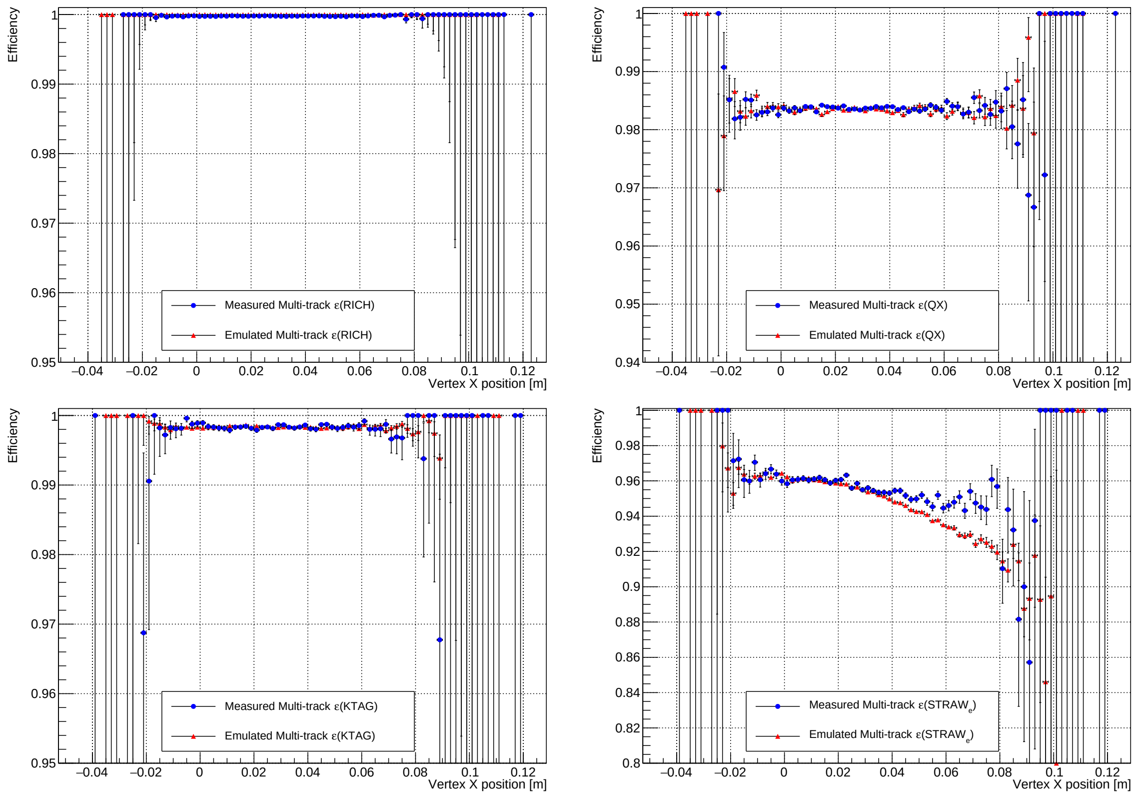

Figure D.7: ε(Multi-track) versus X-position of the decay vertex.

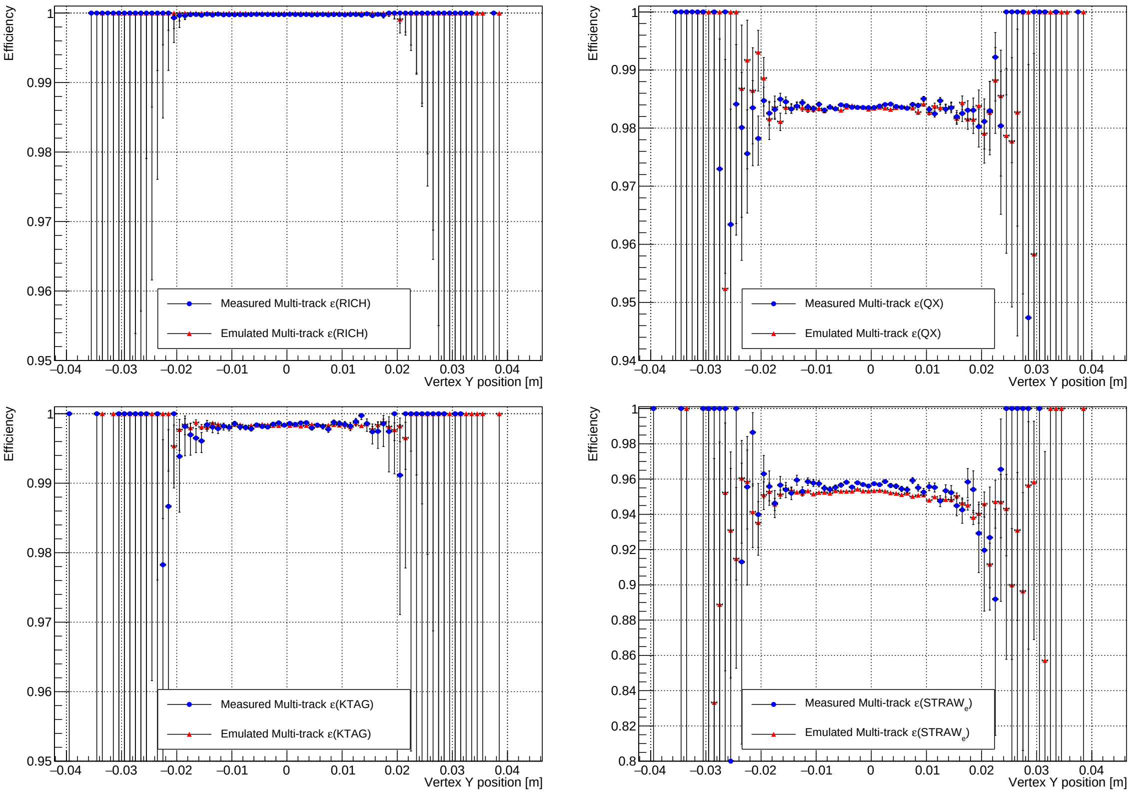

Figure D.8: ε(Multi-track) versus Y-position of the decay vertex.

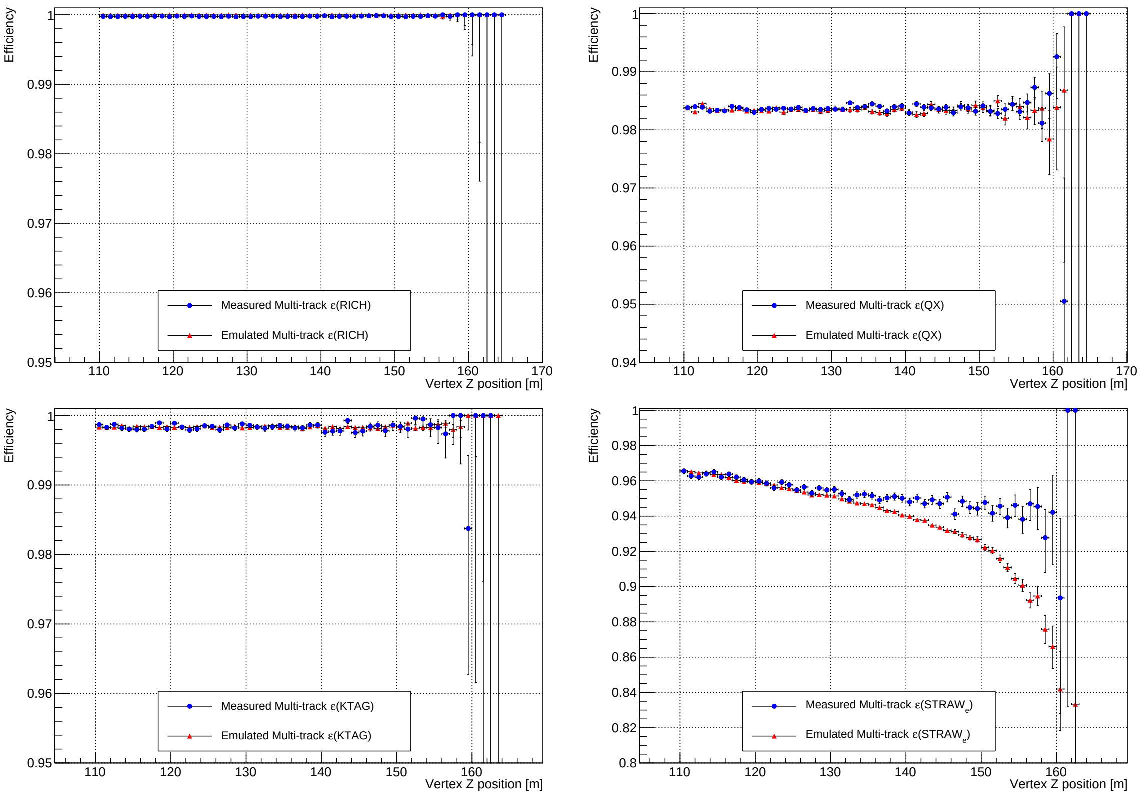

Figure D.9: ε(Multi-track) versus Z-position of the decay vertex.

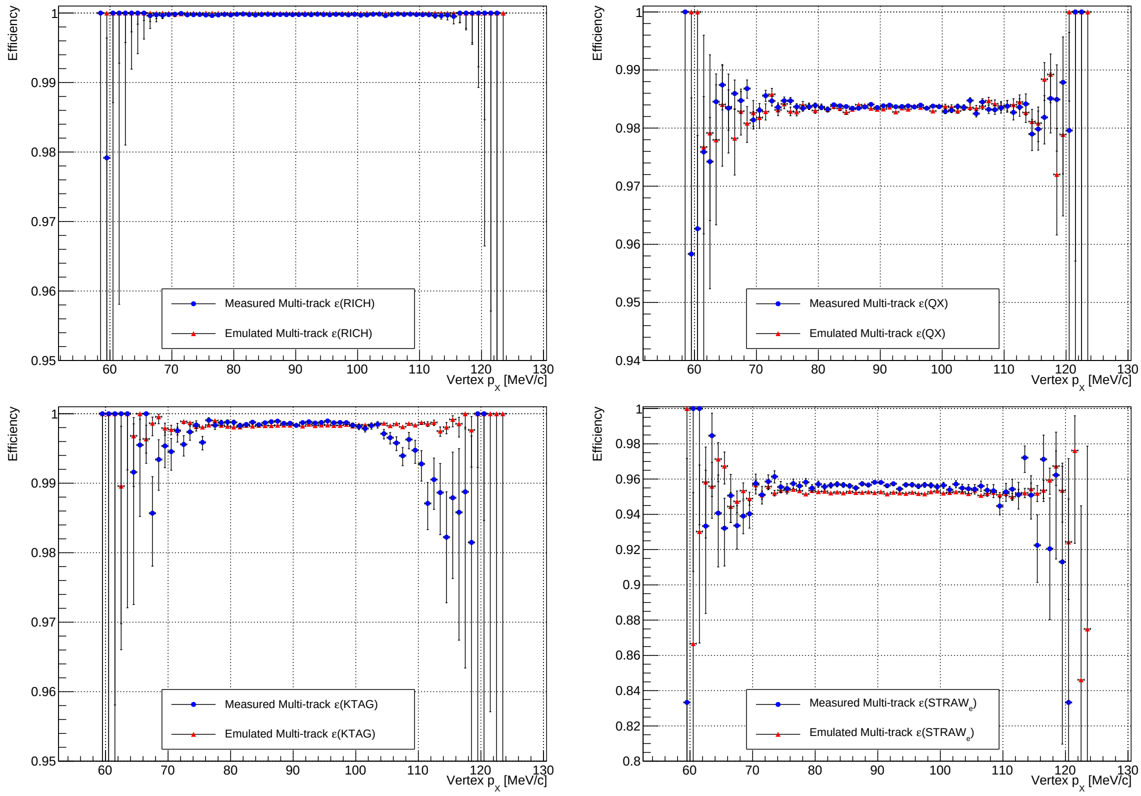

Figure D.10: ε(Multi-track) versus vertex p_X.

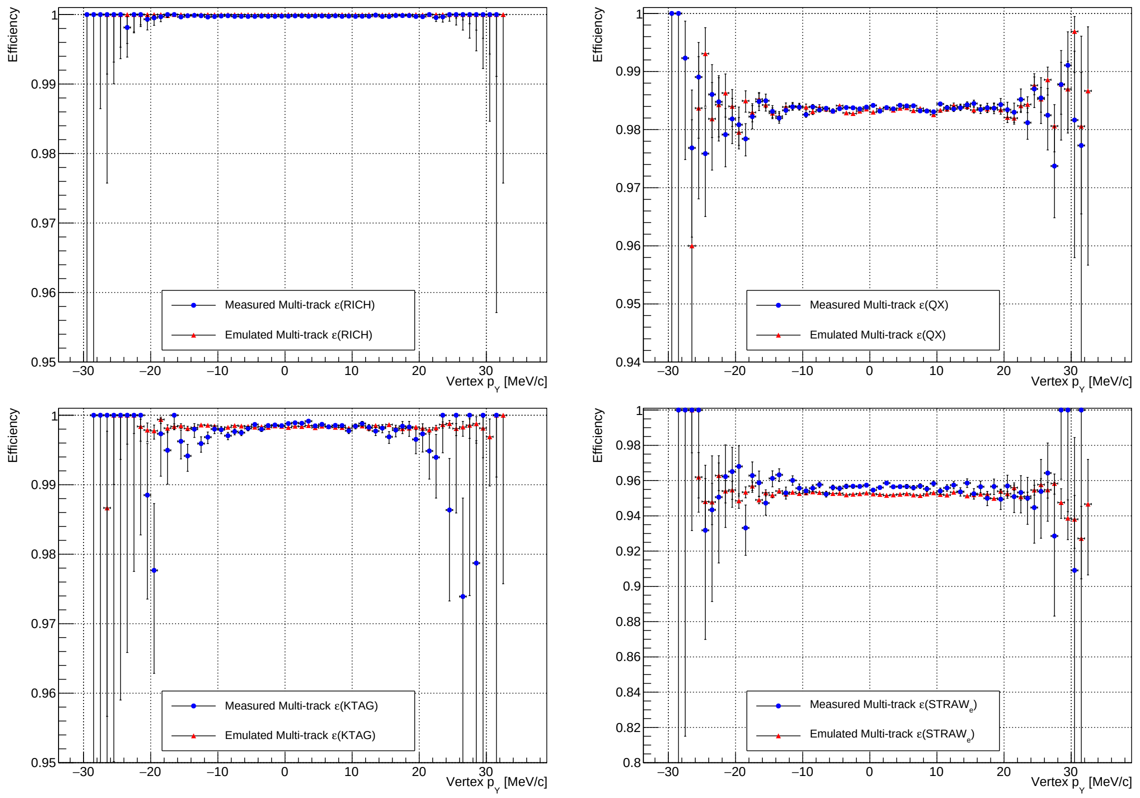

Figure D.11: ε(Multi-track) versus vertex p_Y.

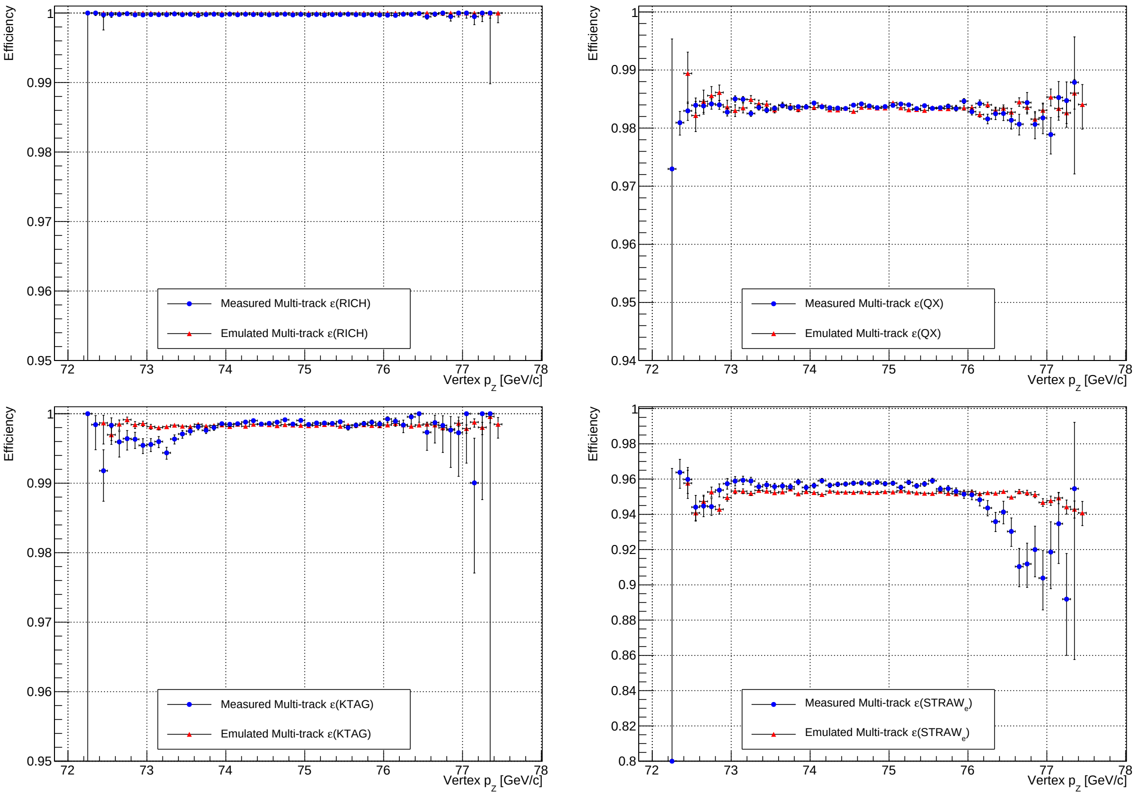

Figure D.12: ε(Multi-track) versus vertex p_Z.

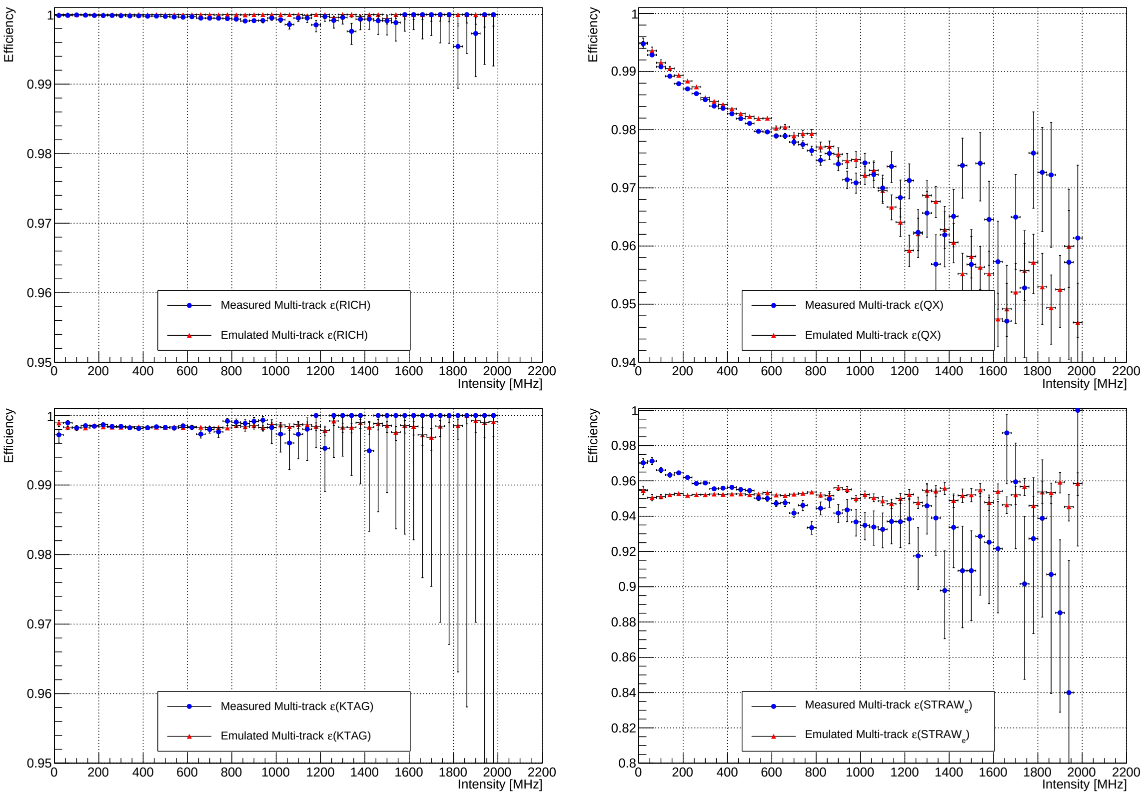

Figure D.13: ε(Multi-track) versus beam intensity.

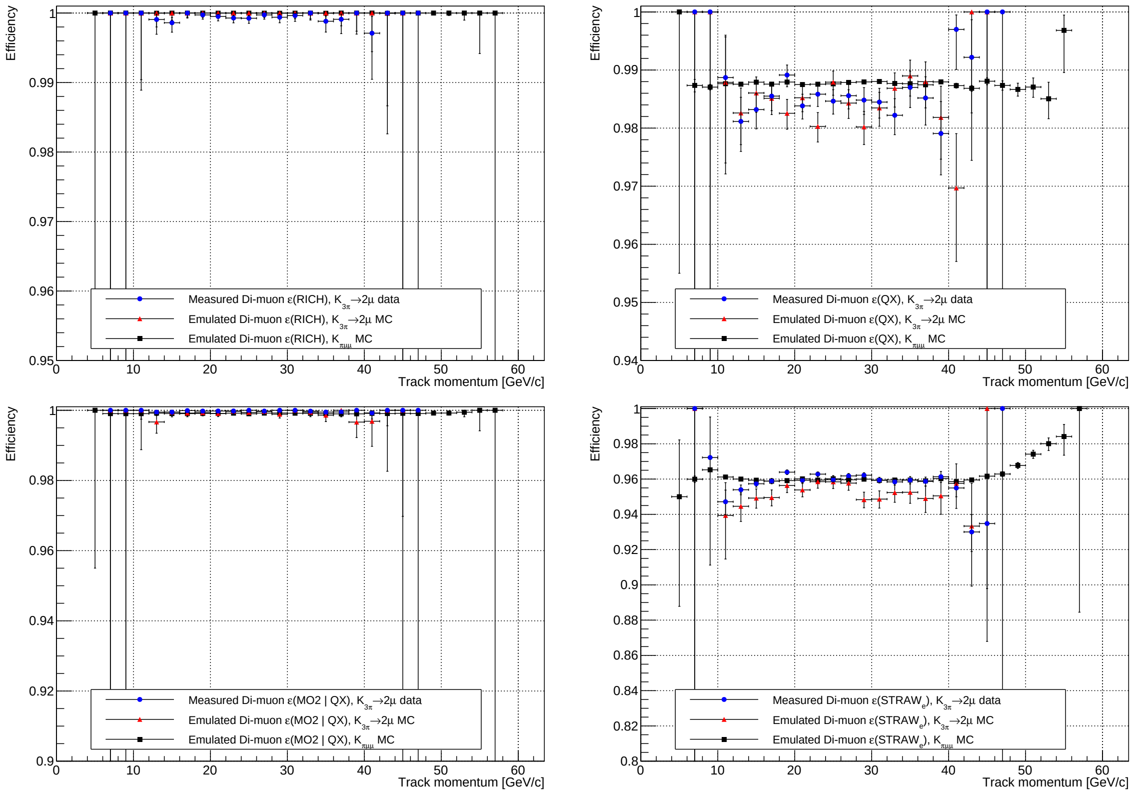

Figure D.14: ε(Di-muon) versus track momenta.

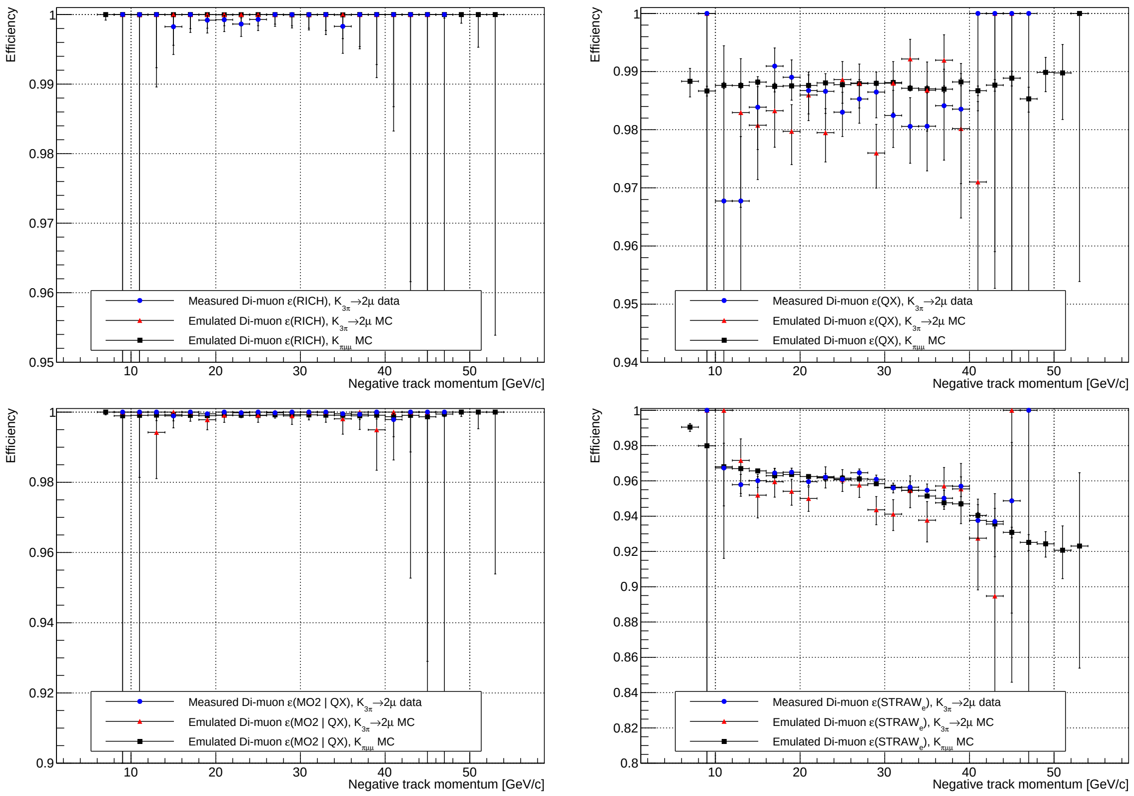

Figure D.15: ε(Di-muon) versus negative track momenta.

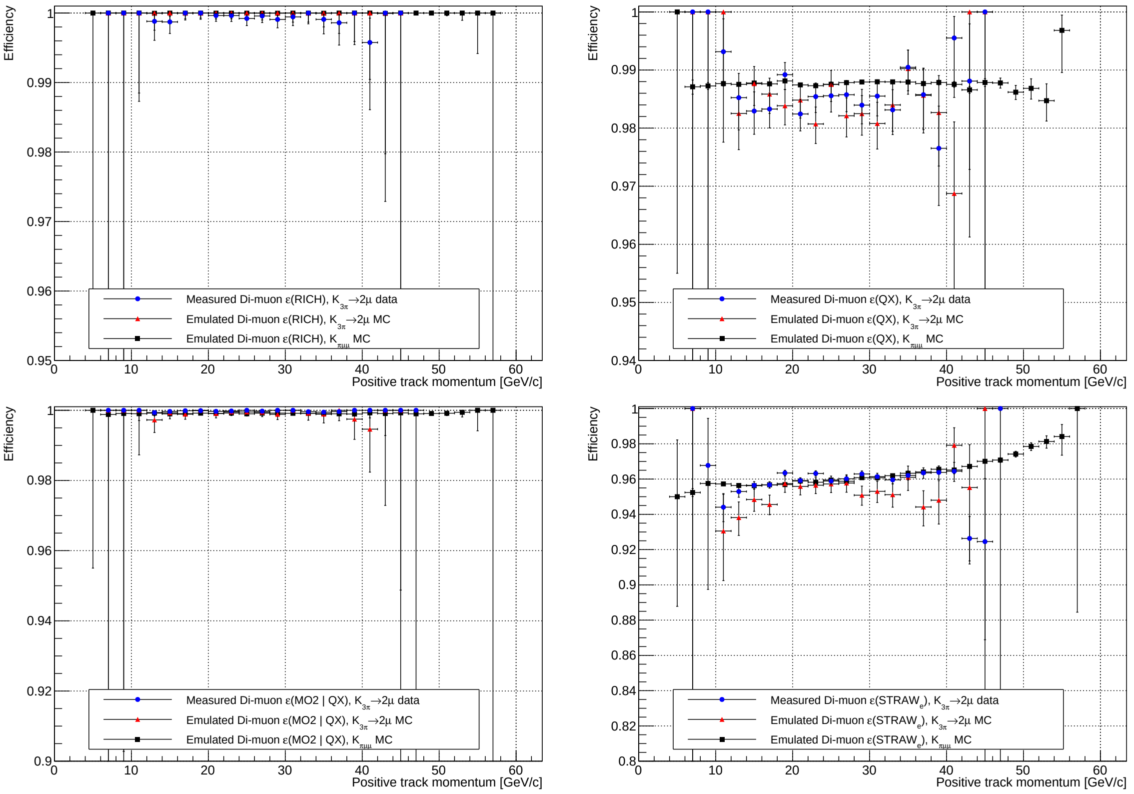

Figure D.16: ε(Di-muon) versus positive track momenta.

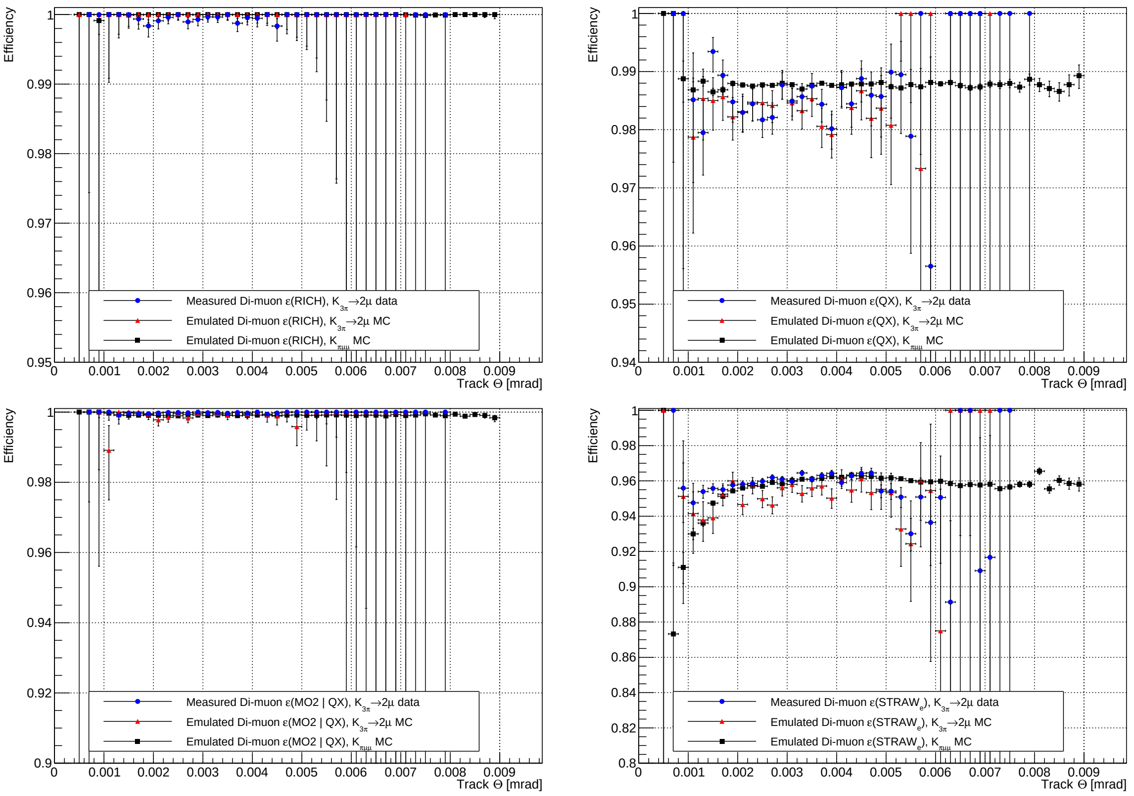

Figure D.17: ε(Di-muon) versus track Θ, defined in section 2.8.

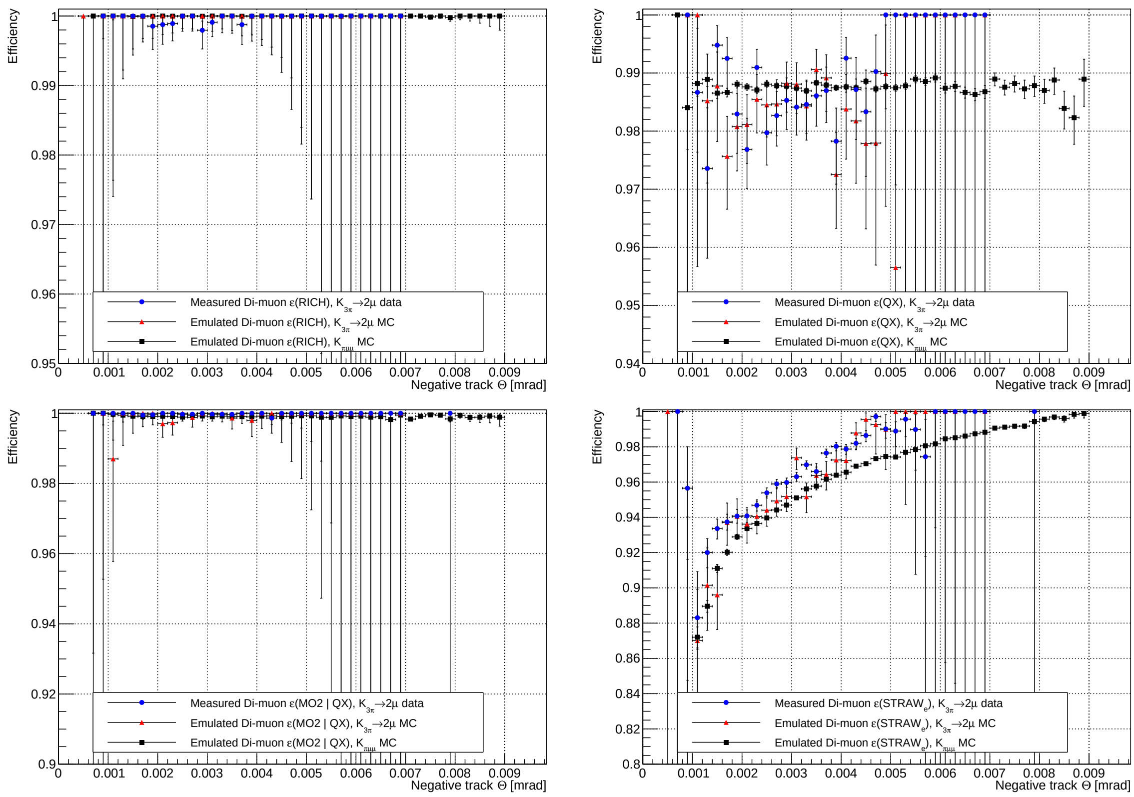

Figure D.18: ε(Di-muon) versus negative track Θ, defined in section 2.8.

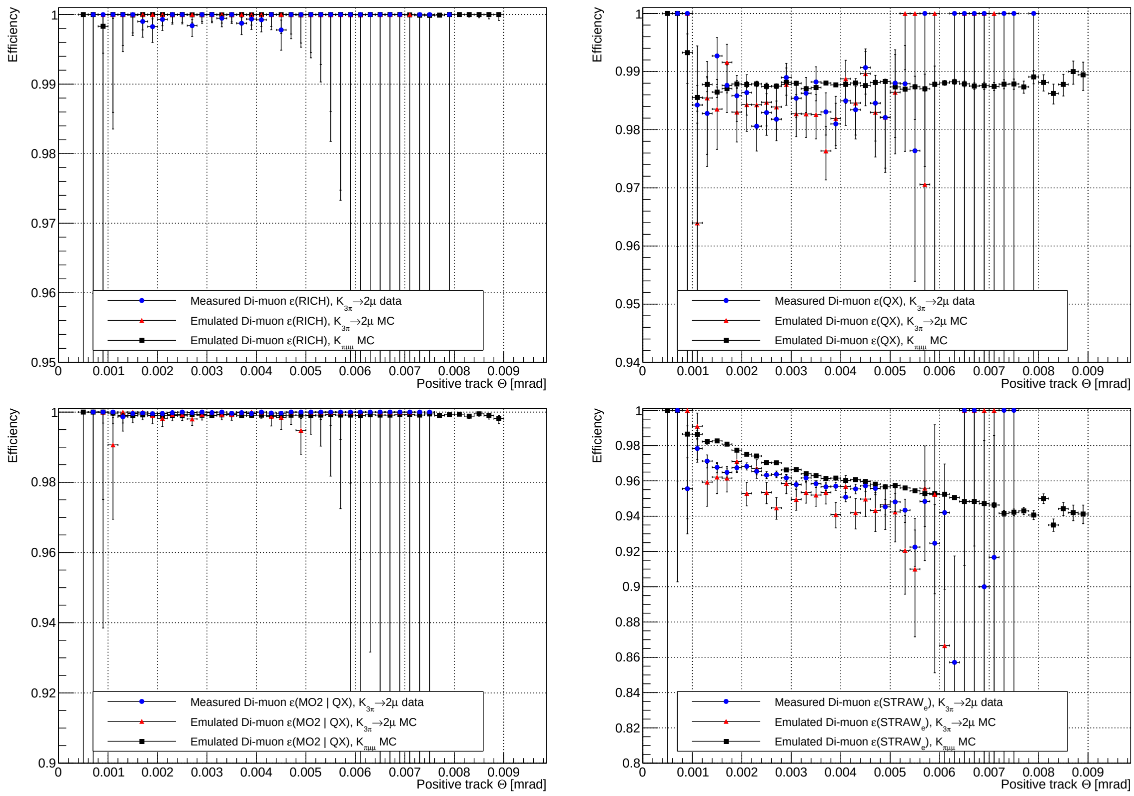

Figure D.19: ε(Di-muon) versus positive track Θ, defined in section 2.8.

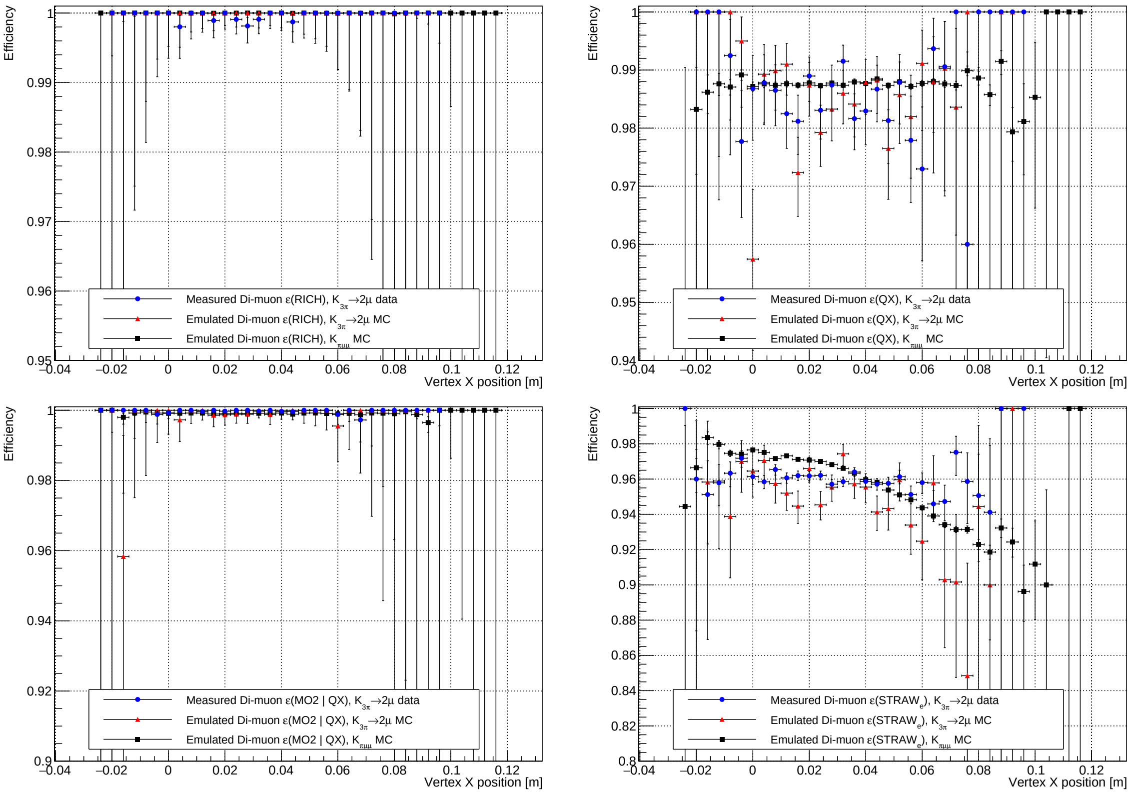

Figure D.20: ε(Di-muon) versus X-position of the decay vertex.

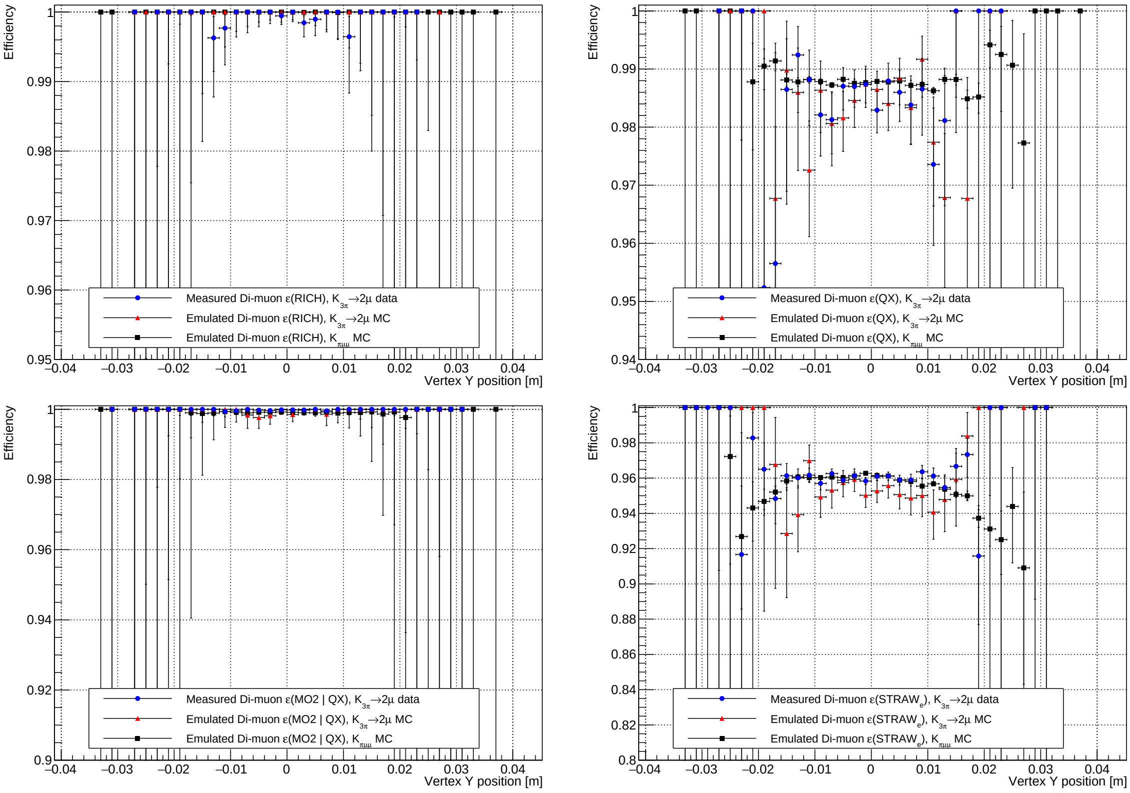

Figure D.21: ε(Di-muon) versus Y-position of the decay vertex.

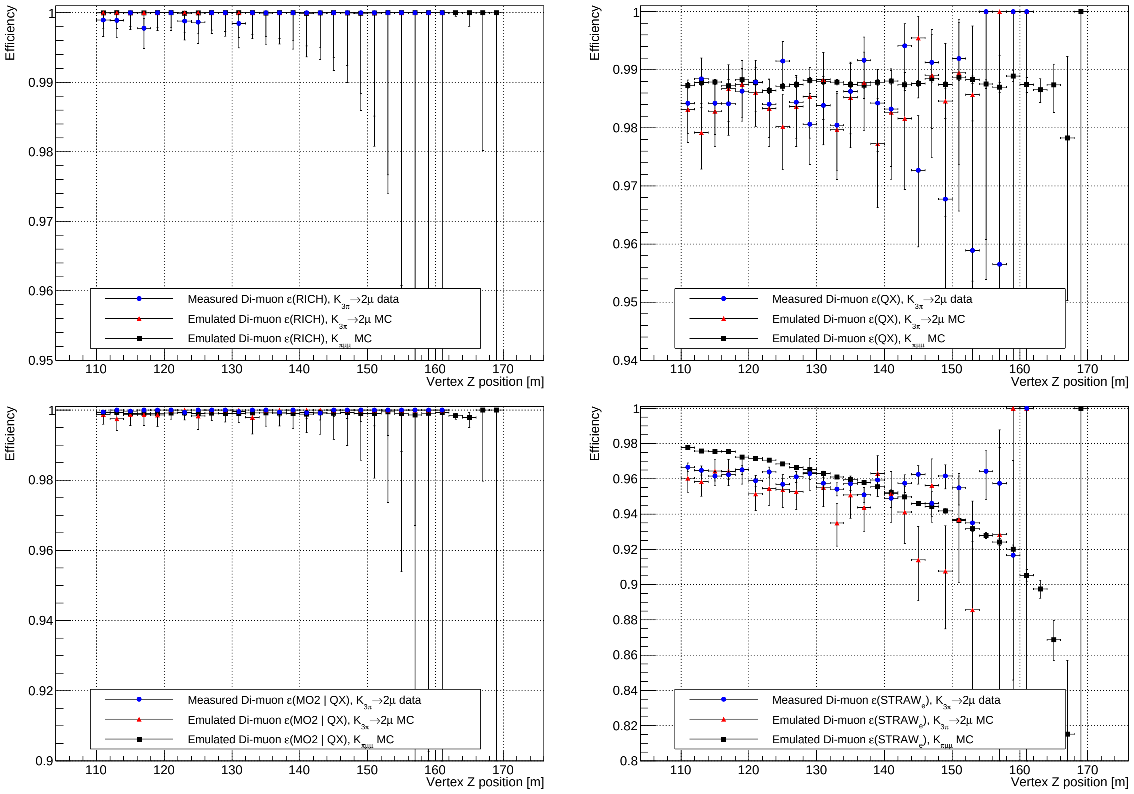

Figure D.22: ε(Di-muon) versus Z-position of the decay vertex.

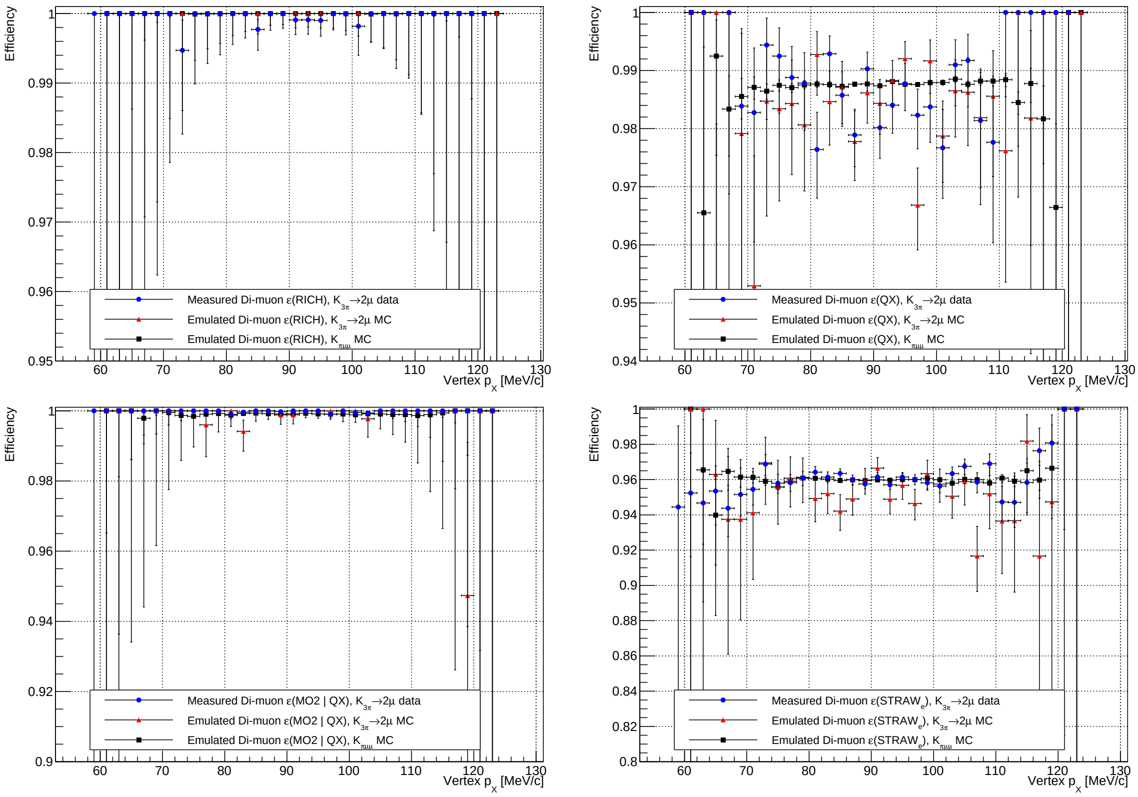

Figure D.23: ε(Di-muon) versus vertex p_X.

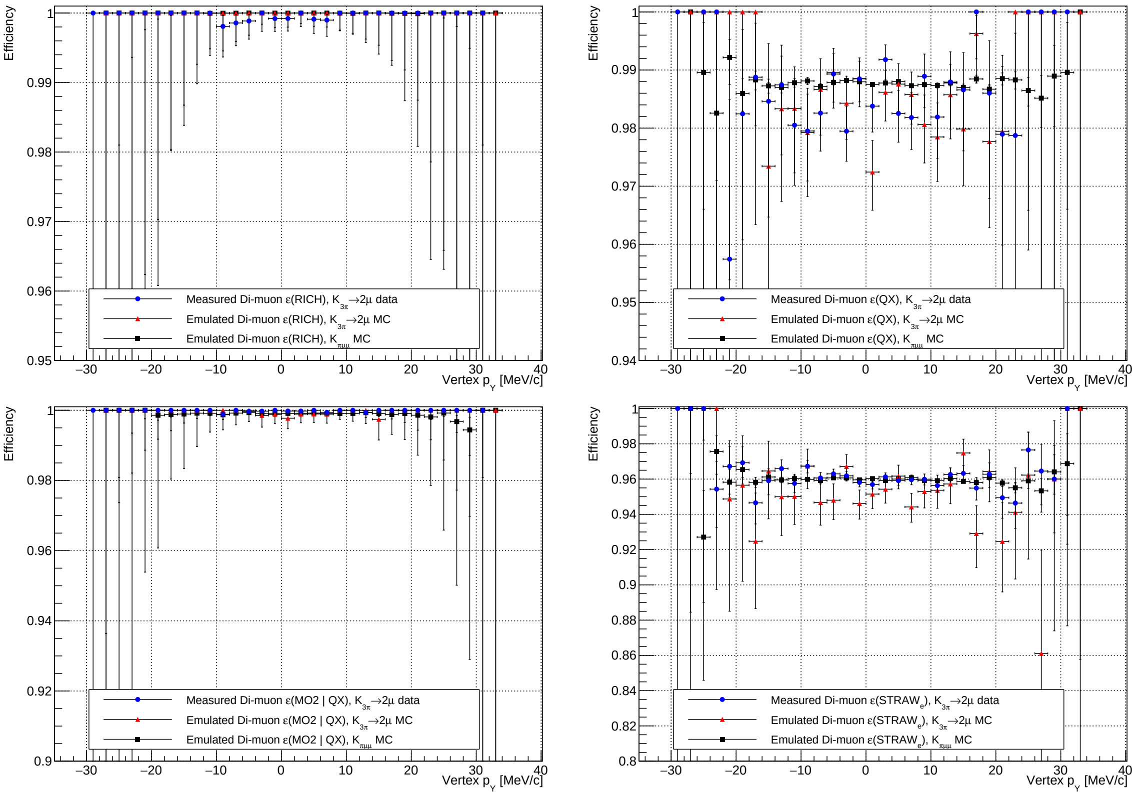

Figure D.24: ε(Di-muon) versus vertex p_Y.

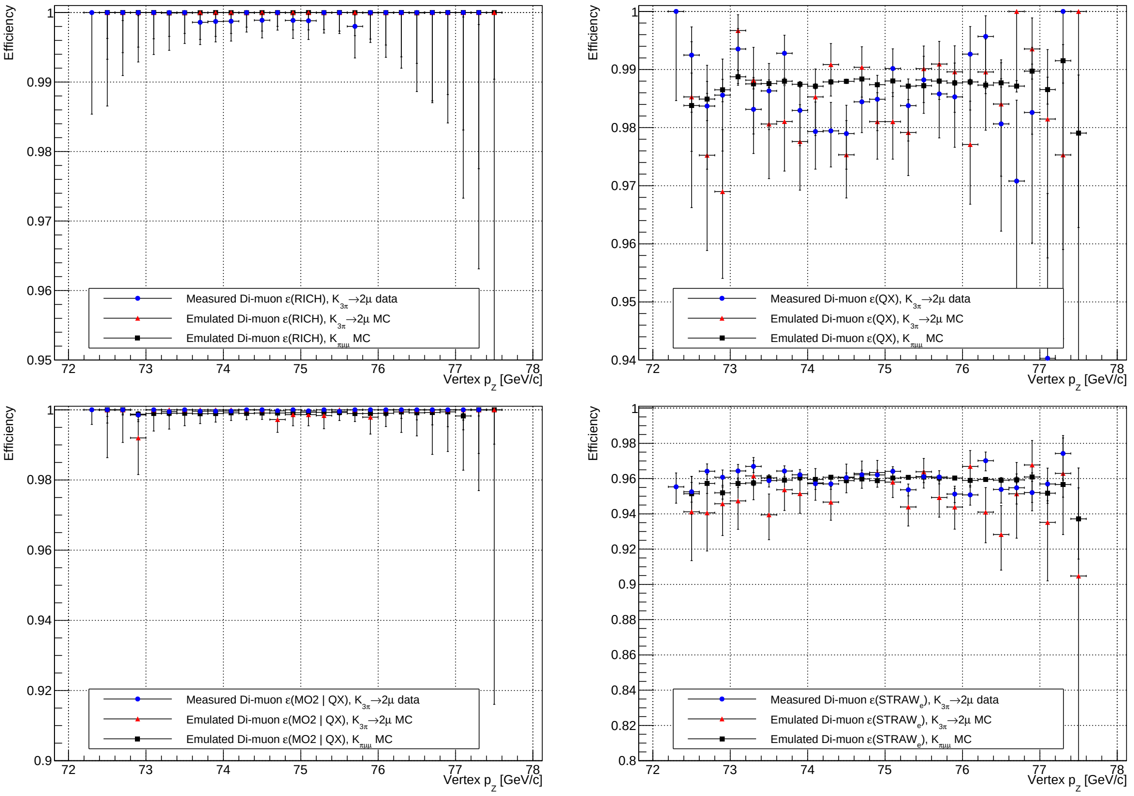

Figure D.25: ε(Di-muon) versus vertex p_Z.

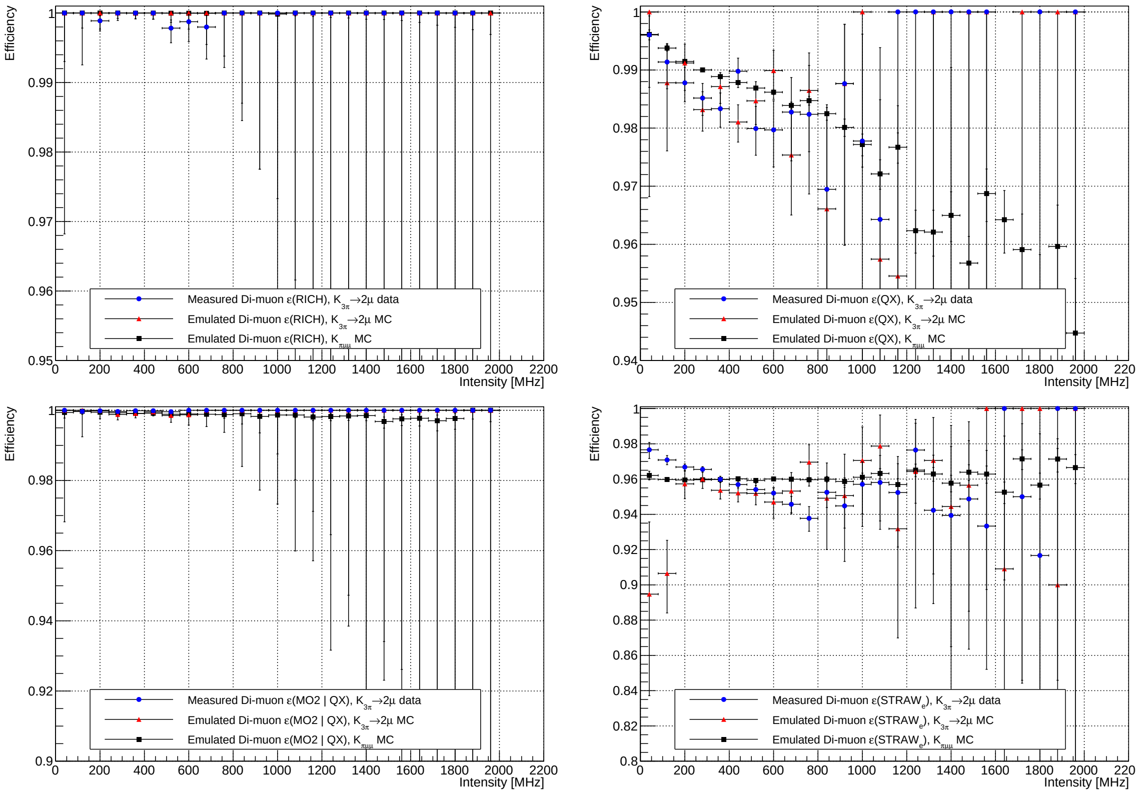

Figure D.26: ε(Di-muon) versus beam intensity.

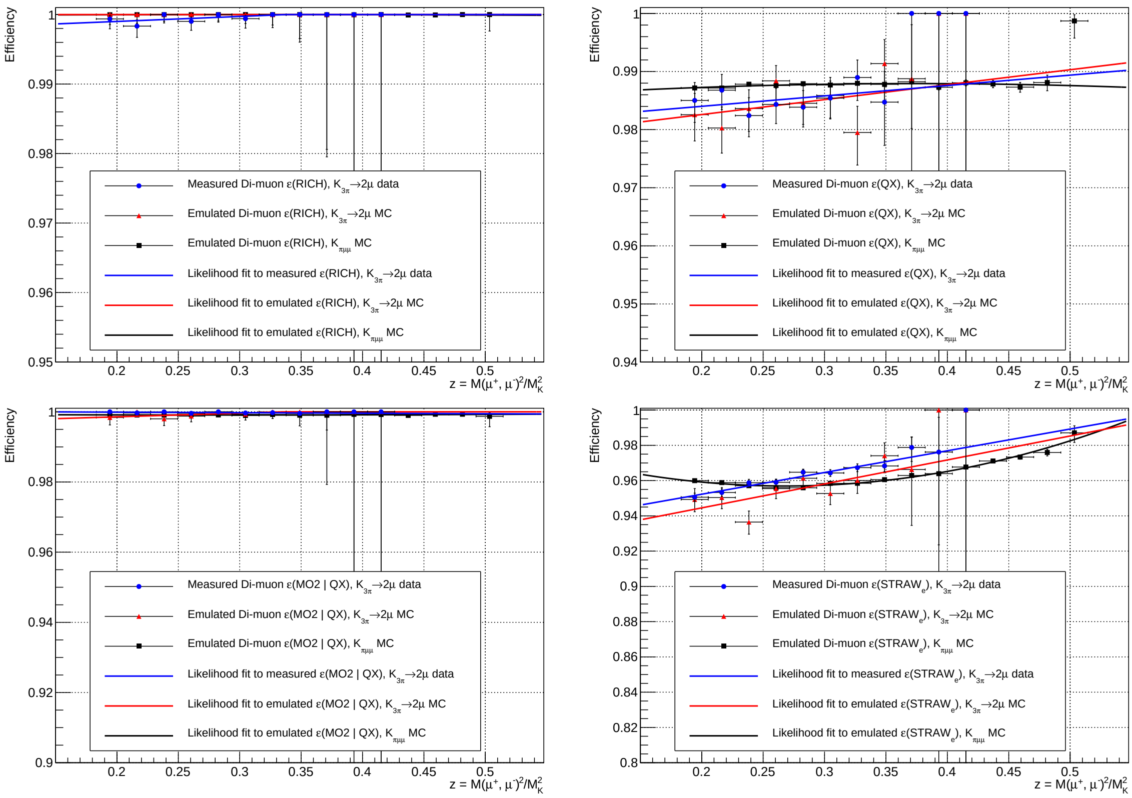

Figure D.27: ε(Di-muon) versus kinematic variable z defined in Eq. 1.28.

Bibliography

[1] S. L. Glashow, *Partial-symmetries of weak interactions*, Nuclear Physics, 22 (1961), pp. 579 – 588.

[2] S. Weinberg, *A model of leptons*, Phys. Rev. Lett., 19 (1967), pp. 1264–1266.

[3] A. Salam, *Weak and Electromagnetic Interactions*, Conf.Proc., C680519 (1968), pp. 367–377.

[4] G. 't Hooft and M. Veltman, *Regularization and renormalization of gauge fields*, Nuclear Physics B, 44 (1972), pp. 189 – 213.

[5] G. Aad et al., *Observation of a new particle in the search for the Standard Model Higgs boson with the ATLAS detector at the LHC*, Phys.Lett., B716 (2012), pp. 1–29, arXiv:1207.7214.

[6] S. Chatrchyan et al., *Observation of a new boson at a mass of 125 GeV with the CMS experiment at the LHC*, Phys.Lett., B716 (2012), pp. 30–61, arXiv:1207.7235.

[7] G. Aad et al., *The ATLAS Experiment at the CERN Large Hadron Collider*, JINST, 3 (2008), p. S08003.

[8] S. Chatrchyan et al., *The CMS Experiment at the CERN LHC*, JINST, 3 (2008), p. S08004.

[9] L. Evans and P. Bryant, *LHC Machine*, JINST, 3 (2008), p. S08001.

[10] T. A. collaboration, *Measurements of the higgs boson production and decay rates and constraints on its couplings from a combined atlas and cms analysis of the lhc pp collision data at* $\sqrt{s} = 7$ *and* 8 *tev*, Journal of High Energy Physics, 2016 (2016), p. 45.

[11] F. Hasert et al., *Observation of neutrino-like interactions without muon or electron in the gargamelle neutrino experiment*, Nuclear Physics B, 73 (1974), pp. 1 – 22.

[12] D. Hanneke, S. F. Hoogerheide, and G. Gabrielse, *Cavity Control of a Single-Electron Quantum Cyclotron: Measuring the Electron Magnetic Moment*, Phys. Rev., A83 (2011), p. 052122, 1009.4831.

[13] J. de Swart, G. Bertone, and J. van Dongen, *How Dark Matter Came to Matter*, (2017), 1703.00013. [Nature Astron.1,0059(2017)].

[14] Y. Fukuda et al., *Measurement of the flux and zenith angle distribution of upward through going muons by Super-Kamiokande*, Phys. Rev. Lett., 82 (1999), pp. 2644–2648, hep-ex/9812014.

[15] K. Eguchi et al., *First results from KamLAND: Evidence for reactor anti-neutrino disappearance*, Phys. Rev. Lett., 90 (2003), p. 021802, hep-ex/0212021.

[16] Q. R. Ahmad et al., *Direct evidence for neutrino flavor transformation from neutral current interactions in the Sudbury Neutrino Observatory*, Phys. Rev. Lett., 89 (2002), p. 011301, nucl-ex/0204008.

[17] L. Canetti, M. Drewes, and M. Shaposhnikov, *Matter and antimatter in the universe*, New Journal of Physics, 14 (2012), p. 095012.

[18] M. Tanabashi et al., *Review of particle physics*, Phys. Rev. D, 98 (2018), p. 030001.

[19] S. L. Glashow, J. Iliopoulos, and L. Maiani, *Weak Interactions with Lepton-Hadron Symmetry*, Phys. Rev., D2 (1970), pp. 1285–1292.

[20] T. L. Collaboration, *The lhcb detector at the lhc*, Journal of Instrumentation, 3 (2008), p. S08005.

[21] R. Aaij et al., *Measurement of Form-Factor-Independent Observables in the Decay* $B^0 \to K^{*0}\mu^+\mu^-$, Phys. Rev. Lett., 111 (2013), p. 191801, 1308.1707.

[22] W. Altmannshofer and D. M. Straub, *New physics in* $b \to s$ *transitions after LHC run 1*, Eur. Phys. J., C75 (2015), p. 382, 1411.3161.

[23] R. Aaij et al., *Test of lepton universality using* $B^+ \to K^+\ell^+\ell^-$ *decays*, Phys. Rev. Lett., 113 (2014), p. 151601, 1406.6482.

[24] R. Aaij et al., *Measurement of the ratio of branching fractions* $\mathcal{B}(\bar{b}^0 \to D^{*+}\tau^-\overline{\nu}_\tau)/\mathcal{B}(\bar{b}^0 \to D^{*+}\mu^-\overline{\nu}_\mu)$, Phys. Rev. Lett., 115 (2015), p. 111803.

[25] ——, *Test of Lepton Flavor Universality by the measurement of the* $B^0 \to D^{*-}\tau^+\nu_\tau$ *branching fraction using three-prong* τ *decays*, Phys. Rev., D97 (2018), p. 072013, 1711.02505.

[26] E. Cortina Gil et al., *The beam and detector of the NA62 experiment at cern*, Journal of Instrumentation, 12 (2017), p. P05025.

[27] G. D. ROCHESTER and C. C. Butler, *Evidence for the existence of new unstable elementary particles.*, Nature, 160 4077 (1947), pp. 855–7.

[28] T. D. Lee and C. N. Yang, *Question of parity conservation in weak interactions*, Phys. Rev., 104 (1956), pp. 254–258.

[29] C. S. Wu, E. Ambler, R. W. Hayward, D. D. Hoppes, and R. P. Hudson, *Experimental test of parity conservation in beta decay*, Phys. Rev., 105 (1957), pp. 1413–1415.

[30] A. Pais, *Some remarks on the v-particles*, Phys. Rev., 86 (1952), pp. 663–672.

[31] M. Gell-Mann, *Isotopic spin and new unstable particles*, Phys. Rev., 92 (1953), pp. 833–834.

[32] J. H. Christenson, J. W. Cronin, V. L. Fitch, and R. Turlay, *Evidence for the* 2π *decay of the* k_2^0 *meson*, Phys. Rev. Lett., 13 (1964), pp. 138–140.

[33] M. Kobayashi and T. Maskawa, *Cp-violation in the renormalizable theory of weak interaction*, Progress of Theoretical Physics, 49 (1973), pp. 652–657.

[34] N. Cabibbo, *Unitary symmetry and leptonic decays*, Phys. Rev. Lett., 10 (1963), pp. 531–533.

[35] J. Batley et al., *A precision measurement of direct cp violation in the decay of neutral kaons into two pions*, Physics Letters B, 544 (2002), pp. 97 – 112.

[36] G. Anzivino, *Measurement of direct CP violation by NA48*, in Multiparticle dynamics. Proceedings, 31st International Symposium, ISMD 2001, Datong, China, September 1-7, 2001, 2001, pp. 7–14, hep-ph/0111393.

[37] E. Abouzaid et al., *Precise Measurements of Direct CP Violation, CPT Symmetry,*

and Other Parameters in the Neutral Kaon System, Phys. Rev., D83 (2011), p. 092001, 1011.0127.

[38] G. D'Ambrosio and G. Isidori, *CP violation in kaon decays*, Int. J. Mod. Phys., A13 (1998), pp. 1–94, hep-ph/9611284.

[39] A. J. Buras and M. Jamin, *epsilon-prime / epsilon at the NLO: 10 years later*, JHEP, 01 (2004), p. 048, hep-ph/0306217.

[40] A. J. Buras, M. Gorbahn, S. Jäger, and M. Jamin, *Improved anatomy of* ε'/ε *in the Standard Model*, JHEP, 11 (2015), p. 202, 1507.06345.

[41] E. Cortina Gil et al., *First search for* $K^+ \to \pi^+\nu\bar{\nu}$ *using the decay-in-flight technique*, (2018), 1811.08508.

[42] J. K. Ahn et al., *Search for the* $K_L\to\pi^0\nu\bar{\nu}$ *and* $K_L\to\pi^0X^0$ *decays at the J-PARC KOTO experiment*, (2018), 1810.09655.

[43] A. J. Buras, *Weak Hamiltonian, CP violation and rare decays*, in Probing the standard model of particle interactions. Proceedings, Summer School in Theoretical Physics, NATO Advanced Study Institute, 68th session, Les Houches, France, July 28-September 5, 1997. Pt. 1, 2, 1998, pp. 281–539, hep-ph/9806471.

[44] G. Buchalla and A. J. Buras, *The rare decays* $K \to \pi\nu\bar{\nu}$*,* $B \to X\nu\bar{\nu}$ *and* $B \to l^+l^-$*: An Update*, Nucl. Phys., B548 (1999), pp. 309–327, hep-ph/9901288.

[45] G. Isidori, F. Mescia, and C. Smith, *Light-quark loops in K —> pi nu anti-nu*, Nucl. Phys., B718 (2005), pp. 319–338, hep-ph/0503107.

[46] A. J. Buras, D. Buttazzo, J. Girrbach-Noe, and R. Knegjens, $K^+ \to \pi^+\nu\nu$ *and* $K_L \to \pi^0\nu\nu$ *in the standard model: status and perspectives*, Journal of High Energy Physics, 2015 (2015), p. 33.

[47] R. Aaij et al., *Measurement of the* $B_s^0 \to \mu^+\mu^-$ *branching fraction and effective lifetime and search for* $B^0 \to \mu^+\mu^-$ *decays*, Phys. Rev. Lett., 118 (2017), p. 191801, 1703.05747.

[48] K. De Bruyn, R. Fleischer, R. Knegjens, P. Koppenburg, M. Merk, A. Pellegrino, and N. Tuning, *Probing New Physics via the* $B_s^0 \to \mu^+\mu^-$ *Effective Lifetime*, Phys. Rev. Lett., 109 (2012), p. 041801, 1204.1737.

[49] C. Bobeth, M. Gorbahn, T. Hermann, M. Misiak, E. Stamou, and M. Steinhauser, $B_{s,d} \to l^+l^-$ *in the Standard Model with Reduced Theoretical Uncertainty*, Phys. Rev. Lett., 112 (2014), p. 101801, 1311.0903.

[50] A. J. Buras, F. Schwab, and S. Uhlig, *Waiting for precise measurements of* $K^+ \to \pi^+\nu\bar{\nu}$ *and* $K_L \to \pi^0\nu\bar{\nu}$, Rev. Mod. Phys., 80 (2008), pp. 965–1007, hep-ph/0405132.

[51] A. J. Buras, D. Buttazzo, and R. Knegjens, $K \to \pi\nu\bar{\nu}$ *and* ε'/ε *in simplified new physics models*, JHEP, 11 (2015), p. 166, 1507.08672.

[52] N. Arkani-Hamed, A. G. Cohen, and H. Georgi, *Electroweak symmetry breaking from dimensional deconstruction*, Phys. Lett., B513 (2001), pp. 232–240, hep-ph/0105239.

[53] N. Arkani-Hamed, A. G. Cohen, E. Katz, and A. E. Nelson, *The Littlest Higgs*, JHEP, 07 (2002), p. 034, hep-ph/0206021.

[54] C. Promberger, S. Schatt, and F. Schwab, *Flavor-changing neutral current effects and cp violation in the minimal 3-3-1 model*, Phys. Rev. D, 75 (2007), p. 115007.

[55] A. J. Buras, P. Gambino, M. Gorbahn, S. Jager, and L. Silvestrini, *epsilon-prime / epsilon and rare K and B decays in the MSSM*, Nucl. Phys., B592 (2001), pp. 55–91, hep-ph/0007313.

[56] T. Blažek and P. Maták, *Left–left squark mixing, $K^+ \to \pi^+\nu\bar{\nu}$ and minimal supersymmetry with large tanβ*, Int. J. Mod. Phys., A29 (2014), p. 1450162, 1410.0055.

[57] M. Bordone, D. Buttazzo, G. Isidori, and J. Monnard, *Probing lepton-flavour universality with $k \to \pi\nu\bar{\nu}$ decays*, The European Physical Journal C, 77 (2017), p. 618.

[58] B. Beckford, *Present status of the search for the $K_L^0 \to \pi^0\nu\bar{\nu}$ decay with the KOTO detector at J-PARC*, in Proceedings, Meeting of the APS Division of Particles and Fields (DPF 2017): Fermilab, Batavia, Illinois, USA, July 31 - August 4, 2017, 2017, 1710.01412.

[59] J. K. Ahn et al., *Experimental study of the decay K0(L) —> pi0 nu nu-bar*, Phys. Rev., D81 (2010), p. 072004, 0911.4789.

[60] A. V. Artamonov et al., *Study of the decay $K^+ \to \pi^+\nu\bar{\nu}$ in the momentum region* $140 < P_\pi < 199$ *MeV/c*, Phys. Rev., D79 (2009), p. 092004, 0903.0030.

[61] A. Datta, B. Dutta, S. Liao, D. Marfatia, and L. E. Strigari, *Neutrino scattering and b anomalies from hidden sector portals*, Journal of High Energy Physics, 2019 (2019), p. 91.

[62] S. Descotes-Genon, T. Hurth, J. Matias, and J. Virto, *Optimizing the basis of $b \to k^* l^+ l^-$ observables in the full kinematic range*, Journal of High Energy Physics, 2013 (2013), p. 137.

[63] S. Descotes-Genon, L. Hofer, J. Matias, and J. Virto, *On the impact of power corrections in the prediction of $B \to K^*\mu^+\mu^-$ observables*, JHEP, 12 (2014), p. 125, 1407.8526.

[64] C. Bobeth, G. Hiller, and G. Piranishvili, *Angular distributions of $\bar{B} \to \bar{K}e^+e^-$ decays*, JHEP, 12 (2007), p. 040, 0709.4174.

[65] S. Fajfer, J. F. Kamenik, and I. Nisandzic, *On the $B \to D^*\tau\bar{\nu}_\tau$ Sensitivity to New Physics*, Phys. Rev., D85 (2012), p. 094025, 1203.2654.

[66] L. C. Tunstall, A. Crivellin, G. D'Ambrosio, and M. Hoferichter, *Probing lepton flavour (universality) violation at NA62 and future kaon experiments*, J. Phys. Conf. Ser., 800 (2017), p. 012014, 1611.00495.

[67] G. Ecker, A. Pich, and E. de Rafael, *$K \to \pi l^+ l^-$ Decays in the Effective Chiral Lagrangian of the Standard Model*, Nucl. Phys., B291 (1987), p. 692.

[68] G. D'Ambrosio, G. Ecker, G. Isidori, and H. Neufeld, *Radiative nonleptonic kaon decays*, in 2nd DAPHNE Physics Handbook:265-313, 1994, pp. 265–313, hep-ph/9411439.

[69] G. D'Ambrosio, G. Ecker, G. Isidori, and J. Portoles, *The Decays $K \to \pi l^+ l^-$ beyond leading order in the chiral expansion*, JHEP, 08 (1998), p. 004, hep-ph/9808289.

[70] S. Friot, D. Greynat, and E. De Rafael, *Rare kaon decays revisited*, Phys. Lett., B595 (2004), pp. 301–308, hep-ph/0404136.

[71] A. Z. Dubnickova, S. Dubnicka, E. Goudzovski, V. N. Pervushin, and M. Secansky, *Kaon decay probe of the weak static interaction*, Phys. Part. Nucl. Lett., 5 (2008), pp. 76–84, hep-ph/0611175.

[72] N. H. Christ, X. Feng, A. Juttner, A. Lawson, A. Portelli, and C. T. Sachrajda, *First exploratory calculation of the long-distance contributions to the rare kaon decays $K \to \pi\ell^+\ell^-$*, Phys. Rev., D94 (2016), p. 114516, 1608.07585.

[73] G. Isidori, *Soft-photon corrections in multi-body meson decays*, Eur. Phys. J., C53 (2008), pp. 567–571, 0709.2439.

[74] J. R. Batley et al., *New measurement of the $K^\pm \to \pi^\pm\mu^+\mu^-$ decay*, Phys. Lett., B697 (2011), pp. 107–115, 1011.4817.

[75] ——, *Precise measurement of the $K^\pm \to \pi^\pm e^+e^-$ decay*, Phys. Lett., B677 (2009), pp. 246–254, 0903.3130.

[76] H. Ma et al., *New measurement of the rare decay $K^+ \to \pi^+\mu^+\mu^-$*, Phys. Rev. Lett., 84 (2000), pp. 2580–2583.

[77] R. Appel et al., *A New measurement of the properties of the rare decay $K^+ \to \pi^+e^+e^-$*, Phys. Rev. Lett., 83 (1999), pp. 4482–4485, hep-ex/9907045.

[78] V. Cirigliano, G. Ecker, H. Neufeld, A. Pich, and J. Portoles, *Kaon Decays in the Standard Model*, Rev. Mod. Phys., 84 (2012), p. 399, 1107.6001.

[79] S. Adler et al., *Observation of the decay $K^+ \to \pi^+\mu^+\mu^-$*, Phys. Rev. Lett., 79 (1997), pp. 4756–4759.

[80] H. K. Park et al., *Observation of the decay $K^- \to \pi^-\mu^+\mu^-$ and measurements of the branching ratios for $K^\pm \to \pi^\pm\mu^+\mu^-$*, Phys. Rev. Lett., 88 (2002), p. 111801.

[81] C. Alliegro et al., *Study of the decay $K^+ \to \pi^+e^+e^-$*, Phys. Rev. Lett., 68 (1992), pp. 278–281.

[82] L. Bician, *$K^+ \to \pi^+\mu^+\mu^-$ Analysis on 2017 Sample A*, NA62 Internal Note, NA62-19-05 (2019).

[83] R. Brun and F. Rademakers, *ROOT: An object oriented data analysis framework*, Nucl. Instrum. Meth., A389 (1997), pp. 81–86.

[84] F. Hahn, F. Ambrosino, A. Ceccucci, H. Danielsson, N. Doble, F. Fantechi, A. Kluge, C. Lazzeroni, M. Lenti, G. Ruggiero, M. Sozzi, P. Valente, and R. Wanke, *NA62: Technical Design Document.* NA62 Internal Note, `http://cds.cern.ch/record/1404985`, Dec 2010.

[85] J. R. Fry, G. Ruggiero, and F. Bergsma, *Precision magnetic field mapping for CERN experiment NA62*, Journal of Physics G: Nuclear and Particle Physics, 43 (2016), p. 125004.

[86] B. Angelucci, E. Pedreschi, M. Sozzi, and F. Spinella, *Tel62: an integrated trigger and data acquisition board*, in 2011 IEEE Nuclear Science Symposium Conference Record, Oct 2011, pp. 823–826.

[87] G. Haefeli, A. Bay, A. Gong, H. Gong, M. Muecke, N. Neufeld, and O. Schneider, *The LHCb DAQ interface board TELL1*, Nucl. Instrum. Meth., A560 (2006), pp. 494–502.

[88] J. Christiansen, *HPTDC High Performance Time to Digital Converter*, tech. rep., CERN, Geneva, 2004. Version 2.2 for HPTDC version 1.3.

[89] D. Moraes, W. Bonivento, N. Pelloux, and W. Riegler, *The CARIOCA Front End Chip for the LHCb muon chambers*, (2003).

[90] A. Ceccucci, R. Fantechi, P. Farthouat, G. Lamanna, J. Rouet, V. Ryjov, and S. Venditti, *The NA62 liquid Krypton calorimeter's new readout system*, Journal of Instrumentation, 9 (2014), p. C01047.

[91] R. O. Duda and P. E. Hart, *Use of the hough transformation to detect lines and curves in pictures*, Commun. ACM, 15 (1972), pp. 11–15.

[92] K. L. Brown and F. C. Iselin, *Decay TURTLE (Trace Unlimited Rays Through Lumped Elements): A Computer Program for Simulating Charged Particle Beam Transport Systems, Including Decay Calculations*, (1974).

[93] S. Agostinelli et al., *GEANT4: A Simulation toolkit*, Nucl. Instrum. Meth., A506 (2003), pp. 250–303.

[94] J. R. Batley et al., *Search for direct CP violation in the decays $K^{\pm} \to 3\pi^{\pm}$*, Phys. Lett., B634 (2006), pp. 474–482, hep-ex/0602014.

[95] L. Robertson, *Computing Services for LHC: From Clusters to Grids*, Springer Berlin Heidelberg, Berlin, Heidelberg, 2012, pp. 69–89.

[96] R. E. Kalman, *A new approach to linear filtering and prediction problems*, Transactions of the ASME–Journal of Basic Engineering, 82 (1960), pp. 35–45.

[97] P. Billoir, R. Frühwirth, and M. Regler, *Track element merging strategy and vertex fitting in complex modular detectors*, Nuclear Instruments and Methods in Physics Research Section A: Accelerators, Spectrometers, Detectors and Associated Equipment, 241 (1985), pp. 115 – 131.

[98] J. e. a. Charles, *CKMfitter Group*, Eur. Phys. J., C41 (2005), pp. 1–131, hep-ph/0406184.

[99] K. Pearson and J. Blakeman, *On the Theory of Contingency and Its Relation to Association and Normal Correlation*, no. pt. 1–4 in A Mathematical Theory of Random Migration, Dulau and Company, 1906.

[100] N. D. Gagunashvili, *Comparison of weighted and unweighted histograms*, ArXiv Physics e-prints, (2006), physics/0605123.

[101] F. James and M. Roos, *Minuit: A System for Function Minimization and Analysis of the Parameter Errors and Correlations*, Comput. Phys. Commun., 10 (1975), pp. 343–367.